



University of Maribor Press

7th Symposium on Applied Electromagnetics **SAEM`18** **C o n f e r e n c e P r o c e e d i n g s**

Editors

Sebastijan Seme, Miralem Hadžiselimović & Bojan Štumberger





University of Maribor

Faculty of Energy Technology

7th Symposium on Applied Electromagnetics SAEM'18

Conference Proceedings

Editors

Sebastijan Seme

Miralem Hadžiselimović

Bojan Štumberger

February 2019

Title	7 th Symposium on Applied Electromagnetics SAEM`18
Subtitle	Conference Proceedings
Editors	<p>assos. prof. Sebastijan Seme, PhD (University of Maribor, Faculty of Energy Technology)</p> <p>full prof. Miralem Hadžiselimović, PhD (University of Maribor, Faculty of Energy Technology)</p> <p>full prof. Bojan Štumberger, PhD (University of Maribor, Faculty of Energy Technology)</p>
Technical editor	Jan Perša, ME (University of Maribor Press)
Cover Designer	Jan Perša, ME (University of Maribor Press)
Cover graphics	SAEM`18
Graphic material	Autorhs
Conference	7 th Symposium on Applied Electromagnetics SAEM`18
Date and location	17 th to 20 th June, 2018, Podčetrtek, Slovenia
International Scientific Committee	Bojan Štumberger – chair (Slovenia), Lidija Petkovska – vice-chair (Macedonia), Andrzej Krawczyk - vice-chair (Poland), Anouar Belahcen (Finland), Lech Borowik (Poland), Nenad Cvetković (Serbia), Goga Cvetkovski (Macedonia), Ivo Doležal (Czech Republic), Dagmar Faktorova (Slovakia), Rastko Fišer (Slovenia), Miralem Hadžiselimović (Slovenia), Slawomir Hausman (Poland), Masateru Ikehata, (Japan), Yoshihiro Kawase (Japan), Ewa Korzeniewska, (Poland), Maria Evelina Mognaschi (Italy), Roman Kubacki, (Poland), Miklos Kuczmann (Hungary), Zdravko Praunseis (Slovenia), Vasilija Sarac (Macedonia), Sebastijan Seme (Slovenia), Gorazd Štumberger (Slovenia), Vesna Arnautovski-Toseva (Macedonia), Mladen Trlep (Slovenia), Mykhaylo Zagirnyak (Ukraine) & Damir Žarko (Croatia).
Local Organising Committee	Miralem Hadžiselimović – chairman (Slovenia), Sebastijan Seme (Slovenia), Klemen Sredenšek (Slovenia), Tine Marčič (Slovenia), Iztok Brinovar (Slovenia) & Gregor Srpič (Slovenia).
Scientific Secretaries	Sebastijan Seme (Slovenia)

Co-published by / Izdajatelj/
University of Maribor, Faculty of Energy Technology
Hočevarjev trg 1, 8270 Krško, Slovenia
<http://fe.um.si>, fe@um.si

Published by / Založnik
University of Maribor Press
Slomškov trg 15, 2000 Maribor, Slovenia
<http://press.um.si>, zalozba@um.si

Edition 1st

Publication type e-book

Available at <http://press.um.si/index.php/ump/catalog/book/394>

Published Maribor, February 2019

© University of Maribor, University Press

All rights reserved. No part of this book may be reprinted or reproduced or utilized in any form or by any electronic, mechanical, or other means, now known or hereafter invented, including photocopying and recording, or in any information storage or retrieval system, without permission in writing from the publisher.

CIP - Kataložni zapis o publikaciji
Univerzitetna knjižnica Maribor

621.3(062)(0.034.2)

SYMPOSIUM on Applied Electromagnetics SAEM'2018 (7 ; 2018 ; Podčetrtek)
Conference proceedings / 7th Symposium on Applied Electromagnetics
SAEM'2018, Podčetrtek, Slovenia, 17-20 June, 2018 [Elektronski vir] ; editors
Sebastijan Seme, Miralem Hadžiselimović, Bojan Štumberger. - 1. izd. - Maribor
: University of Maribor Press, 2019

Način dostopa (URL): <http://press.um.si/index.php/ump/catalog/book/394>

ISBN 978-961-286-241-1 (pdf)

doi: 10.18690/978-961-286-241-1

COBISS.SI-ID [96247297](https://nbn-resolving.org/urn:nbn:si:coibiss-96247297)

ISBN 978-961-286-241-1 (PDF)

DOI <https://doi.org/10.18690/978-961-286-241-1>

Price Free copy

For Publisher full prof. Zdravko Kačič, PhD
Rector, University of Maribor

7th International Symposium on Applied Electromagnetics

SEBASTIJAN SEME, MIRALEM HADŽISELIMOVIĆ & BOJAN ŠTUMBERGER

Abstract The International Symposium on Applied Electromagnetics is aimed at the presentation of research work results in various areas of Applied Electromagnetics. The Symposium is devoted to exchanging ideas, presenting achievements and results, providing the forum for researchers and academics. Open and friendly atmosphere, which our conferences are known for, encourages especially young researchers to present their achievements and ideas, even at an early stage of their research work. The Symposium continues the tradition of joint conferences, organised in previous years by the organisers from Macedonia, Poland, Slovenia and Hungary. The symposium is open for participants from all over the world. This year's symposium took place between 17th and 20th June 2018 in Podčetrtek, Slovenia.

We would like to thank all the participants for their participation at the International Symposium on Applied Electromagnetics and wish them a successful academic career.

Keywords: • applied electromagnetics • electrical machines • electromagnetic field • electromagnetic devices • energy efficiency •

CORRESPONDENCE ADDRESS: Sebastijan Seme, PhD, Associate Professor, University of Maribor, Faculty of Energy Technology, Hočevarjev trg 1, 8270 Krško, Slovenia, e-mail: sebastijan.seme@um.si. Miralem Hadžiselimović, PhD, Full Professor, University of Maribor, Faculty of Energy Technology, Hočevarjev trg 1, 8270 Krško, Slovenia, e-mail: miralem.h@um.si. Bojan Štumberger, PhD, Full Professor, University of Maribor, Faculty of Energy Technology, Hočevarjev trg 1, 8270 Krško, Slovenia, e-mail: bojan.stumberger@um.si.

Table of Contents

Conference Proceedings

Energy Management: The Introduction of Flexible Energy Consumption, Storage, and Generation in Smart Grids, Smart Buildings, and Smart Communities Gorazd Štumberger	1
A Survey of Bio Inspired Optimization Algorithms for Optimal Design of Power Devices Goga Cvetkovski	7
MTPA Control Strategy For Interior Permanent Magnet Synchronous Machines Derived Using Current Dependent Flux Linkage Functions Zlatko Hanić, Damir Vuljaj, Stjepan Stipetić & Damir Žarko	17
FEM Modelling of a Doubly-Fed Induction Machine Mario Vukotić & Damijan Miljavec	31
An Approach to Performance Analysis of a Single-Phase Permanent Magnet Motor Lidija Petkovska & Goga Cvetkovski	37
Optimization by the Evolutionary Algorithm and FEM Tools: Example on Switched Reluctance Motor Marinko Barukčić, Željko Hederić, Tin Benšić & Venco Čorluka	45
The Efficiency Improvement of a Permanent Magnet Synchronous Machine Drive Željko Plantić, Tine Maričić & Gorazd Štumberger	53
Determination of a Crack's Dimensions on the Basis of the Non-Destructive Testing with Eddy Currents Using Metaheuristics Marko Jesenik, Anton Hamler, Miloš Beković & Mladen Trlep	63
Battery Pack Design Problems - EMC Problems Caused by Transverse Magnetic Field Željko Hederić, Marinko Barukčić, Nenad Cvetković & Dejan Krstić	71

Grid-Ground Electrode in Two Layered Non-Homogeneous Ground	81
Nenad Cvetkovic, Dejan Jovanovic, Miodrag Stojanovic & Marinko Barukcic	
The Implementation of Electronic Green Public Procurement Tool in Slovenia	89
Klemen Sredenšek, Gregor Srpčič, Maršenka Marksel, Miralem Hadžiselimović & Sebastijan Seme	
Interdependence Between GDP and Electric Vehicles' Charging Infrastructure in the EU	97
Katja Hanžič, Maršenka Marksel & Stanislav Božičnik	
Method for Determining Battery Health	103
Slavko Brečko, Dalibor Igrec, Aleš Breznik, Amor Chowdhury & Miran Rodič	
Blockchain-Based Solution for Future Energy Management in Existing Infrastructure	109
Dalibor Igrec, Aleš Breznik & Amor Chowdhury	
SWOT Analysis of Pedelecs and E-Cars in Selected Countries of the Danube Region	115
Gregor Srpčič, Iztok Brinovar, Katja Hanžič, Miralem Hadžiselimović & Sebastijan Seme	
The Influence of Increased Moderator Temperature on the Nuclear Characteristics of the NPP Krško	121
Marjan Kromar & Bojan Kurinčič	
Optimal Planning and Operation of the Off-Grid Genset System by an Evolutionary Algorithm	127
Marinko Barukčić, Dejan Barešić, Željko Hederić & Ivan Mijić	
ViMeLa Project: An innovative Concept for Teaching Students in Mechatronics Using Virtual Reality	135
Lidija Petkovska, Goga Cvetkovski, Mihail Digalovski, Maja Celeska, Dorota Kamińska, Slawomir Wiak, Anna Firychnowska, Marcin Lefik, Grzegorz Zwoliński, Tomasz Sapiński, Paolo Di Barba, Maria Evelina Mognaschi, Najmeh Rezaei, Rain Eric Haamer & Gholamreza Anbarjafari	
Virtual Reality Sorting Line: A Scenario for the ViMeLa Project	143
Paolo Di Barba, Maria Evelina Mognaschi, Najmeh Rezaei, Anna Firychnowska, Dorota Kamińska, Marcin Lefik, Tomasz Sapiński, Slawomir Wiak, Grzegorz Zwoliński, Goga Cvetkovski, Lidija Petkovska, Rain Eric Haamer & Gholamreza Anbarjafari	

Virtual Reality as a Tool for Electrical Machines Assembling and Testing	151
Goga Cvetkovski, Lidija Petkovska, Mihail Digalovski, Maja Celeska, Dorota Kaminska, Anna Firyeh-Nowacka, Slawomir Wiak, Tomasz Sapiński, Marcin Lefik, Grzegorz Zwoliński, Paolo Di Barba, Maria Evelina Mognaschi, Rain Eric Haamer & Gholamreza Anbarjafari	
Efficient Full-Wave Electromagnetic Analysis of Arbitrary Grounding Systems	157
Blagoja Markovski, Leonid Grcev, Vesna Arnautovski-Toseva, Jasmina Angelevska & Andrijana Kuhar.	
Calculation of the Earth's Magnetic Field Distortion Caused by the Ferromagnetic Parts in Bed and Its Effects on Health	165
Dejan Krstić, Darko Zigar, Željko Hederić, Nikola Trifunović & Marinko Barukčić	
FEM Modelling and Analysis of Single Sided Linear Synchronous Motor	173
Xevat Sulejmani & Goga Cvetkovski	
Advantages of the Stator Flux Trajectory for Direct Torque Control of Induction Machines with Uncertain Resistances	179
Goran Rafajlovski, Mihail Digalovski & Goga Cvetkovski	
Thermal and Overcurrent Protection on Single Phase Induction Motor by Using Arduino	187
Stefan Mitovski & Goga Cvetkovski	
Power Performance Investigation of a Wind Turbine Using Nonparametric Methods	193
Maja Celeska, Krste Najdenkoski, Vlatko Stoilkov & Vladimir Dimchev	
An Analysis of Possible Applications of Combined Fuzzy Logic to Cause-Effect Analysis	201
Ivica Petrović, Marinko Barukčić, Željko Hederić, & Nenad Cvetković	
Measurement System for Testing of Electric Drives in Electric Vehicles	209
Iztok Brinovar, Gregor Srpčić, Sebastijan Seme, Bojan Štumberger & Miralem Hadžiselimović	

Minimization of Distribution Network Losses Using Optimal PV Installation, Reactive Power Generation and Network Reconfiguration	215
Nevena Srećković, Niko Lukač, Borut Žalik & Gorazd Štumberger	
Differential Evolution Based Mismatch Loss Optimisation in Photovoltaic Arrays	223
Tomislav Matić, Damir Blažević, Dražen Bajer & Ivan Vidović	
Estimation of the Solar Irradiance on Tilted Surface for Different Types of Pyranometers	231
Sebastijan Seme, Klemen Sredenšek, Iztok Brinovar, Gregor Srpčič, Miralem Hadžiselimović & Bojan Štumberger	
Shadow Impact Determination from DEM Data	239
Primož Mavsar	
Experimental and Numerical Research of Micro Wind Turbine for Low Wind Speeds	245
Matej Fike, Marko Pezdevšek, Andrej Predin & Gorazd Hren	
Influence of Numerical Mesh Type on Airfoil Aerodynamic Characteristics	251
Marko Pezdevšek, Matej Fike, Andrej Predin & Gorazd Hren	
Usage of DEM Data for Solar Potential Determination	257
Primož Mavsar	
Automated Optimal Design of Wells for Electromagnetic Cell Stimulation	265
Paolo Di Barba, Lorenzo Fassina, Giovanni Magenes & Maria Evelina Mognaschi	
Is Specific Absorption Rate (SAR) the Parameter of Mobile Phone?	273
Andrzej Krawczyk, Ewa Korzeniewska & Piotr Murawski	
Production, Thermal Analysis and Application of Roll Bond Solar Absorbers for Heating and Cooling in Residential Buildings	281
Jurij Avsec, Daniel Brandl, Helmut Schober, Urška Novosel & Janko Ferčec	
Energy Efficiency Indicators of a Single Unit House	287
Iztok Brinovar, Gregor Srpčič, Zdravko Praunseis, Sebastijan Seme, Bojan Štumberger & Miralem Hadžiselimović	

Evaluation of the Impact of Symmetrical Voltage Sags on the Performance of a Line-Start IPM Synchronous Motor Drive Tine Marčič	293
Accuracy of Rotational Speed and Torque Sensors for Determining the Mechanical Power of Rotating Electrical Machines Gregor Srpčič, Iztok Brinovar, Bojan Štumberger, Sebastijan Seme & Miralem Hadžiselimović	299
Comparison and Analysis of Mechanical Torque and Efficiency of the Multi-Phase Induction Motor Venco Čorluka, Željko Hederić & Marinko Barukčić	305

Energy Management: The Introduction of Flexible Energy Consumption, Storage, and Generation in Smart Grids, Smart Buildings, and Smart Communities

GORAZD ŠTUMBERGER

Abstract According to Energy Efficiency Directive Winter package 2016, the flexibility in energy generation, storage, and consumption is required to provide affordable prices of energy supply. The paper discusses who are the users and providers of energy flexibility services. At the present time these services are mostly limited to electricity and heat supply with possible extensions towards other forms of energy and energy carriers. The majority of electricity supply is carried on by the electricity networks that evolve toward active networks, often called smart grids. Smart grids require active grid users in the form of smart buildings and smart communities. Since the grid users have no time to be available all the time for requests regarding energy flexibility services, their response should be automated by Energy Management Systems (EMS) with an autonomous decision logic, that performs a requested service, if it can provide sufficient benefits for its owner.

Keywords: • energy flexibility services • generation • consumption • storage • energy management systems •

CORRESPONDENCE ADDRESS: Gorazd Štumberger, PhD, Full Professor, University of Maribor, Faculty of Electrical Engineering and Computer Science, Koroška cesta 46, 2000 Maribor, Slovenia, e-mail: gorazd.stumberger@um.si.

DOI <https://doi.org/10.18690/978-961-286-241-1.1>
Available at: <http://press.um.si>.

ISBN 978-961-286-241-1

1 Introduction

The European Commission updated the Energy Efficiency Directive (European Commission, 2012) in 2016 with the Winter package (European Commission, 2016), which represents a political frame for the introduction of flexibility in energy generation, storage, and consumption. Energy Management Systems, the overview of which is given in (Bayrama & Ustunb, 2017), (Carreiro & et. al., 2017), (Celik, 2017), (Meyabadi & Deihimi, 2017), (Rafique & Jianhua, 2018), and (Zheng, 2018), could be one of the key technologies for the implementation of energy flexibility in smart buildings, smart grids, and smart communities. The existing energy management systems can provide a reduction in energy costs without influencing the basic functionalities and the quality of living in buildings. They can be described as automation systems with added remote-control functionality, which are incapable of autonomous decisions. This should be changed with the new generation of energy management systems, where autonomous decisions are required for their participation in market driven services in the field of flexible energy generation, storage, and consumption. The aim of this paper is to present individual actors in the field of FEGSC (Flexibility in Energy Generation, Storage, and Consumption) with a focus on the roles of energy management systems.

2 Flexibility in energy generation, storage, and consumption

The renewable energy sources, such as wind energy and solar energy, are unpredictable and volatile. The introduction of FEGSC can be one of the measures that can increase their utilization, which is only one of the motivations for the FEGSC introduction. However, the FEGSC can be introduced as a market driven service only if there are users of these services ready to pay for them. The Transmission System Operators (TSOs) can include FEGSC in ancillary services (stability control, voltage control, frequency control, restarting systems) (Carreiro & et. al., 2017). The Distribution System Operators (DSOs) can apply FEGSC for the prevention of network element overloads and voltage control, whilst the Balancing Groups (BGs) can use FEGSC to improve their economic results on the energy market. All of them have been identified as potential users of market driven FEGSC services. On the other hand, these services can be provided by the electricity network users that can be classified as energy generation, storage, and consumption units, or their combination which is often called prosumers. In the cases, when the power and energy available for

the FEGSC services is high enough, the service providers can sign direct contracts with the service users. However, when their power and energy are too low to enable a direct interaction between the service providers and service users, an aggregator (Carreiro & et. al., 2017) is introduced, as shown in Fig. 1. Its role is to aggregate actors with small power and energy in such a way that they can be involved in market driven FEGSC services as a group through the aggregator.

The existing form of the FEGSC is known as Demand Response (DR) and Demand Side-Management (DSM) (Meyabadi & Deihimi, 2017). It focuses primarily on the consumption units whilst the storage and generation units are normally not involved. DR has been tested in many demonstration projects. The main idea of DR is the change of consumption based on the requests of TSO, DSO or BG. The requests for DR are transmitted to the network users in the form of messages containing request for action, or in the form of commands that directly switch-off individual consumption units. In the first case the requests are often neglected whilst in the second case the direct switching-off of individual consumption units can be unacceptable for their owners. The best solution seems to be the introduction of an Energy Management System (EMS) with an appropriate decision logic that grants a fast response and considers preferences of the EMS owner. The EMS can be installed in a home (HEMS), in a building (BEMS), in a factory (FEMS), or in a community that covers a particular area (AEMS). Normally, the EMS considers and combines different forms of energy, where the heat and electric energy are the most common. EMS is one of the key elements that can enable fast and user-friendly provision of FEGSC services by the (electricity, heat) network users. The main goal of EMSs is to decrease the energy bill of the network users and to enable them additional incomes by providing FEGSC services, without disturbing comfort and quality of living, functionality of buildings, or production processes in factories.

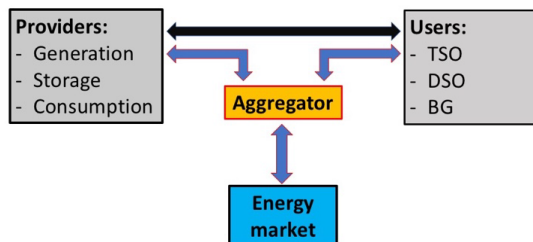


Figure 1: Providers, users and aggregators of market driven FEGSC services

3 EMS and autonomous decision logic

A laboratory implementation of EMS is shown in Fig. 2. It enables grid-connected as well as off-grid operation and consists of a controllable energy generation unit (PV system 3.75 kWp), a controllable energy storage unit (4 kWh lithium titanium oxide battery system with a 5 kW converter), controllable consumption units (six 1 kW air conditioners, 2 kW water heater, refrigerator and additional loads), and a control unit. Its main goal is to provide an experimental environment for the development of EMS functionalities for homes, buildings, factories and communities, considering both aspects: the reduction of costs for energy supply as well as provision of FEGSC services for TSO, DSO and BG, motivated by economic or other benefits for the owner.

There are many different approaches to the realization of EMS decision logic, where those based on the multiagent approach are very popular (Zheng, 2018). Figs. 3 and 4 schematically shows an approach where the decision logic mimics an open market in the case of on-grid operation and a closed market in the case of off-grid operation.



Figure 2: EMS containing the controllable energy generation, storage, and consumption units

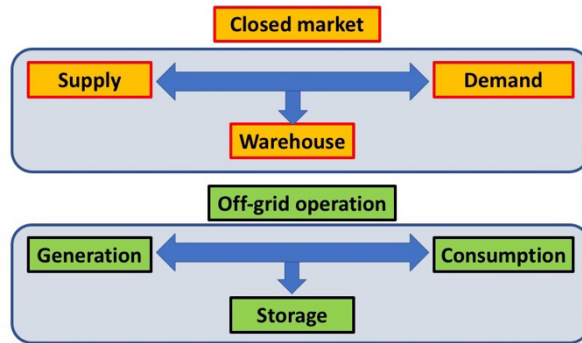


Figure 3: Closed market and its analogy with the off-grid operation

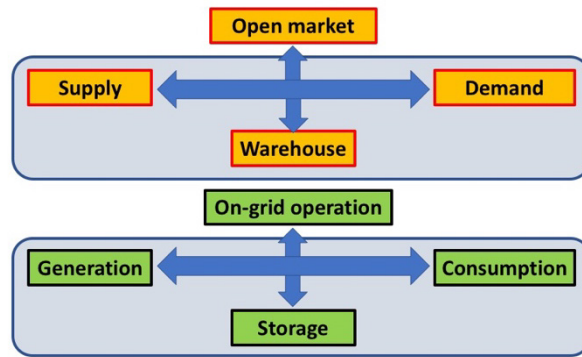


Figure 4: Open market and its analogy with the on-grid operation

The energy generation and consumption have similar roles as the supply and demand, whilst the energy storage has a similar role as the warehouse. The role of the warehouse is different in the cases of open and closed market, as well as is the role of energy storage in the cases of on-grid and off-grid operation.

4 Conclusion

The aim of this paper is to explain why we need FEGSC services, who are providers and users of these services, what is the role of an aggregator, and why EMS is one of the key technologies for the introduction of market driven flexibility services.

Why do we need EMS with autonomous decision logic to provide market driven FEGSC services? People are normally busy and have no time to continuously

check request for FEGSC services. EMS can increase the level of comfort and reliability of responses on DR requests. Moreover, EMS also provides shorter response time which could increase the incomes for FEGSC services.

Acknowledgments

This work was supported in part by the Slovenian Research Agency (ARRS), projects L2-5489 and P2-0115.

References

- Bayrama, I. S., & Ustunb, T. S. (2017). A survey on behind the meter energy management systems in smart grid. *Renewable and Sustainable Energy Reviews*, 1208-1232.
- Carreiro, A. M., & et. al. (2017). Energy management systems aggregators: A literature survey. *Renewable and Sustainable Energy Reviews*, 1160-1172.
- Celik, B. e. (2017). Electric energy management in residential areas through coordination of multiple smart homes. *Renewable and Sustainable Energy Reviews*, 260-275.
- European Commission. (2012). Directive 2012/27/EU OF THE EUROPEAN PARLIAMENT AND OF THE COUNCIL of 25 October 2012 on energy efficiency. *Official Journal of the European Union*.
- European Commission. (2016). *Clean Energy For All Europeans*. European Commission.
- European Commission. (2016). *Clean Energy For All Europeans - Annex 1: Accelerating clean energy in buildings*. European Commission.
- European Commission. (2016). *Clean Energy For All Europeans - Annex 2: Action to boost the clean energy transition*. European Commission.
- Meyabadi, A. F., & Deihimi, M. H. (2017). A review of demand-side management: Reconsidering theoretical framework. *Renewable and Sustainable Energy Reviews*, 367-379.
- Rafique, S. F., & Jianhua, Z. (2018). Energy management system, generation and demand predictors: a review. *IET Generation, Transmission & Distribution*, 519-530.
- Zheng, Y. (2018). Multiagent System Based Microgrid Energy Management via Asynchronous Consensus ADMM. *IEEE Transactions on Energy Conversion*, 886 – 888.

A Survey of Bio Inspired Optimization Algorithms for Optimal Design of Power Devices

GOGA CVETKOVSKI

Abstract Nature is of course a great and immense source of inspiration for solving hard and complex problems in computer science since it exhibits extremely diverse, dynamic, robust, complex and fascinating phenomenon. It always finds the optimal solution to solve its problem maintaining perfect balance among its components. This is the thrust behind bio inspired computing. Nature inspired algorithms are meta heuristics that mimics the nature for solving optimization problems opening a new era in computation. For the past decades, numerous research efforts have been concentrated in this particular area. Still being young and the results being very amazing, broadens the scope and viability of Bio Inspired Algorithms (BIAs) exploring new areas of application and more opportunities in computing. This paper presents the mechanism of performance of several bio-based optimization methods and also presents the results of their optimal design action performed on several power devices.

Keywords: • optimization algorithms • power devices • genetic algorithm • particle swarm optimization • cuckoo search •

CORRESPONDENCE ADDRESS: Goga Cvetkovski, Ph.D., Professor, Ss. Cyril and Methodius University, Faculty of Electrical Engineering and Information technologies, Rugjer Bošković 18, P.O. Box 574, 1000 Skopje, Macedonia, e-mail: gogacvet@feit.ukim.edu.mk.

DOI <https://doi.org/10.18690/978-961-286-241-1.2>
Available at: <http://press.um.si>

ISBN 978-961-286-241-1

1 Introduction

Optimal design of electrical machines generally is usually a complicated process with a lot of optimization parameters, constrains and complex objective functions. Standard deterministic methods can sometimes have difficulties to solve such problems, where on the other hand lately the stochastic methods have proved that they are quite powerful in solving such problems. There is large group of stochastic methods that are bio inspired and based on behavior of certain species in nature.

A vast literature exists on bio inspired approaches for solving an impressive array of problems and, more recently, a number of studies have reported on the success of such techniques for solving difficult problems in all key areas of computer science. The two most predominant and successful classes or directions in bio inspired algorithms (BIAs) involves Evolutionary Algorithms and Swarm based Algorithms which are inspired by the natural evolution and collective behavior in animals respectively. But still, this has been further refined so as to classify the algorithms based on the area of inspiration from nature so as to enhance a broader view over the domain. A presentation of one possible classification of the BIAs is shown in Figure 1.

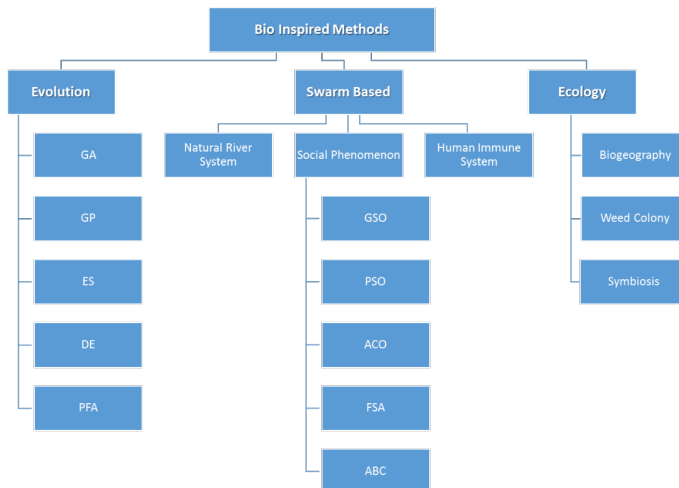


Figure 2: General review of the bio inspired optimization methods (GA-Genetic Algorithm, GP-Genetic Programing, ES-Evolutionary Strategies, DE-Differential Evolution, PFA- Paddy Field Algorithm, GSO-Group Search Optimization , PSO-Particle Swarm Optimization, ACO-Ant Colony Optimization, FSA-Fish Swarm Optimizatoin, ABC-Artificial Bee Colony)

The purpose of this research work is to present the mechanism of performance of several bio-based optimization methods and to present the results of their optimal design performed on several power devices. The objective function in the optimization process in most cases is defined to be the efficiency of the motor, but it can also be any other function such as specific mass, torque, cogging torque etc. The optimization methods that are going to be presented and investigated in the optimal design of several power devices are Genetic Algorithm (GA), Particle Swarm Optimization (PSO) and Cuckoo Search (CS). The results from these optimal designs performed with different optimization methods and on different power devices will be presented and adequate conclusions will be drawn.

2 Genetic Algorithms

Genetic algorithms are an evolutionary based stochastic optimization algorithm with a global search potential proposed by Holland in 1975 (Holland 1995). Genetic algorithms are among the most successful class of algorithms under evolutionary based algorithms which are inspired by the evolutionary ideas of natural selection. They follow the principles of Charles Darwin's Theory of survival of the fittest. The outstanding performance of this method in the optimization process is related to the fact that the method performs the optimization based on the value of the objective function and not on the value of the optimization parameters. The algorithm starts the optimization search by initializing a population of solutions (chromosomes). The chromosome of each solution is a vector of real or binary numbers that represent the solutions for each optimization variable. Then for each chromosome the algorithm calculates the fitness value using an appropriate fitness function suitable for the problem. Based on this, the best chromosomes are selected into the mating pool, where they undergo cross over and mutation thus giving new set of solutions (offspring). The three principal genetic operators in GA involve selection, crossover, and mutation.

The application of genetic algorithm as tool for optimal design using will be shown on the optimisation of the specific power of a permanent magnet synchronous motor (PMSM). The objective function is presented in equation (1) shown on next page.

$$\text{specific power} = \frac{T \cdot \omega_m}{m_{Cu} + m_{Fe\ stator} + m_{PM} + m_{Fe\ rot}} \quad (1)$$

where: T -rated torque, ω_m -synchronous speed, m_{Cu} -total weight of the stator copper windings, $m_{Fe\ stator}$ -total weight of the iron stator, $m_{Fe\ rot}$ -total weight of the iron rotor and m_{PM} -total weight of the permanent magnets. The optimal design process is a maximisation problem of the objective function. The variable design parameters for this optimization are chosen to be as follows: outside radius of the rotor R_r , air-gap length g , permanent magnet fraction α_m , magnet length l_m , and motor axial length L . The results from the optimal design process are shown in Table 1. From the presented results in the table it is evident that there is an increase of the value of the specific power that also results in small decrease in the efficiency of the motor and a reduction of the total mass of the motor. Based on the presented result it can be concluded that the genetic algorithms have a good performance in the optimal design of the permanent magnet synchronous motor and that they can be used very successfully on optimal design of electrical machines and devices in general.

Table 1: GA Optimal Design Results of PMSM

Parameters	Lower bound	Upper bound	Prototype	PMSM GA solution
R_r (m)	0.0378	0.0442	0.042	0.04177
g (m)	0.00072	0.00088	0.0008	0.00072
α_m (/)	0.81	0.99	0.9	0.8898
l_m (m)	0.0018	0.0022	0.002	0.0022
L (m)	0.081	0.099	0.09	0.08498
<i>Specific power</i> (W/kg)	-	-	56.96	67.01
<i>Efficiency</i>	-	-	0.848	0.845
m_{total} (kg)	-	-	18.384	17.177
I_{ph} (A)			17.41	17.59
R_{ph} (ohm)			0.163	0.166

3 Particle Swarm Optimization

Particle swarm optimization (PSO) is a stochastic swarm type of optimization method that has been recently proposed and introduced as an optimization tool (Kennedy et al 2001). PSO is based on the analogy of swarm, as flock of birds or school of fish. PSO mimics the behaviour of individuals in a swarm to maximize the survival of the species. In PSO, each individual makes its decision using own experience together with other individuals' experiences. The algorithm, which is based on a metaphor of social interaction, searches a space by adjusting the trajectories of moving points in a multi-dimensional space. The individual

particles are drawn stochastically toward the position of present velocity of each individual, their own previous best performance, and the best previous performance of their neighbours. The main advantages of PSO algorithm are summarized as simple concept, easy implementation, robustness to control parameters, and computational efficiency when compared with deterministic methods and other stochastic optimization techniques. Unlike the other heuristic techniques, PSO has a flexible and well-balanced mechanism to enhance and adapt both to the global and local exploration abilities.

Similar to evolutionary algorithms, the PSO technique conducts searches using a population of particles, corresponding to individuals. Each particle represents a candidate solution to the problem. In a PSO stem, particles change their positions by flying around in a multidimensional search space until a relatively unchanged position has been encountered, or until computational limitations are exceeded. In social science context, a PSO system combines a social-only model and a cognition-only model. The social-only component suggests that individuals ignore their own experience and adjust their behaviour according to the successful beliefs of individuals in the neighbourhood. On the other hand, the cognition-only component treats individuals as isolated beings. A particle changes its position using these models.

The quality performance of this optimization method is tested on the optimal design of a single-phase permanent magnet brushless DC motor (SPBLDCM). The efficiency of the motor is selected as an objective function of the optimisation and it is defined with equation (2). According to the design characteristics of the designed by hand prototype SPBLDCM, some of the parameters are chosen to be constant and some variable, such as: outside radius of the rotor core R_{ro} , permanent magnet radial thickness l_m , air-gap g , slot opening b_{so} , axial active length of the motor L , and single wire radius r_{cu} . Some of these parameters are presented in Figure 3. The objective function for the optimisation is presented by equation (2).

$$efficiency = \eta = \frac{T \cdot \omega_m}{T \cdot \omega_m + P_{Cu} + P_{Fe} + P_s} \quad (2)$$

where: T -rated torque, ω_m -rated speed, P_{Cu} -ohmic power loss, P_{Fe} -stator iron core power loss and P_r -other constant losses. The optimal design process of the single phase brushless DC motor is a maximisation problem of the objective function, where the torque is one of the predefined constraints. The result from the optimization process are presented in Table 2.

Table 2: PSO Optimal Design Results of SPBLDCM

Parameters	Lower bound	Upper bound	Prototype	SPBLDCM PSO solution
R_m (m)	0.0342	0.0418	0.038	0.0418
l_m (m)	0.0018	0.0022	0.002	0.00194
g (m)	0.0009	0.0011	0.001	0.0009
b_{so} (m)	0.0020	0.0030	0.0023	0.003
L (m)	0.0972	0.1188	0.108	0.0972
r_{st} (m)	0.0003	0.0005	0.0004	0.0005
<i>Efficiency</i>	-	-	0.8823	0.9049
I_{ph} (A)	-	-	3.28	3.50
R_{ph} (ohm)	-	-	6.987	5.045
P_{Cu} (W)	-	-	91.38	61.86
P_{Fe} (W)	-	-	32.06	33.18

From the presented results in Table 2 it is evident that there is an increase of the value of the efficiency of the motor that also results in a decrease of the ohmic resistance of the stator winding, based on which the total ohmic losses decrease by a significant value. Based on the presented result it can be concluded that the particle swarm optimization has a good performance in the optimal design of the SPBLDCM and also it can be used very successfully on optimal design of electrical machines and devices in general.

4 Cuckoo Search Optimization

Cuckoo birds attract attention, due to their unique aggressive reproduction strategy. Cuckoos engage brood parasitism. It is a type of parasitism in which a bird (brood parasite) lays and abandons its eggs in the nest of another species. There are three basic types of brood parasitism: intraspecific brood parasitism, cooperative breeding, and nest takeover. Some species of cuckoo birds lay their eggs in communal nests, though they may remove others' eggs to increase the hatching probability of their own eggs. Some host birds do not behave friendly against intruders and the host bird will throw those alien eggs away. In other situations, more friendly hosts will simply abandon its nest and build a new nest elsewhere.

Cuckoo Search algorithm (Yang and Deb 2001) is population based stochastic global search metaheuristics and is based on the general random walk system. In Cuckoo Search algorithm, potential solutions corresponds to Cuckoo eggs. Due to the complexity of the natural system of the cuckoo birds a simplification of the system is necessary for successful implementation in computer algorithms. One approach is to simplify novel Cuckoo Search algorithm through three below presented approximation rules:

- Cuckoos chose random location (nest) for laying their eggs. Artificial cuckoo can lay only one egg at the time.
- Elitist selection process is applied, so only the eggs with highest quality are passed to the next generation
- Host nests number is not adjustable. Host bird discovers cuckoo egg with probability $p_d \in [0,1]$. If cuckoo egg is disclosed by the host, it may be thrown away, or the host may abandon its own nest and commit it to the cuckoo intruder. A simple representation where one egg in a nest represents a solution and a cuckoo egg represents a new solution is used here. The aim is to use the new and potentially better solutions (cuckoos) to replace worse solutions that are in the nests.

The quality of the optimization process of this method is tested on the optimal design of a permanent magnet disc motor (PMDM) for electric vehicle. The PMDM is a double sided disc motor with two laminated stators having 36 slots and a centred rotor with 8 skewed neodymium-iron-boron permanent magnets that have a remanent flux density of $B_r=1.17$ T and coercitive field of $H_c=-883$ kA/m. In this case the increasement of the efficiency of the motor is of great importance for the autonomy of the electric vehicle. In the case of this design optimisation the following motor parameters are chosen to be variable: inside radius of the stator cores and PM R_i , outside radius of the stator cores and PM R_o , permanent magnet fraction a_m , permanent magnet axial length l_m , air-gap g , single wire diameter d_w , and stator slot width b . The objective function of this optimal design process of the PMDM is selected to be the efficiency of the motor. As it is known the Cuckoo Search is in general a minimisation algorithm and therefore the objective function of the search will be an inverse function of the efficiency of the motor.

The objective function for the PMDM optimisation can be presented with the following equation:

$$F_o = \frac{1}{\text{efficiency}} = \frac{1}{\frac{T \cdot \omega_m}{T \cdot \omega_m + P_{Cu} + P_{Fe} + P_s}} \quad (3)$$

where: T -rated torque, ω_m -rated speed, P_{Cu} -ohmic power losses, P_{Fe} -core losses and P_s -other losses. The comparative optimization parameters data of the initial and the optimized model are presented in Table 3.

From the presented results in Table 3 it is evident that there is an increasement of the value of the objective function and as a result of which the value of the efficiency of the motor is also increased. This is achieved by a significant decrease of the ohmic resistance of the stator winding, based on which the total ohmic losses decrease by a significant value. The iron losses increase by a small value that does not influence the overall decrease of the losses. Based on the presented result it can be concluded that the cuckoo search optimization has a good performance in the optimal design of the PMDM and also it can be used very successfully on optimal design of electrical machines and devices in general.

Table 3: CS Optimal Design Results of PMDM

Parameters	Lower bound	Upper bound	Prototype	PMDM CS solution
R_i (m)	0.070	0.074	072	0.070725
R_o (m)	0.128	0.138	0.133	0.712905
a_m (l)	0.6	0.730	0.6646	0.01068
l_m (m)	0.009	0.0110	0.010	0.001827
g (m)	0.0018	0.0022	0.002	0.139438
d_m (m)	0.0006	0.0014	0.001	0.0014
b_s (m)	0.0070	0.0090	0.008	0.008364
<i>Objective function</i> F_o (l)	-	-	1.2019	1.5567
<i>Efficiency</i> (l)	-	-	0.8325	0.8653
I_{pb} (A)	-	-	8.723	8.33
R_{pb} (ohm)	-	-	1.245	0.570
P_{Cu} (W)	-	-	345.43	144.27
P_{Fe} (W)	-	-	15.03	19.35

5 Conclusion

At the end it can be concluded that all presented methods performed well and gave good results compared to the initial model values. Their performance and quality of the results can be improved by a proper adjustment of the method to the analysed model. Each optimization process is also a problem dependent and the good knowledge about the problem and motor is of great importance for a good quality results.

References

- Holland J. H., (1995). *Adaptation in Natural and Artificial Systems*, Ann Arbor: *University of Michigan Press*.
- Kennedy, J., Eberhart, R.C., Shi, Y. (2001) *Swarm Intelligence: The Morgan Kaufmann Series in Evolutionary Computation*, San Francisco, *Morgan Kaufmann Publishers*.
- Yang X-S, Deb S. (2010). Engineering Optimization by Cuckoo Search: *International Journal of Mathematical Modelling and Numerical Optimization*, Vol. 1 (2010), No. 4, pp. 330–343.

MTPA Control Strategy For Interior Permanent Magnet Synchronous Machines Derived Using Current Dependent Flux Linkage Functions

ZLATKO HANIĆ, DAMIR VULJAJ, STJEPAN STIPETIĆ & DAMIR ŽARKO

Abstract The paper describes a method for calculation of maximum torque per ampere curves for interior permanent magnet synchronous machines which takes into consideration magnetic saturation and its variation with operating point as well as cross-saturation effect. The method uses current depended flux linkage functions and Lagrange multiplier theory for obtaining maximum torque for an arbitrary operating point. The proposed method has been implemented on a model of 48 slot/8 pole interior permanent magnet synchronous machine. Flux linkage functions have been calculated using finite element method and then used for calculation of d and q axis current pairs for every combination of torque and angular speed.

Keywords: • maximum torque per ampere • interior permanent magnet synchronous machines • current dependent flux linkage functions • Lagrange multipliers • reference governor •

CORRESPONDENCE ADDRESS: Zlatko Hanić, PhD, Postdoctoral Researcher, University of Zagreb, Faculty of Electrical Engineering and Computing, Unska 3, 10000 Zagreb, Croatia, e-mail: zlatko.hanic@fer.hr. Damir Vuljaj, Mag. Eng., Motor Development Engineer, Rimac Automobili, Ljubljanska 7, 10431 Sveta Nedelja, Croatia, e-mail: damir.vuljaj@rimac-automobili.com. Stjepan Stipetić, PhD, Assistant Professor, University of Zagreb, Faculty of Electrical Engineering and Computing, Unska 3, 10000 Zagreb, Croatia, e-mail: stjepan.stipetic@fer.hr. Damir Žarko, PhD, Full Professor, University of Zagreb, Faculty of Electrical Engineering and Computing, Unska 3, 10000 Zagreb, Croatia, e-mail: damir.zarko@fer.hr.

1 Introduction

Efficient torque production using electrical machines is very important for traction and propulsion applications due to limited space of installation. Maximum torque per ampere (MTPA) control strategy, which is very common (Chowdhury et al.), (Huang et al., 2011), ensures the most effective torque production for a given current. For interior permanent magnet (IPM) synchronous machines MTPA control strategy is achieved by setting appropriate I_d and I_q current components that maximize torque production. Their values depend on parameters L_{ds} , L_{qs} and Ψ_{md} for a particular operating point. Since L_{ds} , L_{qs} and Ψ_{md} are changing with saturation and cross-magnetization, various models (Miao et al., 2017) and techniques (Tang et al., 2015), (Xu et al., 2017), (Chen et al., 2018), (Bariša et al., 2015), (Fazeli et al., 2009), (Sun et al., 2015) were developed to address those effects and to estimate I_d and I_q components for MTPA control strategy. In order to properly model the variation of the parameters with saturation and cross-magnetization, a current dependent flux linkage model is identified based on finite element calculations. In this paper, we propose the derivation of the MTPA control strategy based on current dependent flux linkage model of IPM synchronous machine.

2 Calculation of MTPA curves using current dependent flux linkage functions

It is assumed that flux linkage functions are known and determined using finite element calculations or by measurements. Let the flux linkage function of the armature windings in d and q axis be $\Psi_d(I_{ds}, I_{qs})$ and $\Psi_q(I_{ds}, I_{qs})$ respectively.

The MTPA curves can be calculated using Lagrange multiplier theory. The goal is to maximize the torque for a given current taking into account the current and voltage limits.

Three different MTPA curves can be distinguished: MTPA curve with current limit, MTPA curve with voltage limit and MTPA curve with current and voltage limit.

2.1 Calculation of MTPA curves using Lagrange multipliers with current limit

For calculating the MTPA curve with current limit, which is the simplest case, the following Lagrange function should be created

$$L_l(I_d, I_q) = \frac{3}{2} p \cdot (\Psi_d(I_d, I_q) \cdot I_q - \Psi_q(I_d, I_q) \cdot I_d) + \alpha \cdot (I_d^2 + I_q^2 - I_l^2) \rightarrow \max! \quad (1)$$

where $L_l(I_d, I_q)$ is the Lagrange function with the current constrain, p is the number of the pole pairs, a is the parameter required by the Lagrange multiplier theory and I_l is the current limit. Left hand term on the right-hand side of (1) represents the expression for torque which will be maximized and the right term represents the current constrain.

In order to find the maximum, which is one point on the MTPA curve, (1) should be differentiated with respect to all variables (I_d , I_q , and a) and equalized with zero. The following system of three nonlinear equations with three unknowns is obtained

$$\frac{\partial L_l}{\partial I_d} = 2\alpha \cdot I_d - \frac{3}{2} \cdot p \cdot \left[\Psi_q(I_d, I_q) - I_q \cdot \frac{\partial \Psi_d(I_d, I_q)}{\partial I_d} + I_d \cdot \frac{\partial \Psi_q(I_d, I_q)}{\partial I_d} \right] = 0 \quad (2)$$

$$\frac{\partial L_l}{\partial I_q} = 2\alpha \cdot I_q + \frac{3}{2} p \cdot \left[\Psi_d(I_d, I_q) + I_q \cdot \frac{\partial \Psi_d(I_d, I_q)}{\partial I_q} - I_d \cdot \frac{\partial \Psi_q(I_d, I_q)}{\partial I_q} \right] = 0 \quad (3)$$

$$\frac{\partial L_l}{\partial \alpha} = I_d^2 + I_q^2 - I_l^2 = 0 \quad (4)$$

The system can be solved using numerical methods like Newton method, or quasi-Newton method. A pair (I_d, I_q) obtained from the solution of the system (2)-(4) represents the MTPA operating point. Note that the value of the parameter a obtained from solving (6)-(8) can be neglected since it has no physical meaning.

2.2 Calculation of MTPA curves using Lagrange multipliers with voltage limit

For calculating the MTPA curve with voltage limit the following Lagrange function should be created

$$L_V(I_d, I_q) = \frac{3}{2} p \cdot (\Psi_d(I_d, I_q) \cdot I_q - \Psi_q(I_d, I_q) \cdot I_d) + \beta \cdot \left[(\omega \cdot \Psi_d(I_d, I_q) + I_q \cdot R)^2 + (-\omega \cdot \Psi_q(I_d, I_q) + I_d \cdot R)^2 - V_l^2 \right] \rightarrow \max! \quad (5)$$

where $L_V(I_d, I_q)$ is the Lagrange function with voltage constrain, β is the parameter required for Lagrange function constrain, ω is the angular frequency, R is the armature resistance and V_l is the voltage limit. Right term on the right-hand side of (5) represent the voltage constrain.

To find the maximum of (5), which is one point on the MTPA curve, (5) should be differentiated with respect to I_d , I_q , and β and equalized with zero. The following system is obtained.

$$\frac{\partial L_V}{\partial I_d} = -\frac{3}{2} p \cdot \left[\Psi_q(I_d, I_q) - I_q \cdot \frac{\partial \Psi_d(I_d, I_q)}{\partial I_d} + I_d \cdot \frac{\partial \Psi_q(I_d, I_q)}{\partial I_d} \right] + \beta \cdot \left[2\omega_r \cdot (I_q \cdot R + \omega_r \cdot \Psi_d(I_d, I_q)) \cdot \frac{\partial \Psi_d(I_d, I_q)}{\partial I_d} + 2 \cdot (I_d \cdot R + \omega_r \cdot \Psi_q(I_d, I_q)) \cdot \left(R + \omega_r \cdot \frac{\partial \Psi_q(I_d, I_q)}{\partial I_d} \right) \right] = 0 \quad (6)$$

$$\frac{\partial L_V}{\partial I_q} = \frac{3}{2} p \cdot \left[\Psi_d(I_d, I_q) + I_q \cdot \frac{\partial \Psi_d(I_d, I_q)}{\partial I_q} - I_d \cdot \frac{\partial \Psi_q(I_d, I_q)}{\partial I_q} \right] + \beta \cdot \left[2 \cdot (I_q \cdot R + \omega_r \cdot \Psi_d(I_d, I_q)) \cdot \left(R + \omega_r \cdot \frac{\partial \Psi_d(I_d, I_q)}{\partial I_q} \right) + 2\omega_r \cdot (I_d \cdot R + \omega_r \cdot \Psi_q(I_d, I_q)) \cdot \frac{\partial \Psi_q(I_d, I_q)}{\partial I_q} \right] = 0 \quad (7)$$

$$\frac{\partial L_V}{\partial \beta} = \left[\omega_r \cdot \Psi_d(I_d, I_q) + I_q \cdot R \right]^2 + \left[\omega_r \cdot \Psi_q(I_d, I_q) - I_d \cdot R \right]^2 - V_l^2 = 0 \quad (8)$$

Similarly, to solve the system (6)-(8) of three equations with three unknowns, numerical methods should be applied. A solution pair (I_d, I_q) represents the operating point on the MTPA curve with voltage constrain. Note that the value of the parameter β obtained by solving (6)-(8) can be neglected since it has no physical meaning.

2.3 Calculation of MTPA curves using Lagrange multipliers with current and voltage limit

The remaining case is the MTPA operating point where current and voltage limits are present simultaneously. For that case the following Lagrange function can be created

$$L_{I,V}(I_d, I_q) = \frac{3}{2} p \cdot (\Psi_d(I_d, I_q) \cdot I_q - \Psi_q(I_d, I_q) \cdot I_d) + \alpha \cdot (I_d^2 + I_q^2 - I_l^2) + \beta \cdot \left[(\omega \cdot \Psi_d(I_d, I_q) + I_q \cdot R)^2 + (-\omega \cdot \Psi_q(I_d, I_q) + I_d \cdot R)^2 - V_l^2 \right] \rightarrow \max! \quad (9)$$

where $L_{I,V}(I_d, I_q)$ is the Lagrange function with the current and voltage constrains. To find the maximum of (9), which is one point on the MTPA curve, it is required to find the derivative of (9) with the respect to all variables $(I_d, I_q, \alpha$ and $\beta)$. The following system of equations is obtained

$$\frac{\partial L_{I,V}}{\partial I_d} = 2\alpha \cdot I_d - \frac{3}{2} p \cdot \left[\Psi_q(I_d, I_q) - I_q \cdot \frac{\partial \Psi_d(I_d, I_q)}{\partial I_d} + I_d \cdot \frac{\partial \Psi_q(I_d, I_q)}{\partial I_d} \right] + \beta \cdot \left[2\omega_r \cdot (I_q \cdot R + \omega_r \cdot \Psi_d(I_d, I_q)) \cdot \frac{\partial \Psi_d(I_d, I_q)}{\partial I_d} + 2 \cdot (I_d \cdot R + \omega_r \cdot \Psi_q(I_d, I_q)) \cdot \left(R + \omega_r \cdot \frac{\partial \Psi_q(I_d, I_q)}{\partial I_d} \right) \right] = 0 \quad (10)$$

$$\frac{\partial L_{I,V}}{\partial I_q} = 2\alpha \cdot I_q + \frac{3}{2} p \cdot \left[\Psi_d(I_d, I_q) + I_q \cdot \frac{\partial \Psi_d(I_d, I_q)}{\partial I_q} - I_d \cdot \frac{\partial \Psi_q(I_d, I_q)}{\partial I_q} \right] + \beta \cdot \left[2 \cdot (I_q \cdot R + \omega_r \cdot \Psi_d(I_d, I_q)) \cdot \left(R + \omega_r \cdot \frac{\partial \Psi_d(I_d, I_q)}{\partial I_q} \right) + 2\omega_r \cdot (I_d \cdot R + \omega_r \cdot \Psi_q(I_d, I_q)) \cdot \frac{\partial \Psi_q(I_d, I_q)}{\partial I_q} \right] = 0 \quad (11)$$

$$\frac{\partial L_{I,V}}{\partial \alpha} = I_d^2 + I_q^2 - I_l^2 = 0 \quad (12)$$

$$\frac{\partial L_{I,V}}{\partial \beta} = [\omega_r \cdot \Psi_d(I_d, I_q) + I_q \cdot R]^2 + [\omega_r \cdot \Psi_q(I_d, I_q) - I_d \cdot R]^2 - V_l^2 = 0 \quad (13)$$

Equations (10)-(13) are a nonlinear system of four equations with four unknowns which can be solved numerically. A solution pair (I_d, I_q) represents the operating point on the MTPA curve with voltage and current constrains. Note that the values of parameters a and β obtained from solving (10)-(12) can be neglected since they have no physical meaning.

2.4 Calculation of MTPA curves using optimization algorithms

The MTPA curves can be calculated numerically using optimization techniques. In that case an optimization problem may be formulated as

$$-\frac{3}{2} p \cdot (\Psi_d(I_d, I_q) \cdot I_q - \Psi_q(I_d, I_q) \cdot I_d) \rightarrow \min! \\ \text{subject to:} \\ I_d^2 + I_q^2 - I_l^2 \leq 0 \\ (\omega \cdot \Psi_d(I_d, I_q) + I_q \cdot R)^2 + (-\omega \cdot \Psi_q(I_d, I_q) + I_d \cdot R)^2 - V_l^2 \leq 0 \quad (14)$$

There are also other different formulations of the optimization problem that can be used for finding the MTPA curves.

2.5 Summary of the MTPA curve calculations

It should be noted that the function $L_f(I_d, I_q)$ does not depend on speed. Therefore, for all speeds below corner speed ω_c , the solution is valid. However, the obtained solution depends on the current limit and since current produces torque, it can be said that the obtained solution depends on torque. The corner speed can be calculated using following expression

$$\omega_c = \frac{\left(I_d R \Psi_q(I_d, I_q) - I_q R \Psi_d(I_d, I_q) + \sqrt{\left(I_d^2 R^2 + V_l^2 \right) \Psi_d^2(I_d, I_q) + \left(V_l^2 - I_q^2 R^2 \right) \Psi_q^2(I_d, I_q)} - \sqrt{-2 I_d I_q R \Psi_d(I_d, I_q) \Psi_q(I_d, I_q)} \right)}{\Psi_d^2(I_d, I_q) + \Psi_q^2(I_d, I_q)} \quad (15)$$

where I_d, I_q are the current components obtained by solving (2)-(4) for the case when the nominal current is set as a current limit.

If it is required to find to find the point on the MTPA curve for the speeds that are higher than ω_c , then it is first required to solve the system (6)-(8), i.e. the system with constant voltage constrain. If the obtained (solution) current is higher than nominal (or maximal allowed), then the system with voltage and current constrain (10)-(13) should be solved.

3 MTPA control strategy

The block schematic for a common MTPA control strategy of the IPM machine is shown in the figure below.

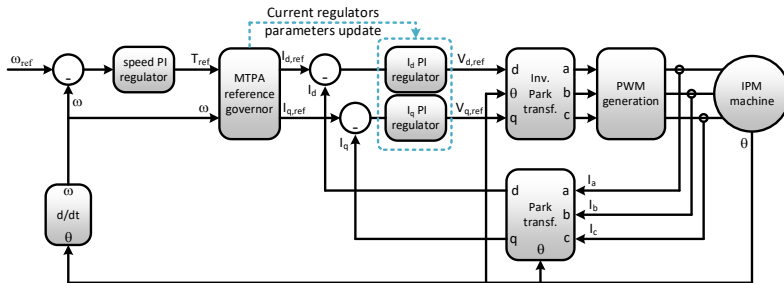


Figure 1: Block schematic of the MTPA control strategy for IMP machine

The main difference in the block schematic compared to the classical vector control is the MTPA reference governor. The MTPA reference governor gives the references I_d and I_q for every combination of torque and speed.

For better performance at high speed, current regulator parameters may also be updated based on information on the current level of machine saturation.

To calculate functions for the MTPA reference governor, it is possible to calculate the MTPA curves for different values of current limits, different values of rotor speed and for a constant value of the voltage limit. Solution pairs I_d and I_q obtained for calculation of MTPA curves can be used for calculation of torque. Now the I_d and I_q current components can be fitted as the functions of torque and speed, i.e. $I_d(T, \omega)$ and $I_q(T, \omega)$ which represent functions used for MTPA reference governor.

3 Case study

In this section the case study is conducted on the IPM machine with 48 slots and 8 poles and one layer of U shape barrier in the rotor. The finite element model of the machine is given in figure 2.

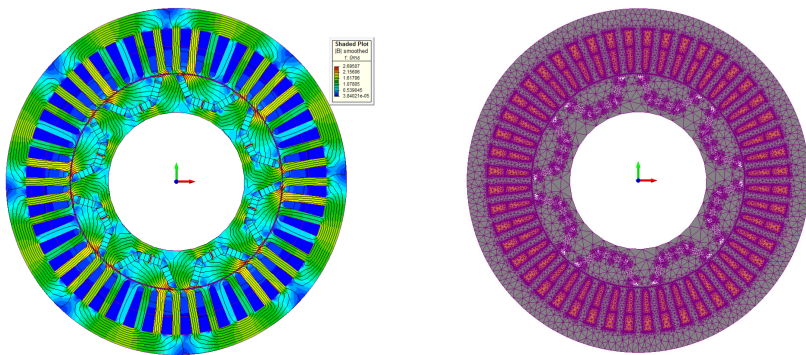


Figure 2: Finite element model of IPM machine used for the case study

Using finite elements, flux linkages in d and q axis of the armature winding were mapped. The grid was circular. Mesh of the operating points used for mapping is shown in figure 3.

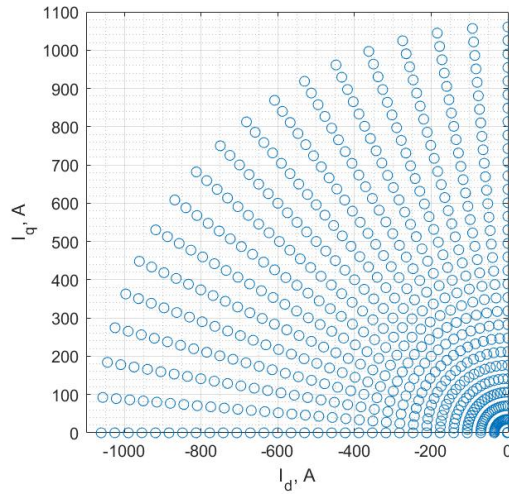


Figure 3: The mesh of the operating points used for mapping of the flux linkage

Obtained flux linkage functions are shown at the figures 4 and 5.

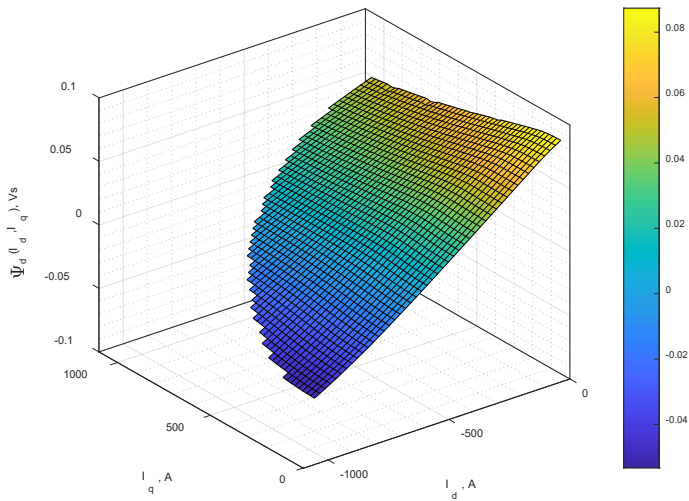


Figure 4: Flux density in d axis as a function of I_d and I_q

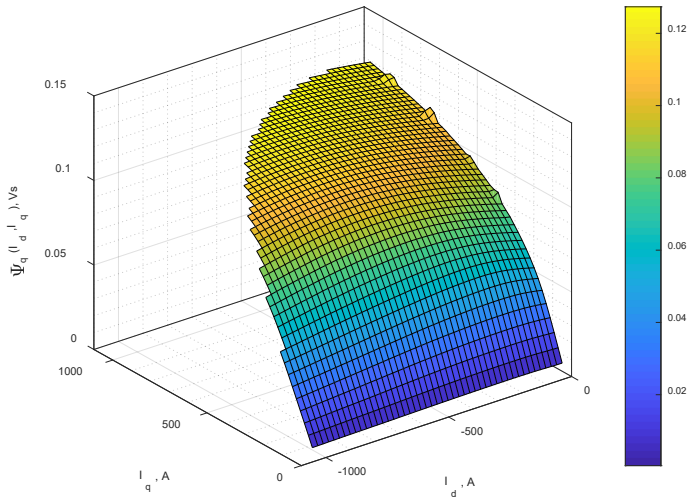


Figure 5: Flux density in q axis as a function of I_d and I_q

Flux linkage functions were used to calculate the MTPA curves as described in Section 2. The results are shown in figure 6. Figure 7 shows the MTPA curves calculated for the case when constant inductances and permanent magnet flux linkage are used.

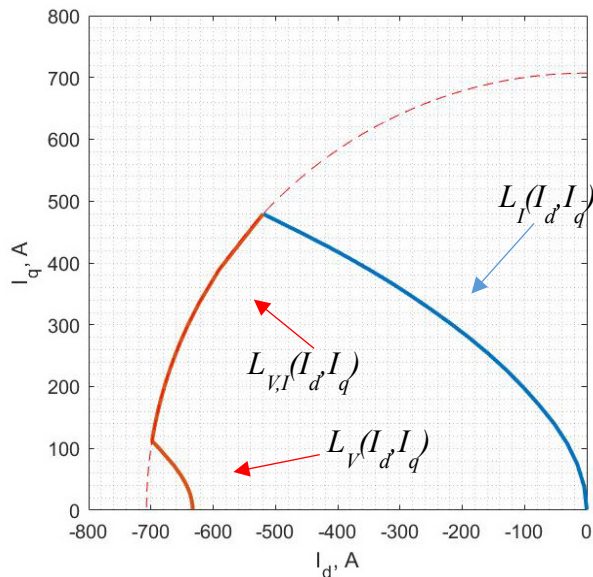


Figure 6: Calculated MTPA curves using proposed flux linkage functions

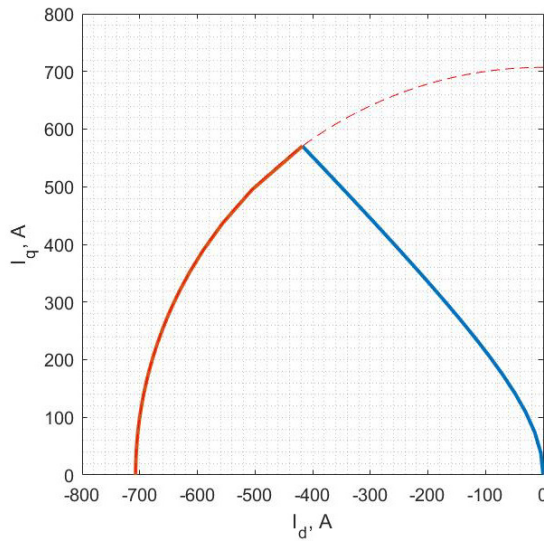


Figure 7: Calculated MTPA curves using constant values of inductances in d and q axis and flux linkage of permanent magnets in d axis

Functions $I_d(T, \omega)$ and $I_q(T, \omega)$ used for the MTPA reference governor are shown in figures 8 and 9.

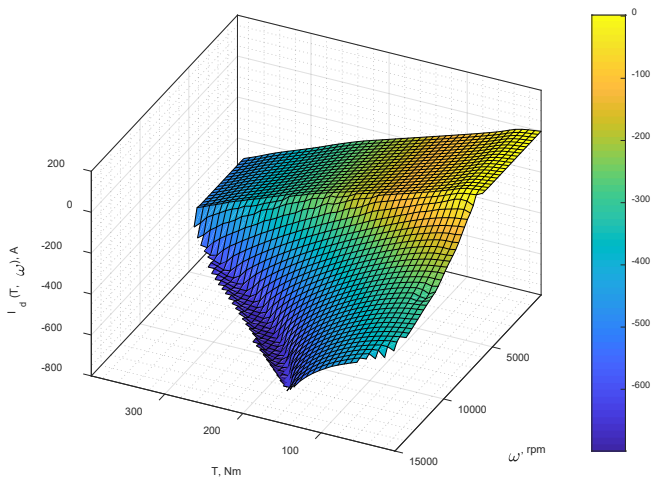


Figure 8: Current in d axis as a function of torque and rotor speed – MTPA governor function

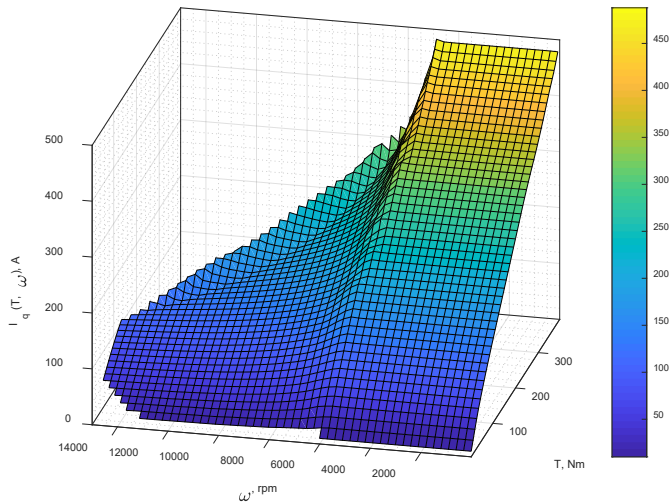


Figure 9: Current in q axis as a function of torque and rotor speed – MTPA governor function

4 Conclusion

This paper presents a method for calculation of MTPA curves and MTPA reference governor functions for IPM synchronous machines. The proposed methodology uses current dependent flux linkage functions and Lagrange multiplier theory. The method was verified on an example of a 48 slot, 8 pole IPM machine with one layer of U shaped barriers. Using the current dependent flux linkage function is crucial for obtaining correct results. Using models with constant inductances and permanent magnet flux linkage produces incorrect results due to neglect of magnetic saturation variation inherently present in IPM machines.

Acknowledgments

This work was supported in part by the Croatian Science Foundation under the Project IP-11-2013-7801 Advanced Electric Drives for Traction Applications.

References

- Bariša, T., Sumina, D. and Kutija, M., (2015). Comparison of maximum torque per ampere and loss minimization control for the interior permanent magnet synchronous generator. *2015 International Conference on Electrical Drives and Power*

- Electronics (EDPE)*, 497-502.
- Chen, J., Li J. and Qu, R., (2018). Maximum-Torque-per-Ampere and Magnetization-State Control of a Variable-Flux Permanent Magnet Machine. *IEEE Transactions on Industrial Electronics*, 65(2), 1158-1169.
- Chowdhury, M. M., Haque, M. E., Saha, S., Mahmud, M. A., Gargoom, A. and Oo, A. M. T. An Enhanced Control Scheme for IPM Synchronous Generator Based Wind Turbine with MTPA Trajectory and Maximum Power Extraction. *IEEE Transactions on Energy Conversion*, vol. PP, no. 99, pp. 1-1.
- Fazeli, S. M., Ping, H. W., Zarchi, H. A. and Soltani, J., (2009). Robust Maximum Torque per Ampere (MTPA) control of Interior Permanent Magnet Synchronous motor drives using Adaptive Input-Output Feedback Linearization approach. *2009 International Conference for Technical Postgraduates (TECHPOS)*, 1-6.
- Huang, P., Miao, C. y., Li, H. q. and Zhang, C., (2011). Maximum-Torque-Per-Ampere Control of Interior Permanent Magnet Synchronous Machine Applied for Hybrid Electric Vehicles. *2011 International Conference on Control, Automation and Systems Engineering (CASE)*, 1-3.
- Miao, Y., Ge, H., Preindl, M., Ye, J., Cheng, B. and Emadi, A., (2017). MTPA Fitting and Torque Estimation Technique Based on a New Flux-Linkage Model for Interior-Permanent-Magnet Synchronous Machines. *IEEE Transactions on Industry Applications*, 53(6), 5451-5460.
- Sun, T., Wang, J. and Chen, X., (2015). Maximum Torque Per Ampere (MTPA) Control for Interior Permanent Magnet Synchronous Machine Drives Based on Virtual Signal Injection. *IEEE Transactions on Power Electronics*, 30(9), 5036-5045.
- Tang, Z. and Akin, B., (2015). A robust V/f based sensorless MTPA control strategy for IPM drives. *2015 IEEE Applied Power Electronics Conference and Exposition (APEC)*, 1575-1581.
- Xu, X., Sun, J., Yan, C. and Zhao, J., (2017). Predictive speed control of interior permanent magnet synchronous motor with maximum torque per ampere control strategy. *2017 36th Chinese Control Conference (CCC)*, 4847-4852.

FEM Modelling of a Doubly-Fed Induction Machine

MARIO VUKOTIĆ & DAMIJAN MILJAVEC

Abstract Doubly-fed induction machine is interesting for variable-speed industrial drives, where the steady-state speed is in the vicinity of the synchronous speed. The power rating of the rotor voltage source can be significantly reduced. Finite element method machine model has been built in order to verify the machine operation with the simplest form of control of the rotor voltage – open loop scalar control (U/f) – without the use of sensor or complex algorithms, where the stator is connected directly to the public network. Machine behaviour in motor operation was observed.

Keywords: • doubly fed induction machine • supersynchronous motor operation • open loop control • finite element method • motor drive system •

CORRESPONDENCE ADDRESS: Mario Vukotić, PhD, University of Ljubljana, Faculty of electrical engineering, Tržaška cesta 25, 1000 Ljubljana, Slovenia, e-mail: mario.vukotic@fe.uni-lj.si. Damijan Miljavec, PhD, Full Professor, University of Ljubljana, Faculty of electrical engineering, Tržaška cesta 25, 1000 Ljubljana, Slovenia, e-mail: damijan.miljavec@fe.uni-lj.si.

1 Introduction

Doubly-fed induction machine (DFIM) is usually used in large-power variable-speed drives with limited range of speed in the vicinity of the synchronous speed using bidirectional power converter (Boldea, 2009; Alias, 2011; Yaramasu, 2015; Muljadi, 2012; Kumar, 2016), e. g. wind turbines, large pumps etc. In this paper, the idea of simple and robust motor drive system using DFIM and unidirectional voltage source (power flow only from the network to the machine) is presented. Larger part of the active power flows through stator winding and smaller part through rotor voltage source and rotor winding, which is used also for speed control. The power rating of the rotor voltage source is then only a fraction of the machine nominal power. The rotor must rotate with supersynchronous speed in order to achieve the desired power flow, as it is shown in Fig. 1.

In the finite element method (FEM) simulation that was made, a scalar open loop control with variable voltage to frequency ratio U/f of the rotor voltage source, as one of the simplest, easy to design and low cost motor control methods (Hannan, 2018; Smith, 2013), was assumed in order to simplify the drive as much as possible. Since there is no feedback from the drive about the rotor speed or position, the synchronous operation might be lost. A method for synchronisation detection should be provided, which can be implemented, e. g. by measuring the power, dc-link current or motor phase currents (either stator or rotor) (Liu, 2017).

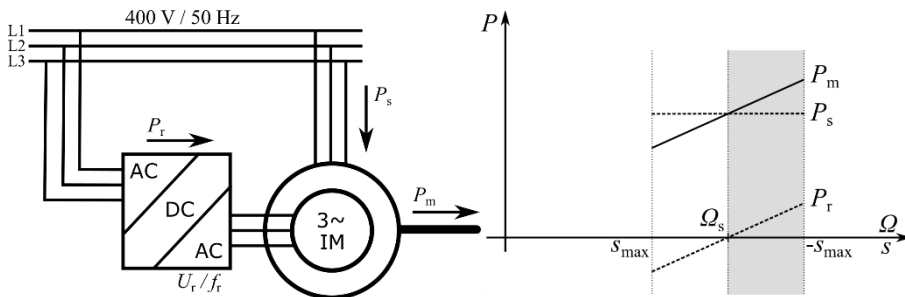


Figure 1: Power flow (left) and operational area of the DFIM (right)

2 Machine description

The simulated machine is a 6 pole induction machine with slip rings with a nominal power of 1.5 kW. The stator has 36 slots. Its dimensions are defined according to the IEC standard to fit into the 100L housing. The rotor design was shaped according to the stator design. The number of rotor slots is selected following the recommendations (Pyrhönen, 2008):

- the number of rotor slots has to be as close to the number of stator slots as possible;
- the number of stator and rotor slots should not be the same (synchronous torques);
- the rotor winding should not produce harmful torques;
- the number of rotor slots has to be divisible by three.

The only number of rotor slots that fits all these requirements is 27. The machine cross section and electric circuit, used in FEM simulations are shown in Fig. 2.

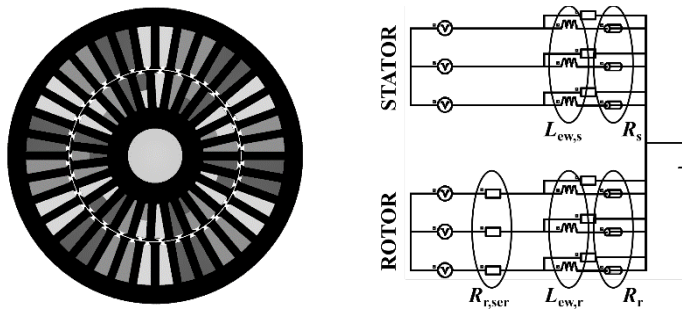


Figure 2: Two-dimensional FEM model and electric circuit

Resistances of the stator and rotor winding, R_s and R_r , are calculated analytically from number of turns in slot z_s , slot cross-section area \mathcal{A} , estimated total length of the wire l and slot fill factor k_{Cu} using the equation (1):

$$R = z^2 \cdot \frac{\rho_{Cu} \cdot l}{\mathcal{A} \cdot k_{Cu}} \quad (1)$$

Since the resistance is calculated at the room temperature, the copper electric resistivity is $\rho_{Cu} = 1.8 \cdot 10^{-8} \Omega m$. End-winding leakage inductances are calculated analytically using eq. (2) because they cannot be evaluated directly in the two-dimensional FEM model. End-winding leakage inductances are included in the FEM analysis within the outer electric circuit. The value of the permeance coefficient λ for two-layer stator and rotor winding is 0.3 (Miljavec, 2009).

$$L_{ew} = \frac{\mu_0}{2p} \cdot (2 \cdot p \cdot q \cdot z)^2 \cdot l_{ew} \cdot \lambda \quad (2)$$

No-load and short-circuit test are simulated in order to determine equivalent-circuit machine data (Table 1), which could be used further in a simplified one-dimensional description of the machine, e. g. in Matlab Simulink. Both tests were simulated at stand-still rotor, once with the low-resistance and once with the high-resistance rotor series resistors, $R_{r,ser}$, (short rotor circuit and open rotor circuit, respectively), shown in Fig. 2 on the rotor side of the circuit. Iron losses are not taken into account in the simulations, but they can be obtained in post-processing and included later.

Table 1. Equivalent-circuit machine data

Stator resistance R_1	4.9 Ω
Stator leakage inductance $L_{\sigma 1}$	12.9 mH
Magnetising inductance L_m	224.4 mH
Rotor leakage inductance $L_{\sigma 2}'$	12.9 mH
Rotor resistance R_2'	6.8 Ω
Number of pole pairs p	6
Synchronous speed n_s	1000 min^{-1}

The machine possesses the properties of both induction and synchronous machine. If the speed of rotor rotating magnetic field and the speed of the stator rotating magnetic field differ, the machine will produce the electromagnetic torque that will tend to synchronise both at the speed, defined by equation (3). This means that the machine is able to self-synchronise and start from the standstill with only a simple three-phase voltage supply from both stator and rotor. In order to ensure synchronisation, sufficient magnetisation from rotor side at certain load torque is needed. Otherwise, the machine speed and torque may start to oscillate.

$$\Omega = \frac{\omega_1 + \omega_2}{p} \quad (3)$$

3 Open-loop control simulation

Fig. 3 shows a 5 second FEM simulation of the operation of the DFIM. In the first second, the machine start-up from standstill to 1200 min^{-1} can be seen. At first second, sudden relatively large load change occurs, which causes the machine to lose synchronization. Synchronization is retrieved by first applying direct current to the rotor winding, thus the rotor starts to rotate synchronously with the stator rotating field (from second 2 to second 3 in Fig. 2). Then, the rotor frequency is increased back to $f_2 = 10$ Hz by keeping U/f ratio at the increased value in order to increase magnetisation. The rotor rotates again at 1200 min^{-1} (from second 3 to second 4). At the end of the simulation (from second 4 to second 5), the rotor frequency is decreased to 5 Hz with unchanged U/f ratio and the rotor speed decreases to 1100 min^{-1} .

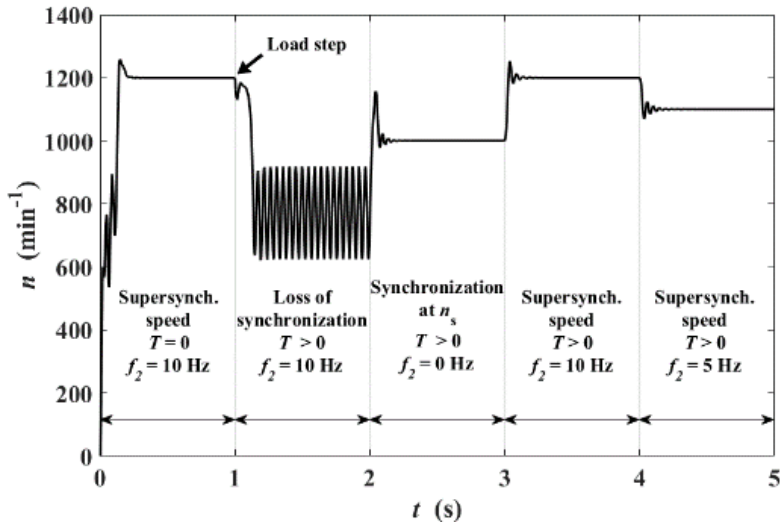


Figure 3: Simulation with open-loop control

4 Conclusion

Simulations show that DFIM in open-loop operation can be used as a motor in a limited speed range industrial drive, where the low cost and robustness are the main requirements and where high dynamics is not required. Using a unidirectional power source instead of bidirectional for the rotor winding can lower the cost even more, but limits the area of operation to the supersynchronous speed. The machine is able to self-synchronise and then operate with the exactly predefined speed at different loads.

Acknowledgements

This work is supported by the Slovenian Research Agency (project ID L2-8187 (C)). The authors acknowledge the project entitled Premium efficiency class electrical motors (project ID L2-8187 (C)) was financially supported by the Slovenian Research Agency.

References

- Boldea I., Nasar S. A. (2009). *The Induction Machines Design Handbook*, Second Edition, Boca Raton: CRC Press
- Alias A., Rahim N. A., Hussain M. A. (2011). Bidirectional Three Phase Power Converter, *IEEE First Conference on Clean Energy and Technology*, doi:10.1109/CET.2011.6041487
- Yaramasu V., Bin W., Sen P. C., Kouro S., Narimani M. (2015). High-Power Wind Energy Conversion Systems: State-of-the-Art and Emerging Technologies, *Proceedings of the IEEE*, 103, No. 5, 740-788, doi:10.1109/JPROC.2014.2378692
- Muljadi E., Singh M, Gevorgian V. (2012). Doubly Fed Induction Generator in an Offshore Wind Power Plant Operated at Rated V/Hz, *IEEE Energy Conversion Congress and Exhibition*, 49, No. 5, 2197-2205, doi:10.1109/TIA.2013.2261043
- Kumar N., Chelliah T. R., Srivastava S. P. (2016). Analysis of doubly-fed induction machine operating at motor mode subjected to voltage sag, *Engineering Science and Technology, an International Journal*, 19, 1117-1131, doi:10.1016/j.jestch.2016.01.015
- Hannan M. A., Ali J. A., Mohamed A., Hussain A. (2018). Optimization techniques to enhance the performance of induction motor drives: A review, *Renewable and Sustainable Energy Reviews*, 81, No. 2, 1611-1626, doi:10.1016/j.rser.2017.05.240
- Smith A., Gadoue S., Armstrong M., Finch J. (2013). Improved method for the scalar control of induction motor drives, *IET Electric Power Applications*, 7, No. 6, 487-498, doi:10.1049/iet-epa.2012.0384
- Liu J., Nondahl T. A., Schmidt P. B., Royak S., Rowan T. M. (2017). Generalized Stability Control for Open-Loop Operation of Motor Drives, *IEEE Transactions on Industry Applications*, 53, No. 3, 2517-2525, doi:10.1109/TIA.2017.2661249
- Pyrhönen J., Jokinen T., Hrabovcová V. (2008). *Design of Rotating Electrical Machines*, Chichester: John Wiley & Sons
- Miljavec D., Jereb P. (2009). *Vezna teorija električnih strojev (Circuit Theory of Electrical Machines)*, Ljubljana: Založba FE in FRI (in Slovenian)

An Approach to Performance Analysis of a Single-Phase Permanent Magnet Motor

LIDIJA PETKOVSKA & GOGA CVETKOVSKI

Abstract Small Permanent Magnet Motors (PMMs), usually supplied by a single-phase source, are widely used as low-power motors in many domestic appliances. The present paper deals with calculation and analysis of a single-phase PM motor characteristics at various working conditions. A combined analytical–numerical–experimental–simulation approach is presented. At the beginning, the magnetic circuit theory as a fundamental analytical approach and the Finite Element Method (FEM) as a powerful numerical approach are employed for determination of the basic motor parameters and steady-state characteristics. Afterwards, the calculated parameters are combined in MATLAB/Simulink environment. Using this simulation approach at a variety of the motor starting conditions, the dynamic characteristics of the permanent magnet motor are developed and analysed. On the basis of the calculated characteristics, the full performance analysis, including steady-state and transient operation of the studied motor is carried out. Where possible, the results are proved with experimental data.

Keywords: • single-phase permanent magnet motor • finite element method • simulation method • steady-state characteristics • dynamic characteristics •

CORRESPONDENCE ADDRESS: Lidija Petkovska PhD, Professor, Ss. Cyril and Methodius University, Faculty of Electrical Engineering and Information Technologies, Rugjer Bošković 18, 1000 Skopje, Macedonia, e-mail: lidijap@feit.ukim.edu.mk. Goga Cvetkovski, PhD, Professor, Ss. Cyril and Methodius University, Faculty of Electrical Engineering and Information technologies, Rugjer Bošković 18, P.O. Box574, 1000 Skopje, Macedonia, e-mail: gogacvet@feit.ukim.edu.mk.

DOI <https://doi.org/10.18690/978-961-286-241-1.5>
Available at: <http://press.um.si>

ISBN 978-961-286-241-1

1 Introduction

Small electric motors are widely used in various devices. Many of the domestic appliances require low-power motors that basically operate at constant speed. Since the single-phase alternative voltage is commonly available, these fractional horsepower motors are usually supplied by a single-phase source. The self-starting single phase permanent magnet motors have found growing applications. The main motor advantages are simple design, low cost production, as well as higher efficiency than rival motors. However, on the other hand, these favourable properties of the single-phase permanent magnet motor stand opposite to the restrictions concerning their self-starting ability and stability (Ertan, Dag & Capolino, 2005).

The present paper deals with calculation and analysis of the motor characteristics at various working conditions. We present a combined analytical–numerical–experimental approach for determination of steady state motor characteristics (Petkovska, Cvetkovski, 2008). After, by using previously computed quantities and by combining them with simulation method, dynamic characteristics of the studied motor will be determined and the transient operation is analysed. Where possible, the computed results are proved in laboratory, by measurements and compared accordingly.

2 Case study

Line start single phase permanent magnet synchronous motors can provide a good alternative to their counterpart induction motors at constant speed use in a low power range of applications. Like all permanent magnet motors, if the single-phase PM synchronous motor has to be utilized in a self-starting mode, usually problems occur. The starting behavior of this motor is fully dependent on the initial rotor position known as rest position θ_o , on load inertia τ_L and friction k_B . The studied object is a single-phase permanent magnet motor SPM-25/PM with rated data: supply 230 V@50 Hz, input power 26W, current 0.25 A, speed 3000 rpm; the ferrite two-pole PM rotor is with parallel magnetisation. The motor topology in 2D and 3D view is depicted in Figure 1.

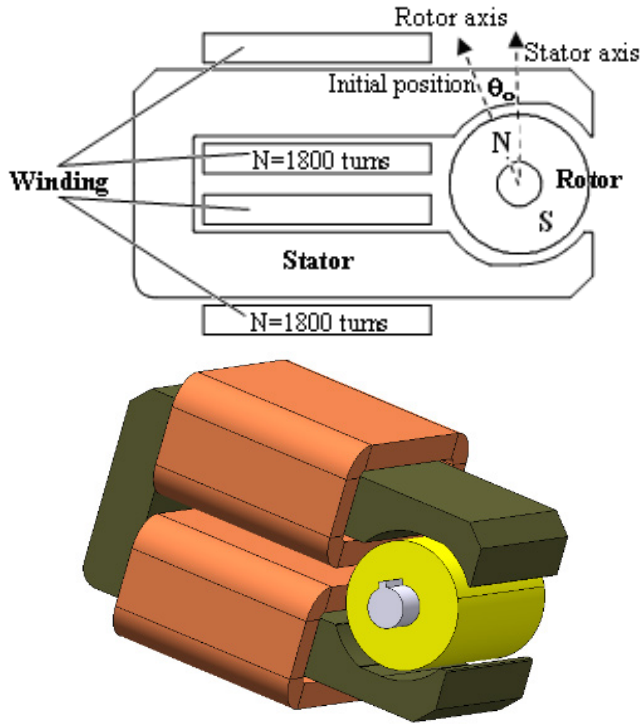


Figure 1: Topology of the studied motor in 2D and 3D view

In order to develop the self-starting torque and impart the preferred direction of the motor rotation, an asymmetric tapered air-gap is employed. In this way, a reluctance torque component is produced to complement the main electromagnetic torque. Thus, a part of stator core geometry shape, which is surrounding the rotor, is determining the stand-still rotor position under no excitation – *rest position*.

The angle corresponding to the rest position of the rotor θ_0 is a parameter with the greatest importance for the motor self-starting ability and its dynamic behavior. The angle θ_0 also defines the initial value of the permanent magnet flux linkage λ_{PM} which is of the most significant influence on the starting torque capability of the PMSM, as well as the dynamic characteristics of the motor. Consequently, it is very important to determine the angle of the rest position θ_0 , as exact as possible.

3 Analysis approach

The applied methodology is a blended approach by using analytical–numerical–experimental–simulation methods. The equations of motion are also added, where the terms and parameters are identified from analytical or FEM motor model. The transient operation at start-up of the motor is simulated, and dynamic analysis of the motor is carried out.

A preliminary determination of the motor characteristics is carried out by using analytical calculations when applying a magnetic circuit model (MCM). Each part of the magnetic flux path of a device is presented by a corresponding lumped parameter, which is associated with an equation. The main challenge is finding the best ratio of the complexity of equivalent circuit and accuracy of the results. The manipulation and solution of the equivalent magnetic circuit is performed in an identical manner as to the electric circuits.

The numerical approach to motor analysis is performed by employing the 2D/3D FEM motor model for the magnetic field calculations under various steady-state and transient working conditions. The FEM has been used for numerical calculation of characteristics and parameters at various motor operations. These calculations are used for fine–tune of the analytically computed motor characteristics. The calculations are performed by simultaneous variation of winding current $I=0\div I_n$ and rotor position along one full CCW rotation $\theta=0\div 360^\circ$. For initial rotor position and for angle $\theta=0^\circ$ is selected the instant of time when the axes of stator and rotor magnetic field are aligned. In Figure 2 is presented the 3D/2D magnetic field distribution at rated current and initial rotor position.

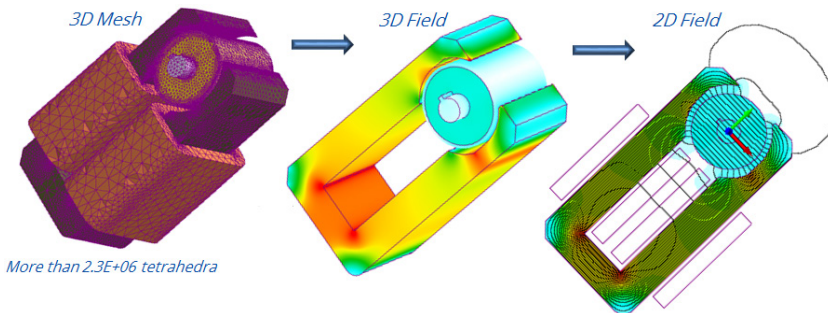


Figure 2: Magnetic field at rated current I_n and initial position $\theta_0=0^\circ$

3.1 Rest position

FEM simulations and magnetic field computations, enable to determine the value of the *rest position* angle θ_0 . From reasons known in electromagnetic theory, a permanent magnet rotor with its particular magnetization direction tends to get into a stand-still position, where the field permeance is maximum, i.e. the air-gap length is minimum. Consequently, in this position the magnetic coenergy of the rotor gets the maximum value, while the torque tends to zero value. From series of FE simulations the chart $W' = f(\theta)$ is obtained, and presented in Figure 3. The angle that determines the maximum coenergy, i.e. zero torque, defines the rest position θ_0 . Thus, for the rest position is found $\theta_0 = 26.5^\circ$, moved from the initial position in CCW direction.

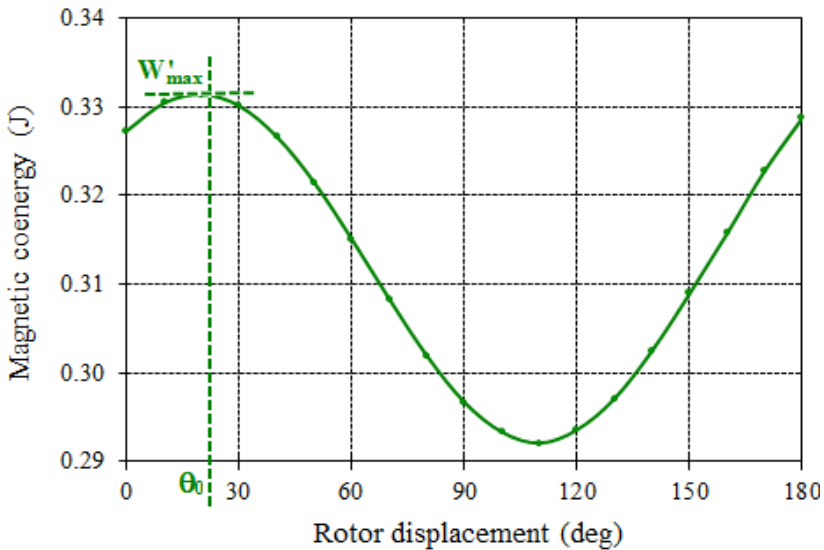


Figure 3: Magnetic coenergy of PM rotor ($I=0$) and determination of $\theta_0=26.5^\circ$

3.2 Results

The magnetic field excited by PM only, generates *reluctance torque*; when the stator winding is connected to a power supply, then the resultant *static torque* takes place. The electromagnetic torque characteristics along one rotor revolution are presented in Figure 4.

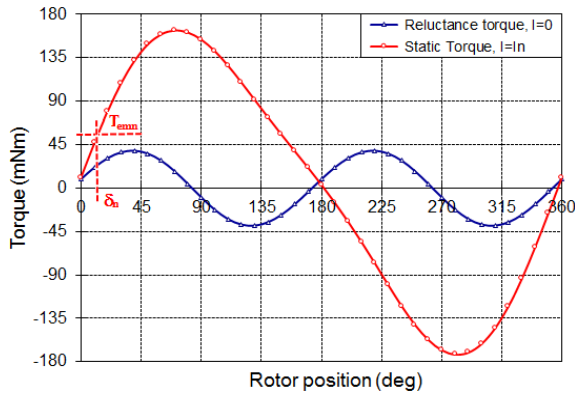


Figure 4: Static torque characteristics

The single-phase PM motor is investigated in transient operation mode at no-load, locked rotor and at rated operation. As an example, dynamic characteristic of torque at start-up at no-load (free acceleration) and with rated shaft load are shown in Figure 5 (a) and (b) respectively.

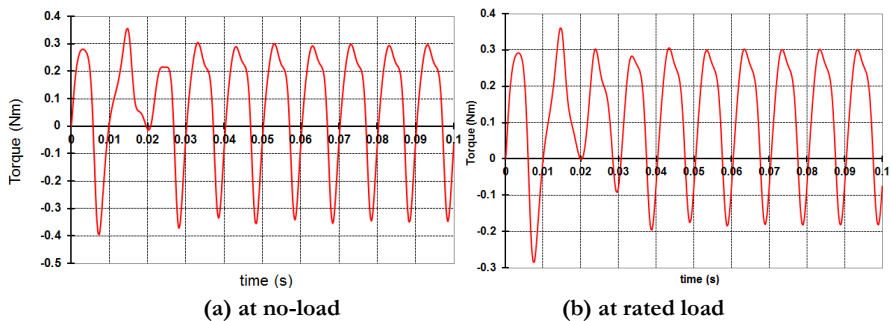


Figure 5: Start-up torque characteristics

Comparative results for the electromagnetic torque at no-load and rated load, obtained by various methods and by combined approach, are presented in Table 1.

Table 1: Electromagnetic torque comparison

Operation	FEM	Simulation	Measured	Combined
No-load (mNm)	20.6	24.7	21.5	22.3
Rated load (mNm)	53.5	59.4	56.4	58.7

4 Conclusions

Single phase line-start permanent magnet motors are good alternative for low power domestic appliances, especially for pumps and fans. A simple U-shape construction is used for ease of manufacture and a low unit cost. The tapered asymmetrical air-gap produces a starting torque with reasonable value. The motor is capable for self-starting, providing the starting torque, and continuing running synchronously.

In the paper an analytical-numerical approach is developed. The combination of magnetic circuit theory and finite element method has been shown to be computationally efficient for simulating the steady-state motor performance characteristics. The 3D FEM simulations are used for magnetic field computations of the PM synchronous motor. The steady-state torque characteristics are computed. An efficient approach for accurate determination of the angle θ_0 is presented. The Simulink model in MATLAB environment is developed, and simulations of the motor start-up at various loads on the shaft are performed. Results are proved by measurements; they show good agreement and confirm the combined approach as accurate.

References

- Ertan, H. B., Dag, B. Capolino, G. A. (2005). Calculation of Parameters of Single-Phase PM Motor for Design Optimization, *IEEE Transactions on Energy Conversion* 20 (3), pp. 538-548.
- Petkovska, L., Cvetkovski, G. (2008). Study on Electromagnetic Field of a Single-Phase PM Synchronous Motor, *Proceedings of the International Conference of Electrical Engineering – ICEE*, Okinawa, Japan, paper No. O-001 published on CD, pp. 1-6.

Optimization by the Evolutionary Algorithm and FEM Tools: Example on Switched Reluctance Motor

MARINKO BARUKČIĆ, ŽELJKO HEDERIĆ, TIN BENŠIĆ &
VENCO ĆORLUKA

Abstract Usage of the numerical method in the electromagnetic analysis of the electrical devices improves the quality of the simulations making the simulations more realistic and exact. There are simulation tools for performing such simulations based on numeric electromagnetic field calculations. Using these tools in optimization procedure during the device design ensure achieving more quality solutions. On other hand implementing such simulation tools require robust optimization techniques capable to perform black-box optimization procedure. The optimization methods appropriate for this are metaheuristic optimization methods. The coworking procedure of the FEM simulation tool and evolutionary optimization method on switched reluctance motor example is presented in the paper. The FEMM electromagnetic field analysis tool and MIDACO metaheuristic optimization solver are used for this purpose.

Keywords: • coworking simulation • evolutionary optimization • FEM tool • switched reluctance motor • torque •

CORRESPONDENCE ADDRESS: Marinko Barukčić, PhD, Associate Professor, Josip Juraj Strossmayer University of Osijek, Faculty of Electrical Engineering, Computer Science and Information Technology Osijek, Kneza Trpimira 2B, 31 000 Osijek, Croatia, e-mail: marinko.barukcic@ferit.hr. Željko Hederić, PhD, Associate Professor, Josip Juraj Strossmayer University of Osijek, Faculty of Electrical Engineering, Computer Science and Information Technology Osijek, Kneza Trpimira 2B, 31 000 Osijek, Croatia, e-mail: zeljko.hederic@ferit.hr. Tin Benšić, PhD student, Josip Juraj Strossmayer University of Osijek, Faculty of Electrical Engineering, Computer Science and Information Technology Osijek, Kneza Trpimira 2B, 31 000 Osijek, Croatia, e-mail: tin.bensic@ferit.hr. Venco Ćorluka, Ph.D., Josip Juraj Strossmayer University of Osijek, Faculty of Electrical Engineering, Computer Science and Information Technology Osijek, Kneza Trpimira 2B, 31 000 Osijek, Croatia, e-mail: venco.corluka@ferit.hr.

1 Introduction

The optimization of the electrical devices in the design phase is widely used with the aim to obtain more quality device. For the purpose of the optimization, the mathematical model of the device is usually used. Such mathematical models are an approximation of the real devices and include within more or less neglecting. These approximations are required due to the complexity of modeling all physical processes in the device or the possibility of solving the model. Application of evolutionary and population-based optimization method for optimal design of the electrical machines using analytical calculated objective functions are presented in (Šarac and Cvetkovski, 2014; Cvetkovski, Petkovska and Lefley, 2018).

The application of the numerical mathematic calculation makes possible to solve very complex mathematical device models. This ensures performing more accurate simulation and calculation results. In case of the electrical machines, the calculation of the electromagnetic fields based on the Finite Element Method (FEM) is usually used for this purpose. Using the FEM numerical method for simulation of the switched reluctance motor (SRM) calculations with higher accuracy can be obtained. The examples of the optimization of the SRM design can be found in (Ohyama et al., no date; Kumar, Shaik and Deepika, 2010). In (Peniak et al., 2017) the optimization of the SRM based on numerical calculation and in (Rebahi et al., 2015) application of the different metaheuristic optimizer for SRM design optimization are presented.

Using simulation tools based on numerical calculations of the electromagnetic fields in the optimization process of the SRM design required black-box optimization approach. This is due to the character of such methods because numerical calculations give numerical data on output and the objective function is not available in analytic form. The optimization method for black-box optimization need to be used for this purpose. The Evolutionary Algorithms (EA) are used here because they belong to the class of global optimizer and metaheuristic method. Global optimizer no need additional information about the objective function but only the numerical values of the objective function. Based on the above-given problem description can be concluded that the FEM analysis tool and a metaheuristic optimizer have to work in a coworking environment. The coworking setup is implemented using FEMM simulation tools (Meeker, no date) and MIDACO metaheuristic optimizer (Schlueter et al.,

2013). A similar approach of applying metaheuristic optimization techniques for design optimization of SMR and other machines can be found in (Phuangmalai, Konghirun, and Chayopitak, 2012; Kheireddine et al., 2018).

The rest of the paper is organized as follows. The mathematical model of the problem is defined first then the simulation setup and results are presented and the conclusion is given at the end.

2 Optimization problem and coworking setup

The optimization problem considers maximization of the average electromagnetic torque per one stator pole:

$$T_{av}(d\vec{v}) \rightarrow \max \quad (1)$$

where $d\vec{v}$ denotes a set of decision variables in form of the vector.

The optimization problem defined by the objective (1) includes constraints regarding the decision variables ranges:

$$dv_{i,L} \leq dv_i \leq dv_{i,U} \quad (2)$$

Also, other inequality and equality constraints can be included in the optimization problem but for example presented here an additional constraint are not considered.

The problem decision variables are the geometric dimensions of the SRM noted in general form as a vector:

$$d\vec{v} = [dv_1 \quad \dots \quad dv_i \quad \dots \quad dv_N] \quad (3)$$

The number of the decision variables defines dimensionality of the problem and in this case, 11 geometric parameters of the SRM are considered.

$$d\vec{v} = [R_s \quad J_l \quad S_p \quad \alpha_s \quad r_{S1} \quad r_{S2} \quad \delta \quad R_p \quad \alpha_r \quad r_{R1} \quad r_{R2}] \quad (4)$$

Where R_s is the outer radius of the stator, J_t is stator yoke thickness, S_p is high of the stator pole, a_s is the angle of the stator pole, r_{s1} and r_{s2} are radii of edge rounding of stator pole, δ is air gap thickness, R_p is high of the rotor pole, a_r is angle of the rotor pole and r_{r1} and r_{r2} are radii of edge rounding of rotor pole. The optimization problem defined by (1) and (2) is implemented in the Python programming environment and solved by using MIDACO optimization solver (Schlueter *et al.*, 2013). The MIDACO solver is a global optimizer using Ant Colony Optimization (ACO) technique. The ACO is a metaheuristic method using the solution population during the research of the solution space. The MIDACO solver finds the optimization problem solution near to the global optimum. During the optimization process calculation of the objective function value (1) is done by the FEMM simulation tools. The scheme of the coworking simulation setup consists of the FEMM and MIDACO tools and programming environment is shown in Fig. 1.

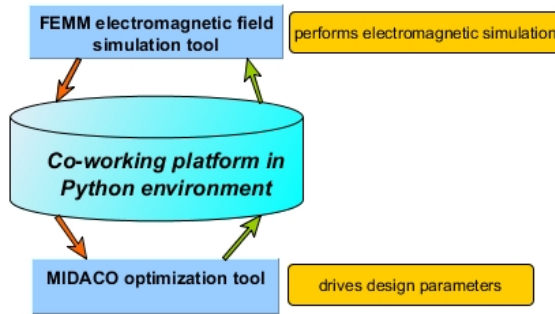


Figure 3: Scheme of the used co-working approach

3 Optimization procedure results on a SRM example

The proposed coworking setup is applied to an example of SRM for data given below. The ranges of the decision variables used in the simulated example are given in table 1.

The average electromagnetic torque is calculated for all torque values for rotor angles in the range of the aligned and unaligned positions of the rotor pole. The angle step of the rotor rotation is set at 2.5° , the stator winding current on 1 A and turns of the stator winding on 80 in simulations. The initial design is defined for lower range bound of the decision variables as a starting point in the optimization procedure. In Fig. 2 the simulations results for initial and optimized

designs are given. The impact of pole edges rounding on the torque curve is shown in Fig. 3.

Table 1: Ranges of the decision variables used in simulations

Decision variable	R_S [mm]	J_t [mm]	S_p [mm]	α_S [°]	r_{S1} [mm]	r_{S2} [mm]
Variable range	40 - 50	5 - 15	5 - 15	10 - 25	0.1 - 2	0.1 - 2
Decision variable	δ [mm]	R_p [mm]	α_R [°]	r_{R1} [mm]	r_{R2} [mm]	
Variable range	0.25 - 0.5	2.5 - 10	10 - 45	0.1 - 2	0.1 - 2	

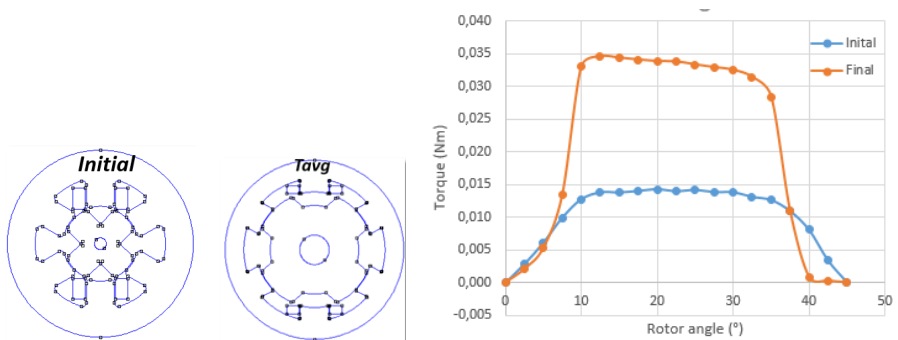


Figure 2: Initial, optimized design and simulation results of SRM design optimization

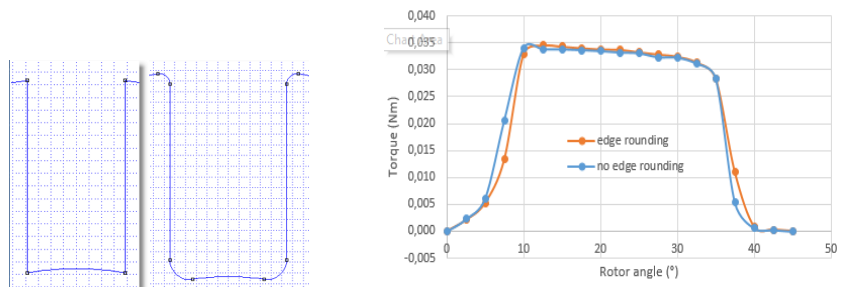


Figure 3: Comparison of torques for optimized SRM design with and without the edge rounding of the stator and rotor poles

4 Conclusion

The optimization of the SRM design in coworking setup is presented in the paper. The FEMM electromagnetic field simulation tool and MIDACO metaheuristic optimization method are implemented. The numerical simulation and optimization tools are required to have the possibility for interfacing with each other. This is a limiting factor in choosing the simulation and optimization tools in presented setup. The simulation results show that using the proposed procedure is possible to achieve increasing the average value of the SRM static torque. The improving of the average torque value for optimized SRM design is about 135 % in relation to the average torque of the initial design. According to the simulation results, it seems that edge rounding of the rotor and stator poles has no significant impact on the average value of the electromagnetic torque as well as on torque curve in general. The main drawback of the used setup is high computational time (about 650 sec) caused by using the numerical calculation of the electromagnetic field for a large number of the possible design solutions.

References

- Cvetkovski, G. V., Petkovska, L. and Lefley, P. (2018) 'Cuckoo search as a tool for optimal design of PM brushless DC motor', *COMPEL - The international journal for computation and mathematics in electrical and electronic engineering*, Emerald Publishing Limited, p. COMPEL-01-2018-0025. doi: 10.1108/COMPEL-01-2018-0025.
- Kheireddine, B. *et al.* (2018) 'Application of PSO and TLBO algorithms with neural network for optimal design of electrical machines', *COMPEL - The international journal for computation and mathematics in electrical and electronic engineering*, Emerald Publishing Limited, 37(2), pp. 549–564. doi: 10.1108/COMPEL-12-2016-0532.
- Kumar, R. Y. U., Shaik, a. a. and Deepika, K. S. R. (2010) 'Design analysis and performance characteristics of Switched Reluctance Motor', *Industrial and Information Systems (ICIIS), 2010 International Conference on*, pp. 574–579. doi: 10.1109/ICIINFS.2010.5578639.
- Meeker, D. C. (no date) *Finite Element Method Magnetics, Version 4.2 ((12Jan2016) Build)*, Available at: <http://www.femm.info> (Accessed: 21 January 2018).
- Ohyama, K. *et al.* (no date) 'Design using Finite Element Analysis of Switched Reluctance Motor for Electric Vehicle', in *2006 2nd International Conference on Information & Communication Technologies*. IEEE, pp. 727–732. doi: 10.1109/ICITTA.2006.1684462.
- Peniak, A. *et al.* (2017) 'Design and optimization of switched reluctance motor for electrical vehicles', *Electrical Engineering*, 99(4), pp. 1393–1401. doi: 10.1007/s00202-017-0621-4.
- Phuangmalai, W., Konghirun, M. and Chayopitak, N. (2012) 'A design study of 4/2 switched reluctance motor using particle swarm optimization', in *2012 9th International Conference on Electrical Engineering/Electronics, Computer,*

- Telecommunications and Information Technology*. IEEE, pp. 1–4. doi: 10.1109/ECTICON.2012.6254302.
- Rebahi, F. *et al.* (2015) ‘Multi-objective Optimization Design of 8/6 Switched Reluctance Motor using GA and PSO Algorithms’, *Journal of Electrical Engineering*, 15(4), pp. 1–8. Available at: <http://www.jee.ro/covers/editions.php?act=art&art=WP1428966227W552c4b53c6c29> (Accessed: 30 August 2018).
- Šarac, V. and Cvetkovski, G. (2014) ‘Efficiency optimization of single phase motor using GA approach’, *PRZEGLĄD ELEKTROTECHNICZNY*, 12, pp. 153–156. doi: 10.12915/pe.2014.12.37.
- Schlueter, M. *et al.* (2013) ‘MIDACO on MINLP space applications’, *Advances in Space Research*. Pergamon, 51(7), pp. 1116–1131. doi: 10.1016/J.ASR.2012.11.006.

The Efficiency Improvement of a Permanent Magnet Synchronous Machine Drive

ŽELJKO PLANTIĆ, TINE MARIČIČ & GORAZD ŠTUMERGER

Abstract This paper presents the efficiency improvement in a speed closed-loop controlled Permanent Magnet Synchronous Machine (PMSM) drive. Generally, the drive efficiency can be improved by minimizing the inverter and PMSM losses. This is achieved by the proper selection of dc-bus voltage and switching frequency of the inverter. The direct (d-) and quadrature (q-) axis current references generation methods, discussed in this paper, further improve the drive's efficiency. The Maximum Torque Per Ampere (MTPA) characteristic is normally applied to generate the d- and q-axis current references in vector controlled PMSM drives. It assures control with maximum torque per unit of current, but cannot assure maximum efficiency. In order to improve efficiency of the PMSM drive, this paper proposes the generation of d- and q-axis current references based on Maximum Efficiency (ME) characteristic.

Keywords: • permanent magnet synchronous machine • speed controlled drive • MTPA characteristic • maximum efficiency (ME) characteristic • efficiency improvement •

CORRESPONDENCE ADDRESS: Željko Plantić, Ph.D., Energy Institute Hrvoje Požar, Savska cesta 136, 10001 Zagreb, Croatia, e-mail: zplantic@eihp.hr. Tine Marčič, Ph.D., Energy Agency of the Republic of Slovenia, Strossmayerjeva ulica 30, SI-2000 Maribor, Slovenia, e-mail: tine.marctic@agen-rs.si. Gorazd Štumberger, Ph.D., Professor, University of Maribor, Faculty of Electrical Engineering and computer science, Koroška cesta 46, 2000 Maribor, Slovenia, e-mail: gorazd.stumberger@um.si.

1 Introduction

The increasing energy consumption leads to energy shortages and increasing energy prices. For this reason, more and more researchers are occupied with improving the efficiency of electrical drives. Due to its high efficiency, high power density and wide operating range of speed, the Permanent Magnet Synchronous Machine (PMSM) is often used in such drives. The drive efficiency can be improved by minimizing losses, which includes a proper selection of dc-bus voltage and switching frequency of the power inverter, and a proper control of the PMSM. In the case of vector controlled PMSM, a proper selection of the direct (d) and quadrature (q) axis current references can improve drive efficiency. In industrial applications, the Maximum Torque Per Ampere (MTPA) characteristic (De Doncker, 2011), (Pan, 2015), which considers only PMSM copper losses, is normally used for generation of current references. When applied, the PMSM drive produces maximum torque per unit of stator current, but cannot reach the maximum efficiency due to the neglected iron core losses. The Maximum Efficiency (ME) characteristic considers copper losses as well as iron core losses of PMSM. When it is applied for generation of current references, the maximum efficiency of a PMSM drive can be achieved.

Authors in (Monajemy, 2001), (Cavallaro, 2005) and (Hassan, 2012) use the steady-state PMSM model to consider the copper and iron core losses. The power losses in an inverter fed PMSM are discussed in (Hassan, 2012), (Pohlenz, 2010), while (Pohlenz, 2010) also deals with MTPA and ME characteristics in drives with wide speed and torque range.

In this paper, the PMSM model is used to explain the differences between the MTPA and ME characteristics. The MTPA and ME characteristics are determined experimentally by measurements performed on the tested vector controlled PMSM drive. The existing control algorithm is extended by a current references generator, where the determined MTPA and ME characteristics are applied to generate the d- and q-axis current references. The speed closed-loop vector control of PMSM, obtained in this way, is used to measure the efficiency of the entire drive.

2 PSMS drive losses

A PMSM drive normally consists of the PMSM, power inverter, load, and the control system. In the PMSM drive, load is the element, which dictates the proper selection of the other drive elements. The energy conversion process inevitable includes losses, mostly in the power inverter and PMSM. These loss components substantially influence the drive efficiency. This paper focuses on the detailed research of PMSM losses, which are minimized in the speed closed-loop controlled PMSM drive by a proper generation of d- and q-axis current references, whereas the power inverter losses are considered by measurements only.

2.1 Power Losses in Power Inverter

The power losses in a power inverter consist of conduction or Ohm's losses and switching losses (Hassan, 2012). In this work they are minimized by a proper selection of dc-bus voltage and switching frequency. Their values are determined experiment-ally by measurements performed on the tested PMSM drive.

2.2 Power Losses in PMSM

The analysis of power losses in the PMSM is based on the two-axis steady-state PMSM model with lumped parameters, written in the d-q reference frame. The d-axis is aligned with the flux linkage vector due to the permanent magnets while the q-axis leads for electrical $\pi/2$. The model is schematically shown in Fig. 1. The copper losses are considered by the stator resistance R_s , while the iron core losses are accounted for by the iron core resistance R_r . In the steady-state model, written in the d-q reference frame, the indices d and q refer to the d- and q-axis, U_d and U_q are the stator voltages, I_d and I_q are stator currents, I_{md} and I_{mq} are the magnetizing currents, I_{cd} and I_{cq} are the iron core currents, $L_{d\sigma}$ and $L_{q\sigma}$ are the stator inductances, ω_{md} is the flux linkage due to the permanent magnets, T_e is the electromagnetic torque, ω_e is the electrical rotor speed and p_p is the number of pole pairs.

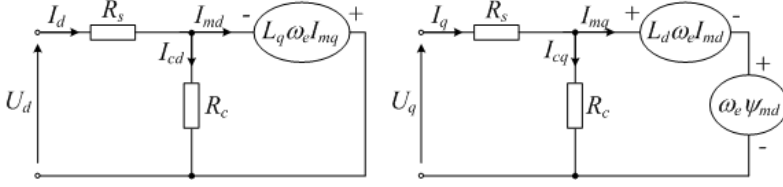


Figure 4: Applied steady-state model of PMSM in d-q reference frame

Considering Fig. 1, the voltage equations (1) and the torque equation (2) can be written:

$$U_d = R_s I_d - \omega_e L_q I_{mq}, \quad U_q = R_s I_q + \omega_e L_d I_{md} + \omega_e \psi_{md} \quad (1)$$

$$T_e = p_p I_{mq} (\psi_{md} + (L_d - L_q) I_{md}) \quad (2)$$

where

$$I_d = I_{md} + I_{cd} = I_{md} - \frac{\omega_e L_q I_{mq}}{R_c}, \quad I_q = I_{mq} + I_{cq} = I_{mq} + \frac{\omega_e}{R_c} (L_d I_{md} + \psi_{md}) \quad (3)$$

The power losses in the PMSM $P_{loss, PMSM}$ can be divided into controllable losses, which are the copper losses $P_{loss, Cu}$ and the iron core losses $P_{loss, Fe}$, and uncontrollable losses, which are the mechanical and additional losses (Cavallaro, 2005). Neglecting the uncontrollable losses, (4) describes the PMSM losses.

$$P_{loss, PMSM} = P_{loss, Cu} + P_{loss, Fe} \quad (4)$$

Considering Fig. 1 and (1) to (4), $P_{loss, Cu}$ and $P_{loss, Fe}$ can be expressed by (5) and (6).

$$P_{loss, Cu} = R_s (I_d^2 + I_q^2) = R_s \left(I_{md} - \frac{\omega_e L_q I_{mq}}{R_c} \right)^2 + R_s \left(I_{mq} + \frac{\omega_e (L_d I_{md} + \psi_{md})}{R_c} \right)^2 \quad (5)$$

$$P_{loss, Fe} = R_c (I_{cd}^2 + I_{cq}^2) = \frac{\omega_e^2}{R_c} \left[(L_q I_{mq})^2 + (L_d I_{md} + \psi_{md})^2 \right] \quad (6)$$

3 Improving efficiency of the drive

The PMSM drive efficiency can be improved by minimizing the inverter and PMSM losses. According to (Hassan, 2012), the inverter losses can be mostly influenced by the closed-loop control or a proper choice of dc-bus voltage and by an optimal choice of switching frequency. The PMSM losses can be influenced by the voltage and current total harmonic distortion that depend on the switching frequency and in the case of vector controlled PMSM by the generation of the d- and q-axis current references. The generation of current references is normally based on the MTPA characteristic (Monajemy, 2001). It assures the maximum torque per unit of current and not the maximum efficiency of the entire drive (Pohlensz, 2010). The last can be achieved when the ME characteristic is applied for generation of the d- and q-axis current references.

3.1 Theoretical Background of the MTPA and ME Characteristics

Let us consider all parameters of the PMSM steady-state model, shown in Fig. 1 and described by (1) to (6), as constant. The starting point for derivation of the MTPA characteristic is the torque equation (2) and the PMSM steady-state model shown in Fig. 1, where the iron core resistance is neglected ($R_r \rightarrow \infty$). Consequently, according to (3), I_{d1} and I_{q1} equal zero which leads to $I_d = I_{md}$ and $I_q = I_{mq}$. Considering the angle of the stator current vector α , shown in Fig. 2b), the relation between the d- and q-axis currents, that provides the maximum torque per unit of current, can be determined from (2) by (7), which yields (8) (Pan, 2015).

$$\max(T_e) \Rightarrow \frac{dT_e}{d\alpha} = 0 \quad (7)$$

$$I_{d_{1,2}} = \frac{-\psi_{md}}{2(L_d - L_q)} \pm \sqrt{\frac{\psi_{md}^2}{4(L_d - L_q)^2} + I_q^2} \quad (8)$$

Similarly, the ME characteristic describes the relation between the d- and q-axis current that provides the minimum of PMSM losses, which leads to the maximum efficiency of the PMSM drive. According to (Cavallaro, 2005) and (Hassan, 2012), the PMSM losses (4) can be minimized for each combination of T_e and ω_e . Considering (2) in (5) and (6), (4) can be expressed as a function of

I_{md} , T_e , and ω_e . In the case of steady-state operation, T_e and ω_e are constants, which means that the PMSM power losses $P_{loss,PMSM}$ (4) can be described as a function of I_{md} . However, because T_e (2) depends on I_{md} and I_{mq} , the PMSM power losses can be minimized by (9), which yields (10) (Hassan, 2012), where (10) describes the ME characteristic.

$$\min(P_{loss,PMSM}) \Rightarrow \left. \frac{dP_{loss,PMSM}(I_{md}, I_{mq}, \omega_e)}{dI_{md}} \right|_{T_e, \omega_e} = 0 \quad (9)$$

$$I_{md} = - \frac{\omega_e^2 L_d \psi_{md} (R_s + R_c) + R_s R_c \omega_e (L_d - L_q) I_{mq}}{\omega_e^2 L_d^2 (R_s + R_c) + R_s R_c^2} \quad (10)$$

The MTPA and ME characteristics of the tested PMSM, obtained by the described procedures, are shown in Fig. 2a) for the nominal speed. Fig. 2b) shows the stator current vector \mathbf{I}_s and its components I_d and I_q . $|\mathbf{I}_s|$ denotes the length of \mathbf{I}_s .

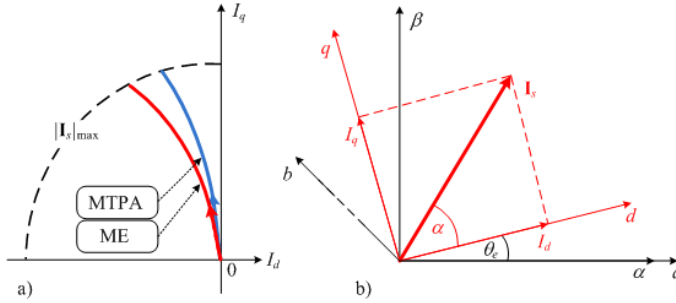


Figure 2: MTPA and ME characteristics (a) and stator current vector in α - and d-q-reference frame (b)

3.2 Experimentally determined MTPA and ME characteristics

The MTPA and ME characteristics derived theoretically in the section 3.1 are based on the steady-state PMSM model with constant parameters. Therefore, they are not accurate enough to improve the efficiency of the tested PMSM drive. To improve the PMSM drive efficiency, the MTPA and ME characteristics were determined by measurement performed on the PMSM drive. The PMSM (Domel AZ 150-45, 400 V, 1.6 kW, outer-rotor, surface mounted magnets) was torque controlled and fed by an inverter. The vector control of PMSM was realized on

the control system dSPACE PPC 1103. The rotor speed was closed-loop controlled by an active load (IM). The input and output power of the inverter and PMSM, and their efficiencies, were measured by the power analyzers Norma D5255M and Norma D6100. The determined MTPA and ME characteristics are shown in Fig. 4 for different rotor speeds. Similarly as in the calculated results show in Fig. 2a), the measured ME characteristics require higher values of the negative d-axis currents than the MTPA characteristics at the same rotor speeds. The value of the negative d-axis current component increases with the increasing rotor speed.

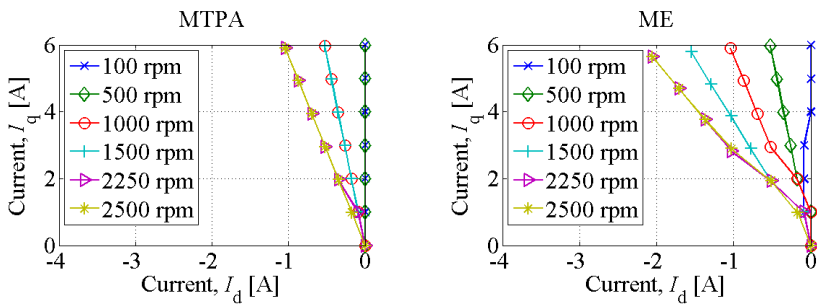


Figure 3: Experimentally determined MTPA and ME characteristics

4 Results

The experimentally determined MTPA and ME characteristic were applied to determine the d-and q-axis current references i_{dr} and i_{qr} required in the speed control of a PMSM performed in the d-q reference frame. The obtained experimental results are shown in Fig. 4.

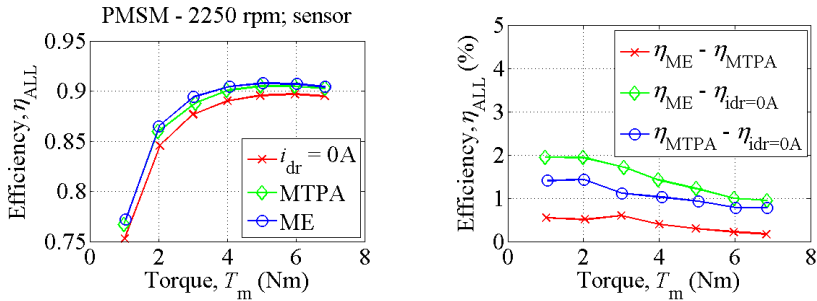


Figure 4: Measured efficiencies of the speed closed-loop controlled PMSM drive and their differences for the control realization in the cases when i_{dr} and i_{qr} are determined with MTPA and ME characteristics and in the case when $i_{dr}=0$ A.

5 Conclusion

The work clearly demonstrates that the use of ME characteristic instead of MTPA characteristic in the current references generation improves the efficiency of PMSM drive. The improvements are in the range between 1 and 2 %, when ME characteristic is applied instead of $i_{dr} = 0$, and between 0.2 and 0.5 %, when ME characteristic is instead of MTPA characteristic.

Acknowledgments

This work was supported in part by the Slovenian Research Agency (ARRS), projects L2-2060, L2-4114 and P2-0115.

References

- De Doncker, R., Pule, D. W. J., Veltman, A. (2011). Advanced Electrical Drives – Analysis, Modeling, Control, *Springer*, 165-221.
- Pan, VEN C.-T., Sue, S. -M. (2015). A Linear Maximum Torque Per Ampere Control for IPMSM Drives Over Full-Speed Range. *IEEE Trans. on Energy Conv.*, 20/2, 359-366.

- Monajemy, R., Krishnan, R. (2001). Control and Dynamics of Constant-Power-Loss-Based Operation of Permanent-Magnet Synchronous Motor Drive System. *IEEE Trans. on Ind. Electronics*, 48/4, 839-844.
- Cavallaro, C., DiTommaso, A. O., Miceli, R., Raciti, A. (2005). Efficiency Enhancement of Permanent-Magnet Synchronous Motor Drives by Online Loss Minimization Approaches. *IEEE Trans. on Ind. Electronics*, 52-4, 1153-1160.
- Hassan, W., Wang, B. (2012). Efficiency Optimisation of PMSM Based Drive System. *7th IEEE International Power Electronics and Motion Control Conference (IPEMC)*, 2, 1027-1033.
- Pohlenz, D., Böcker, J. (2010). Efficiency Improvement of an IPMSM Using Maximum Efficiency Operating Strategy. *14th IEEE International Power Electronics and Motion Control Conference (EPE-PEMC)*, T5,15-T5,19.

Determination of a Crack's Dimensions on the Basis of the Non-Destructive Testing with Eddy Currents Using Metaheuristics

MARKO JESENİK, ANTON HAMLER, MILOŠ BEKOVIĆ & MLADEN TRLEP

Abstract This paper introduces a procedure for finding the position, length, depth, and width of a crack within a material, based on eddy current non-destructive testing. The measured values of the magnetic flux density are used for the crack parameters' identification. The crack's position and length are found by considering the differences in the measured magnetic flux densities between neighbouring measurement points. The crack's depth and width are found by using a stochastic optimization method – differential evolution connected with a finite element model. This procedure was tested in the case of aluminium and austenitic stainless steel plate with a crack.

Keywords: • finite element method • differential evolution • non-destructive testing • magnetic fields • crack's dimensions •

CORRESPONDENCE ADDRESS: Marko Jesenik, PhD, Assistant Professor, University of Maribor, Faculty of Electrical Engineering and Computer Science, Koroška cesta 46, 2000 Maribor, Slovenia, e-mail: marko.jesenik@um.si. Anton Hamler, PhD, Full Professor, University of Maribor, Faculty of Electrical Engineering and Computer Science, Koroška cesta 46, 2000 Maribor, Slovenia, e-mail: anton.hamler@um.si. Miloš Beković, PhD, Assistant Professor, University of Maribor, Faculty of Electrical Engineering and Computer Science, Koroška cesta 46, 2000 Maribor, Slovenia, e-mail: milos.bekovic@um.si. Mladen Trlep, PhD, Full Professor, University of Maribor, Faculty of Electrical Engineering and Computer Science, Koroška cesta 46, 2000 Maribor, Slovenia, e-mail: mladen.trlep@um.si.

1 Introduction

Non-destructive testing is now used more and more often for the testing of materials. One of non-destructive methods is testing using eddy currents. In this testing case we measure the magnetic flux density within the vicinity of the tested material which has changed because of the material damage.

Our problem is a conductive plate with a crack, and is limited to a crack of rectangular geometry having a constant depth. The crack's position, crack's length l , crack's depth d and crack's width w must be found.

The first part of the research was searching for the crack's position and length. These were found by consideration of the differences between the measured magnetic flux densities and the neighbouring measurement points.

Second, the more complex part of the research was searching for the crack's depth and width. We used an evolutionary method for determining the crack's depth and width. The Finite Element Method (FEM) (Vasić et al., 2007; Zent et al., 2010) model was used for the evaluation of cost function.

2 Measurements

Measurements were carried out for one test-case. For the tests we used a plate made of aluminium of 30 mm thickness and dimensions of 330 x 285 mm. The crack had length of 40 mm, depth of 10 mm, and width of 0.5 mm. The crack was in the middle of the plate.

The used measuring system, together with the test plate, is shown in Fig. 1.

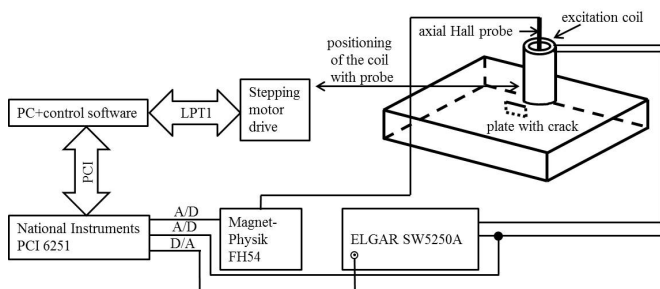


Figure 1: Measuring system

The excitation coil had an inner diameter of 36.8 mm, an outer diameter of 53 mm, and a height of 56 mm. It had 566 turns and was supplied with a sinusoidal current of 1A and a frequency of 500 Hz. An axial Hall-probe HS-AGB5-4805 was placed within a bore at the centre of the coil. The Hall probe measured the z component of the magnetic flux density. When, in the continuation of the paper, we talk about the magnetic flux density above the plate, we mean the z component of the magnetic flux density.

The position of the coil, together with the Hall-probe, was changed by the use of a stepping-motor. The step in the x direction was approximately 0.2 mm and in the y direction approximately 0.4 mm. The result of the measurement was the measured value of the magnetic flux density z -component in each position of the measuring coil. The result can be presented by the surface over the plate. Because eddy currents were absent in the area of the crack, the magnetic flux density above the crack was higher than the magnetic flux density above the plate without the crack.

The control software was developed with the use of Lab-View. The control software positioned the coil together with the Hall-sensor and captured the measured values. Figure 2 shows the results of the measurements above the aluminium plate.

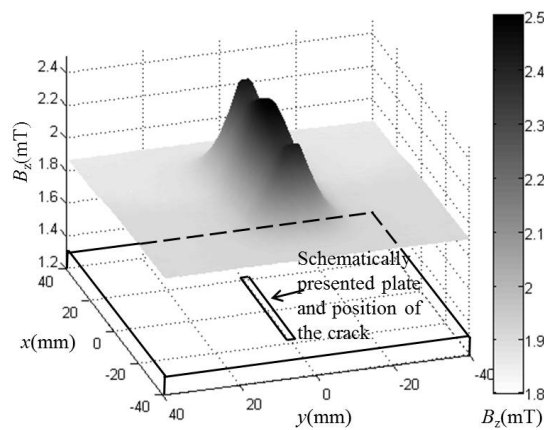


Figure 2: Measuring results above the aluminium plate

3 Determination of crack's position and crack's dimensions

3.1 Crack's position and crack's length

The position and crack's length were determined by considering the changes between the measured magnetic flux densities - calculated based on the derivatives on the surface in measured points.

The derivatives calculated from the centre point towards eight neighbouring points were calculated analytically and expressed using angles. The obtained angle can be positive if the magnetic flux density in the neighbouring point is higher, negative if in the neighbouring point it is lower or approximately zero if in the neighbouring point it is approximately the same as the magnetic flux density at the centre point. We can define the crack position and length if we know the maximum and minimum angles, which are found between the eight angles calculated for each measuring point.

The crack occurs depending on the values of the minimum and maximum angles, as presented in Table 1.

Table 1: Crack depending on the minimum and maximum angles

Minimum angle	Maximum angle	Crack
≈ 0	≈ 0	NO
≈ 0	> 0	NO
< 0	> 0	NO
< 0	≈ 0	YES
< 0	< 0	YES

The results for the test example of the aluminium plate are presented in Fig. 3.

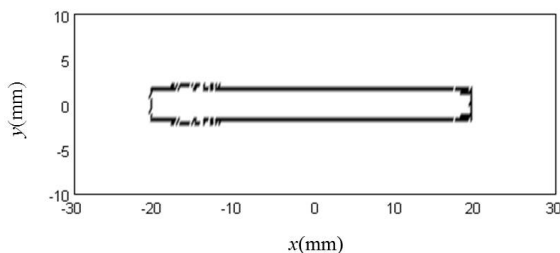


Figure 3: Position and length of the crack

From Fig. 3 we can determine the length of the crack, which was 39.4 mm.

3.2 Crack's depth and width calculation

Our goal was also to determine the crack's depth and width. We did not know the values of the crack's depth and width, but we did know the magnetic flux density for each measured point above the plate. If we want to calculate the magnetic flux density for a certain point, we must create a model. As already explained, we used a differential evolution for determining the crack's depth and width.

The measured values at the selected points, as presented in Fig. 4 a), depend on the crack's depth and width. Using the FEM model we searched for such values of depth and width where the calculated values at these points were as close as possible to the measured values.

The finite element mesh was made in such a way that the bands of the finite elements were parallel with the crack, so we could only adjust the crack's width by moving the finite element mesh nodes. The used finite elements were prisms with the basic plane lying within the xy plane. We could change the crack's depth by changing the finite element's height.

Using our own FEM software connected with differential evolution allowed us to make a calculation of d and w within a continuous process. The calculation procedure, together with the differential evolution, is presented in Fig. 4 b).

The objective function (cost function) was calculated for each pair (depth and width) of the population. We defined the objective function as the sum of the squares of the differences in the measured and calculated magnetic flux densities, expressed using (1).

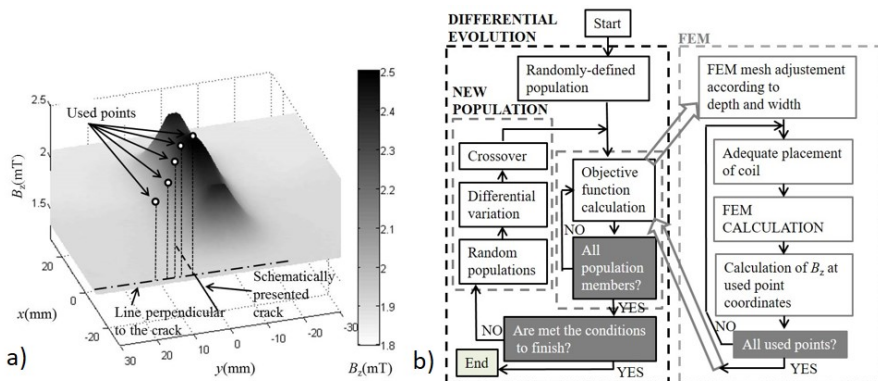


Figure 4: a) Points used for the depth and width determination, b) flow chart of the calculation procedure

$$f = \sum_{i=1}^n (B_{i_calculated} - B_{i_measured})^2 \quad (1)$$

The calculation results are presented in Table 2.

Table 2: Calculated results for aluminium plate

Calculation	1	2
Depth (mm)	10.04796	10.08355
Width (mm)	0.54016	0.55238
Objective function	$1.215 \cdot 10^{-10}$	$1.114 \cdot 10^{-10}$
Deviation of d (%)	0.48	0.84
Deviation of w (%)	8.03	10.48

4 Conclusions

A differential evolution is appropriate for the described problem because it is able to overcome any local minimums which might appear because of measurement or calculation inaccuracies. Despite the very sensitive problem, and the measuring and FEM calculation mistakes, the differential evolution was stable and gave us correct results for all six test calculations. Method can be used only for rectangular crack, which is a disadvantage. For more applicability crack can be divided in smaller parts, but with that the problem will be much more complicated and time-consuming, what could be future work on this problem.

References

- Vasić D., Bilas V., Šnajder B., (2007), Analytical modelling in low-frequency electromagnetic measurements of steel casing properties, *NDT&E International*, 40, 103-111
- Zeng, L., Udpa, I., Udpa, S. S. (2010). Finite-element model for simulation of ferrite-core eddy-current probe, *IEEE Transactions on Magnetics*, 46, 905-909

Battery Pack Design Problems - EMC Problems Caused by Transverse Magnetic Field

ŽELJKO HEDERIĆ, MARINKO BARUKČIĆ, NENAD CVETKOVIĆ &
DEJAN KRSTIĆ

Abstract The battery pack design significantly influences on electric vehicle (EV) drive characteristics as a primary source of energy. Control of the energy flows inside EV is obtained using high-frequency power electronic components. The design of the battery pack, that is prereduced as an objective for a safe and reliable energy source, must not introduce an excessive electromagnetic disturbance to anything in that environment. Presence of high harmonics superimposed on the DC component of the battery current in combination with the design of the battery pack as result alternatively provide space for EMC problems. Nature of two coupling fields being detected under EMI/EMC definitions as problematical: inductive coupling in electric circuits and capacitive coupling. This paper examines the influence of the distribution of the transversal magnetic field inside of the battery pack as a result of design that influence on battery parameters.

Keywords: • battery pack design • EMC problems • transversal magnetic field • electric vehicle • internal battery resistance •

CORRESPONDENCE ADDRESS: Željko Hederić, PhD, Associate Professor, Faculty of Electrical Engineering, Computer Science and Information Technology Osijek, Kneza Trpimira 2B, HR-31000 Osijek, Croatia, e-mail: zeljko.hederic@ferit.hr. Marinko Barukčić, PhD, Assistant Professor, Faculty of Electrical Engineering, Computer Science and Information Technology Osijek, Kneza Trpimira 2B, HR-31000 Osijek, Croatia, e-mail: marinko.barukcic@ferit.hr. Nenad Cvetković, PhD, Assistant Professor, Faculty of Electronic Engineering, A. Medvedeva 14, 18000 Niš, Serbia, e-mail: nenad.cvetkovic@elfak.ni.ac.rs. Dejan Krstić, PhD, Associate Professor, University of Niš, Faculty of Occupational Safety, Čarnojevića Street 10A, 18000 Niš, Serbia, e-mail: dekihrs@gmail.com.

1 Introduction

The battery pack as source of energy is an essential part of electric vehicles (EV), so its design significantly influences EV drive characteristics and consequently the possible EMC problem due to energy flows inside EV. Power electronic device control inside EV energy flows using high-frequency power electronic components that cause the appearance of high harmonics super-imposed on the DC component of the battery current (MIT Electric Vehicle Team, 2008).

The design of the battery pack requires, as an objective for a safe and reliable energy source, must not introduce an excessive electromagnetic disturbance to anything in that environment (Texas Instruments, 2016), (Tsang, 2012). Under EMI/EMC definitions, especially are emphasized inductive coupling in electric circuits (magnetic coupling occurs when there two current loops are close to each other, then the source circuit produce magnetic flux that in victim circuit induce additional parasitic voltage) shown on Figure 1 and capacitive coupling (electric field coupling of adjacent electric circuits modeled as capacitance effect) shown on Figure 2 (Texas Instruments, 2016), (Weber *et al.*, 2003).

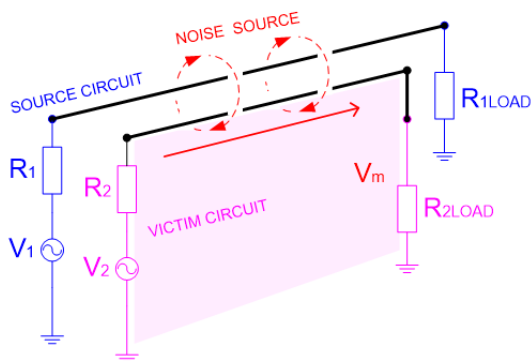


Figure 1: EMC problem of an inductive coupling in electric circuits

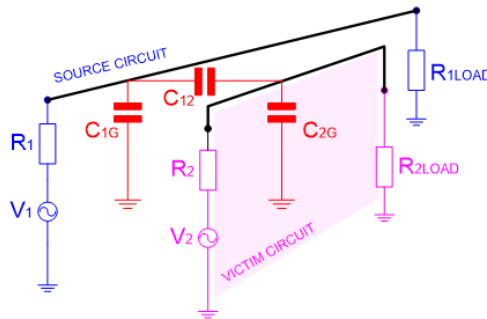


Figure 2: EMC problem of an capacitive coupling

As prevention of those (and other similar) effects in practice used numerous EMI suppression filters and electromagnetic shielding (surrounding EV electronic components and signal lines by conductive or magnetic materials to reduce EM emissions) (Texas Instruments, 2016), (Tsang, 2012), (Guttowski *et al.*, 2003). Because of the use of the HV (usual 24V in fossil-fuelled car in the EV rise up to 800V) common EMC problems of automotive component become coupling between HV and LV, a specially as sterically electro-magnetic coupling (components inside the same housing) (Tsang, 2012), (Pulomena, 2017).



Figure 3: EMC problem of an inductive and capacitive coupling in electric circuits of solar electric car prototype CROsolar01.

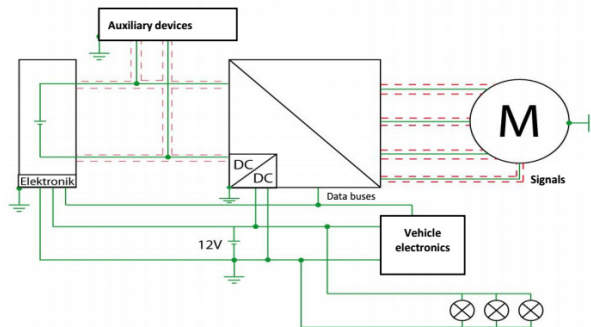


Figure 4: Schematic presentation of coupling between HV and LV, (Tsang, 2012).

Figure 3 shows HV and LV cable distribution inside the prototype of the solar electric car CROsolar01 designed in 2016 by the faculty team and made according to the propositions of the World Solar Challenge. Because of the narrow space for cable corridor the HV and the LV line are often in the same space (distance in mm). The protection shielding of cable lines was satisfactory during laboratory testing on sterical electromagnetic coupling and functional coupling (data buses, power supply 12V). But during the testing of the vehicle on road at nominal speed 70km/h when power lines provide over 20A line currents with a lot of harmonic distortion (control of the motors from inverters) the battery management start to produce odd control signals that give wrong data for control units. Figure 4 show schematic presentation of coupling between HV and LV in similar surroundings in testing during Albatros Project research (Tsang, 2012).

2 Battery pack design problems

The way of cell merging into the total packet depends on a large number of design requirements (energy availability, temperature protection, ...), and the most commonly accomplished topology merge cells in parallel to the battery block in order to secure the capacity, and then the blocks are merged serially into a battery pack for the purpose of voltage levels. What often been forgotten is that a battery does not store electricity, they are reservoirs of the chemicals that by reaction produce electricity and reverse (MIT Electric Vehicle Team, 2008), (Mohanta *et al.*, 1976). Therefore battery does not have the characteristic of an electric circuit to be switched off or on, basically, they are always on. If by design a situation to have a short circuit (parallel connection of battery cells) been provided, these chemicals will react and produced electricity. Short circuit inside

of parallel block of battery (not equal cell voltage case) ultimately brings to discharging and irreversible degradation of electrolyte (Mohanta *et al.*, 1976), (Hallaj *et al.*, 2016).

The Battery block shown in Figure 6 is realized from 15 cells in parallel connection through upper and downer plates and via interconnect bar to upper plates contact (prototype design of the battery block for use in the solar electric vehicle).



Figure 5: Testing of the CROsolar01 solar electric car in realistic road condition.

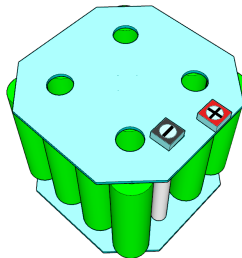


Figure 6: Battery block built by 15 parallel cells and interconnection bar.

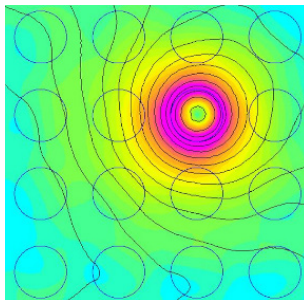


Figure 7: Transversal magnetic field distribution as result of battery block current

The problem with this design is that each battery cell in parallel block has closed loop with interconnection bar (gray connector in Fig.6) that is practically square shaped (Fig. 8), providing the area for induced EMF (Faraday's law). If battery cell is considered as a constant voltage DC source connected to dynamically changed load (as shown in Fig.9), the produced current will be time changeable in the relation of variable load). Therefore, according to the Faraday law, will exist EMF that can be modelled as a variable voltage source that opposes the battery voltage source. Consequently, this effect can be observed as in the battery cell model an additional serial connected voltage source (Fig.9) dependable of a total battery block electric current time change and the heat source in battery cell that derive additional degradation of battery chemical reaction (Mohanta *et al.*, 1976). The battery cell model has different variations of approach in relation to the complexity of the power drive model. For relatively precise calculation (huge demand of calculation power and time consumption) the Shepard model is often used (Tremblay *et al.*, 2009).

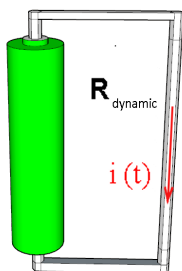


Figure 8: Lumped model of the electric circuit consists of one cell and interconnection bar, (Benšić *et al.*, 2017).

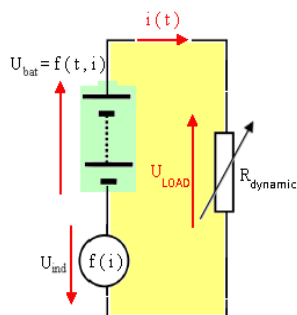


Figure 9: Lumped model of electric circuit for one battery cell as part of the battery parallel block, (Benšić *et al.*, 2017).

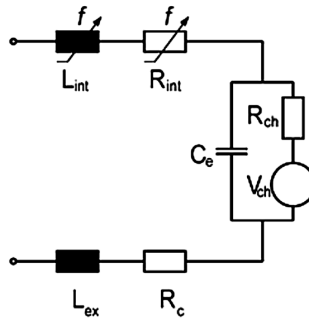


Figure 10: Equivalent Circuit to Model Rf-Characteristics of Batteries in Regarded Frequency Range (Tremblay *et al.*, 2009).

That model calculates with different parameters that determine total cell voltage as battery current, Polarization resistance, Extracted capacity, maximum capacity and drop off exponential capacity. These parameters have been taken from charging/discharging battery characteristics given from the manufacturer, so in the end, this model has calculated voltage of the battery dependable on just one parameter: State-Of-Charge (SOC).

In (Benšić *et al.*, 2017) is proposed upgrade of the Shepard model (Tremblay *et al.*, 2009) with additional internal serial voltage source and parallel resistors for modelling magnetic effect on battery cell as a result of the battery block design. For modelling magnetic field influence of battery block design (presented in Fig.6) to battery model, it must be taken into consideration that the electric circuit (Fig.9) is flush with the total battery power and (apart from the DC component) there are more harmonics caused by the power electronics. In the case of the dynamic load of the battery ($di / dt \neq 0$), the induction voltage, modelled as a voltage source depending on the load current, opposed to the change of current will appear. Resistor (dynamic) present load that waste battery energy for propulsion. Equation (1) present Ohmic law for Lumped model (Fig.9) of the single electric circuit with modeled battery cell as voltage source dependable of cell current (Hallaj *et al.*, 2016).

$$U_{bat}(t,i) - U_{ind}(i) = i(t) \cdot R_{dynamic}(t) \quad (1)$$

The load, presented as a dynamic resistor, is a function of time (EV drive demand for energy from the battery as a function of time in control loop system). Finally, the induced voltage source as a function of cell current (for given geometry presented in Fig.6) and correspond to a yellow marked area on Fig.9. To calculate the induced EMF for square shaped design (shown on Fig.8) for Faraday law need to be calculated inductance. This is the well-known relation that can be taken in simplified form:

$$L_{\text{square}} \approx N^2 \frac{2w\mu}{\pi} \left[\ln\left(\frac{w}{a}\right) - 0,77401 \right] \quad (2)$$

where are: w-dimension of the square loop, a-diameter of the wire, μ -permeability, N-number of turns.

3 Conclusion

This paper examines EMC problems influenced by the distribution of the transversal magnetic field inside of the battery pack of electric vehicle depending on battery pack design. The DC component of the transversal magnetic field inside of battery cells cause Hall effect ions path allocation that is reflected on internal battery resistance negative change. The AC component of the transversal magnetic field in electrically closed loops within battery pack induced e.m.s. that also causes negative phenomena on battery pack parameters. IEC standards for electric vehicle cover some EMC issues including batteries and LF and HF phenomena on connection lines - specifies test methods and requirements under IEC 61851-21-1: 2017. Detected BMC problems of built-in wrong lumped model of battery cells directly influence on SOC estimation of the battery and therefore influences on the control of the vehicle. The battery management is basically not able to solve or detect problems within parallel cells that can cause irreversible discharge process.

References

- MIT Electric Vehicle Team, (2008). A guide to understanding battery specifications, <http://web.mit.edu>
- Texas Instruments (2016). Designing EMI/EMC Safe Battery Pack. Application Report, SLUA776
- Tsang J. (2012). Albatross Projects. Presentation for IEEE HK EMC Society,

- <http://www.ee.cityu.edu.hk/~emc/20121124P2.pdf>
- Weber, S., Guttowski, E., Hoene, E., John, W., and Reichl, H. (2003). EMC Issues in Cars with Electric Drives, *Electromagnetic Compatibility, 2003, EMC 2003, IEEE International Symposium on* 777–782, doi:10.1109/ISEMC.2003.1236706
- Pulomena J. (2017). Dealing with EMC filtering in today's electric and hybrid vehicles, posted by Charged EVs, <https://chargedevs.com/newswire/>
- Mohanta S., Fahidy T. Z. (1976). The effect of a magnetic field on electrolyte conductivity. *Electrochimica Acta*, Volume 21, Issue 1, pp. 25-27.
- Hallaj J.P, Trovao F. (2016). A lithium-ion battery electro-thermal model of parallellized cells. *Vehicle Technology Conference (VTC-Fall), IEEE 84th*, 1-6.
- Benšić T., Hederić Ž., Barukčić M., Cvetković N., Krstić D. (2017). Battery Pack Design Problems – Influence of the Transverse Magnetic Field on Internal Battery Resistance. *Safety engineering*, Vol7 Issue2; 49-53
- Guttowski S., Weber S., Hoene E. (2003). EMC issues in cars with electric drives. *IEEE Symposium on Electromagnetic Compatibility*
- Tremblay O., Dessaint L.A. (2009). Experimental validation of a battery dynamic model for EV applications. *World Electric Vehicle Journal*, Vol. 3,2009, pp. 289-298.

Grid-Ground Electrode in Two Layered Non-Homogeneous Ground

NENAD CVETKOVIC, DEJAN JOVANOVIC, MIODRAG STOJANOVIC & MARINKO BARUKCIC

Abstract The procedure for characterization of grounding grid electrode placed in non-homogenous ground approximated with two homogeneous horizontal layers is presented in the paper. It includes application of the Green's function for a point source in multi-layered media and the Method of Moments. The Green's functions are obtained by solving the Poisson's, i.e. the Laplace's equation for electric scalar potential. The obtained results are compared with the ones obtained by simulations in COMSOL software package. The described method can be applied for solving quasi-stationary problems which include soil of semi-conducting characteristics.

Keywords: • Green's functions methods • grounding • electric scalar potential • soil properties • resistance •

CORRESPONDENCE ADDRESS: Nenad Cvetkovic, PhD, Assistant professor, University of Niš, Faculty of Electronic Engineering, A. Medvedeva 14, Niš, 18000, Serbia, e-mail: nenad.cvetkovic@elfak.ni.ac.rs. Dejan Jovanovic, MSc, Assistant, University of Niš, Faculty of Electronic Engineering, A. Medvedeva 14, Niš, 18000, Serbia, e-mail: dejan.jovanovic@elfak.ni.ac.rs. Miodrag Stojanovic, MSc, Assistant, University of Niš, Faculty of Electronic Engineering, A. Medvedeva 14, Niš, 18000, Serbia, e-mail: miodrag.stojanovic@elfak.ni.ac.rs. Marinko Barukcic, PhD, Associate professor J. J. Strossmayer University of Osijek, Faculty of Electrical Engineering, Computer Science and Information Technology, Kneza Trpimira 2b, Osijek, 31000, Croatia, e-mail: marinko.barukcic@ferit.hr.

1 Introduction

Generally, all grounding systems, regardless of the shape and design, have the same purpose - to lead fault current into the surrounding soil safely and without consequences for the working environment. In order to ensure proper functioning of the grounding system, a necessary requirement is that the resistance value of the grounding system is as low as possible. Very often, grounding system is realized with grid electrode as main ground electrode [1-8]. It contains several rod electrodes connected to each other, usually in a square or rectangular shape.

There are different procedures for analyzing grounding grid electrode in homogenous ground and determining its resistance as the most significant characteristic. In (Laurent, 1972), (Nahman, 1996), (Dwight, 1936), (Schwartz, 1956) and (Nahman, 2006) this problem has been solved using known empirical equations. The results obtained using various procedures (method of images, filter theory and direct numerical integration) are compared with measured values in (Dawalibi, 1991), while parametric analysis of measured characteristic values of grid ground electrode is carried out in (Dawalibi, 1991). The approach based on numerical determining of Green's function for the point source is presented and applied in (Zou, 2004).

In this paper, a procedure including using of the Green's functions for a point source in multilayered media obtained by solving the Poisson's i.e. Laplace's equation for the electric scalar potential and the Method of Moments-MoM (Harrington, 1969) for analyzing described problem is adopted.

2 Grid ground electrode in two-layered soil

The procedure for characterizing grid ground electrode placed in two-layered soil of conductivity $\sigma_i, i=1,2$ Figure 1. The corresponding Decartes' coordinate system has been defined and attached to the problem. The procedure is based on Green's functions for the electric scalar potential and the MoM.

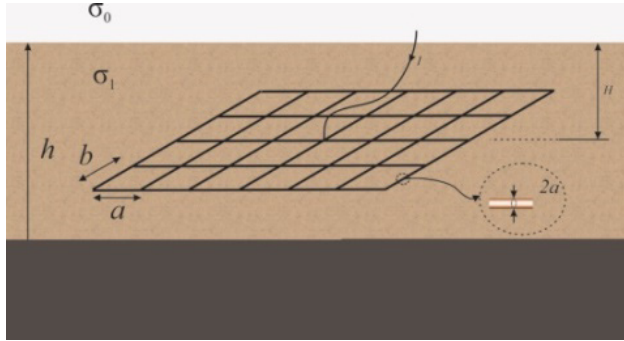


Figure 5: Grid ground electrode in two-layered ground

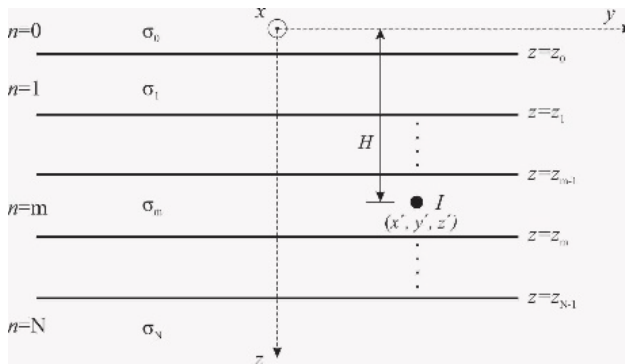


Figure 2: Point current source in multilayered media

2.1 Green's function

The point source of current I placed in non-homogenous domain approximated with total of $N + 1$ homogenous horizontal layers of specific conductivity $\sigma_n, n = 0, 1, \dots, N$ is observed (Figure 2). The source is placed at the point defined by the field vector $\vec{r}' = x'\hat{x} + y'\hat{y} + z'\hat{z}$.

The potential of the system from Figure 2 at the point defined by the field vector $\vec{r} = x\hat{x} + y\hat{y} + z\hat{z}$ satisfies the Laplace's, i.e. the Poisson's equation

$$\Delta\varphi = \begin{cases} 0, & n \neq m, n = 0, 1, \dots, N \\ -\frac{I}{2\pi\sigma_n} \delta(x-x')\delta(y-y')\delta(z-z'), & n = m, n = 0, 1, \dots, N \end{cases} \quad (1)$$

In (1), δ is a one-dimensional Dirac delta function.

General solution of the differential equation (1) can be assumed in the form (Jovanović, 2017),

$$\varphi_{g\,nm}(\vec{r}, \vec{r}') = \int_0^{\infty} f_{nm}(z, k) J_0(kr_p) k \, dk, n = 0, 1, \dots, N, r_p = \sqrt{(x-x')^2 + (y-y')^2}, \text{ where} \quad (2a)$$

$$f_{nm}(z, k) = \begin{cases} A_n e^{kz} + B_n e^{-kz}, n = 0, N, n \neq m \\ A_m e^{kz} + B_m e^{-kz}, n = m, z_{m-1} \leq z \leq z' \\ \left(A_m - \frac{I}{4\pi\sigma_m k} e^{-kz'} \right) e^{kz} + \left(B_m + \frac{I}{4\pi\sigma_m k} e^{kz'} \right) e^{-kz}, n = m, z' \leq z \leq z_m \end{cases} \quad (2b)$$

In (2a), $\varphi_{g\,nm}$, $n, m = 0, 1, \dots, N$ is the potential at points in the n -th layer, when source is in layer m , A_n , B_n , $n = 0, 1, \dots, N$ are unknown coefficients, while J_0 denotes the Bessel function of the first kind of zero order. Unknown coefficients $A_n, B_n, n = 0, 1, \dots, N$ from (2b) can be determined from the boundary conditions for the potential, normal component of the conducting current and the potential finite value, i.e.:

$$\varphi(z = z_n^-) = \varphi(z = z_n^+), \sigma_n \frac{\partial \varphi}{\partial z}(z = z_n^-) = \sigma_{n+1} \frac{\partial \varphi}{\partial z}(z = z_n^+), (n = 0, N-1) \text{ and} \quad \lim_{z \rightarrow \pm\infty} \varphi = 0 \quad (3)$$

2.2 Two-layered soil structure

To determine parameters of a vertical ground electrode from Figure 1, it is necessary to obtain the Green's function of a point source placed in the non-homogeneous ground approximated with two horizontal homogeneous layers $n = 1, 2$ ($N = 2$), while layer labelled by $n = 0$ corresponds to air, ($\sigma_0 = 0$), as it is shown in Figure 3 and Figure 4. The Green's function can be obtained based on the general solution (2) and boundary conditions (3). Based on (2), the potential in the n -th ($n = 1, 2$) layer from the point source placed at the point defined by

the field vector $\vec{r} = x'\hat{x} + y'\hat{y} + z'\hat{z}$, at the point defined by the field vector $\vec{r}' = x'\hat{x} + y'\hat{y} + z'\hat{z}$ in the layer of specific conductivity σ_1 ($m=1$ in (2)), Figure 3, is

$$\Phi_{g n1}(\vec{r}, \vec{r}') = \int_0^{\infty} f_{n1}(z, k) J_0(kr_p) k \, dk, n = 1, 2, r_p = \sqrt{(x-x')^2 + (y-y')^2} \quad (4)$$

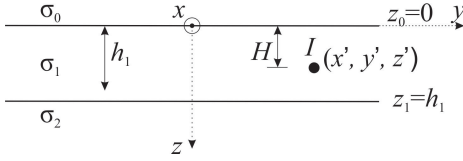


Figure 3. Point current source in two-layered ground (layer 1)

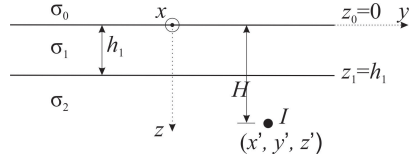


Figure 4. Point current source in two-layered ground (layer 2)

Similarly, based on (2) the potential in the n -th ($n=1,2$) layer from the point source placed in the layer of specific conductivity σ_2 ($m=2$), Figure 4, is

$$\Phi_{g n2}(\vec{r}, \vec{r}') = \int_0^{\infty} f_{n2}(z, k) J_0(kr_p) k \, dk, n = 1, 2, r_p = \sqrt{(x-x')^2 + (y-y')^2} \quad (5)$$

The expressions for potential $\Phi_{g n1}$ (4) and $\Phi_{g n2}$ (5) are obtained from (2) and (3) and in details given in (Jovanović, 2017). Now, the Green's function can be determined as

$$G_{nm}(\vec{r}, \vec{r}') = \Phi_{g nm}(\vec{r}, \vec{r}') / I, m, n = 1, 2 \quad (6)$$

2.3 Determination of the system's potential and resistance

The horizontal grid ground electrode formed from N straight wire conductors of length l_k and circular cross-section of radius a_k , $a_k \ll l_k$, $k = 1, 2, \dots, N$, placed in layer 2 of specific conductivity σ_2 is observed, Figure 1. Dimensions of the arbitrary oriented grounding grid buried at the depth h are $a \times b$. Assuming leakage current density from each conductor to be constant, the potential in the

vicinity of the grid grounding electrode, Fig. 1, at the point in the ground defined by the field vector $\vec{r} = x\hat{x} + y\hat{y} + z\hat{z}$, can be determined as

$$\varphi_n(\vec{r}) = \sum_{k=1}^N \int_{l_k} I_{\text{leak}k}(s'_k) G_{n2}(\vec{r}, \vec{r}') ds'_k = \sum_{k=1}^N \frac{I_k}{l_k} \int_{l_k} G_{n2}(\vec{r}, \vec{r}') ds'_k, n=1,2 \quad (9)$$

In (9), $I_{\text{leak}}(s'_k) = I_k/l_k$, $k=1, \dots, N$ is the leakage current per unit length from the element of the k -th conductor $k=1, \dots, N$ defined by the field vector \vec{r}' . Also, I_k , $k=1, \dots, N$ are the total leakage currents from N straight wire conductors.

Based on previous analysis, the MoM is applied for solving the system from Figure 3. Matching the potential given by (9), at surface points in the middle of segments on the conductors defined by the vector \vec{R}_k , $k=1, \dots, N$, the system of linear equation is formed as

$$\varphi_1(\vec{R}_k) \cong U = \sum_{k=1}^N \left[\frac{I_k}{l_k} \right] \int_{l_k} G_{n1}(\vec{r}, \vec{r}') ds'_k, k=1, \dots, N \quad (10)$$

Solutions of the system of equations (10) are the total leakage currents of the conductors I_k , $k=1, \dots, N$. Now, potential can be determined from (9), and the resistance of the grounding system can be determined as

$$R_g = U / \sum_{k=1}^N I_k \quad (11)$$

3 Numerical results

The described procedure has been applied for determining resistance of grid grounding system of a substation with voltage level of 35kV (Official Gazete SRJ, 1995) while soil structure and characteristics have been adopted based on values given in (Jovanović, 2015). The obtained result is compared with the ones obtained by COMSOL software package. The grid of dimension 20x30m consists of 24 cells of dimension $a=b=5$ m, Figure 1. The electrode is horizontally placed at depth $H=1$ m. The depth of the boundary surface between two layers of specific conductivities $\sigma_1=0.01$ S/m and $\sigma_2=0.05$ S/m is $h=1.5$ m. The wire radius is 0.025 m. The values of substation grid electrode resistance obtained

using proposed procedure and COMSOL package are shown in Table 1. The distribution of the potential at the ground surface above the grid electrode is given in Figure 5.

Table 1. Comparison of the obtained results for substation grounding grid resistance R_g .

Method	$R_g[\Omega]$
Proposed procedure	0.5984
COMSOL	0.5595

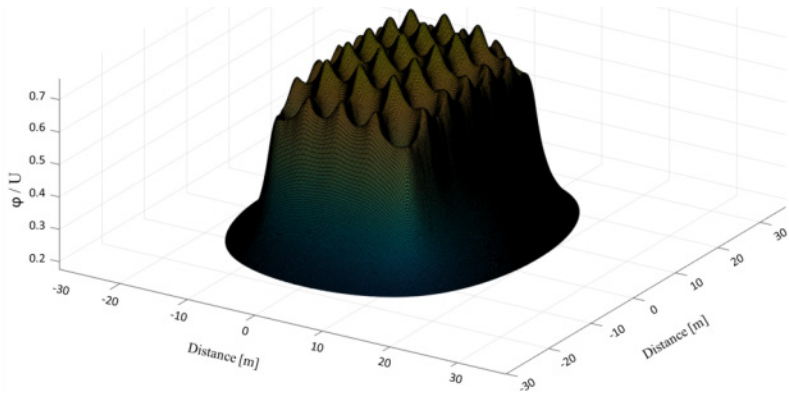


Figure 5. Potential distribution on the ground surface

3 Conclusions

The procedure for analyzing grid ground electrode placed in nonhomogeneous ground approximated with two horizontal homogeneous layers is given in the paper. It is applied to a grid electrode realized in practice and the results are compared with the results obtained by COMSOL software package.

References

- Laurent, P. G. (1972). Guide sur le calcul l' execution et la mesure des prises de terre, *Rev. Gen. Electr.*, 53, 455-467, 563-572. [in French]
- Nahman, J., Djordjevic V. (1996). Resistance to ground of combined grid-multiple rods electrodes. *IEEE Trans. on Power Delivery* 11, 1337-1342. doi: 10.1109/61.517488.
- Dwight, H. B. (1936). Calculations of resistances to ground. *Trans. of the American Institute of Electrical Engineers*, 1319-1328. doi: 10.1109/T-AIEE.1936.5057209.

- Schwartz, S. J. (1954). Analytical expression for resistance of grounding systems. *Power Apparatus and Systems, Part III. Trans. of the American Institute of Electrical Engineers* 73, 1011-1016, doi: 10.1109/AIEEPAS.1954.4498923.
- Nahman, J., Paunovic, I. (2006). Resistance to earth of earthing grids buried in multi-layer soil. *Electrical Engineering* 88, 281-287. doi: 10.1007/s00202-004-0282-y.
- Dawalibi, F., Barbeito, N. (1991). Measurements and computations of the performance of grounding systems buried in multilayer soils. *IEEE Trans. on Power Delivery* 6, 1483-1490. doi: 10.1109/61.97681.
- Dawalibi, F. P., Ma, J., Southey, R. D. (1994). Behaviour of grounding systems in multilayer soils: a parametric analysis. *IEEE Trans. on Power Delivery* 9, 334-342. doi: 10.1109/61.277704.
- Zou, J., Zeng, R., He, J. L., Guo, J., Gao Y.Q., Chen, S.M. (2004). Numerical Green's function of a point current source in horizontal multilayer soils by utilizing the vector matrix pencil technique. *IEEE Trans. on Magnetics*, 40, 730-733. doi: 10.1109/TMAG.20alo04.825014.
- Harrington, R. F. (1969). Field computation by Moment Methods. *The Macmillan Company: New York*.
- Jovanović, D., Cvetković, N., Stojanović, M., Barukčić M., Hederić, Ž., Stanković, V. (2017). One approximate analytical expression for resistance of the vertical grounding electrode placed in multilayered media, *The 13th International Conference on Applied Electromagnetics*, Niš, August 30 - September 1, 2017, CD Proceedings, ISBN 978-86-6125-185-6, Paper P-12
- Official Gazete SRJ (1995). Regulations of technical standards for grounding of power plant with a nominal voltage above 1000V, *Official Gazette SRJ*, 61/95). <http://bit.ly/1M75fEu>
- Jovanovic, D. B., Cvetkovic, N. N., Stojanovic, M. S., Ristic, A. T., Krstic, D. D., Cvetkovski, G. (2015). Numerical and practical analysis of substation grounding grid electrode. *Proceedings of XVII ISEF 2015*, Valencia, Spain, September 10-12, 2015, Paper ID RS130, ISBN: 978-84-606-9102-0.

The Implementation of Electronic Green Public Procurement Tool in Slovenia

KLEMEN SREDENŠEK, GREGOR SRPČIČ, MARŠENKA MARKSEL,
MIRALEM HADŽISELIMOVIĆ & SEBASTIJAN SEME

Abstract This paper deals with implementation of electronic green public procurement tool for achieving environmental protection and sustainable development. The electronic green public procurement tool used within the living labs has been tested by stakeholders which proposed several valuable improvements. The evaluation analysis has shown that the living labs stakeholders knowledge on electronic green public procurement topics was improved.

Keywords: • green public procurement • implement • improve • living lab • electronic green public procurement tool •

CORRESPONDENCE ADDRESS: Klemen Sredenšek, MSc, Researcher, University of Maribor, Faculty of Energy Technology, Hočevarjev trg 1, 8270 Krško, Slovenia, e-mail: klemen.sredensek@um.si. Gregor Srpčič, MSc, Assistant, University of Maribor, Faculty of Energy Technology, Hočevarjev trg 1, 8270 Krško, Slovenia, e-mail: gregor.srpcic@um.si. Maršenka Marksel, MSc, Assistant, University of Maribor, Faculty of Civil Engineering, Transportation Engineering and Architecture, Smetanova ulica 17, 2000 Maribor, Slovenia, e-mail: marsenka.marksel@um.si. Miralem Hadžiselimović, PhD, Full Professor, University of Maribor, Faculty of Energy Technology, Hočevarjev trg 1, 8270 Krško, Slovenia, e-mail: miralem.h@um.si. Sebastijan Seme, PhD, Associate Professor, University of Maribor, Faculty of Energy Technology, Hočevarjev trg 1, 8270 Krško, Slovenia, e-mail: sebastijan.seme@um.si.

1 Introduction

Environmental protection and sustainable development are two important topics of the day. One popular policy tool that government uses to promote sustainable development and to protect the environment is green public procurement (Qiao et al., 2010). Green Public Procurement is an important tool to achieve environmental policy goals relating to climate change, resource use and sustainable consumption and production – especially given the importance of public sector spending on goods and services in Europe. Public authorities use the public procurement system based on the strategy “Europe 2020”, where public procurement is defined as one of the most important tools for achieving sustainable development. Suitability and efficiency must also be taken into account in urban transport. Transport of passengers and goods has become a major concern of policy makers worldwide (Letnik et al., 2018).

2 Green Public Procurement

Public procurement has always served as a policy tool (Murphy, 2011). Green public procurement (GPP) is defined as “a process whereby public authorities seek to procure goods, services and works with a reduced environmental impact throughout their life cycle when compared to goods, services and works with the same primary function that would otherwise be procured” (Testa et al., 2016). A series of research in the European Union has shown that the public authorities has a great opportunity and the power to accelerate the use of new, environmentally friendly products and research into innovation towards the development of green products and new environmental technologies. Thus, improves the competitiveness of the European and national economies.

In Slovenia, the estimated value of public procurement in 2007 was 12.98 % of GDP (Action plan for green public procurement 2009 – 2012), which led to the implementation of green public procurement in 2008. In Slovenia, the Public Procurement Directorate (PPD) is responsible for the public procurement system, which in addition to the preparation of the regulatory framework of the public procurement system (e.g. preparation of regulations, coordination of the Slovenian public procurement legislation with the European acquis, and systemic monitoring and participation in coordinating the public procurement regulations of the European Union and World Trade Organisation) also provides user support for the public procurement system. The PPD is divided into three

departments, namely the Department for Public Procurement System, the Department for the Implementation of Public Procurement, and the Department of e-procurement, consultation and analysis. Despite the fact that Slovenia has a fairly well-developed regulatory and policy framework for public procurement, a significant gap persists between the rules on paper and actual practices due to a series of structural challenges. Slovenia has an ambitious agenda for strengthening public administration, which in turn should have a positive impact on public procurement. With the newly adopted Strategy for Public Administration 2015-2020, the country is making a multi-pronged effort to tackle corruption and enhance capacity.

3 Electronic public procurement program

Information and communication technologies provide ways of drastically reducing different categories of transaction and communication costs. In achieving efficient procurement practices, both private and public play a key role as they ensure reduction of wasteful activities (Ozbilgin et al., 2011). Electronic-procurement is another area that can be greatly strengthened in Slovenia. As mentioned above the PPD also performs tasks relating to electronic public procurement (ePP), including development and management of a system which fully supports electronic public procurements. Parts of the system are integrated in the corresponding back-office systems (registration of financial obligations, storage of electronic documents in the document system, and acquiring data from public records). Although in Slovenia the green public procurement is set in place and legalized, the level of its implementation varies among public authorities. Additionally, the public authorities (PAs) and also small and medium-sized enterprises (SMEs), are still less in favor of electronic public procurement and are still using paper version tender implementation.

In order to present to the stakeholders, the green public procurement and enhance awareness of its advantages GRASPINNO project has established several living labs, among other also in Slovenia. The purpose of living labs was to educate stakeholders about energy efficiency, energy management and electronic green public procurement tool (eGPP) and to provide them counselling about modern energy efficient materials, building furniture, energy efficient lighting and machines, energy efficiency renovation of buildings. The

initiative for establishing the eGPP Living Lab in Slovenia was the new Green Procurement Regulation (GPP), which became valid on 1. 1. 2018.

The Slovenian Public Procurement Act is intended to improve Slovenian public procurement and, in turn, increase the participation of (foreign) tenders. According to the Public Procurement Act, the contracting authority orders goods, services or constructions that, in comparison with ordinary goods, services and constructions throughout the life-cycle have less impact on the environment and provide savings in natural resources, materials and energy and have the same or better functionality. The Living Lab methodology was composed of 6 phases: connect, train and educate, implement, improve, evaluate and disseminate. In Slovenian e GPP Living Lab the main topic was to implement and later to improve the e GPP tool, which was provided by GRASPINNO project partner. Regarding the use of eGPP tool for electronic green public procurement, stakeholders quickly gained skills and knowledge to use the tool, due its simplicity. They found it very useful, but they also recommended few improvements such as more products to be uploaded, information regarding the uploaded products to be checked by a public expertise team or to implement a credible certificate for products, more countries to be included, products regarding other issues rather than energy efficiency should be added, etc., so as to become even more user friendly and have chances to be used as the national green public procurement tool. It was suggested to upload more products in order to be a reliable tool for market analysis and assessing the level of green performance and associated budgets that can be realistically expected when preparing tenders. The range of products and the set of green criteria must also be extended. Beside including new features and criteria, products should be regularly revised, for that a team of experts should be established to provide control over registered products in e GPP platform. To motivate SMEs in usage of e GPP tool, the most important is to minimize the time needed for entering the products, as currently manual entering is very time consuming. Therefore, the option to import the products into tool in form of xml or Excel databases would save time significantly. One of improvement that this tool needs, beside the automatic upload of products data, is translations into native languages, as it reduces the input time. Additionally, the e GPP tool must be upgraded, based on new laws, rules and green criteria.

Based on the Living Lab methodology the stakeholders needed to evaluate the Slovenian e GPP Living Lab with the help of online questionnaire. Figure 1 and 2 shows the knowledge on e GPP topics before and after the participation in Living Lab.

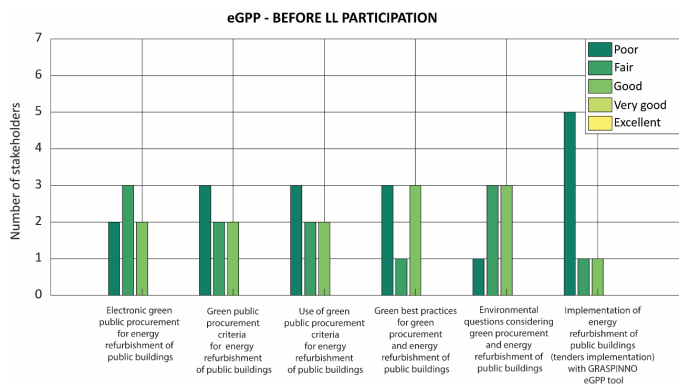


Figure 1: Knowledge on e GPP topics before participating in Slovenian Living Lab.

From Fig. 1 it is clear that the great majority of the participants were not well informed about the electronic green public procurement in Slovenia before participating in the e GPP Living Lab. Generally, this graph of the knowledge on e GPP topics before participating in the Living Lab shows the lack of information of the stakeholders in the field of GPP criteria for energy refurbishment and its usage. The Living Lab has significantly improved the knowledge of participants as seen from the Fig. 2 below.

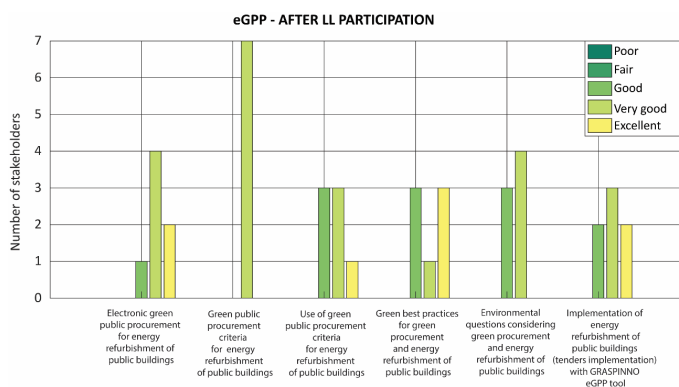


Figure 2: Knowledge on e GPP topics after participating in Slovenian Living Lab.

The results are quite encouraging, since the majority of the participants improved their level of knowledge. For example, all 7 survey participants declared that they now have a very good knowledge on green public procurement criteria for energy refurbishment of public buildings.

4 Conclusion

With green public procurement not only public but also private actors with their green products can significantly contribute to green sustainable growth. While, information and communication technologies can lead to new tools, such as e GPP tool used for electronic green public procurement, stakeholder are still less in favor of using such new technologies. The reasons could be different, form lack of experience, time, resources or just being used of doing things “old fashioned way”. Therefore, the living lab concept, which provides resources, gathers end users (Pas and SMEs) and not only educate them but also stimulates them to provide improvements, can significantly influence on wider use of such tools as it is e GPP tool. No doubly, we can notice that by participating in the Slovenia e GPP living labs, stakeholder improved their knowledge on electronic green public procurement, best practices, environmental questions and implementation aspect of energy refurbishment.

Acknowledgments

The authors would like to thank the Interreg Mediterranean Graspino project for the financial support of this paper. GRASPINNO project is co-financed by the European Regional Development Fund.

References

- Action plan for green public procurement 2009 - 2012, (2009). *The government of the republic of Slovenia*, No. 43000-10/2009/6, Ljubljana.
- Letnik, T., Marksel, M., Luppino, G., Bardi, A., Božičnik, S., (2018). Review of policies and measures for sustainable and energy efficient urban transport. *Energy*, 163, 245-257.
- Murphy, T., (2011). A review of Christopher McCrudden, Buying social justice: Equality, government procurement and legal change. *International Journal of Law and Context*, 7, 505-512.
- Ozbilgin, I. G., Imamoglu, M.Y., (2011). The impact of dynamic purchasing systems in the electronic public procurement processes. *Procedia Computer Science*, 3, 1571-1575.

- Qiao, Y., Wang, C., (2010). China green public procurement program: Issues and challenges in its implementation. *Proceedings of the 4th International Public Procurement Conference*.
- Testa, F., Annunziata, E., Iraldo, F., Frey, M., (2016). Drawbacks and opportunities of green public procurement: and effective tool for sustainable production. *Journal of Cleaner Production*, 112, 1893-1900.

Interdependence Between GDP and Electric Vehicles' Charging Infrastructure in the EU

KATJA HANŽIČ, MARŠENKA MARKSEL & STANISLAV BOŽIČNIK

Abstract The interdependency between charging infrastructure and uptake of electric vehicles (EV) is well acknowledged – for development of robust EV market sufficient publicly accessible charging network is needed. The availability of adequate quantity and quality of charging infrastructure is one of the most important enablers for deployment of EVs in Europe on a larger scale. In order to stimulate faster market uptake of EVs and other vehicles using alternative fuels, EU countries have adopted a mix of policies and measures ranging from financial incentives for vehicle purchase, tax exemptions for investments in charging/refuelling infrastructure. However, we are faced with different levels of economic development of EU countries (GDP) as well as with diverse levels of available investment funds to be invested into EVs market. We can thus expect further slow adoption of EVs in countries with lower GDP as long as the public sector is taking the lead in charging infrastructure investments.

Keywords: • electro mobility • EU • charging infrastructure • GDP
• plug in electric vehicles •

CORRESPONDENCE ADDRESS: Katja Hanžič, University of Maribor, Faculty of Civil Engineering, Transportation Engineering and Architecture, Smetanova ul. 17, 2000 Maribor, Slovenia, e-mail: katja.hanzic@um.si. Maršenka Marksel, MSc, Assistant, University of Maribor, Faculty of Civil Engineering, Transportation Engineering and Architecture, Smetanova ulica 17, 2000 Maribor, Slovenia, e-mail: marsenka.marksel@um.si. Stanislav Božičnik, PhD, Associate Professor, University of Maribor, Faculty of Civil Engineering, Transportation Engineering and Architecture, Smetanova ul. 17, 2000 Maribor, Slovenia, e-mail: stane.bozicnik@um.si.

1 Introduction

Electric road vehicles are not a novel invention for they have been around since 1900s. Even though they failed to compete with internal combustion engine (ICE) vehicles for different reasons, but the concept was never abandoned. With present-day understanding of negative impacts of transport's emissions on the environment, ICE emissions' contribution to climate change, electric cars are making a comeback as electrification of transport (electro mobility) has become a priority in the EU. The transport industry is of high importance globally, as well as in EU, where the transport sector employs 5 million Europeans. But it also contributes to almost one fifth of EU's greenhouse gas emissions (EUROSTAT (a), 2018). EU's has opted for an irreversible shift to low-emission mobility in terms of carbon and air pollutants. The ambition is clear: by mid-century, greenhouse gas emissions from transport will need to be at least 60% lower than in 1990 and be firmly on the path towards zero (European Commission, 2016). Yet despite this clearly stated political aim, the uptake of EV's is not progressing as desired. Focusing on Plug-in Electric Vehicles (PiEV = Plug-in Hybrid Electric Vehicles (PHEV) and Battery Electric Vehicles (BEV)) major obstacles to their mass-market adoption are twofold - battery technology limitations coupled with high battery cost (Egbue & Long, 2012) and the availability of public charging infrastructure. The range anxiety (the fear of fully depleting a BEV's battery in the middle of a trip, leaving the driver stranded (Neubauer & Wood, 2014)) can be overcome only with dense network of publicly accessible charging infrastructure regardless of EV type (BEV or Fuel Cell Vehicle (FCV)). The availability of charging/refuelling infrastructure is an absolute necessity and is completely independent from the average mileage driven by EV per day (Lieven, 2015).

This interdependency between charging infrastructure and uptake of EVs was acknowledged by the Council of the European Union: "Creating a sufficient network of recharging and refuelling stations is considered crucial in order to drive consumer demand for vehicles powered by "clean fuel", such as electricity, hydrogen and natural gas, and to encourage manufacturers to develop such vehicles and to sell them at competitive prices." (Council of the European Union, 2014). In order to stimulate faster market uptake of EVs and other vehicles using alternative fuels, EU countries have adopted a mix of policies and measures ranging from financial incentives for vehicle purchase, tax exemptions, and are investing in charging/refuelling infrastructure. This artificial stimulation of the

demand for EVs is seen as necessary for development of robust EV market for without subsidies, a robust EV market will not develop (Winegarten, 2018).

2 GDP and electro mobility

The availability of adequate re-charging infrastructure was identified as one of the most important enablers for a larger scale deployment of EVs in Europe (Zubaryeva, Thiel, Zaccarelli, Barbone, & Mercier, 2012), it becomes obvious that significant funds are needed for investments in order to stimulate PiEVs adoption. But EU countries are quite diverse in terms of development, in 2016 the GDP per capita ranged from 90.700 EUR (Luxemburg) to 6.800 (Bulgaria). This disparity is reflected in state of the PiEV market, both in terms of PiEVs' share - European Automobile Manufacturers association ACEA (ACEA, 2017) clearly stated: "In fact, in countries with a GDP below €17,000 the market share remains close to zero – including the new EU member states in Central and Eastern Europe, as well as in crisis-torn Greece. Affordability is clearly a major barrier". The interconnection is shown below: Figure 10 shows GDP per capita in 2016 while Figure 11 shows the percentage of PiEVs for passenger cars in the same year. At the same time the GDP levels are also reflected in availability of charging infrastructure. Figure 12 shows absolute number of charging positions in the EU countries in 2016. But the absolute number of charging positions is related also to country's size and population density, the number of charging positions per 1 million inhabitants population was calculated and is shown in the Figure 13 below.

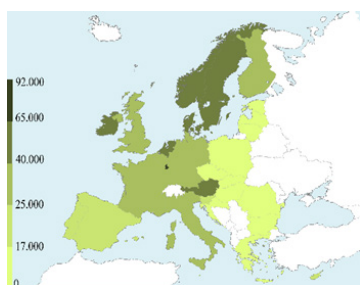


Figure1: GPD per capita in EU 2016 ¹

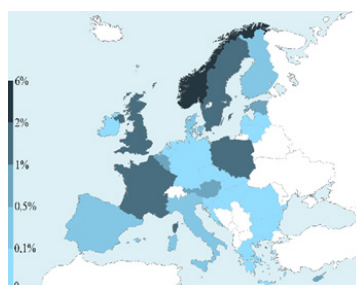


Figure 2 : Percent of PiEV for passenger cars in EU in 2016²

¹ own figure, data source (EUROSTAT (b), 2018)

² own figure, data source (EUROSTAT (b), 2018) (EAFO, 2018)

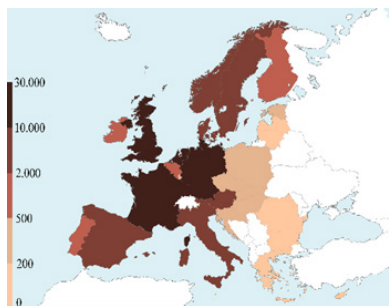


Figure 3: Absolute number of charging positions in EU in 2016³

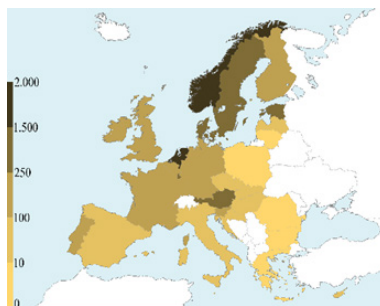


Figure 4: Number of charging positions per 1 mio. inhabitants in EU in 2016²

It may be stated from the Figure 1 and Figure 2 above that market penetration of PiEVs is higher in countries with higher GDP. The same seems to be true for charging infrastructure – countries with higher GDP have better developed charging infrastructure in terms of number of available PiEVs' charging positions. Most likely we can expect further slower adoption of EVs in countries with lower GDP because of lack of available funds needed for investments for faster development of EV market (be it by incentives for EV's purchase or with investments into charging infrastructure). It can be also concluded that even in countries with higher GDPs the EVs market adoption is not as high as expected (with exception of Norway).

3 Conclusions

The market adoption of EVs and, even more so, the existence of charging infrastructure seem to be interrelated with the level of development (GDP) of a country. As recharging infrastructure is considered one of the critical parameters in market penetration of EVs, the EU policy is focused on guaranteeing a minimum ratio of charging positions. The e-mobility market will remain dependant on public finances until commercial viability is achieved. As long as the public sector is taking the lead in charging infrastructure investments, we can expect further slow development of EV market in countries with lower GDP.

³ own figure, data source (EAFO, 2018)

Acknowledgments

The authors would like to thank the Interreg Danube eGUTS project for contributions of this paper. eGUTS project is co-financed by the European Regional Development Fund.

References

- ACEA. (2017). EU market for electric cars highly fragmented. Brussels, Belgium. Retrieved from <https://www.acea.be/press-releases/article/eu-market-for-electric-cars-highly-fragmented-new-data-shows-as-commission>
- Council of the European Union. (2014, March 24). Clean fuel infrastructure rules agreed by the Council and the European Parliament. 8203/14. Brussels. Retrieved from http://www.consilium.europa.eu/uedocs/cms_data/docs/pressdata/en/trans/141906.pdf
- EAF0. (2018, March). Electric vehicle charging infrastructure. Retrieved from European Alternative Fuels Observatory: <http://www.eafo.eu/electric-vehicle-charging-infrastructure>
- Egbue, O., & Long, S. (2012). Barriers to wide spread adoption of electric vehicles: An analysis of consumer attitudes and perceptions. *Energy Policy*, 48, 717-729.
- European Commission. (2016, July 07). A European Strategy for Low-Emission Mobility. Communication from the Commission to the European parliament, the Council, the European economic and social committee and the Committee of the regions. Brussels, Belgium, Belgium: European Commission.
- EUROSTAT (a). (2018, February). Greenhouse gas emission statistics - emission inventories. Retrieved from http://ec.europa.eu/eurostat/statistics-explained/index.php?title=Greenhouse_gas_emission_statistics_-_emission_inventories
- EUROSTAT (b). (2018, March). National accounts (including GDP. Retrieved from European Commission Eurostat: <http://ec.europa.eu/eurostat/web/national-accounts/data/database>
- Lieven, T. (2015). Policy measures to promote electric mobility – A global perspective. *Transportation Research Part A: Policy and Practice*, 82, 78-93. doi:<https://doi.org/10.1016/j.TRA.2015.09.008>
- Neubauer, J., & Wood, E. (2014). The impact of range anxiety and home, workplace, and public charging infrastructure on simulated battery electric vehicle lifetime utility. *Journal of Power Sources*, 257, 12-20.
- Winegarden, W. (2018). *Costly Subsidies For the Rich: Quantifying the Subsidies Offered to Battery Electric Powered Cars*. San Francisco (CA): Pacific Research Institute.
- Zubaryeva, A., Thiel, C., Zaccarelli, N., Barbone, E., & Mercier, A. (2012). Spatial multi-criteria assessment of potential lead markets. *Transportation Research Part A*, 46(9), 1477-1489. Retrieved from <https://doi.org/10.1016/j.tra.2012.05.018>

Method for Determining Battery Health

SLAVKO BREČKO, DALIBOR IGREC, ALEŠ BREZNIK, AMOR CHOWDHURY
& MIRAN RODIČ

Abstract This paper presents a method for automatic state of health estimation for lithium ion batteries. A pulse method for determining battery characteristics using a specially developed electronic measuring device is presented. Measurement results show characteristics of several measured batteries exhibiting different states of health with estimation possible even with a protection circuit present on the battery.

Keywords: • Li-ion • state of health • battery testing • measurement circuit • estimation method •

CORRESPONDENCE ADDRESS: Slavko Brečko, Tester, Margento R&D d.o.o., Gosposvetska cesta 84, 2000 Maribor, Slovenia, e-mail: slavko.brecko@margento.com. Dalibor Igréc, PhD, Technical Consultant, Margento R&D d.o.o., Gosposvetska cesta 84, 2000 Maribor, Slovenia, e-mail: dalibor.igrec@margento.com. Aleš Breznik, Researcher, Margento R&D d.o.o., Gosposvetska cesta 84, 2000 Maribor, Slovenia, e-mail: ales.breznik@margento.com. Amor Chowdhury, PhD, CEO, Margento R&D d.o.o., Gosposvetska cesta 84, 2000 Maribor, Slovenia, e-mail: amor.chowdhury@margento.com. Miran Rodič, PhD, Assistant professor, University of Maribor, Faculty of Electrical Engineering and Computer Science, Koroška cesta 46, 2000 Maribor, Slovenia, e-mail: miran.rodic@um.si.

1 Introduction

Lithium ion batteries are very common in electronics today but can be dangerous due to the toxicity and volatility of the material used in these batteries. Misusing or mishandling them can even cause explosions. Due to this reason, and to ensure quality of operation of electronic devices, determining battery health is important.

This paper presents a method for automatic determination of battery health based on internal resistance and equivalent capacitance of the battery itself estimated using the Thevenin battery model and using a pulse method.

2 Lithium ion batteries

Battery health can decrease due to multiple reasons. Firstly, the quality of batteries differs from manufacturer to manufacturer due to construction differences and type of battery material used. Poor battery construction can result in the battery losing operational capacity very rapidly resulting in low current supply and dropping voltage with a connected load to the battery, especially in the case of varying loads.

There are mostly three materials used in these batteries, differing them by type namely cobalt, manganese and phosphate. These materials result in the battery with differing capacity, voltage, internal resistance and other parameters.

While li-ion batteries have a lifetime of between 500 to over 1000 charging and discharging cycles, environmental parameters and usage of the battery can significantly impact battery health. These are mainly the temperature, load and charging style. These significantly contribute to battery aging with use.

With the aging of the battery, its capacity and performance decrease mainly due to mechanical degradation of the electrodes, which increases internal resistance and impacts its capacitance (Buchmann, 2017).

3 A method for battery state of health estimation

Pulse method, as presented in (Mousavi et al., 2014), is used to estimate the battery state of health. The battery is supplied with a constant current when charging, and loaded with power resistance when discharging. In both cases voltage response is measured. Internal resistance is calculated from the response and the dynamic part of battery response is estimated. Thevenin battery model is used to calculate the parameters. This model represents the battery with an equivalent circuit.

4 Battery testing procedure

The testing procedure is able to determine the state of health (SoH) (Buchmann, 2017) of a li-ion battery quite rapidly compared to commonly used tests, such as the full charge capacity method, and does not require complex algorithms such as frequency tests, while still providing a relatively accurate result (Min et al., 2006).

Our method estimates state of health of the battery based on the time-constant of charging and discharging of the battery from 100% to 63% of full charge and measuring the required time for the cycle.

5 Development of the measurement circuit

The circuit consists of the charging, measuring and connecting part. Adjustable charger BQ24715 ensures constant current when charging the battery. The measuring part consists of the integrated circuit INA260 and a power resistor. The STM32F407 microprocessor from the STM32F4DISCOVERY development board communicates with the measurement circuit and manages charging/discharging of a battery.

Communication with the battery circuit is implemented with the 1-Wire protocol. The charger and the INA260 communicate with the processor through I²C and SMBus protocols. Communication between the STM32F4DISCOVERY development board and the computer is implemented with ST-LINK and UART protocols. ST-LINK enables programming and debugging on the development

7 Measurement results

A device circuit and algorithm was specially designed for automated measurement and testing of batteries that can be used as a stand-alone device or as part of a larger assembly.

The state of health of the battery is estimated based on the Thevenin battery model (Mousavi et al., 2014) and calculated from comparison of internal resistance and capacitance at differing times of operation. The test was designed to work for both charging and discharging and at smaller time intervals resulting in a continuous measurement while the battery is in use.

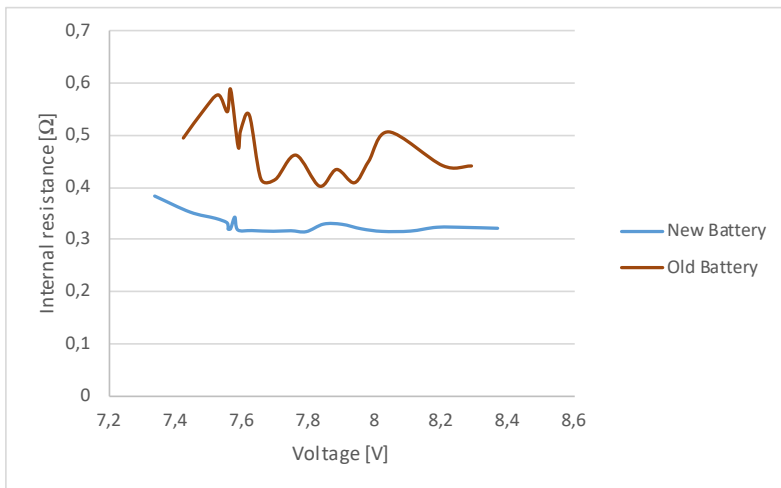


Figure 2: Comparison of internal resistance

A clear distinction can be observed between old and new batteries in terms of internal resistance difference and capacitance. Figure 2 represents a continuous measurement of internal resistance of an old battery and a new one with a clear distinction with the new battery exhibiting internal resistance of around 325 mΩ and the old battery exhibiting internal resistance of around 500 mΩ. The same distinction can be observed in capacitance of the batteries in Figure 3 with the new battery exhibiting a capacitance of around 500 F, which is around 200 F for the old battery.

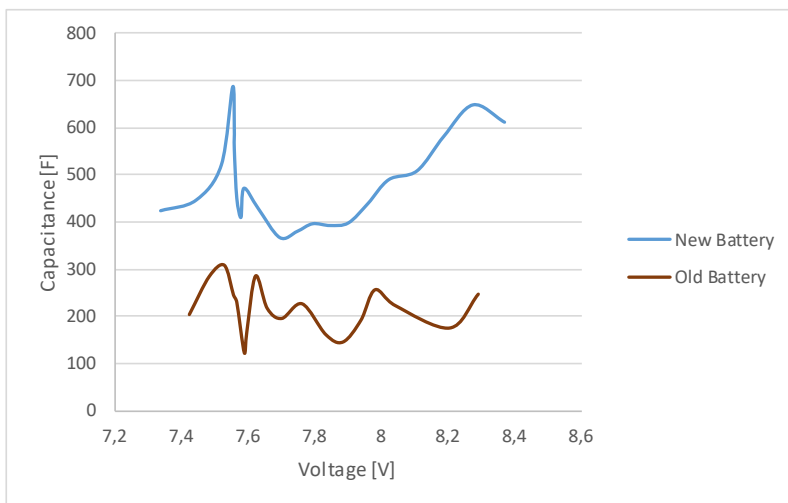


Figure 3: Comparison of capacitance

8 Conclusion

Based on presented results of internal resistance and capacitance a good estimate can be made on the state of health of the battery. A state of health can be deemed as good if the internal resistance is below 350 m Ω and capacitance above 300 F while charging. These values however differ if the test is carried out at battery discharge with a good battery exhibiting internal resistance below 400 m Ω and capacitance higher than 350 F (Brečko, 2018). The method is demonstrated as reliably accurate and appropriate for operational use.

References

- Brečko, S., (2018). Avtomatizacija testiranja stanja Li-ion baterij, magistrsko delo.
- Buchmann, I., "BU-808b: What Causes Li-ion to Die?", Battery university, 2017.
URL: http://batteryuniversity.com/learn/article/bu_808b_what_causes_li_ion_to_die [19.04.2018].
- Buchmann, I., "BU-907a: Battery Rapid-test Methods", Battery university, 2017.
- Min, C., Rincon-Mora, G. A., (2006). Accurate electrical battery model capable of predicting runtime and I-V performance. *Energy Conversion, IEEE Transactions on*, 21, 504-511.
- S. M. Mousavi G and M. Nikdel, (2014). Various battery models for various simulation studies and applications. *Renewable and Sustainable Energy Reviews*, 32, 477-485.

Blockchain-Based Solution for Future Energy Management in Existing Infrastructure

DALIBOR IGREC, ALEŠ BREZNIK & AMOR CHOWDHURY

Abstract The paper presents a possible solution for implementing blockchain technology in smart grid systems. The proposed solution presents new and improved smart grid management and operational overview options to all parties involved in energy generation, distribution and consumption, without any required hardware modifications and installments. The paper concluded with possible socio-economic implications of such technology.

Keywords: • blockchain • smart grid • energy management • prosumer • sustainability •

CORRESPONDENCE ADDRESS: Dalibor Igrec, PhD, Technical Consultant, Margento R&D d.o.o., Gosposvetska cesta 84, 2000 Maribor, Slovenia, e-mail: dalibor.igrec@margento.com. Aleš Breznik, Researcher, Margento R&D d.o.o., Gosposvetska cesta 84, 2000 Maribor, Slovenia, e-mail: ales.breznik@margento.com. Amor Chowdhury, PhD, CEO, Margento R&D d.o.o., Gosposvetska cesta 84, 2000 Maribor, Slovenia, e-mail: amor.chowdhury@margento.com.

1 Introduction

The rise of blockchain-based solutions in virtually all market segments in the past year has been unprecedented. Only in the area of energy there were 133 organizations and 40 active projects between Q2 2017 and Q1 2018 (Colleen, M., 2018).

With a vast potential this technology has to offer, in this article we present a forward-looking solution for energy tracking and management based on the blockchain technology, offering a system upgrade for smart, real-time and automatic energy provider management based on predefined criteria such as energy source, price and similar.

The proposed solution herein represents a possible upgrade to existing infrastructure without any additional hardware installations and without tampering with existing operation of the energy grid infrastructure.

2 Fundamentals of blockchain

Blockchain technology can roughly be understood within the framework of two features, namely cryptocurrency and smart contracts. Smart contracts are automatic scripts with predefined parameters that are tamper-proof upon activation (Hertig, A., 2018). This is due to the distributed nature of the ledger and validation procedures within the blockchain technology.

With multiple parties holding the entire track record of the network, tampering and manipulation is very difficult. The validation procedure, called mining, relies on mathematically ensuring the integrity of data recorded on the blockchain itself, making operations on the blockchain transparent and trackable thereby drastically minimizing fraudulent behavior.

For the aforementioned reasons of transparency, immutability and tracking, the blockchain is an ideal technology to be used in the emerging market of distributed and decentralized energy generation and management.

While many cryptocurrency systems offer fully public ledgers, in the sense that transaction confirmation operations (so-called mining) can be carried out by anyone on the network, such solutions are unfit for delicate systems, which are

heavily dependent on robust operation, stability and resilience to outside influences. Due to the intricate nature of the subject of energy distribution and management, the only rationally viable form of blockchain applicable to this ecosystem would be in the form of a federated and permissioned network of trusted parties (such as energy providers) validating all transactions of energy transfer (Advanced metering infrastructure, 2018).

3 Existing energy infrastructure

Existing energy infrastructure already contains smart meters in most of the developed world. Energy companies are already tracking their customers' energy consumption remotely through the so called advanced metering infrastructure (AMI) of energy infrastructure providers. The purpose of AMI is to provide energy companies with real-time energy consumption data while providing consumers with the information needed to make decisions based on energy consumption and energy price at time of use (Advanced metering infrastructure, 2018). AMI is a key component of smart grids.

Energy meters transmit their data to local energy hubs using power line communication (PLC) (Power-line communication, 2018). These energy hubs contain internet-connected nodes that enable two-way communication between the nodes and energy companies. These hubs forward data via ethernet to the energy infrastructure provider and can be here forth accessed by other parties exclusively through services offered by infrastructure providers.

4 Blockchain and decentralized smart grids

Our proposed solution only requires a software upgrade of internet-connected nodes within energy hubs to include a blockchain node without any hardware installations or interference with existing operation of the energy grid.

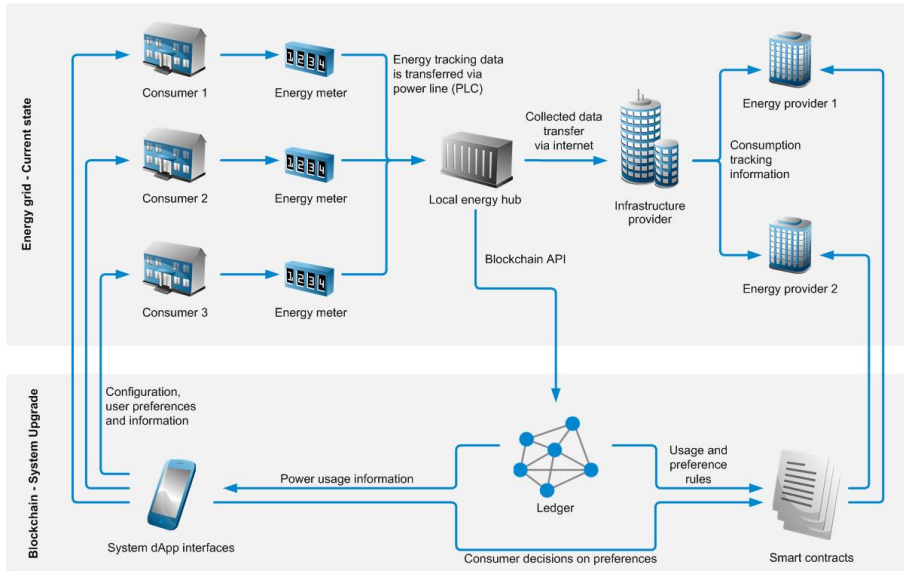


Figure 1: System upgrade solution diagram of information flow

General overview of information flow within the proposed system is shown in Figure 1. With the existing infrastructure unchanged, all information is still handled the same way as it is currently in existing systems of energy infrastructure.

The addition of the blockchain solution does not interfere with existing operation of the energy grid, which merely broadcasts this same information that is readily available within the energy grid, to the blockchain network. Information regarding network status, individual energy consumption, power quality and other available data is then used by smart contracts to automatically enforce terms and conditions of each respective contract as agreed upon between consumers and energy providers.

Consumers may review and monitor this data within the mobile or webpage app in real-time. The applications enable setting and editing of any parameters of individual contracts, such as, for example, purchase or sale of energy depending on current market prices. The applications would enable the creation and monitoring of smart contracts and, by proxy, review and comparison of individual providers along with any information on energy and policy they provide, such as for example energy source, current purchase and sale price, additional offers and notifications and news, which opens up new possibilities of

engaging consumers in energy grid management, operations and enables advanced methods of communication between individual parties in the energy ecosystem that are currently not available.

With power consumption-related data widely available in near real-time compared to current per-request models, a wide array of advanced power management and energy generation optimization solutions become available.

Smart grid operators would have a much easier task of handling demand-response actions, remote service disconnects, managing micro-power generation as well as enable advanced disconnect and decreased power supply strategies and services to consumers based on grid demand and individual consumer preference.

5 Self-sustainability paradigm

With the rise of personal micro-power generation with wind, solar or water and compound systems is increasing the pressure on providers and infrastructure operators to integrate these micro-producers into the energy grid. On the other hand, these systems are able to offer near self-sufficiency to households and local communities without the need for outside regulation or management. Our proposed solution supports integration of these micro-grids with available information on power production, power quality and grid operation, infrastructure operators can seamlessly integrate these micro-grids into their energy grid as new entities that consumes and produces power, *prosumers*.

Prosumers are a new emerging entity within the energy ecosystem. With many households already generating their own electricity and the trend only on the rise, the need to manage and intelligently integrate these entities is becoming an ever-increasing issue. Prosumers present a new challenge regarding grid management, since they produce differentiating amount of electricity at different times.

Energy distribution at a small distance additionally increases efficiency due to lower losses in the conducting wires, presenting a more efficient energy source, while at the same time far less stable one. Due to this changing energy production, prosumers at times act as regular consumers and at others as energy producers. Infrastructure providers must account for these spikes in production

for example, on a sunny day, while at night a prosumer will most likely require more energy than they produce. The advent of household batteries somewhat mitigates this issue, but the challenge of accounting for local production and consumption with regard to infrastructure is still an unresolved issue hindering the rise of localized self-sufficient microgrids.

6 Conclusion

As presented in this article blockchain represents a technology that will surely find its place in future solutions. The numerous benefits all parties gain with the implementation of the proposed solution herein would greatly increase the satisfaction with the energy supply and quality as well as decrease expenses while opening new business models at the same time. A new paradigm shift mentioned herein is already underway. There has been a rise in micro power generation across the developed world stimulated by new technologies on the rise in the area. Most notably, the development of solar, wind and hydro in individually manageable sizes while maintaining modularity has resulted in widespread rise in adoption of such technologies.

While the solution proposed herein is technically feasible today, the trailing policies in the area of energy generation, distribution and management hinder implementation of such systems.

References

- “Advanced metering infrastructure (AMI)”, *TechTarget*, 2018
- “Power-line communication”, *Wikipedia*, May, 2018
- Colleen M., “Blockchain for Energy 2018”, *gtmresearch*, March, 2018
- Hertig A., “How Do Ethereum Smart Contracts Work?”, *CoinDesk Inc.*, 2018

SWOT Analysis of Pedelecs and E-Cars in Selected Countries of the Danube Region

GREGOR SRPČIČ, IZTOK BRINOVAR, KATJA HANŽIČ, MIRALEM
HADŽISELIMOVIĆ & SEBASTIJAN SEME

Abstract This paper deals with pedelecs and e-cars in urban transport systems in selected countries of the Danube region. Within the EU project eGUTS a feasibility study focused on pedelecs and e-cars was made. Country specific information on e-mobility (pedelecs and e-cars) was gathered and is briefly presented in chapter 2. In addition, a common SWOT analysis for all selected countries of the Danube region was made and is presented in the conclusion of the paper.

Keywords: • pedelecs • e-cars • electric vehicles • SWOT analysis • Danube region •

CORRESPONDENCE ADDRESS: Gregor Srpčič, Assistant, University of Maribor, Faculty of Energy Technology, Hočevarjev trg 1, 8270 Krško, Slovenia, grega.srpcic@um.si. Iztok Brinovar, Assistant, University of Maribor, Faculty of Energy Technology, Hočevarjev trg 1, 8270 Krško, Slovenia, iztok.brinovar@um.si. Katja Hanžič, University of Maribor, Faculty of Civil Engineering, Transportation Engineering and Architecture, Smetanova ulica 17, SI-2000 Maribor, Slovenia, katja.hanzic@um.si. Miralem Hadžiselimović, PhD, Full Professor, University of Maribor, Faculty of Energy Technology, Hočevarjev trg 1, 8270 Krško, Slovenia, miralem.h@um.si. Sebastijan Seme, PhD, Associate Professor, University of Maribor, Faculty of Energy Technology, Hočevarjev trg 1, 8270 Krško, Slovenia, sebastijan.seme@um.si.

1 Introduction

Electric vehicles have been around for more than hundred years with the first mass-produced electric vehicles appearing in America in the early 1900s. For various reasons electric cars failed to gain public acceptance and road transport market was, and still is, dominated by vehicles with internal combustion engines. With advanced understanding of negative impacts of transport's emissions on the environment and its contribution to climate changes, electrification of transport has become a priority. With the electrification of road transport, greenhouse gas emissions, air pollution as well as fossil fuel dependency can be reduced, (Department of energy, 2015).

Within the eGUTS project (Electric, Electronic and Green Urban Transport Systems), a feasibility study focused on pedelecs and e-cars was made. In the course of the feasibility study, specific information on e-cars and pedelecs from participating countries of the Danube region were collected. Each country made a SWOT analysis on pedelecs and e-cars according to information specific for their country. Next, a common SWOT analysis for all selected countries of the Danube region was made, (eGUTS project, 2017).

2 Country specific information on pedelecs and e-cars

Austria - At a national level, Austria's energy strategy supports the promotion of new drive systems (such as electric mobility) in order to reduce emissions in the transport sector and to achieve employment policy effects. In 2017, 13350 electric cars were registered in Austria. The most widely used vehicle with electric motor in Austria remains the electric bicycle, in most cases with pedal support. According to this, around 50000 pedelecs were sold in Austria in 2014. This corresponds to a share of 12,5 % of the total of 400000 bicycles sold, (eGUTS project, 2017; EAFO, 2018).

Croatia - Taking into consideration the European rate of adopting electric vehicles, Croatia has been at the lower end of the scale. There are numerous reasons for that, but obviously the lower purchasing power, longer than in the rest of the European Union lasting crisis, lack of charging facilities and the overall small size of the market have contributed to this. Electric vehicles present a very small, minor part of the overall number of cars in Croatia. In 2017, only 87 e-

cars were registered in Croatia, (eGUTS project, 2017; Smart City Wien, 2016; EAFO, 2018).

Czech Republic - There are neither official nor unofficial sales statistics for pedelecs. The surveys are usually performed at the level of stakeholders questioning, or based on their expert estimates. In 2016, the sales of pedelecs were estimated to reach approximately 40000. In contrast to bicycles, the statistical data for personal vehicles are very detailed. The number of sold battery electric vehicles (BEV) has been growing since 2009. The exceptions were the years 2013 and 2016 when the sales of BEVs decreased. In 2017, 1145 electric cars were registered in Czech Republic, (eGUTS project, 2017; EAFO, 2018).

Hungary - Unfortunately, the use of e-vehicles in Hungary is still in its infancy. Numerous models are available and quite a few types of pedelecs are also manufactured in Hungary, although mainly for export. Only 600-800 pedelecs are sold domestically. This is due to the current high price of these vehicles. The situation is similar with electric cars. In 2017, 1145 e-cars were registered in Hungary, (eGUTS project, 2017; EAFO, 2018).

Montenegro - The development and production of electrical vehicles powered by batteries as a source of energy or pedals does not exist in Montenegro, and use of electric vehicles in Montenegro is insufficient. A few hybrid vehicles are used for taxi service for passenger transportation. In addition, some tourist vehicles and electric vehicles with pedals are used in the coastal touristic area of Montenegro, (eGUTS project, 2017).

Romania - The Romanian electric bicycle market has just started to develop. Selling around 2000 units in 2016, but the production of these vehicles marks one of the highest values at the level of the European Union, according to data provided by the European Confederation of Bicycle Industry. In 2017 e-cars sales in Romania increased by 24 % in the first 7 months of the year, but they remain at a low level compared to other European countries. In 2017, 335 e-cars were registered in Romania, (eGUTS project, 2017; EAFO, 2018).

Serbia – Only about 30 electric cars are registered in Serbia. At present, electric cars cannot be registered in Serbia. They can only be registered temporarily. There is a large offer of pedelecs manufacturers from the EU and China on the market. However, the sale is very limited.

Slovakia - Electro mobility in the Slovakia has a growing tendency. In spite of the relatively low absolute numbers of registered e-cars, in 2011-2015, the growth in the number of e-cars is obvious, what indicates the future development in the context of the global trend. In 2017, 439 e-cars were registered in Slovakia, (eGUTS project, 2017; EAFO, 2018).

Slovenia - In Slovenia electric cars are still in minority, compared to classic internal combustion type of cars. Altogether, there are 706 registered electric cars driving on Slovenian roads. The number of e-bikes is growing in Slovenia. Already some companies that offer e-bikes for rent exist. Most of sellers of regular bikes also offer modern electric bikes for sale, (eGUTS project, 2017; EAFO, 2018).

3 Conclusion – SWOT analysis

As already mentioned, each country made a SWOT analysis on pedelecs and e-cars according to strengths, weaknesses, opportunities and threats specific for their country and then a common SWOT analysis for pedelecs and e-cars together in all selected countries of the Danube region was made. The SWOT analysis is presented in Table 1. Together with SWOT analysis, barriers for deployment of e-cars and pedelecs were identified.

Table 1: SWOT analysis for e-mobility sector (e-cars/pedelecs), (eGUTS project, 2017)

Strengths	Weaknesses
<ul style="list-style-type: none"> • E-vehicles have higher energy efficiency than ICE vehicles. • No dependence on crude oil. • Reduced green-house-gas emissions. • Less air-pollution and noise from transport at places with dense traffic. • Availability of electricity and its relatively favourable price compared to conventional fuels (lower energy cost per km). • The electric motor is characterized by its simplicity of construction and thus also by simpler maintenance/repairs resulting into lower operation/maintenance costs. • Pedelecs allow for longer distances to be cycled with the same level of effort, easier to overcome natural obstacles like hills or headwinds, enable to transport heavier goods than conventional bikes and are an option for solving problems with congestions and land-taken in limited urban spaces. 	<ul style="list-style-type: none"> • High initial investments in the e-vehicle. • Currently insufficient infrastructure for e-vehicles recharging. • Small user comfort from the point of view of the need for frequent recharging. • Non-harmonized standards and norms. • High costs of battery rent or new battery purchase. • Non-acceptance of various access cards at charging stations (roaming for electric vehicle charging is not solved) • Non-environmentally-friendly production of batteries. • E-cars do not solve the problems with congestions and land-taken in urban areas (parking, new roads) in contrast to e-bikes (pedelecs). • Low density of servicing network. • Usage of pedelecs is dependent on the weather conditions.
Opportunities	Threats
<ul style="list-style-type: none"> • Strong EU interest in e-mobility and incorporation into various policies and directives. • Interest of all major automobile companies in the development and serial production of their own e-vehicles. • Creation of new innovative business models and services (battery/e-vehicles renting schemes, car-sharing, bike-sharing, cargo-bikes services, etc.). • Use of e-vehicles in smart grids. • Existence of various incentives for e-mobility support. • Opportunity for use of locally produced electricity mainly from renewable energy sources. • Limiting operation of conventional vehicles in urban areas (e.g. introduction of low-emission-zones in town centres) 	<ul style="list-style-type: none"> • Low purchase power of the population and companies. • Excessive demand for electricity and inability to provide sufficient amount of electricity from renewable sources. • Oil price dropping or rising electricity prices. • Non-sufficiently developed cycle route network in some countries/regions/cities, lower culture of cycling and lower respect to cyclists from car-driver's side. • Incompatibility of charging systems (many different charging plugs/sockets).

References

- Department of energy, (2015). The history of the electric car. Available at: <https://www.energy.gov/articles/history-electric-car>
- eGUTS project, (2017). D4.2.2 “Pedelecs vs e-cars in urban transport systems”.
- Smart City Wien. Stadtentwicklung Wien, (2016). E-mobilitätsstrategie. Available at: <https://www.wien.gv.at/stadtentwicklung/studien/pdf/b008435.pdf>

EAFO, (2018). Electric vehicle charging infrastructure. Available at: European Alternative Fuels Observatory: <http://www.eafo.eu/>

The Influence of Increased Moderator Temperature on the Nuclear Characteristics of the NPP Krško

MARJAN KROMAR & BOJAN KURINČIČ

Abstract NPP Krško safety analysis has been performed in such a way to allow operation with primary system average coolant temperature – T_{avg} inside a prescribed range, which constitute the so-called operating window. The T_{avg} window enables certain flexibility to select an optimum value within the T_{avg} range taking into account safety, operational and economical considerations. Increase of the reactor coolant temperature in general improves thermodynamic efficiency of the Pressurized Water Reactor (PWR) plant yielding to increase in the electricity production. However, higher temperature causes lower water density in the reactor core altering the neutron moderation and consequently neutron transport in the reactor. This impact on the nuclear core characteristics is investigated for the NPP Krško reactor core.

Keywords: • pressurized water reactor • nuclear design calculations
• reactor coolant temperature optimization • critical boron concentration • Nuclear Power Plant Krško •

CORRESPONDENCE ADDRESS: Marjan Kromar, PhD, Assistant Professor, “Jožef Stefan” Institute, Reactor Physics Division, Jamova 39, SI-1001 Ljubljana, Slovenia, e-mail: marjan.kromar@ijs.si. Bojan Kurinčič, Nuclear Power Plant Krško, Engineering Division - Nuclear Fuel & Reactor Core, Vrbina 12, SI-8270 Krško, Slovenia, e-mail: bojan.kurincic@nek.si.

DOI <https://doi.org/10.18690/978-961-286-241-1.16>
Available at: <http://press.um.si>

ISBN 978-961-286-241-1

1 Introduction

The Krško modernization analyses after the power uprate have been performed in such a way as to cover operation in a range of average reactor coolant temperatures (T_{avg}), and for a range of steam generator tube plugging levels from 0 to 5%. These ranges constitute the so-called operating window. The T_{avg} window enables certain flexibility to select an optimum value within the T_{avg} range taking into account safety, operational and economical considerations.

Increase of the reactor coolant temperature in general improves thermodynamic efficiency of the Pressurized Water Reactor (PWR) plant yielding to increase in the electricity production. However, higher temperature causes lower water density in the reactor core altering the neutron moderation. Moderation reduction causes harder neutron spectrum, lower multiplication factor and consequently has direct impact on the nuclear chain reaction. This impact on the nuclear characteristics is investigated for the NPP Krško reactor core.

2 Brief NPP Krško Core Description

The Krško plant is a 2-loop Westinghouse PWR that began electricity production in 1981. The start-up core had a rated thermal capacity of 1,876 MWt, and a 626 MWe gross electric power. Currently, the thermal rating is 1,994 MWt with 727 MWe gross electric power. The core consists of 121 fuel assemblies. Each assembly has 235 fuel rods arranged in a 16×16 array. The remaining 21 positions contain guide tubes and are intended for control rods, neutron source and in-core instrumentation. The core features 33 Reactivity Control Cluster Assemblies (RCCA) arranged in 6 banks.

3 Results and discussion

Calculations in this paper are performed with the CORD-2 calculation package (Kromar et al., 2009). The CORD-2 system has been developed by the Reactor Physics Department of the Jožef Stefan Institute and is intended for core design calculations of PWRs. The CORD-2 system consists of two basic reactor physics codes: WIMS-D (Askew et al., 1966), and GNOMER (Trkov, 1993). WIMS-D is a well-known and widely used lattice code. Version WIMS-D5 is available from the NEA data bank in Paris. A 69-group neutron cross-section library based on the ENDFB-VII.0 neutron data files has been used. GNOMER solves the

neutron diffusion equation in three-dimensional Cartesian geometry by using Green's function nodal method (Trkov, 1990). It also includes advanced features for cross-section homogenization and a simple thermal-hydraulic module so that thermal feedback can be taken into account. The CORD-2 system enables determination of the core reactivity and power distribution. The package has been validated for the nuclear design calculations of PWR cores and has been used for the verification of the NPP Krško reload cores since 1990.

3.1 Critical Boron concentrations

To analyze changes in nuclear properties 6 operational cycles, starting with cycle 24, have been examined assuming 1°K increase in core inlet temperature. Higher moderator temperature results in lower water density. Since PWR's operate at under moderated condition, additional shortage of the Hydrogen atoms lower effective multiplication factor. Critical Boron concentrations are therefore lower. Boron differences for the Hot Full Power (HFP), All Rods Out (ARO) conditions are shown in Fig. 1. Differences are the largest at the first operational cycle with higher inlet temperature (e.g. cycle 24) with magnitude rising over the cycle (from -5 ppm to -11 ppm). Differences are little smaller in later cycles, due to higher Pu production caused by neutron energy spectral shift to higher energies.

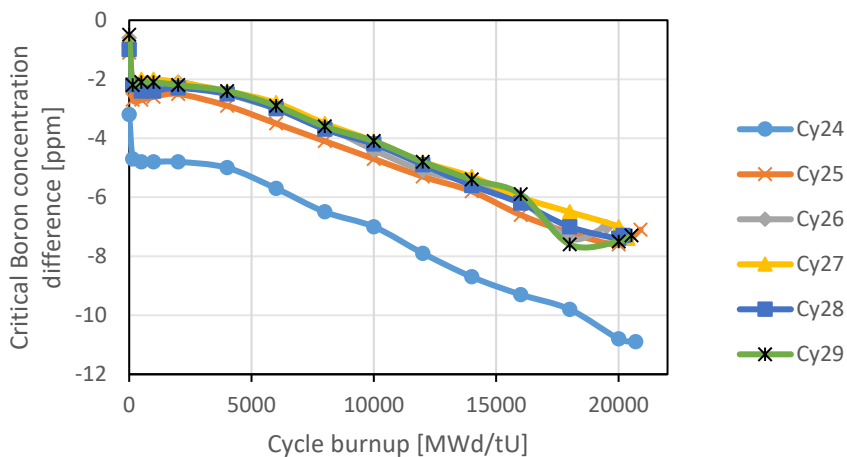


Figure 1: Critical Boron concentration difference at HFP, ARO conditions.

3.2 Power distributions

Radial power distributions are only slightly changed. Maximum difference in radial peaking factors for all 6 cycles during core burnout is 0.003, which is almost negligible. In addition, the core designer has considerable flexibility with adjustment of core loading pattern and can easily achieve imposed radial peaking factor requirements.

Changes in axial power distribution require more consideration, because the core designer has no direct influence on it. Since the water density is not linearly dependent on the temperature, with increased core inlet temperature at Hot Full Power (HFP) conditions, axial power distributions are skewed to the core bottom. The water density at core top regions is namely unproportionally lower compared to the bottom regions. Due to undermoderated operational conditions, power is decreased at the top and increased on the bottom. Power axial offset ($(P_{top}-P_{bottom})/(P_{top}+P_{bottom})$) shown at Beginning Of Cycle (BOC) and End Of Cycle (EOC) in Table 1 is little more negative. The effect is the largest in the first cycle with increased inlet temperature (e.g. cycle 24). In subsequent cycles and during the core burnout the effect is smaller. Average axial power distribution differences in cycle 24 are less than 0.5 % and less than 0.2 % in subsequent cycles.

Table 1: Power axial offset at HFP

Cycle	Power axial offset [%]					
	BOC			EOC		
	Nominal	Nom.+1 °K	Diff.	Nominal	Nom.+1 °K	Diff.
24	1.167	0.917	-0.250	-2.674	-2.808	-0.134
25	0.681	0.674	-0.007	-2.862	-2.904	-0.042
26	1.450	1.371	-0.079	-2.726	-2.734	-0.008
27	0.916	0.863	-0.053	-2.778	-2.830	-0.052
28	0.242	0.201	-0.041	-2.722	-2.724	-0.002
29	1.099	1.057	-0.042	-2.795	-2.756	+0.039

3.3 HZP reactivity consideration

HZP condition is defined as core statepoint at temperature 564.82 °K. Since temperatures are the same in both cases, only slightly different isotopic composition causes different reactor core behavior. Control rods worth and Boron worth coefficients at BOC are presented in Table 2. Rods worth are only slightly less reactive (less than 0.05 %), while the Boron worth coefficient at 2400 ppm is almost the same and on the verge of numerical accuracy.

Table 2: Control rods worth and Boron coefficient at BOC

Cycle	Control rods worth [pcm]			Boron worth coefficient [pcm/ppm]		
	Nominal	Nom.+1 °K	Diff.	Nominal	Nom.+1 °K	Diff.
25	6245	6242	-3	-5.372	-5.373	-0.001
26	6397	6394	-3	-5.386	-5.383	+0.003
27	6243	6241	-2	-5.407	-5.407	+0.000
28	6374	6372	-2	-5.434	-5.431	+0.003
29	6244	6241	-3	-5.403	-5.402	+0.001

4 Conclusion

The impact of the increased inlet water temperature on the nuclear characteristics of the NPP Krško reactor core is investigated.

Critical boron concentrations are lowered for up to -11 ppm in the first cycle and up to -5 ppm in subsequent cycles. Lowered critical boron concentration would imply approximately 2.5 and 1.2 less operational days of the power plant. If the same cycle length is required, initial enrichment should be increased accordingly.

Power distributions are only slightly affected. Radial power peaking factors differences are less than 0.003, while the axial distributions are inside the 0.5 %. Impact on the control rod worth and Boron worth coefficient at HZP is negligible.

Obtained results provide support to the NEK decision regarding operation at higher reactor coolant temperature.

References

- Askew, J. R., Fayers, F. J., Kemshell, P. B., (1966). A General Description of the Code WIMS. *J. Br. Nucl. Energy Soc.*, 5, 564.
- Kromar, M., Trkov, A., (2009). Nuclear Design Calculations of the NPP Krško core. *Journal of Energy Technology*, 2(4), 41-50.
- Trkov, A., (1993). GNOMER - Multigroup 3-Dimensional Neutron Diffusion Nodal Code. Institute Jožef Stefan, Ljubljana, Slovenia, IJS-DP-6688.
- Trkov, A., Najžer, M., Škerget, L., (1990). Variant of Green's Function Nodal Method for Neutron Diffusion. *J. Nucl. Sci. Technol.*, 27(8), 766-777.

Optimal Planning and Operation of the Off-Grid Genset System by an Evolutionary Algorithm

MARINKO BARUKČIĆ, DEJAN BAREŠIĆ, ŽELJKO HEDERIĆ & IVAN MIJIĆ

Abstract Optimal usage of more gensets to supply the loads in off-grid mode can be challenging to solve in both the planning and operational phases. Due to loads changing through the time, some of the gensets will operate in intermittent operation. The question arises from the load variability is what is the optimal number and sizes of the gensets from an economic point of view. Generally speaking, what is more economic: one high size genset or smaller gensets (of which some will be turned off is some period) to supply variable loads. Because this is an optimization issue some of the optimization procedure should be used to solve the problem. The optimization problem is a mixed integer nonlinear problem including discrete variables and objective function with equality and inequality constraints. The formulation of the optimization problem and procedure to solve the problem by using the metaheuristic optimization technique for optimal planning and operation of the gensets is presented in the research.

Keywords: • evolutionary algorithm • genset • off-grid operation • optimization • variable load •

CORRESPONDENCE ADDRESS: Marinko Barukčić, PhD, Associate Professor, Josip Juraj Strossmayer University of Osijek, Faculty of Electrical Engineering, Computer Science and Information Technology Osijek, Kneza Trpimira 2B, 31 000 Osijek, Croatia, e-mail: marinko.barukcic@ferit.hr. Dejan Barešić, PhD student, University of Zagreb, Croatian Military Academy "Dr. Franjo Tuđman", Ilica 256b, 10000 Zagreb, Croatia, e-mail: dejan.baresic@morh.hr. Željko Hederić, PhD, Associate Professor, Josip Juraj Strossmayer University of Osijek, Faculty of Electrical Engineering, Computer Science and Information Technology Osijek, Kneza Trpimira 2B, 31 000 Osijek, Croatia, e-mail: zeljko.hederic@ferit.hr. Ivan Mijić, MSc, Josip Juraj Strossmayer University of Osijek, Faculty of Electrical Engineering, Computer Science and Information Technology Osijek, Kneza Trpimira 2B, 31 000 Osijek, Croatia, ivan.mijic@ferit.hr

1 Introduction

Application of the gensets as energy supplying source in off-grid mode can be of interests in case of different purposes when reliable and controllable electricity sources are required. The use of such genset system can generally be in case of need for temporary electricity supplying on some area such are in case of natural disasters (when power grid infrastructure is damaged) or in case of the mobile military camps. In case of using the gensets as distributed generation unit on some area the technical and economic analysis (for example as given in (Seme *et al.*, 2018)) should be done with aim to found the most appropriate sources among gensets, wind plants, photovoltaics or small hydro plants. Using more different gensets in parallel off-grid operation required the dispatch of their power production with an aim to achieve their operation as economically as possible. There are a number of research work on operation optimization ordinary power plants regarding optimization of unit commitment as can be found in (Zheng, Wang and Liu, 2015; Khazaei *et al.*, 2016). Also, researches considering unit commitment optimization of a power system including renewable sources are present in the literature as in (Lorca and Sun, 2017; Sun *et al.*, 2017). In the case of off-grid operation of the microgrid including genset and different renewable sources, there are researches can be found in (Cristóbal-Monreal and Dufo-López, 2016; Askarzadeh, 2017; Dufo-López *et al.*, 2017a). However, researches of off-grid operation optimization of the genset system including more gensets are not so wide in the literature. In (Matt *et al.*, 2005) research about the optimal operation of more genset in parallel operation is presented. In the research (Matt *et al.*, 2005) the number of gensets is fixed before the optimization solution is started. The gensets' sizes are determined by enumeration approach of all possible combinations of available gensets. The optimization procedure is used, for a given number of gensets and the gensets combinations, to obtain optimal gensets' powers on the hourly level for the given load profile in (Matt *et al.*, 2005).

Because the optimization problem is hard to solve (mixed decision variables, discrete objective function, non-differentiable objective function, equality constraint), the robust, metaheuristic optimization technique belongs to an evolutionary class of the optimization method is used here. The similar optimization approach by using the population-based optimization solver for unit commitment optimization is presented in (Pappala and Erlich, 2008).

The rest of the paper is organized as follows. The mathematical model of the problem is defined first then the simulation setup and results are presented and the conclusion is given at the end.

2 Mathematical description of the optimization problem and optimization method

The mathematical formulation of the optimization problem in general form is:

$$\begin{aligned} f(dv) \rightarrow \min \quad & \text{objective function} \\ \text{subject to: } g_i(dv) = 0 \quad & \text{equality constraints and } h_j(dv) < 0 \quad \text{inequality constraints} \end{aligned} \quad (1)$$

where dv denotes a set of decision variables in form of the vector.

The objective function is here defined as:

$$f(dv) = C_{RF} \cdot C_p + F_c \cdot C_f \quad (2)$$

where C_{RF} is the capital recovery factor, C_p is the cost of gensets purchase, F_c is fuel consumption and C_f is the cost of fuel. Capital recovery factor is calculated as:

$$C_{RF} = \left[IR \cdot (1 + IR)^{PP} \right] / \left[(1 + IR)^{PP} - 1 \right] \quad (3)$$

where IR is interest rate and PP is payback period.

Because the working of gensets under low load is not recommended due to increased wear and decreasing the maintenance period, this is considered as inequality constraints in (1):

$$P_{G, \min} \leq P_{G, i, j} \leq P_{G, \text{nom}} \quad (4)$$

According to constraint (4) output power $P_{G, i, j}$ of the i^{th} genset in j^{th} hour need to be between the allowed minimum value $P_{G, \min}$ and nominal power $P_{G, \text{nom}}$.

In (Matt *et al.*, 2005) is proposed that load of a genset is no less than 30 %. Here the lower limit of the genset load of 25 % is used. The inequality constraint defining that installed power of all N gensets should be equal or greater than the maximal load appears in an hour is used here to avoid solutions do not satisfy this requirement:

$$\sum_{i=1}^N P_{G,i,nom} \geq P_{L,max} \quad (5)$$

Also, the equality constraint describing the power balance between total produced power ($\sum P_{G,j}$) by all gensets and total load ($P_{L,j}$) in each hour is used as the problem constraint:

$$\sum_{i=1}^N P_{G,i,j} \geq P_{L,j} \quad (6)$$

The problem decision variables are the gensets productions in each hour and sizes (G_j) of the installed gensets:

$$dv = [P_{G,1,1} \quad \dots \quad P_{G,N,H} \quad Gs_1 \quad \dots \quad Gs_N] \quad (7)$$

The fuel consumption between loads given in the genset data is determined by linearization between two neighborhood points (Fig. 1). In most of the literature, the specific fuel consumption (in l/kW/h) is used to calculate the objective functions. Here the fuel consumption in l/h is used rather than the specific fuel consumption. In (Cristóbal-Monreal and Dufo-López, 2016; Dufo-López *et al.*, 2017b) the additional fuel consumption due to the cold start of genset is considered. Here this additional fuel consumption is taking into account as 5 min consumption at full load (Bleijs, Nightingale and Infield, 1993) in case that the genset was off during the previous hour.

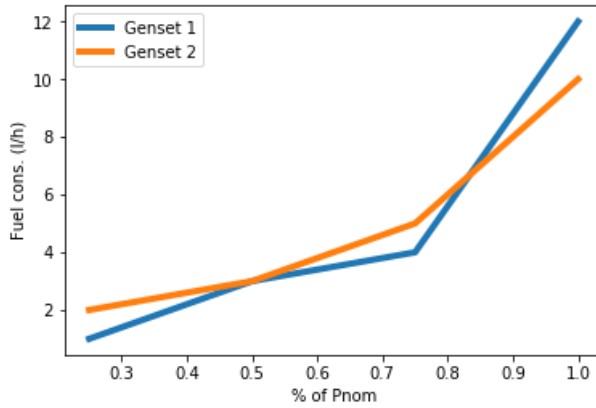


Figure 6: Linearized fuel consumption curve of a genset

The optimization problem (1) defined by (2) to (7) is implemented in the Python programming environment and solved by using MIDACO optimization solver (Schlueter *et al.*, 2013). The MIDACO solver is robust metaheuristic optimizer based on Ant Colony Optimization (ACO) technique belong to the class of population-based optimization method. The MIDACO solver can handle with mixed integer optimization problems have a high number of the objective functions, constraints and decision variables. It is capable to find the solution near to the global optimum.

3 Simulation example and results

The example of the optimization problem given above is used to apply the proposed optimization procedure. The given number of the gensets can be installed is limited on 20 gensets. The genset data are collected for real gensets by using data available on (*Diesel Generator Hardy Diesel*, no date; *Central main diesel*, no date). The 18 different gensets is considered for which data are given in Table 1. The fuel cost is set as 1.5 \$/l.

Table 1: Given genset data used in simulations

Genset type	Purchase price [\$]	Size [kW]	Fuel cons. at 100 % [l/h]	Fuel cons. at 75 % [l/h]	Fuel cons. at 50 % [l/h]	Fuel cons. at 25 % [l/h]
1	3500	5	1.25	1.10	0.88	0.77
2	3000	6.5	2.13	1.65	1.25	1.03
3	5500	8	3.15	2.35	1.69	1.43
4	7500	8	3.50	2.80	2.10	1.20
5	5600	10	3.45	2.79	2.02	1.69
6	8000	10	4.00	3.15	2.60	2.16
7	5000	10	4.00	2.70	2.00	1.30
8	7500	12	3.56	2.90	2.13	1.80
9	9000	12	4.90	3.90	2.90	1.70
10	8200	15	6.50	5.20	3.90	2.30
11	12000	20	7.30	5.60	4.10	2.80
12	11000	20	7.80	6.20	4.70	2.70
13	9200	21	6.64	5.17	3.59	3.23
14	8300	25	6.97	5.87	4.40	3.30
15	11300	30	9.40	7.20	5.70	3.40
16	15000	33	11.40	9.10	6.80	4.00
17	10500	40	10.27	7.70	5.87	4.77
18	13500	50	16.60	12.80	9.00	5.20

The daily load profile with hourly resolution given in Fig. 2 is used in the simulations. The problem of dimensionality, in this case, is $20+20 \times 24 = 500$.

The simulation results for two different load maximum are obtained:

- for 15 kW load maximum: $2 \times 5 \text{ kW} + 6.5 \text{ kW}$ (cost 188 \$/day)
- for 150 kW load maximum: $25 \text{ kW} + 40 \text{ kW} + 2 \times 50 \text{ kW}$ (cost 1069 \$/day)

The optimal hourly operation of the gensets for a maximal load of 15 kW is given in Fig. 2.

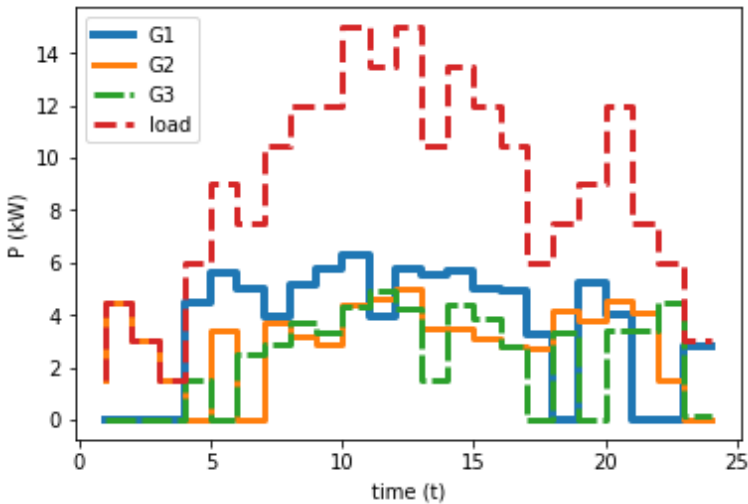


Figure 2: Load curve and optimized operation of the gensets

4 Conclusion

The optimization of the off-grid genset system in planning and operational phases is very complex to solve. The optimization problem is the mixed integer type with a high number of decision variables, discrete variables, nondifferentiable objective function what makes the problem hard to solve. The proposed procedure shows that this very complex optimization problem can be successfully solved by using the metaheuristic optimization technique. The use of such optimization methods makes able to consider simultaneously optimization of a number of the gensets in the planning phase and power control in the operational phase of the system.

References

- Askarzadeh, A. (2017) 'Distribution generation by photovoltaic and diesel generator systems: Energy management and size optimization by a new approach for a stand-alone application', *Energy*. Pergamon, 122, pp. 542–551. doi: 10.1016/J.ENERGY.2017.01.105.
- Bleijns, J. A. M., Nightingale, C. J. E. and Infield, D. G. (1993) 'Wear Implications of Intermittent Diesel Operation in Wind/Diesel Systems', *Wind Engineering*. Sage Publications, Ltd., 17, pp. 206–219. doi: 10.2307/43749514.
- Central main diesel* (no date). Available at: <https://www.centralmainediesel.com/order/printable/Kubota-GL11000->

- Lowboy-Diesel-Generator.asp?page=1019 (Accessed: 6 April 2018).
- Cristóbal-Monreal, I. R. and Dufo-López, R. (2016) 'Optimisation of photovoltaic–diesel–battery stand-alone systems minimising system weight', *Energy Conversion and Management*. Pergamon, 119, pp. 279–288. doi: 10.1016/J.ENCONMAN.2016.04.050.
- Diesel Generator Hardy Diesel* (no date). Available at: <http://www.hardydiesel.com/> (Accessed: 6 April 2018).
- Dufo-López, R., Fernández-Jiménez, L. A., Ramírez-Rosado, I. J., Artal-Sevil, J. S., Domínguez-Navarro, J. A. and Bernal-Agustín, J. L. (2017a) 'Daily operation optimisation of hybrid stand-alone system by model predictive control considering ageing model', *Energy Conversion and Management*. Pergamon, 134, pp. 167–177. doi: 10.1016/j.enconman.2016.12.036.
- Dufo-López, R., Fernández-Jiménez, L. A., Ramírez-Rosado, I. J., Artal-Sevil, J. S., Domínguez-Navarro, J. A. and Bernal-Agustín, J. L. (2017b) 'Daily operation optimisation of hybrid stand-alone system by model predictive control considering ageing model', *Energy Conversion and Management*. Pergamon, 134, pp. 167–177. doi: 10.1016/J.ENCONMAN.2016.12.036.
- Khazaei, P., Dabbaghjamesh, M., Kalantarzadeh, A. and Mousavi, H. (2016) 'Applying the modified TLBO algorithm to solve the unit commitment problem', in *2016 World Automation Congress (WAC)*. IEEE, pp. 1–6. doi: 10.1109/WAC.2016.7583026.
- Lorca, A. and Sun, X. A. (2017) 'Multistage Robust Unit Commitment With Dynamic Uncertainty Sets and Energy Storage', *IEEE Transactions on Power Systems*, 32(3), pp. 1678–1688. doi: 10.1109/TPWRS.2016.2593422.
- Matt, C. F., Vieira, L. S. R., Soares, G. F. W. and De Faria, L. P. T. (2005) '6th World Congress on Structural and Multidisciplinary Optimization Optimization of the Operation of Isolated Industrial Diesel Stations', in *6th World Congress on Structural and Multidisciplinary Optimization*. Rio de Janeiro. Available at: <http://citeseerx.ist.psu.edu/viewdoc/download?doi=10.1.1.60.3968&rep=rep1&type=pdf> (Accessed: 16 February 2018).
- Pappala, V. S. and Erlich, I. (2008) 'A new approach for solving the unit commitment problem by adaptive particle swarm optimization', in *2008 IEEE Power and Energy Society General Meeting - Conversion and Delivery of Electrical Energy in the 21st Century*. IEEE, pp. 1–6. doi: 10.1109/PES.2008.4596390.
- Conversion and Delivery of Electrical Energy in the 21st Century. IEEE, pp. 1–6. doi: 10.1109/PES.2008.4596390
- Schlueter, M., Erb, S. O., Gerdts, M., Kemble, S. and Rückmann, J.-J. (2013) 'MIDACO on MINLP space applications', *Advances in Space Research*. Pergamon, 51(7), pp. 1116–1131. doi: 10.1016/J.ASR.2012.11.006.
- Seme, S. et al. (2018) 'Optimal price of electricity of solar power plants and small hydro power plants – Technical and economical part of investments', *Energy*. Pergamon, 157, pp. 87–95. doi: 10.1016/J.ENERGY.2018.05.121.
- Sun, D., Zhang, L., Su, D. and Yuan, Y. (2017) 'Two-Stage Robust Security-Constrained Unit Commitment with Optimizable Interval of Uncertain Wind Power Output', *Mathematical Problems in Engineering*. Hindawi, 2017, pp. 1–11. doi: 10.1155/2017/9153297.
- Zheng, Q. P., Wang, J. and Liu, A. L. (2015) 'Stochastic Optimization for Unit Commitment—A Review', *IEEE Transactions on Power Systems*, 30(4), pp. 1913–1924. doi: 10.1109/TPWRS.2014.2355204.

ViMeLa Project: an Innovative Concept for Teaching Students in Mechatronics Using Virtual Reality

LIDIJA PETKOVSKA, GOGA CVETKOVSKI, MIHAIL DIGALOVSKI, MAJA CELESKA, DOROTA KAMIŃSKA, SLAWOMIR WIAK, ANNA FIRYCH-NOWACKA, MARCIN LEFIK, GRZEGORZ ZWOLIŃSKI, TOMASZ SAPIŃSKI, PAOLO DI BARBA, MARIA EVELINA MOGNASCHI, NAJMEH REZAEI, RAIN ERIC HAAMER & GHOLAMREZA ANBARJAFARI

Abstract Nowadays, traditional education and teaching methods, although with significantly improved teaching techniques, can not keep enough interest of the students that grew up with web, mobiles and tablets. Hence, in the 21st century higher education has moved from boards, paper and pens to the use of interactive technologies to help understanding and impart knowledge. The idea to create a Virtual Mechatronic Laboratory for an innovative concept of learning and teaching students in Mechatronics, came from the University of Technology in Lodz, with participation of University Ss. Cyril and Methodius in Skopje, University of Pavia and University of Tartu. The ViMeLa project is based on a blended-learning method using theory classes and virtual reality (VR) as experimentation tool. In the frame of the project ViMeLa, flexible solutions will be developed. Three scenarios are part of the project: design, construction and operating principles of electric motors; industrial automation solution for controlling the process of sorting packages in a warehouse; industrial and domestic waste sorting line with belt.

Keywords: • mechatronics • virtual reality • virtual laboratory • ViMeLa project • electrical machines • sensors and actuators •

CORRESPONDENCE ADDRESS: Lidija Petkovska PhD, Professor, Ss. Cyril and Methodius University, Faculty of Electrical Engineering and Information Technologies, Rugjer Bošković 18, 1000 Skopje, Macedonia, e-mail: lidijap@feit.ukim.edu.mk. Goga Cvetkovski, PhD, Professor, Ss. Cyril and Methodius University, Faculty of Electrical Engineering and Information technologies, Rugjer Bošković 18, P.O. Box574, 1000 Skopje, Macedonia, e-mail: gogacvet@feit.ukim.edu.mk. Mihail Digoalovski, Ss. Cyril and Methodius University, Faculty of Electrical Engineering and Information technologies, Rugjer Bošković 18, P.O. Box574, 1000 Skopje, Macedonia, e-mail: mihaild@feit.ukim.edu.mk. Maja Celeska, PhD, Teaching and Research Associate, Ss. Cyril and Methodius University, Faculty of Electrical Engineering and Information technologies, Rugjer Bošković 18, P.O. Box574, 1000 Skopje, Macedonia, e-mail: celeska@feit.ukim.ed.mk. Dorota

Kamińska, PhD, Lodz University of Technology, Institute of Mechatronics, Stefanowskiego 18/22 Str, 90-924 Lodz, Poland, e-mail: dorota.kaminska@p.lodz.pl. Slawomir Wiak, PhD, Professor, Lodz University of Technology, Institute of Mechatronics, Stefanowskiego 18/22 Str, 90-924 Lodz, Poland, e-mail: slawomir.wiak@p.lodz.pl. Anna Firychn-Nowacka, PhD, Lodz University of Technology, Institute of Mechatronics, Stefanowskiego 18/22 Str, 90-924 Lodz, Poland, e-mail: anna.firychn-nowacka@p.lodz.pl. Marcin Lefik, PhD, Lodz University of Technology, Institute of Mechatronics, Stefanowskiego 18/22 Str, 90-924 Lodz, Poland, e-mail: marcin.lefik@p.lodz.pl. Grzegorz Zwoliński, PhD, Lodz University of Technology, Institute of Mechatronics, Stefanowskiego 18/22 Str, 90-924 Lodz, Poland, e-mail: grzegorz.zwolinski@p.lodz.pl. Tomasz Sapiński, MSc, Lodz University of Technology, Institute of Mechatronics, Stefanowskiego 18/22 Str, 90-924 Lodz, Poland, e-mail: tomazs.sapinski@p.lodz.pl. Paolo Di Barba, PhD, Full Professor, University of Pavia, Department of Electrical, Computer and Biomedical Engineering, Via A. Ferrata 5, 271000 Pavia, Italy, e-mail: paolo.dibarba@unipv.it. Maria Evelina Mognaschi, University Researcher, University of Pavia, Department of Electrical, Computer and Biomedical Engineering, Via A. Ferrata 5, 271000 Pavia, Italy, e-mail: eve.mognaschi@unipv.it. Najmeh Rezaei, PhD Candidate, University of Pavia, Department of Electrical, Computer and Biomedical Engineering, Via A. Ferrata 5, 271000 Pavia, Italy, e-mail: najmeh.rezaei@unipv.it. Rain Eric Haamer, University of Tartu, Faculty of Science and Technology, Institute of Technology, iCV Lab, Vanemuise 46-208, 51014 Tartu, Estonia, e-mail: rain.haamer@ut.ee. Gholamreza Anbarjafari, PhD, Associate Professor, University of Tartu, Faculty of Science and Technology, Institute of Technology, iCV Lab, Vanemuise 46-208, 51014 Tartu, Estonia, e-mail: gholamreza.anbarjafari@ut.ee.

1 Introduction

In the 21st century, higher education has moved from books and pens to the use of interactive technologies to help students understanding and impart knowledge. Traditional education methods, although with significantly improved teaching techniques, can't keep enough interest of the students that grew up with *www*, mobiles and tablets. Especially sensitive to these issues are students in engineering, computers and, in particular, in mechatronics.

Modern information technology is rapidly being adopted in Mechatronics Engineering education as a tool for enriching the practical experience of the students. The practical training is a vital part of Mechatronics Engineering education (Popescu *et al.*, 2015). However, the high cost needed to implement laboratory experiments (for educational purposes) led to development of virtual facilities where physical systems can be virtually controlled via the *Virtual Reality* (VR) simulations. Multimedia and VR technologies offer great potential for presenting theory and laboratory experiments in an enhancing and interesting, but in an economical, way.

2 Teaching and learning Mechatronics

Mechatronics is a synergy and an interaction of mechanical, electrical and computer systems as seen in Figure 1. Hence, it is an interactive combination of mechanical engineering, electronic control and computer technology, with the aim of achieving an ideal balance between mechanical structure and its overall control and performance. Subsystems of mechatronics are electromechanics, robotics and control. The multidisciplinary concepts that merge in mechatronic engineering require an academic education that provides an appropriate balance between research and development capabilities, as well as skilled engineers and technicians trained for manufacturing, implementation and service provision in their professional areas (Dieter, 2005).

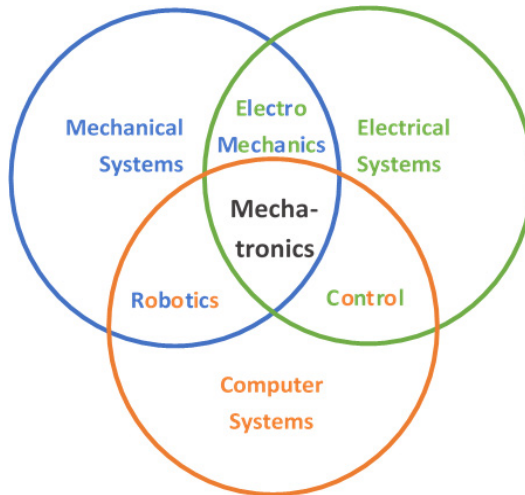


Figure 1: Structure and key elements of mechatronics

Currently, mechatronics classes are divided into two parts: the theoretical lectures and laboratory courses with experiments following the "learning by doing" model. In this practical laboratory part, although the students get limited access to the machines, provides a deeper understanding of theoretical lessons. However, expensive laboratory equipment and limited time for practical training, do not provide sufficient educational platforms. Moreover, due to the fact that each laboratory is supervised by technical staff, as well as that students are divided into small(er) groups, there is a limited time window for each type of exercise to be conducted (Petrović *et al.*, 2017). In some cases, students conduct computer based simulations and learn how mechatronic systems and devices operate in reality. It should be underlined that it may seem abstract and unclear for students, and does not fully reflect the physical phenomena of particular processes.

The described drawbacks of mechatronic study are greatly improved when classroom teaching is supported by *virtual reality tools*. Recently, *VR technology* is expected to assist teaching and learning of mechatronics in several ways. It allows students to visualize abstract concepts, to observe events at micro or macro scales, to visit various environments and interact with events and devices that usually due to distance, time, or safety factor are unavailable. Activities supported by this modern technology, promote current educational thinking that students and graduates are better able to master, retain, and generalize new knowledge when they are actively involved in constructing that knowledge in a hand-on learning environment. *Virtual laboratories* are inside this group of solutions, as

Virtual Reality tools have already demonstrated the importance and effectiveness of practical experiences.

3 Virtual vs Real world

Virtual reality has existed in various forms as far back as the 1960s when the first digital flight simulators were developed and employed by the world's major airlines and air forces. These early simulators used a camera and projector to display the pilot's view and often employed motion to improve the realism and immersion of the simulation.

As technology developed, "*virtual reality*" became the phrase to represent devices that create an immersive, interactive environment with visual realism. The least immersive type of virtual reality is considered Desktop VR, in which a 3D virtual world is shown on a standard computer monitor. Desktop VR emerged during the early 2000s because personal computers became powerful enough to simulate and render 3D virtual worlds.

As a matter of fact, virtual reality simulation is a use of 3D objects and environments to create immersive and engaging learning experiences. The principle of virtual reality e-learning is to impart, practice and check the user's knowledge using interactive scenarios and environments to reflect real-life situations. Using 3D technology, which is referred to as *real world environments*, it is created any environment or situation. Thus, virtual reality simulation provides a truly interactive experience. Users can move freely around the environment, interact with objects, carry out tests, make decisions and mistakes, until they have mastered the subject.

4 ViMeLa Project

The idea to create a *Virtual Mechatronic Laboratory* for an innovative teaching and learning of Mechatronics, came from the University of Technology in Lodz, Poland, supported by the University Ss. Cyril and Methodius in Skopje, University of Pavia and University of Tartu. The *ViMeLa* project is based on a blended-learning method using theory classes and *virtual reality* – VR as experimentation tool. Blended learning here is a hybrid method, which combines

digital media (through VR) with traditional classroom methods, which is more effective than purely face-to-face classes.

<http://vimela.p.lodz.pl/>



Virtual
Mechatronic
Laboratory

To enable an effective learning and teaching in Mechatronics at a reasonable/low cost, in the frame of the project ViMeLa, flexible solutions will be developed. Three scenarios are parts of the project:

- Construction, operating principles and performance of electric motors;
- Sorting line with pneumatic components;
- Waste sorting line with belt.

The ability to easily change the virtual world opens new possibilities in testing and design. For instance, digital prototypes can be copied, modified, and tested without the expense and time required to build and test physical prototypes. This allows the students to refine and test their design quickly and inexpensively before creating a physical objects' version.

4.1 The concept

Over the past two decades, numerous studies have shown the *strengths of virtual reality* use in the classroom. One of the most significant strengths is that they change the role of the teacher from a deliverer of knowledge into a facilitator who helps the students to explore and learn. Furthermore, virtual reality can help students learn abstract concepts because they can experience and visualize these concepts in the virtual environment.

The innovation of proposed approach lies in developing and disseminating an original and novel mechatronic learning system, based on VR technology. It is created an interactive computer generated environment – *a factory* in which the students can watch, enter and easily move through, with possibility to dynamical changes of scenarios. VR simulates user's physical presence in an artificially

generated world and allows to interact with the environment, through three scenarios, created for the project objectives.



Figure 2: Factory hall created in ViMeLa using VR

4.2 Project goals

- *For mechatronics graduates:* ▪ learning complex operation principles of advanced mechatronic systems; ▪ principles and electric machine structures; ▪ real life scenarios in the field of mechatronics; ▪ handling and avoiding states of emergency; ▪ controllers and sensors operating; ▪ calibration of physical quantities characterizing the work of mechatronic systems and their components; ▪ gaining experience from virtual factory.
- *For universities and academics:* ▪ access to simulations of state-of-the-art equipment, which is rarely available or is too expensive; ▪ more accessible laboratories due to reduced need of supervision; ▪ attractive teaching tool tailored to fit the university curricula in mechatronics.
- *For business perspective:* ▪ graduates with higher and solid qualifications; ▪ less need for training for new employees; ▪ possibility to prepare the students for future work i.e. by providing specific machinery specifications to be put in the VR application.

5 Conclusions

In today's digital world, finding new ways to engage students is more difficult ever. When home technologies such as mobile phones, tablets and games consoles are highly advanced, finding educational engagement with technology in the classroom can be even harder. Hence, virtual reality has become an important and useful tool in engineering education. Virtual reality use in teaching mechatronics provides a unique opportunity to create a truly exciting and engaging learning experience for students. At the same time the traditional role of teachers as dispensers of knowledge, in today's digital world, will be transformed to a role of effective facilitators of knowledge. In the paper are presented main features of ViMeLa project, which intends to introduce an innovative concept of teaching mechatronics using virtual reality and to bring industry into classroom. *Entering* in an environment of a virtual factory, students will learn basics of mechatronics, experiencing three scenarios created in the frame of the project.

Acknowledgments

This publication has been co-funded by the Erasmus+ Programme of the European Union (Strategic Partnership, ViMeLa, 2017-1-PL01-KA203-038675). This publication reflects the views only of the authors, the National Agency and European Commission cannot be held responsible for any use, which may be made of the information contained therein.

References

- Dieter (editor) M. (2005). MARVEL – Mechatronics Training in Real and Virtual Environments: Concepts, Practices, and Recommendations, *A Leonardo da Vinci Pilot Project*, Bremen, pp. 99.
- Petrović V.M., Nikolić B., Jovanović K., Potkonjak V. (2017). Development of Virtual Laboratory for Mechatronic Systems. In: Rodić A., Borangiu T. (eds) *Advances in Robot Design and Intelligent Control. RAAD 2016. Advances in Intelligent Systems and Computing*, Vol. 540, Springer, Cham.
- Popescu, D., Stoian V., Petrisor A., Popescu R. (2015). Virtual Engineering for Mechatronics Laboratory, *Proceedings of 6th International Conference "Computational Mechanics and Virtual Engineering" – COMEC'2015*, pp. 316-322, Braşov, Romania.

Virtual Reality Sorting Line: a Scenario for the ViMeLa Project

PAOLO DI BARBA, MARIA EVELINA MOGNASCHI, NAJMEH REZAEI,
ANNA FIRYCH-NOWACKA, DOROTA KAMIŃSKA, MARCIN LEFIK,
TOMASZ SAPIŃSKI, SLAWOMIR WIAK, GRZEGORZ ZWOLIŃSKI, GOGA
CVETKOVSKI, LIDIJA PETKOVSKA, RAIN ERIC HAAMER
& GHOLAMREZA ANBARJAFARI

Abstract The Virtual Mechatronics Laboratory (ViMeLa) project is a biennial European project, started on November 2017 and participated by the Lodz University of Technology (coordinator), University of Pavia, Ss. Cyril and Methodius University of Skopje and University of Tartu, financed under the frame of the Erasmus+. The project aims to build three virtual laboratory scenarios in mechatronics, devoted to students. In this paper, Scenario 3 of the virtual laboratory, a waste sorting line with belt, is described. In particular, the sensors and actuators belonging to the sorting line are under study: the relevant results obtained by means of finite-element simulations are shown.

Keywords: • numerical field models • virtual reality • virtual laboratory • sensors and actuators • finite element method •

CORRESPONDENCE ADDRESS: Paolo Di Barba, PhD, Full Professor, University of Pavia, Department of Electrical, Computer and Biomedical Engineering, Via A. Ferrata 5, 271000 Pavia, Italy, e-mail: paolo.dibarba@unipv.it. Maria Evelina Mognaschi, University Researcher, University of Pavia, Department of Electrical, Computer and Biomedical Engineering, Via A. Ferrata 5, 271000 Pavia, Italy, e-mail: eve.mognaschi@unipv.it. Najmeh Rezaei, PhD Candidate, University of Pavia, Department of Electrical, Computer and Biomedical Engineering, Via A. Ferrata 5, 271000 Pavia, Italy, e-mail: najmeh.rezaei@unipv.it. Anna Firychn-Nowacka, PhD, Lodz University of Technology, Institute of Mechatronics, Stefanowskiego 18/22 Str, 90-924 Lodz, Poland, e-mail: anna.firychn-nowacka@p.lodz.pl. Dorota Kamińska, PhD, Lodz University of Technology, Institute of Mechatronics, Stefanowskiego 18/22 Str, 90-924 Lodz, Poland, e-mail: dorota.kaminska@p.lodz.pl. Marcin Lefik, PhD, Lodz University of Technology, Institute of Mechatronics, Stefanowskiego 18/22 Str, 90-924 Lodz, Poland, e-mail: marcin.lefik@p.lodz.pl. Slawomir Wiak, PhD, Professor, Lodz University of Technology, Institute of Mechatronics, Stefanowskiego 18/22 Str, 90-924 Lodz, Poland, e-mail: slawomir.wiak@p.lodz.pl. Tomasz Sapiński, MSc, Lodz University of Technology, Institute of Mechatronics, Stefanowskiego 18/22 Str, 90-924 Lodz, Poland, e-mail: tomazs.sapinski@p.lodz.pl. Grzegorz Zwoliński, PhD, Lodz

University of Technology, Institute of Mechatronics, Stefanowskiego 18/22 Str, 90-924 Lodz, Poland, e-mail: grzegorz.zwolinski@p.lodz.pl. Goga Cvetkovski, PhD, Professor, Ss. Cyril and Methodius University, Faculty of Electrical Engineering and Information technologies, Rugier Bošković 18, P.O. Box574, 1000 Skopje, Macedonia, e-mail: gogacvet@feit.ukim.edu.mk. Lidija Petkovska PhD, Professor, Ss. Cyril and Methodius University, Faculty of Electrical Engineering and Information Technologies, Rugier Bošković 18, 1000 Skopje, Macedonia, e-mail: lidijap@feit.ukim.edu.mk. Rain Eric Haamer, University of Tartu, Faculty of Science and Technology, Institute of Technology, iCV Lab, Vanemuise 46-208, 51014 Tartu, Estonia, e-mail: rain.haamer@ut.ee. Gholamreza Anbarjafari, PhD, Associate Professor, University of Tartu, Faculty of Science and Technology, Institute of Technology, iCV Lab, Vanemuise 46-208, 51014 Tartu, Estonia, e-mail: gholamreza.anbarjafari@ut.ee.

1 The ViMeLa project

In the virtual mechatronics laboratory, three scenarios are available to the user: 1) construction and operating principles of electric motors, 2) sorting line with pneumatic components, 3) waste sorting line with belt. In the paper, the attention is drawn on the waste sorting line with belt.

2 Waste sorting line: general functioning

In this scenario the students are going to become familiar with recycling process which mainly includes the sorting of waste. There are two sub categories of sorting, namely domestic waste and industrial waste, therefore, there should be two scenarios in the Virtual Reality (VR) for students to choose from: domestic waste and industrial waste sorting, respectively.

A menu button gives the students the opportunity to choose which scenario they want to work on:

- Domestic waste.
- Industrial waste.

In the domestic waste sorting (scenario A), there are three categories of material:

- Organic waste;
- Glass (bottles);
- Plastic (food packaging).

In the industrial waste sorting (scenario B), there are three types of material:

- Ferromagnetic and non-conductive (such as ferrite in motor core and cable shielding);
- Conductive and non-ferromagnetic (such as aluminium and copper of motor bar and coils);
- Plastic (parts of the motors in plastic).

In the first step, the user needs to setup the sorting line.

The scenario includes a shelf with sensors, actuators, five coloured bins and connecting cables. In particular, one magnetic actuator and two different kind of sensors (an inductive one and a capacitive one) can be used. The user can set their properties like e.g. frequency and magnitude of current or voltage to further optimise the sorting line.

The user should pick up these sensors and put it in the predefined position on the sorting belt (each spaced by 20 cm). Then, each sensor must be connected by cable to one actuator. Finally, one coloured bin must be put in front of each actuator. To optimize the exercise outcome, the user can also put one bin at the end of the belt. A button on the cable allows the user to set the delay time for each actuator. At this stage, after a rudimentary sorting line has been constructed, the user is presented by a red button.

The red button allows the user to start or stop/pause the exercise. By first clicking on the button, the exercise starts, making the belt run with a fixed speed and dispensing unsorted waste out of a dispenser. A single object of trash is pushed at a time on the belt in a random position (e.g. it can be in the middle of the belt or on the border of the belt), thus affecting the sensor functioning.

In case of any hazards or when there is the need for changing the position of an object (e.g. sensors or cables), the user needs to push the stop/pause button. For the sake of an example, a possible configuration for each Scenario is shown in Fig. 1.

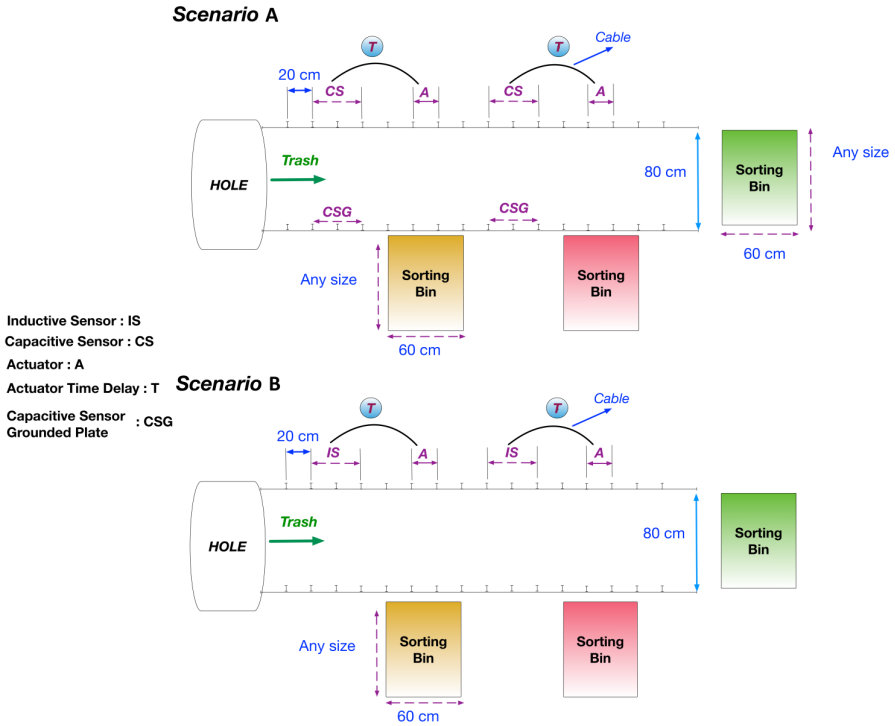


Figure 1: Example of sorting line configuration for each scenario.

There is no time limit for setting up the sorting line, while the user can only run the sorting line for 2 minutes. At the end of the two minutes, based on the number of correctly sorted pieces of material, the user will get a score e.g. 80%.

3 FE characterization of sensors and actuator

In order to create the Scenario, the characterization of the sensors and actuators in terms of input-output transfer function is modelled by means of the Finite Element Models (FEMs). The simulations are implemented with the Mentor-Infolytica software.

3.1 The inductive sensor

The inductive sensor is able to detect conductive and ferromagnetic objects. The sensor is made of an iron-cored coil and a conducting screen (Di Barba, 2009). The coil is supplied by AC voltage, with frequency ranging from 50 Hz to 100 kHz. When a conductive objective is in front of the sensor, the impedance of the coil becomes lower. In turn, when a ferromagnetic objective is in front of the sensor, the impedance of the coil becomes higher. The shape of the inductive sensor is shown in Fig. 2a, while in Fig. 2b the flux lines obtained by means of FEM are represented.

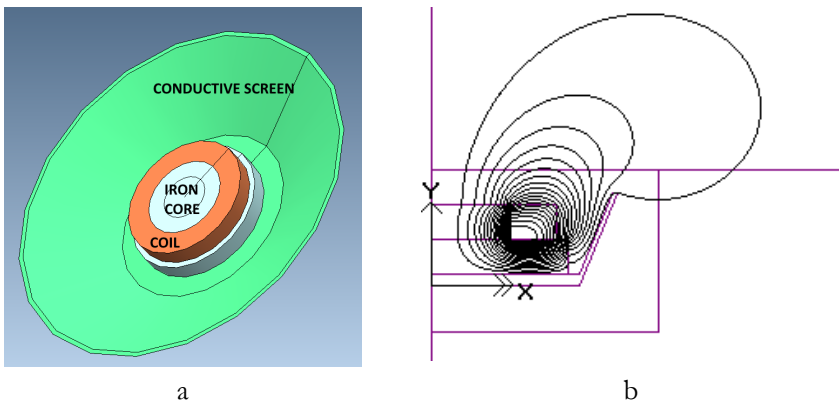


Figure 2: Inductive sensor - 3D geometry (a), magnetic flux lines (b).

3.2 The capacitive sensor

The capacitive sensor is able to sense objects with different dielectric permittivity. The capacitive sensor consists of two electrode plates: one is grounded, the other is fed by an AC voltage. The piece of waste to be detected and sorted should pass through these plates. When a dielectric objective is in the middle of the plates, the capacitance of the sensor becomes higher. The capacitive sensor has the aspect shown in Fig. 3a and the relevant field map is shown in Fig. 3b.

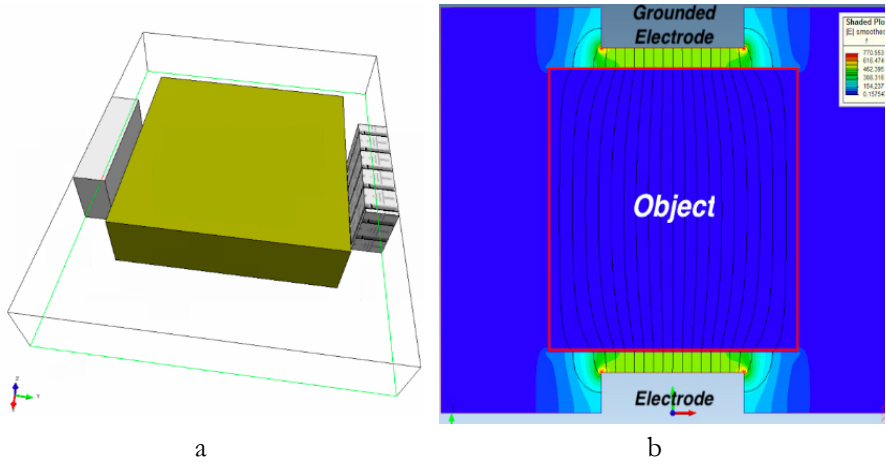


Figure 3: Capacitive sensor - 3D geometry (a), electric field map (b).

3.3 The electromagnetic actuator

The actuator used in the sorting line with belt is an electromagnetic actuator. It is composed of a magnetic circuit and a coil. When the current flows in the coil, the movable part of the actuator (in red in Fig.4a) is pulled inside the actuator (movement bottom-up in Fig. 4a) and hence the anchor (in green in Fig. 4a) pushes the piece of waste. In contrast, when the current is off, the movable part exits from the actuator (movement from up to down in Fig. 4a) and the anchor is retained inside it. The current pulse exhibits a trapezoidal shape and the user can set its rise time, duration, decay time and amplitude.

The cross-section of the 3D model of the cylindrical electromagnet along with the magnetic flux lines are shown in Fig. 4a and 4b, respectively.

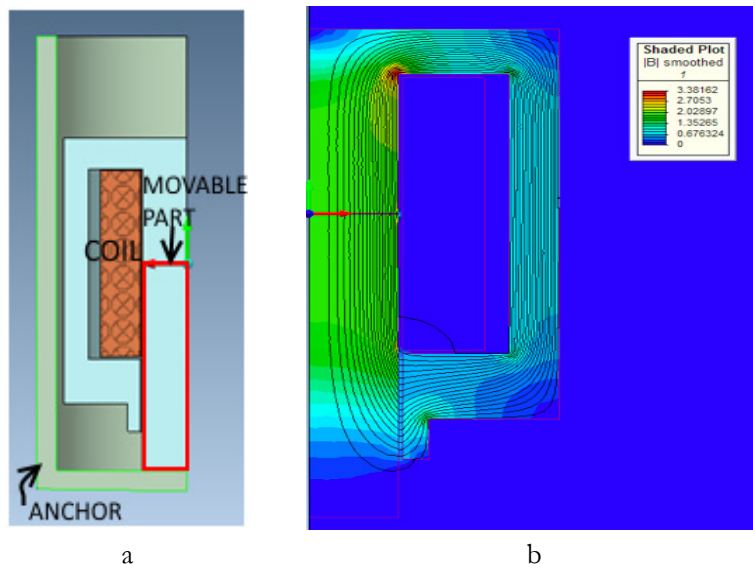


Figure 4: Electromagnetic actuator - cross-section (a), magnetic flux lines (b).

4 Conclusion

The behaviour of sensors and actuators composing the sorting line has been characterized by means of field models. In turn, this makes it possible to identify the transfer function of each device, eventually helping the computer engineers in programming the sorting line within the virtual mechatronics laboratory.

Acknowledgments

This publication has been co-funded by the Erasmus+ Programme of the European Union (Strategic Partnership, ViMeLa, 2017-1-PL01-KA203-038675). This publication reflects the views only of the authors, the National Agency and European Commission cannot be held responsible for any use, which may be made of the information contained therein.

References

Di Barba, P., Mognaschi, M.E., Palka, R., Savini, A. (2009). Optimization of the MIT field exciter by a multiobjective design. *IEEE Trans. Magnetics*, 45(3), 1530-1533.

Virtual Reality as a Tool for Electrical Machines Assembling and Testing

GOGA CVETKOVSKI, LIDIJA PETKOVSKA, MIHAIL DIGALOVSKI, MAJA CELESKA, DOROTA KAMINSKA, ANNA FIRYCH-NOWACKA, SLAWOMIR WIAK, TOMASZ SAPIŃSKI, MARCIN LEFIK, GRZEGORZ ZWOLIŃSKI, PAOLO DI BARBA, MARIA EVELINA MOGNASCHI, RAIN ERIC HAAMER, & GHOLAMREZA ANBARJAFARI

Abstract This paper deals with an implementation of virtual reality tools for teaching and training students in mechatronics. The software for this purpose is consisted of three scenarios. The first scenario is about teaching and training students regarding the process of assembling and testing electrical machines. In this paper the concept of this scenario will be presented, as well as some of the main features of it. Scenario 1 is consisted of two exercise parts: Assembling of different types of electric motors and investigation of operating principles of permanent magnet synchronous motor. The study presented in this paper is part of an Erasmus+ Project under the acronym ViMeLa that stand for Virtual Mechatronics Laboratory. The purpose of this project is to improve the learning concepts in the subject area of mechatronics.

Keywords: • virtual reality • electrical machines • assembling of electrical machines • testing of electrical machines • permanent magnet synchronous motor •

CORRESPONDENCE ADDRESS: Goga Cvetkovski, PhD, Professor, Ss. Cyril and Methodius University, Faculty of Electrical Engineering and Information technologies, Rugjer Bošković 18, P.O. Box574, 1000 Skopje, Macedonia, e-mail: gogacvet@feit.ukim.edu.mk. Lidija Petkovska PhD, Professor, Ss. Cyril and Methodius University, Faculty of Electrical Engineering and Information Technologies, Rugjer Bošković 18, 1000 Skopje, Macedonia, e-mail: lidijap@feit.ukim.edu.mk. Mihail Digalovski, Ss. Cyril and Methodius University, Faculty of Electrical Engineering and Information technologies, Rugjer Bošković 18, P.O. Box574, 1000 Skopje, Macedonia, e-mail: mihaild@feit.ukim.edu.mk. Maja Celeska, PhD, Teaching and Research Associate, Ss. Cyril and Methodius University, Faculty of Electrical Engineering and Information technologies, Rugjer Bošković 18, P.O. Box574, 1000 Skopje, Macedonia, e-mail: celeska@feit.ukim.edu.mk. Dorota Kamińska, PhD, Lodz University of Technology, Institute of Mechatronics, Stefanowskiego 18/22 Str, 90-924 Lodz, Poland, e-mail: dorota.kaminska@p.lodz.pl. Anna Firychnowacka, PhD, Lodz

University of Technology, Institute of Mechatronics, Stefanowskiego 18/22 Str, 90-924 Lodz, Poland, e-mail: anna.firych-nowacka@p.lodz.pl. Slawomir Wiak, PhD, Professor, Lodz University of Technology, Institute of Mechatronics, Stefanowskiego 18/22 Str, 90-924 Lodz, Poland, e-mail: slawomir.wiak@p.lodz.pl. Tomasz Sapiński, MSc, Lodz University of Technology, Institute of Mechatronics, Stefanowskiego 18/22 Str, 90-924 Lodz, Poland, e-mail: tomazs.sapinski@p.lodz.pl. Marcin Lefik, PhD, Lodz University of Technology, Institute of Mechatronics, Stefanowskiego 18/22 Str, 90-924 Lodz, Poland, e-mail: marcin.lefik@p.lodz.pl. Grzegorz Zwoliński, PhD, Lodz University of Technology, Institute of Mechatronics, Stefanowskiego 18/22 Str, 90-924 Lodz, Poland, e-mail: grzegorz.zwolinski@p.lodz.pl. Paolo Di Barba, PhD, Full Professor, University of Pavia, Department of Electrical, Computer and Biomedical Engineering, Via A. Ferrata 5, 271000 Pavia, Italy, e-mail: paolo.dibarba@unipv.it. Maria Evelina Mognaschi, University Researcher, University of Pavia, Department of Electrical, Computer and Biomedical Engineering, Via A. Ferrata 5, 271000 Pavia, Italy, e-mail: eve.mognaschi@unipv.it. Rain Eric Haamer, University of Tartu, Faculty of Science and Technology, Institute of Technology, iCV Lab, Vanemuise 46-208, 51014 Tartu, Estonia, e-mail: rain.haamer@ut.ee. Gholamreza Anbarjafari, PhD, Associate Professor, University of Tartu, Faculty of Science and Technology, Institute of Technology, iCV Lab, Vanemuise 46-208, 51014 Tartu, Estonia, e-mail: gholamreza.anbarjafari@ut.ee.

1 Introduction

In modern technical education and training, an important role is played by learning concepts which closely link learning and work, and which develop key skills that equip employees to cope with open work assignments and the rapid pace of change. The need for work-related learning based on the blending of theoretical learning and learning in practical tasks, experimentation and field work is obvious. Accordingly, there is a growing need for innovative concepts, capable of supporting the necessary education and training platforms. eLearning systems and virtual learning sessions (online labs, simulations) extending to real labs or to the workplace can contribute significantly to a successful outcome of this learning process (Piovesan, S. D. et al, 2012). The ViMeLa project (Virtual Mechatronics Laboratory) is designed to improve the learning concepts that serve these actual needs in the subject area of mechatronics.

Learning in a 3D environment allows greater interaction with contents in a unique way as students perceive it as being really there. Simulations are being designed, a combination of real-world environment with the information supplied by devices, where measurements can be replicated and data analyzed. This study presents a virtual scenario of an assembling and testing of mechatronic devices (electric motors) in virtual laboratory environment. Electrical Engineering courses aim to train students to succeed in meeting the challenges within competitive and ever-changing professional contexts. In order to prepare undergraduate students for ongoing success, the courses must provide effective training in the application and development of practices, typically implemented in large projects and organizations. Developing high quality engineering course units is definitely a challenging task.

In this paper the authors present the basic concepts of scenario 1 in the Virtual reality platform that is going to be realized in the framework of the ViMeLa project. Scenario 1 is consisted of two exercise parts: Assembling of different types of electric motors and investigation of operating principles of permanent magnet synchronous motor.

2 Assembling of different types of electric motors

In this part of the VR application the user will get familiar with the different types of electric motors, as well as their construction. The 3D models that are going to be designed will be based on authentic devices, according to their technical documentation. The different 3D parts for various electric motors are going to be placed on a shelf. The user will have a task to assemble a certain type of electric motor based on its selection done at the beginning of the exercise. This means that the user will have to select from the shelf the appropriate 3D parts (stator, rotor with shaft, permanent magnets, housing, brushes, rotor bars etc.) in order to realize the task. For a certain type of motor there will be only one set of parts with no possibility to alter the type of winding or skewing angle. After the assembling process is finished, using the VR tools, the assembled motor will be checked and a mark will be given. If the electric motor is not properly assembled the user will have two more attempts to properly assemble the motor. For the time being 3D parts are made for the permanent magnet synchronous motor, and we also plan to make for induction motor, switched reluctance motor, DC commutator motor, permanent magnet DC commutator motor and permanent magnet generator. In Figure 1 a presentation of the parts and the assembled permanent magnet synchronous motor is shown. In addition to this in Figure 2 a presentation of an induction motor parts and assembled motor is shown.

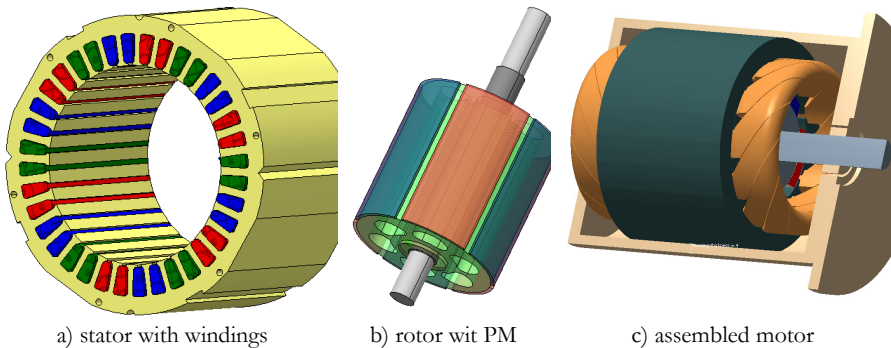


Figure 1: Permanent magnet synchronous motor assembling parts

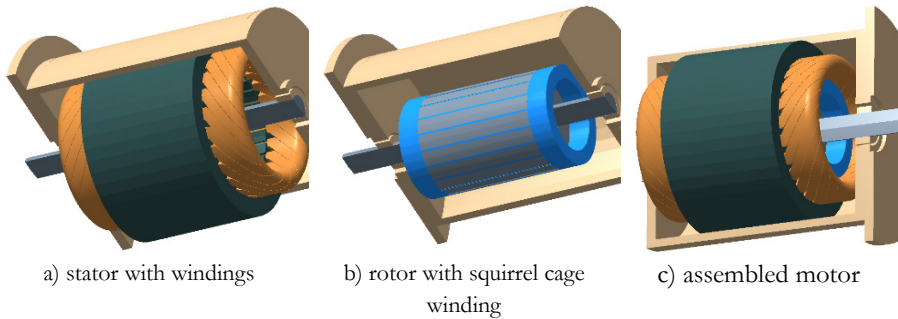


Figure 2: Induction motor assembling parts

3 Investigation of operating principles of PM synchronous motor

In this part of the VR application the user will be able to perform various investigations of the working principles of a pre-defined model of permanent magnet synchronous motor. This means that the rating and the motor parameters will be also predefined, with no possibility to be altered. In the background of the VR environment a proper mathematical model will be defined that will simulate the operating principles and performance characteristics of the investigated motor. First of all, the user will have to put the tested motor on the testing bench and do the appropriate connections with the power supply, control and the adequate instrumentation. After all the connections are realized the user will get an information if the wiring is properly done or not. Here the user will also have two more attempts to realize the correct connections. After the connections are properly done the user can perform the investigation of the operating principles of the permanent magnet synchronous motor at different working conditions (voltage and frequency) and loads. The measured values such as voltage, frequency, input current, input power, speed and torque are going to be presented on a display. The VR testing environment will enable the user to also perform even a more hazardous investigation of the motor, such as an overload of the motor, for which the user will get a certain signalization of the problematic working condition. A proposed view of this testing bench is presented in Figure 3.



Figure 3: VR testing bench

4 Conclusion

The construction of an electric motor especially selecting the adequate parts for a certain predefined motor type, as well as the investigation of the operating conditions and working characteristics of electric motors in a virtual laboratory environment is going to add a new dimension to the learning and practicing process of electric motors in virtual mechatronics laboratory.

Acknowledgment



This project has been co-funded by the Erasmus+ Programme of the European Union (Strategic Partnership [ViMeLa Project, 2017-1-PL01-KA203-038675]). This publication reflects the views only of the authors, the National Agency and European Commission cannot be held responsible for any use, which may be made of the information contained therein.

References

Piovesan, S. D. Passerino, L. M. Pereira, A. S. (2012) Virtual Reality as a Tool in the Education: *LADIS International Conference on Cognition and Exploratory Learning in Digital Age (CELDA 2012)*, 295-298, ISBN: 978-989-8533-12-8 © 2012 IADIS.

Efficient Full-Wave Electromagnetic Analysis of Arbitrary Grounding Systems

BLAGOJA MARKOVSKI, LEONID GRCEV, VESNA ARNAUTOVSKI-TOSEVA,
JASMINA ANGELEVSKA & ANDRIJANA KUHAR

Abstract This paper presents efficient procedure approach for full-wave modeling of grounding systems with arbitrary shape. First the electric field integral equations are cast in form that is more suitable for grounding analysis, since it provides exact solutions from dc to frequencies in the MHz range and improved convergence and behavior of the Sommerfeld integrals. Then numerical evaluation of the new form of Sommerfeld integrals is substituted by bivariate cubic interpolation of the solutions from the pre-computed interpolation grid. This procedure provides substantial improvement of efficiency of the full-wave electromagnetic analysis of grounding systems, while introducing a negligible error in the results. Accuracy and efficiency of the presented procedure are validated by results comparison with full-wave model that utilizes direct numerical integration of Sommerfeld integrals.

Keywords: • grounding • interpolation • lightning • modeling • Sommerfeld integrals •

CORRESPONDENCE ADDRESS: Blagoja Markovski, Ss Cyril and Methodius University in Skopje, Faculty of Electrical Engineering and Information Technologies, Rugjer Boskovic 18, P.O. box 574, Skopje, Republic of Macedonia, e-mail: bmarkovski@feit.ukim.edu.mk. Leonid Grcev, Ss Cyril and Methodius University in Skopje, Faculty of Electrical Engineering and Information Technologies, Rugjer Boskovic 18, P.O. box 574, Skopje, Republic of Macedonia, e-mail: lgrcev@feit.ukim.edu.mk. Vesna Arnavovski-Toseva, Ss Cyril and Methodius University in Skopje, Faculty of Electrical Engineering and Information Technologies, Rugjer Boskovic 18, P.O. box 574, Skopje, Republic of Macedonia, e-mail: atvesna@feit.ukim.edu.mk. Jasmina Angelevska, Ss Cyril and Methodius University in Skopje, Faculty of Electrical Engineering and Information Technologies, Rugjer Boskovic 18, P.O. box 574, Skopje, Republic of Macedonia, e-mail: jasmina.angelevska@hotmail.com. Andrijana Kuhar, Ss Cyril and Methodius University in Skopje, Faculty of Electrical Engineering and Information Technologies, Rugjer Boskovic 18, P.O. box 574, Skopje, Republic of Macedonia, e-mail: kuhar@feit.ukim.edu.mk.

1 Introduction

The electromagnetic model preferred for modeling of arbitrary large and complex grounding structures (Grcev, 1990), is based on the mixed potential integral equation (MPIE) representation of electric field (Michalski, 1985), and the method of moments (MoM) (Harrington, 1967). One difficulty in implementation of the mathematically exact solution for the electric field for semi-infinite conducting medium in practical problems is the numerical evaluation of singular, oscillatory and slow converging Sommerfeld integrals, which is numerically unstable and extremely time consuming procedure. Another common problem in the application of antenna theory based methods for analysis of buried conductors is that they may not provide exact solutions for low frequencies approaching 0 Hz, either due to improper treatment of the images of currents in conductors (Arnautovski-Toseva, 2016) or due to numerical instabilities at such frequencies.

This paper presents efficient procedure for full-wave modeling of grounding systems with arbitrary shape. First the electric field integral equations are cast in form that is more suitable for grounding analysis, since it provides exact solutions from dc to frequencies in the MHz range and improved behavior of the Sommerfeld integrals. Then numerical evaluation of the new form of Sommerfeld integrals is substituted by bivariate cubic interpolation from pre-computed solutions in interpolation grid. This procedure provides substantial improvement of efficiency of the full-wave electromagnetic analysis of grounding systems, while introducing a negligible error in the results. Accuracy and efficiency of the presented procedure are validated by comparison with full-wave model that utilizes direct numerical integration.

2 Analysis of behaviour of different forms of Green's functions

In MPIE formulation, the scattered electric field vector $\vec{E}^s(\vec{r})$ due to longitudinal current $I(\vec{r}')$ along the axis of the source segment ℓ' can be expressed as:

$$\vec{E}^s(\vec{r}) = -\frac{j\omega\mu_0}{4\pi} \int_{\ell'} \vec{G}_A(\vec{r}, \vec{r}') I_n(\vec{r}') d\vec{\ell}' + \frac{1}{4\pi\sigma_1} \nabla \int_{\ell'} G_\Phi(\vec{r}, \vec{r}') \nabla' I(\vec{r}') d\ell' \quad (1)$$

Here, $\bar{\bar{G}}_A$ is a dyadic Green's function of the magnetic vector potential and G_ϕ is a Green's function of electric scalar potential. Different formulations of Green's functions for magnetic vector potentials are available (Michalski, 1990). Here we adopt formulation B for source and evaluation points in semi-infinite conducting medium, as one possible choice for analysis of arbitrary structures. The dyadic Green's function for magnetic vector potential can be expressed by contributions of horizontal (HED) and vertical electric dipole (VED):

$$\bar{\bar{G}}_A = \hat{x}\hat{x}'G_A^{xx} + \hat{y}\hat{y}'G_A^{yy} + (\hat{x}\hat{y}' + \hat{y}\hat{x}')G_A^{xy} + \hat{z}\hat{z}'G_A^{zz} \quad (2)$$

where \hat{x}' , \hat{y}' and \hat{z}' are direction cosines of source dipole, and \hat{x} , \hat{y} and \hat{z} are direction cosines of calculated magnetic vector potential in local coordinate system shown in Fig. 1.

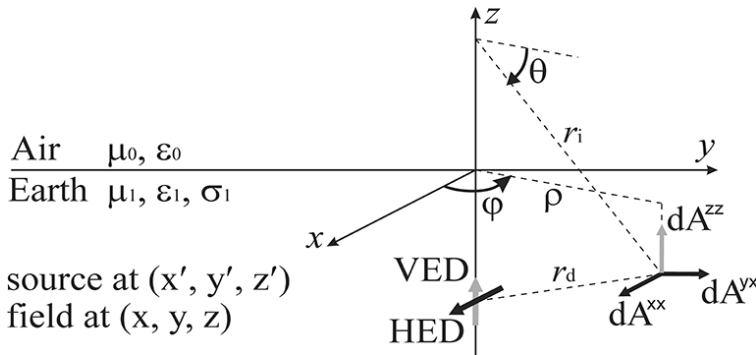


Figure 1: Components of magnetic vector potential due to HED and VED

In the most general form as provided in (Michalski, 1997), Green's functions are written as a sum of the contributions from direct term and the influence of the air-earth interface in integral form. In this paper we provide form that is more suitable for grounding analysis, obtained by extraction of singularities from the Sommerfeld integrals I'_1 , I'_2 and I'_3 in form of their quasi-static approximations (Bunger, 1997). The terms related to I_1 , I_2 and I_3 in the new form are the difference between the application of the low frequency approximation of Green's functions for formulation B and the full-wave electromagnetic theory.

Table 1: Different forms of Spatial-domain Green's functions for formulation B

General form of Green's functions	Proposed form for grounding analysis
$G_A^{xx} = \frac{e^{-jk_z r_d}}{r_d} + \frac{1}{2}(I'_1 + \cos(2\varphi)I'_2)$	$G_A^{xx} = \frac{e^{-jk_z r_d}}{r_d} + R_{10} \frac{e^{-jk_z r_i}}{2r_i} - R_{10} \cos(2\varphi) \left(\frac{e^{-jk_z z+z' } - e^{-jk_z r_i}}{jk \rho^2} - \frac{e^{-jk_z r_i}}{2r_i} \right) + \frac{1}{2}(I_1 + \cos(2\varphi)I_2)$
$G_A^{xy} = \frac{1}{2} \sin(2\varphi) I'_2$	$G_A^{xy} = -R_{10} \sin(2\varphi) \left(\frac{e^{-jk_z z+z' } - e^{-jk_z r_i}}{jk \rho^2} - \frac{e^{-jk_z r_i}}{2r_i} \right) - \frac{1}{2} \sin(2\varphi) I_2$
$G_A^{zz} = \frac{e^{-jk_z r_d}}{r_d} + I'_3$	$G_A^{zz} = \frac{e^{-jk_z r_d}}{r_d} - R_{10} \frac{e^{-jk_z r_i}}{r_i} + I_3$
$G_\Phi = \frac{e^{-jk_z r_d}}{r_d} - I'_3$	$G_\Phi = \frac{e^{-jk_z r_d}}{r_d} + R_{10} \frac{e^{-jk_z r_i}}{r_i} - I_3$
$I'_1 = \int_0^\infty (R_{10}^{TE} - R_{10}^{TM}) \frac{e^{-jk_{z1} z+z' }}{jk_{z1}} J_0(k_\rho \rho) k_\rho dk_\rho$	$I_1 = \int_0^\infty (R_{10}^{TE} - R_{10}^{TM} - R_{10}) \frac{e^{-jk_{z1} z+z' }}{jk_{z1}} J_0(k_\rho \rho) k_\rho dk_\rho$
$I'_2 = \int_0^\infty (R_{10}^{TE} + R_{10}^{TM}) \frac{e^{-jk_{z1} z+z' }}{jk_{z1}} J_2(k_\rho \rho) k_\rho dk_\rho$	$I_2 = \int_0^\infty (R_{10}^{TE} + R_{10}^{TM} + R_{10}) \frac{e^{-jk_{z1} z+z' }}{jk_{z1}} J_2(k_\rho \rho) k_\rho dk_\rho$
$I'_3 = \int_0^\infty R_{10}^{TM} \frac{e^{-jk_{z1} z+z' }}{jk_{z1}} J_0(k_\rho \rho) k_\rho dk_\rho$	$I_3 = \int_0^\infty (R_{10}^{TM} + R_{10}) \frac{e^{-jk_{z1} z+z' }}{jk_{z1}} J_0(k_\rho \rho) k_\rho dk_\rho$

To avoid numerical instability at low frequencies approaching to 0 Hz, all frequency dependent parameters in equations in Table 1, shall be expressed in terms of the complex conductivity $\underline{\sigma}_n$ ($n=0$ for the air and $n=1$ for the earth):

$$\underline{\sigma}_n = \sigma_n + j\omega\varepsilon_n, \quad k_n = \sqrt{-j\omega\mu_n \underline{\sigma}_n}, \quad k_{zn} = \sqrt{k_n^2 - k_\rho^2}, \quad R_{10} = \frac{\underline{\sigma}_1 - \underline{\sigma}_0}{\underline{\sigma}_1 + \underline{\sigma}_0}, \quad R_{10}^{TE} = \frac{k_{z1} - k_{z0}}{k_{z1} + k_{z0}}$$

$$\text{and } R_{10}^{TM} = \frac{\underline{\sigma}_0 k_{z1} - \underline{\sigma}_1 k_{z0}}{\underline{\sigma}_0 k_{z1} + \underline{\sigma}_1 k_{z0}}.$$

The integral equations in the Green's functions can be expressed as function of two geometric quantities r_i and θ , illustrated on Fig. 1. This allows for named integral equations to be pre-computed for a discrete set of values for r_i and θ in a two-dimensional interpolation grid, and then, the required solutions of integral parts in Green's functions can be readily obtained by suitable interpolation method. Interpolation of the Sommerfeld integrals is commonly used method for improving the efficiency in antenna analysis (Burke, 1984; Brittingham, 1977), and is already implemented for improving the efficiency of the well known antenna code NEC (Burke, 1992) and electromagnetic simulation software FEKO, but for a different set of integral equations optimized for antenna analysis. Here, similar procedure is applied, for evaluation of the integral equations provided in Table 1.

For a fixed set of parameters $f=10$ MHz, $\sigma_1=0.01$ S/m, $\epsilon_1=10\epsilon_0$ and $\mu_1=\mu_0$, using the numerical integration procedure provided in (Lytle, 1974), following interpolation surfaces and convergence characteristics of Sommerfeld integrals, for both forms are obtained:

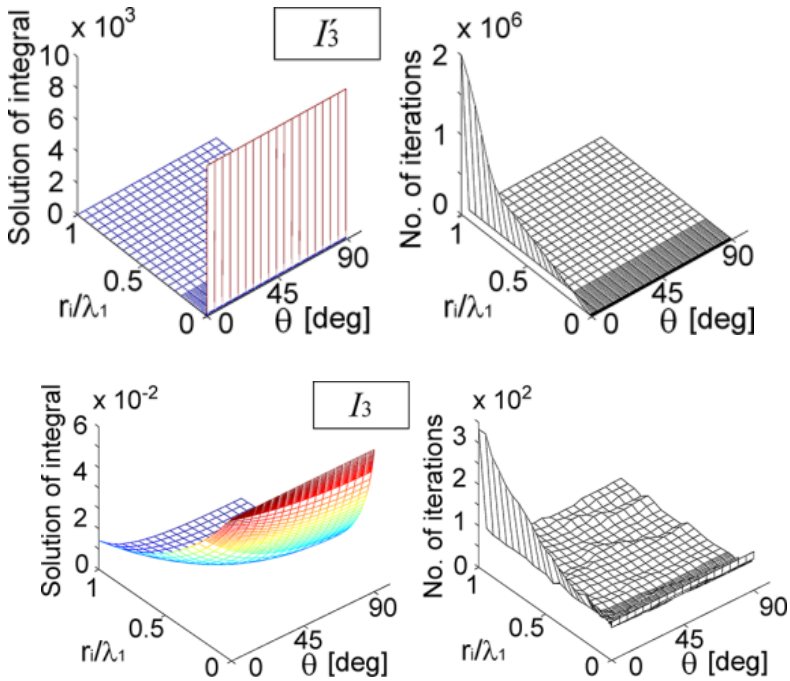


Figure 2: Solutions and number of iterations for convergence for integrals I'_3 and I_3 .

The Sommerfeld integrals I_1 , I_2 and I_3 , as illustrated on Fig. 2 for I_3 , show singular behavior and numerical instability for $r_i/\lambda_1 \rightarrow 0$, and slow convergence (up to $2 \cdot 10^6$ calls of integrand) for $\theta \rightarrow 0$. These conditions are satisfied for source and evaluation points at great distance and near the earth surface, which is especially unfortunate for analysis of grounding systems. Due to the steep variation of solutions, obtained surfaces are not suitable for interpolation.

In the proposed form of Green's functions, the extraction of the singularities significantly increases the efficiency of numerical evaluation of Green's functions. Integrals do not show singular behavior and instability, while the convergence is substantially improved. More important, the interpolation surfaces are significantly smoothed, which permits use of sparse interpolation grids. Reduced number of points in the interpolation grids and the improved convergence, provides substantial reduction of computation times, which is especially important for time-domain analysis in transient and lightning related studies where high number of frequencies are involved.

3 Validation of efficiency and accuracy of the presented procedure

The presented procedure is validated by two examples, illustrated on Fig. 3:

- 1) horizontal grounding grid with 50 x 100 m side lengths, buried at depth of 0.5 m,
- 2) wind turbine grounding system with arbitrarily oriented electrodes and size 15 x 15 x 3 m.

For a given set of parameters for both cases, ($\rho_1=30, 300$ and $3000 \Omega\text{m}$, $\epsilon_1=10\epsilon_0$ and $\mu_1=\mu_0$), efficiency and accuracy of the proposed method are validated by comparison of:

- ratio of evaluation times for currents distribution on structures in both cases, obtained by numerical integration (t_N) and with bivariate interpolation of the Sommerfeld integrals (t_I);
- the RMS error for longitudinal currents in electrodes of grounding systems, obtained by numerical integration and bivariate interpolation of the Sommerfeld integrals (Poggio, 1974).

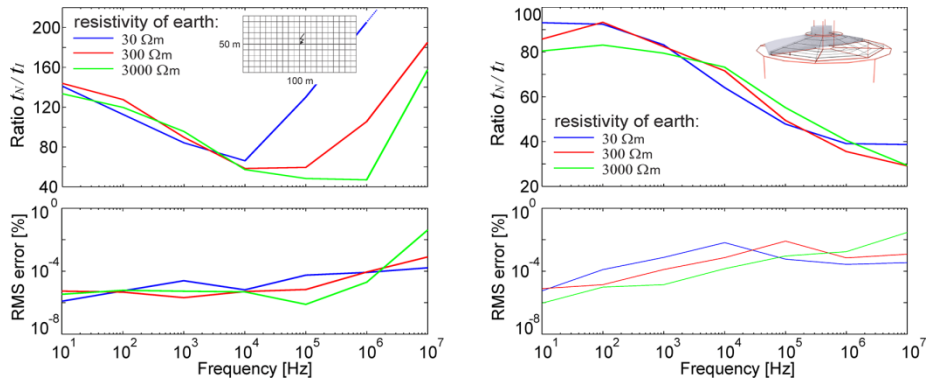


Figure 3: Validation of efficiency (upper) and accuracy of analysis (lower figure) for horizontal grounding grid and wind turbine grounding system

4 Conclusions

With the presented adjustments of the MPIE formulated integral equations and the implemented interpolation method, following benefits are achieved:

- electric field integral equations are cast in form that provides exact solution for all frequencies of interest, starting from dc to frequencies in the MHz range;
- by extraction of the singularities from the corresponding integral equations, their convergence is substantially improved;
- interpolation surfaces are smoother, and therefore, sparse interpolation grids with less elements are required;
- the presented procedure provides substantial reduction of computation times, from 30 to 200 times depending on the analyzed case, as illustrated on Fig. 3;
- the interpolation procedure provides nearly exact results, with introduced errors smaller than 0.1% for longitudinal currents distribution in electrodes, as illustrated on Fig. 3;
- considering the minor introduced errors, this procedure can be considered to provide nearly exact results that may serve as reference for scientific and practical applications.

References

- Arnautovski-Toseva, V. and L. Grcev. (2016). On the image model of a buried horizontal wire. *IEEE Trans. Electromagn. Compat.*, vol. 58, no. 1, pp. 278-286.
- Brittingham, J. N., E. K. Miller and J. T. Okada. (1977). A bivariate interpolation approach of efficiently and accurately modeling of antennas near a half space. *Electronics Letters*, vol. 13, no. 23, pp. 690–691.
- Bunger R. and F. Arndt. (1997). Efficient MPIE approach for the analysis of threedimensional microstrip structures in layered media. *IEEE Trans. on Microwave Theory and Techniques*, vol. 45, no. 8, pp. 1141–1153.
- Burke, G. J. and E. K. Miller. (1984). Modeling antennas near to and penetrating a lossy interface. *IEEE Trans. Antennas Propagat.*, vol. 32, no. 10, pp. 1040–1049.
- Burke, G.J. (1992). Numerical Electromagnetic Code – NEC4, UCRL-MA-109338
- Grcev, L. and F. Dawalibi. (1990). An electromagnetic model for transients in grounding systems. *IEEE Trans. Power Del.*, vol. 5, no. 2, pp. 1773–1781.
- Harrington, R. F. (1967). Matrix methods for field problems. *Proc. of IEEE*, vol. 55, no. 2, pp. 136-149.
- Lytle, R. J. and D. L. Lager. (1974). Numerical evaluation of Sommerfeld integrals, UCRL-51688, Lawrence Livermore National Laboratory, CA.
- Michalski, K. A. (1985). The mixed-potential electric field integral equation for objects in layered media. *Archiv fur Elektronik und Übertragungstechnik*, vol. 39, pp. 317-322.
- Michalski, K. A. and D. Zheng. (1990). Electromagnetic scattering and radiation by surfaces of arbitrary shape in layered media, Part I: Theory. *IEEE Trans. Antennas Propagat.*, vol. 38, no. 3, pp. 335-344.
- Michalski, K. A. (1997). On the scalar potential of a point charge associated with a time-dependent harmonic dipole in a layered medium. *IEEE Trans. Antennas Propagat.*, vol. 35, no. 11, pp. 1299–1301.
- Poggio, A., R. Bevensee, and E. K. Miller. (1974). Evaluation of some thin wire computer programs. *IEEE Antennas Propag. Symp.*, vol. 12, pp. 181–184.

Calculation of the Earth's Magnetic Field Distortion Caused by the Ferromagnetic Parts in Bed and its Effects on Health

DEJAN KRSTIĆ, DARKO ZIGAR, ŽELJKO HEDERIĆ, NIKOLA TRIFUNOVIĆ
& MARINKO BARUKČIĆ

Abstract Abstract Introducing of ferromagnetic objects and electromagnetic sources into the space of man's life produce a magnetic field changes in relation to the magnetic field of the earth. These procedures result in the formation of anomalous magnetic fields (AMF) in which people spend most of their time. One way of determining the spatial distribution of these fields is numerical calculation of the magnetic field by numerical methods, and another way is by measuring. According to existing scientific knowledge, longer stay in the AMF can produce significant health effects. Therefore, it is important to carry out calculation of the magnetic field for different construction types of beds with mattresses with ferrite core (springs). Calculation of the magnetic field in the bed area for particular bed constructions, such as single bed, bed with a back with a ferrite core and a double bed on two levels been carried out.

Keywords: • magnetic field • anomalous magnetic field • numerical simulation of magnetic field • effects of magnetic field on health • ferromagnetic parts in bed •

CORRESPONDENCE ADDRESS: Dejan Krstić, PhD, Associate Professor, University of Niš, Faculty of Occupational Safety, Čarnojevića Street 10A, 18000 Niš, Serbia, e-mail: dekihrs@gmail.com. Darko Zigar, PhD, Assistant professor, University of Niš, Faculty of Occupational Safety, Čarnojevića Street 10A, 18000 Niš, Serbia, e-mail: darko.zigar@znrfaq.ni.ac.rs. Željko Hederić, PhD, Associate Professor, Faculty of Electrical Engineering, Computer Science and Information Technology Osijek, Kneza Trpimira 2B, HR-31000 Osijek, Croatia; e-mail: zeljko.hederic@ferit.hr. Nikola Trifunović, Geoinstitut, Retired Geophysicist, Juzni Bulevar, 32, Belgrade, Serbia, e-mail: ntrifunovic41@yahoo.com. Marinko Barukčić, PhD, Assistant Professor, Faculty of Electrical Engineering, Computer Science and Information Technology Osijek, Kneza Trpimira 2B, HR-31000 Osijek, Croatia, e-mail: marinko.barukcic@ferit.hr.

1 Introduction

Many scientific studies verify deformation of the Earth's magnetic field caused by the non-natural living environment in normal life. As humans spent part of daytime in bed with ferromagnetic parts that create distortion of that field, a question is how that effect on human health. Statistically, breast cancer commonly happens in the left breast among both women and men (Hallberg 2010, Hallberg 2008). Some explanations for left-sided breast cancer include handedness, size difference, nursing preference, but that is more suggestions and assumptions. Increasing rates of skin melanoma have been associated with immune-disruptive radiation from FM/TV transmitters (Hallberg 2008). Urban areas covered by several transmitters show higher incidences of melanoma than areas covered by one transmitter. In this paper presented are that a breast cancer and melanoma on the left side of the body may be a logical consequence of sleeping in beds having mattresses of metal parts.

2 Methods of investigation

Influence of the ferromagnetic objects and electrical devices on modification of electric, magnetic and/or variable electromagnetic fields been well known. Certain scientific papers have indicated that if there is a change in the magnetic field in the bed area compared to the natural geomagnetic field value, this can be brought into correlation with health-endangering (Hallberg 2010, Roychoudhuri 2006). For this reason, was carry out a magnetic field simulation in an area of the bed made of a metal core with ferromagnetic wires and analyze whether such a magnetic field in which people stay during a night's sleep can lead to health problems.

2.1 Theoretical basis

It is not difficult to prove that animals and humans are electromagnetic beings, but the influence of electromagnetic fields at the level of the cell and cell organelles up to the molecular level has not been fully explained, which certainly slows down the development of medicine. The cell metabolism is conditioned by an electric field on both sides of the cell membrane and magnetic properties of cell organelles and magnetic fields of surroundings. The behaviour of ferromagnetic materials in the external magnetic field is characterized by a shape of hysteresis loop, with the most significant sizes coercivity H_c and saturation

remanence Mr. The ferromagnetic parts of the bed will magnetize in an enlarged external technically generated magnetic field or electromagnetic field. Some part of magnetism will retain even when the external field is reduced and decrease the intensity of resulting magnetic field in this area space. Such parts can be treated as magnets that in their vicinity generate the resulting magnetic field that is different from the natural magnetic field of the Earth.

Earth electric and magnetic fields are indispensable part of human life (De Ninno 2017, Liboff 2016), so it is logical that all processes in tissues and cells largely depend on the value of electromagnetic quantities that follow the parameters of these fields. This fact has not been significantly and sufficiently analyzed in the literature (De Ninno 2017). The areas with increased values in relation to the natural field values are called anomalous zones or the so called pathological magnetic and electromagnetic fields and represent the areas in which people live and may be often affected by various health problems. Important are new findings about the influence of the earth magnetic field on normal functioning of the human organism and its systems, as well as those about the effect of anomalous magnetic field on disbalance of functioning of organs and its role in the development of cancer, diabetes and autoimmune diseases (Trifunović 2015, Čizmić 2016).

2.2 Research method and hypothesis

It can be safely argued that the healthy functioning of a man is conditioned by life in the natural magnetic fields of the earth. A man spent most of his time in bed, and accordingly, the focus of the research was on the metal structures of beds. The working hypothesis is that if the metal parts of the beds significantly change the resulting magnetic field in the bed area relative to the value of the intensity of the natural magnitude of the earth then this fact may be related to endangering human health.

The determination of the resulting magnetic field in the vicinity of ferromagnetic objects in the magnetic field of the earth can be performed by measuring suitable instruments or calculations using simulation techniques and numerical methods of the calculation.

3 Determining the magnetic field in the beds

Analyzing the construction of beds and mattresses, we focused on the mattress with a steel core composed of springs. The research included 2 most commonly used bed constructions: a single bed (Fig. 1a), and double-decker (Fig 1b).

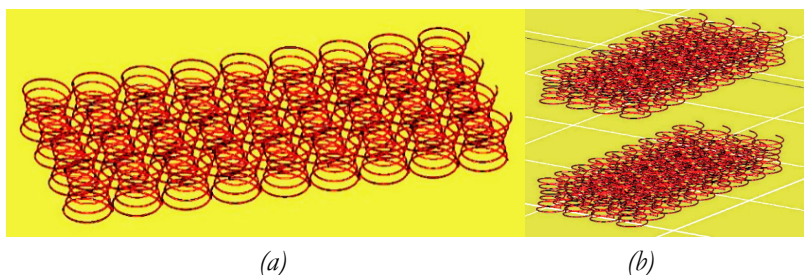


Figure 1. a) Mattress model with steel core and b) double-decker model with mattress

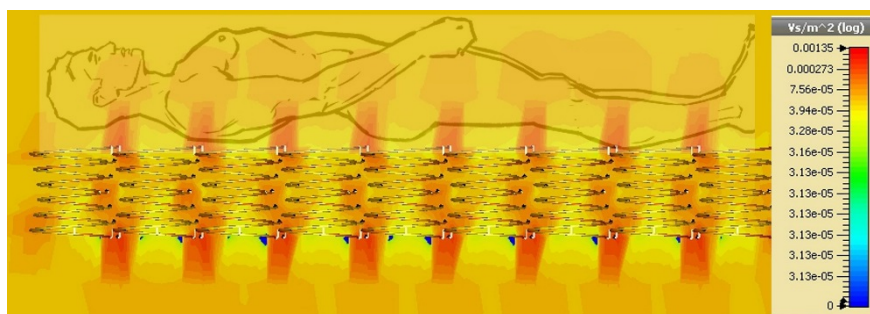


Figure 2. Distribution of magnetic field $B[\mu\text{T}]$ u mattress crosssection

Bedsprings are helicoidally structures made up of six coils having approximately the same radius. Modelling of the structure of standard 90x200 cm mattresses is performed with a simulation of a network of 9x4 springs of 10 cm radius, which were equidistantly placed, and in galvanic bond (Fig. 1a). The springs (helix) is made from ferromagnetic material and is characterized as $\mu_r = 1000$, $\sigma = 1,04 \cdot 10^{-7} \text{ S/m}$. and the magnetization curve for the materials in work point is defined by values $H=38 \text{ A/m}$, $B=0,6 \text{ T}$. Mean value of natural magnetic field $B=47,8 \text{ T}$ was measured and it is default value for an exciting magnetic field. The mattress was set at the height of 25 cm from the ground.

3.1 Results of simulation

For the simulated parameters defined here, the calculation of the magnetic field in the immediate surroundings of the construction was carried out. The following figures show distribution of intensity of magnetic induction vectors in the bed area where human body is at rest. Fig. 2 shows relative position of a person lying on the bed, whereby electromagnetic characteristics of a person were not taken for calculation. The control of the values obtained from calculation and the values obtained by measuring on a similar physical model showed a satisfactory agreement. It may be noticed that the intensity of magnetic induction decreases with distance, which will produce unequal exposure to the magnetic field of individual organs depending on the physiological position in sleep.

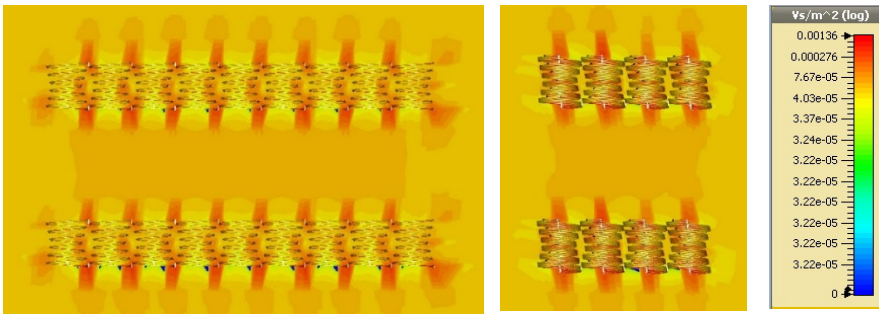


Figure 3. $B[\mu T]$ in crosssection of a double-decker –two crosssections

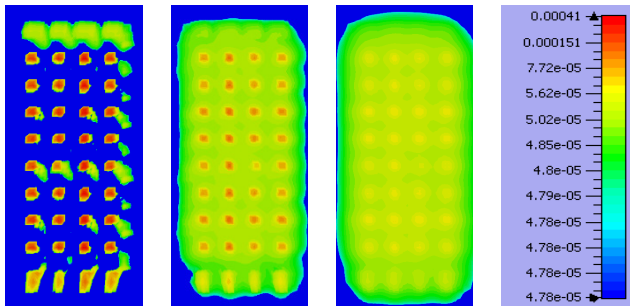


Figure 4. Distribution $B[\mu T]$, at the height of 5, 10 and 15 cm from wire core of lower bed

Simulation and calculation of the magnetic field was performed for a double-decker bed, where the mattresses are located at a distance of 60 cm (Fig. 1b). In this simulation, the construction of the bed was not taken into account, considering that it is made of wood and in magnetic sense did not have any influence on this calculation. The calculation results are given in Fig. 3 and Fig. 4.

3.2 Analysis of results

Analysis of the results suggests that the homogeneity of the natural magnetic field is affected by change of the intensity of magnetic induction in the following way:

- in a single bed local maximum values of magnetic field intensity that are 5.6 times greater than natural intensity of magnetic field are observed (Fig. 2).
- in a double-decker apart from local maximum values there is greater homogenous field values of magnetic induction greater than natural that is present between 2 mattresses (Fig. 3)
- distributions of the absolute value of magnetic induction at the distance of 5cm, 10cm, and 15 cm from the upper surface of the core is in range $76 \div 265 \mu\text{T}$.

4 Conclusions

When considering the structure of the bed with a frame of metal rods and the real human position over the mattress (with deformation in the mattress due to the weight of the person), there will be one or more continuous zones with the abnormal magnetic fields. Hundreds of Case studies have shown (Ćizmić, 2016) a correlation between these anomalous zones and the position of cancer development in the examinees. The facts that remained unclear in the (Hallberg 2010) now can be explained using simulation results. In general, there is a statistically proven fact of a habit of human sleep on the right side (easily heart work feelings) and the incidence of lung cancer is higher on the left side. That can be correlated with research that if some part of the human body is exposed to higher magnetic field that induced the formation of body viscous magnetization (Trifunović, 2015) and it is easier to form it in a single mass structure. Since the mass of the left lung wings is greater, the possibility of

incidence of cancer is also greater, as is confirmed by statistical data from multiple study.

The implications of this study should promote a critical consideration of population exposure to anomalous magnetic fields, especially during the night. Because of permanent exposure to elevated values of the magnetic field during the sleep period, ultimately that leads to the possibility of developing cancer. In order to avoid this, it is necessary to replace ferromagnetic materials as constitutive bed parts with non-ferromagnetic materials. In this way, anomalies of the magnetic field in the bed space relative to the naturally homogeneous magnetic field could be avoided. Therefore, this could be safe environment for normal functioning of human immune system. Such research indicates that it is necessary to constantly reconsider how people out of ignorance could make an environment harmful for proper functioning of the organism. Electromagnetic environmental pollution emphasizes the need for development of electromagnetic ecology of living and working space, which has already been suggested by scientific community.

Acknowledgments

This work was supported by projects III43011 and III43012 of the Serbian Ministry of Education and Science.

References

- Čizmić V. (2016). Cause of Autoimmune diseases Anomalous magnetic Fealds. *Journal of Pharmacy and Pharmacology* 4 , 574-582.
- De Ninno A. (2017). Electromagnetic homeostasis and the role of low-amplitude electromagnetic fields on life organization. *Electromagn Biol Med.* 36 (2),115-122, doi: 10.1080/15368378.2016.1194293
- Ekblom A. (1994). Epidemiologic correlates of breast cancer laterality (Sweden). *Cancer Causes Control* 5, 510–516.
- Goodman M.T. (2006). Comparative epidemiology of breast cancer among men and women in the US 1996 to 2000. *Cancer Causes Control* 17, 127–136.
- Hallberg Ö. (2010). Sleep on the right side - get cancer on the left?. *Pathophysiology* 17, 157-160.
- Hallberg Ö. (2008). A reduced repair efficiency can explain increasing melanoma rates. *Eur. J. Cancer Prev.* 17, 147–152.
- Liboff A.R. (2016). Magnetic correlates in electromagnetic consciousness. *Electromagn Biol Med.* 35(3), 228-236, doi: 10.3109/15368378.2015.1057641.
- Roychoudhuri R. R. (2006). Cancer and laterality: a study of the five major paired organs (UK). *Cancer Causes Control* 17, 655–662.

- Trifunović N. (2014). Breathing Enable the Magnetic Properties of Erythrocytes (Hem Fe Oxygen, Cells and Carbon dioxide). *Journal of Health Science* 2, 270-283
- Trifunović N. (2015). The Effect of Anomalous Magnetic Fields on Malignant Diseases. *Open Access Library Journal*, Vol2, No.4, doi: 10.4236/oalib.1101459

FEM Modelling and Analysis of Single Sided Linear Synchronous Motor

XEVAT SULEJMANI & GOGA CVETKOVSKI

Abstract In this paper, an adequate Finite Element Method modelling and analysis for a single sided linear synchronous motor is presented. The motor that is analyzed is a DC excited linear synchronous motor applied in a MAGLEV low, medium and high speed guideway applications. Linear synchronous motors are under development for a variety of demanding applications including high speed ground transportation and specific industrial applications. These applications require machines that can produce large forces, operate at high speeds, and can be controlled precisely to meet performance requirements. The design and implementation of these systems require fast and accurate techniques for performing system simulation and control system design.

Keywords: • linear synchronous motor • magnetic field • finite element method • thrust force (propulsion) • electromagnetic characteristics •

CORRESPONDENCE ADDRESS: Xevat Sulejmani, MSc Student, Ss. Cyril and Methodius University, Faculty of Electrical Engineering and Information Technologies, Rugjer Bošković 18, 1000, Skopje Republic of Macedonia, e-mail: xh-n@live.com. Goga Cvetkovski, PhD, Professor, Ss. Cyril and Methodius University, Faculty of Electrical Engineering and Information technologies, Rugjer Bošković 18, P.O. Box574, 1000 Skopje, Macedonia, e-mail: gogacvet@feit.ukim.edu.mk.

1 Introduction

Linear synchronous motors are under development for a variety of demanding applications including high speed ground transportation and specific industrial applications. These applications require machines that can produce large forces, operate at high speeds, and can be controlled precisely to meet performance requirements. The design and implementation of these systems require fast and accurate techniques for performing system simulation and control system design.

Linear electric motors can drive a linear motion load without intermediate gears, screws or crank shafts. A linear synchronous motor (LSM) is a linear motor in which the mechanical motion is in synchronism with the magnetic field, i.e. the mechanical speed is the same as the speed of travelling magnetic field. The thrust (propulsion force) can be generated as an action of:

- travelling magnetic field produced by a polyphase winding and an array of magnetic poles N, S,...N, S or a variable reluctance ferromagnetic rail (LSMs with a.c. armature windings);
- magnetic field produced by electronically switched d.c. windings and an array of magnetic Poles N, S,...N, S or variable reluctance ferromagnetic rail (linear stepping or switched reluctance motors).

The part producing the travelling magnetic field is called *the armature* or *forcer*. The part which provides the d.c. magnetic flux or variable reluctance is called the *field excitation system* (if the excitation system exists) or salient-pole rail, reaction rail or variable reluctance platen. The operation of a LSM does not depend which part is movable and which one is stationary. Traditionally, a.c. polyphase synchronous motors are motors with d.c. electromagnetic excitation, the propulsion force of which has two components: (1) due to the travelling magnetic field and d.c. current magnetic flux (synchronous component) and (2) due to the travelling magnetic field and variable reluctance in d and q axis (reluctance component).

In this paper, an adequate Finite Element Method modelling and analysis for a single sided linear synchronous motor is presented. The motor that is analysed is a DC excited linear synchronous motor applied in a MAGLEV low, medium and high speed guideway applications.

2 Linear Synchronous Motor Presentation

The investigated motor is a single sided linear synchronous motor with DC excitation. The stator, the bottom part, has a laminated core with open slots and $q=1$, single-layer, aluminium cable three-phase windings, as in Fig. 1. The top part is the moving part on which the DC excitation windings are placed. In Fig. 1 only a partial presentation of this part consisting of 4 whole poles and 2 half poles. The size of the segment is determined based on the manufactural procedures and it is about 1.3 m long. Also, to harvest energy on board of mover (vehicle), a two-phase ac winding is placed in dedicated slots on the dc exciter poles. Two-phase tooth-wound coils on the dc exciter poles “collect” by electromagnetic induction the mmf open-slot stator harmonics energy.

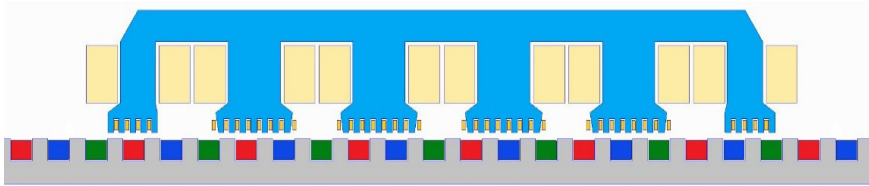


Figure 7: Single sided linear synchronous motor presentation

3 Linear Synchronous Motor Performance Analysis

Electrical machine modeling is crucial and important as it saves time and it is economical because it saves money for building the prototypes. Consequently, it is regularly difficult to calculate and analyze the motor overall performance with consistent accuracy through the classical circuit methods. Therefore, numerical techniques are found more fascinating and advantageous. Hence for motor design and performance analysis of any kind of motor, the finite element method (FEM) has shown its reliability and accuracy. In this paper the performance analysis of the single sided linear synchronous motor using the FEM software is performed. The performance analysis is going to be performed for different current loads in the stator windings, as well as for different air gaps, different moving part positions and different values of the excitation field DC current. As an example the magnetic field distribution and the air gap flux density distribution for rated stator current load and rated excitation field for 10 cm air gap in Fig. 2 and Fig. 3, respectively, is presented. In following figures (Fig. 4,

and Fig. 5) respectively, air-gap flux density in single sided linear synchronous motor for different values of air gap (8 mm and 12 mm) and different rotor positions is presented.

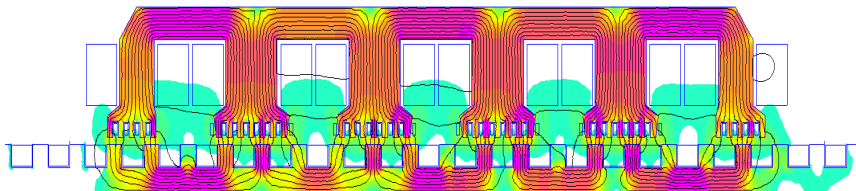


Figure 2: Magnetic field distribution in single sided linear synchronous motor at rated conditions

Significant influence on air-gap flux density is indicated by the change of air gap value, which is directly related to B_{fg} of single sided linear synchronous motor. While, when moving the rotor against the stator (different positions), the movement of the magnetic field and the variable reluctance is spotted, which is a reason of generation the propulsion force (thrust) in linear synchronous motors.

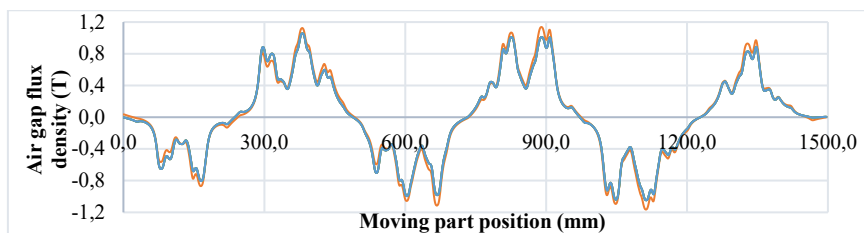


Figure 3: Air-gap flux density distribution in single sided linear synchronous motor for two different current loads in stator windings

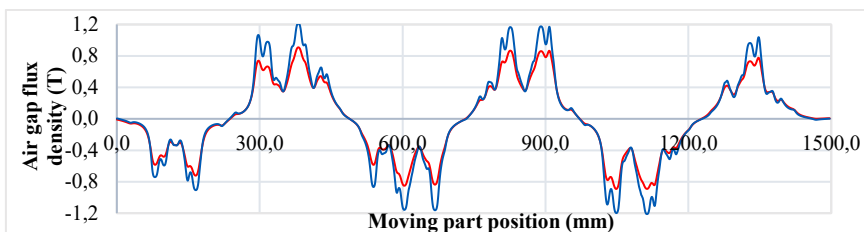


Figure 4: Air-gap flux density distribution in single sided linear synchronous motor for different values of air gap (8 and 12 mm)

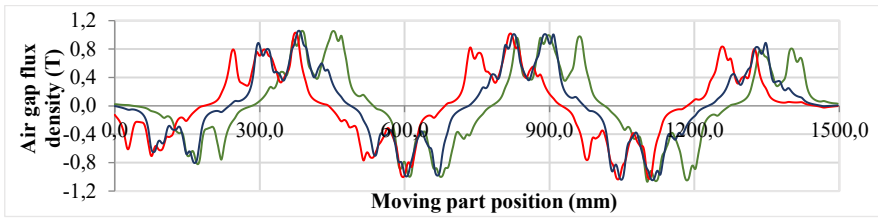


Figure 5: Air-gap flux density distribution in single sided linear synchronous motor for different rotor positions

Using FEMM programming package, which also contains tools for calculating various parameters, in this paper, the thrust force and power is calculated through numerical method. Numerical values of the above listed parameters coincide with analytically calculated which are presented in (Boldea, I. 2013). Due to the specific constructive performance of single sided linear synchronous motor, where the size of the slot in which the two-phase coil of the rotor is placed is relatively smaller than the size of stator's slot, when the rotor is moved relative to the stator, the two-phase pole pitch of the rotor are unevenly loaded, i.e. they have different magnetic induction. Two half poles of the rotor that are smaller than the other rotor poles are deliberately placed on both end, which is why they are leading when moving the rotor in both directions.

References

Boldea, I., (2013). Linear Electric Machines, Drives and MAGLEVs Handbook, CRC Press, Chapter 7, pp. 165-81.

Advantages of the Stator Flux Trajectory for Direct Torque Control of Induction Machines with Uncertain Resistances

GORAN RAFAJLOVSKI, MIHAIL DIGALOVSKI & GOGA CVETKOVSKI

Abstract In direct torque vector control systems voltage source inverter is applied. The basic characteristics of stator flux space vector is analyzed for two different types of space vector modulation techniques. The first one is full block space vector modulation and the second one is pulse edge space vector modulation. It is described that the absolute error in determining the stator flux space vector is independent of the angular frequency. As a result neglecting the stator resistance voltage drop at low frequencies is allowed. The only restriction is that the IM drive state should be considered only in a short sampling intervals which in practical microprocessor implementation of vector control is always fulfilled. Furthermore by mathematical analysis and simulation of amplitude and phase vector errors at different drive modes, it is shown that neglecting the voltage drop due to stator resistance uncertainty is permitted at low frequencies and short sampling intervals.

Keywords: • direct torque vector control (DTC) • induction machine • voltage source inverter (VSI) • stator flux trajectory • vector error • pulse edge space vector modulation •

Correspondence Address: Goran Rafajlovski, Ph.D., Professor, Ss. Cyril and Methodius University, Faculty of Electrical Engineering and Information Technologies, Rugjer Boskovic 18, P.O. Box 574, 1000 Skopje, Macedonia, e-mail: goran@feit.ukim.edu.mk. Mihail Digalovski, Ph.D., Assistant Professor, Ss. Cyril and Methodius University, Faculty of Electrical Engineering and Information Technologies, Rugjer Boskovic 18, P.O. Box 574, 1000 Skopje, Macedonia, e-mail: mihaild@feit.ukim.edu.mk. Goga Cvetkovski, Ph.D., Professor, Ss. Cyril and Methodius University, Faculty of Electrical Engineering and Information Technologies, Rugjer Boskovic 18, P.O. Box 574, 1000 Skopje, Macedonia, e-mail: gogacvet@feit.ukim.edu.mk.

1 Advantages of the $\vec{\psi}_1$ trajectory

The selection of the states of the power switches S_a, S_b, S_c depends on the rotation direction of vector $\vec{\psi}_1$ and is carried out so that the error between the real value of $|\vec{\psi}_1|$ and the reference (assigned) value of $|\vec{\psi}_1^*|$ moves within the limits of $\Delta|\vec{\psi}_1|$ as defined by the hysteresis band (Fig.1) of the flux controller.

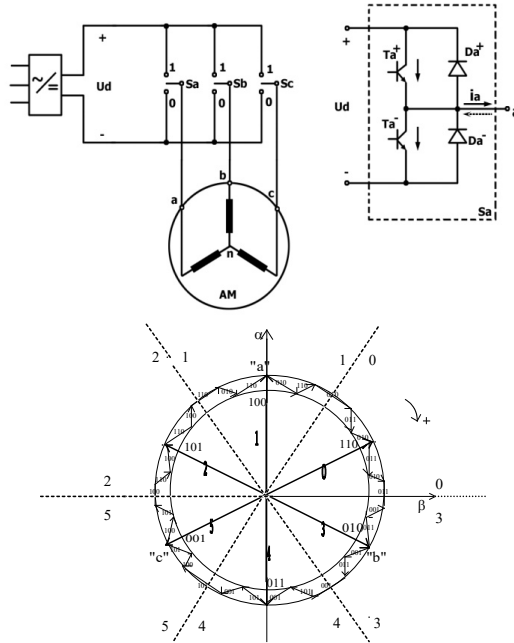


Figure 1: VSI for DTC selecting the voltage vector for optimum stator flux trajectory

For this purpose, the stationary reference domain $\alpha - \beta$ is divided into 6 (six) equal parts (zones). Each zone has its own carrier voltage space vector. Thus, for instance, the carrier vector of the '0' zone is vector $\vec{U}_6(110)$. The stator flux space vector $\vec{\psi}_1$ in VSI is:

$$\frac{d\vec{\psi}_1}{dt} = \vec{u}_1 - R_1 \cdot \vec{i}_1 \tag{1}$$

Below is shown that neglecting R_1 is possible also in the area of low frequencies if only a short time interval $0 \leq t \leq T$ is considered. By integrating equation (1) with stator resistance neglected the following is obtained:

$$\vec{\psi}_1(t) = \vec{\psi}_1(0) + \int_0^T \vec{u}_1(t) dt \quad 0 \leq t \leq T \quad (2)$$

Or with stator resistance integral has the form:

$$\vec{\psi}_1(t) = \vec{\psi}_1(0) - R_1 \cdot \int_0^T \vec{i}_1(t) dt + \int_0^T \vec{u}_1(t) dt \quad 0 \leq t \leq T \quad (3)$$

The starting stator flux vector in both equations, (2) and (3), is identical and so absolute error may be defined as:

$$|\Delta \vec{\psi}_1(t)| = R_1 \cdot \left| \int_0^T \vec{i}_1(t) dt \right| \quad 0 \leq t \leq T \quad (4)$$

To estimate absolute error of the stator flux space vector, the fundamental harmonic of the stator current space vector can be used:

$$\vec{i}_1(t) = \vec{i}_{1g}(t) = \vec{i}_{1g}(0) \cdot e^{j \cdot \omega_g \cdot t} \quad 0 \leq t \leq T \quad (5)$$

Combining the equations (4) and (5) gives the absolute stator flux vector error:

$$|\Delta \vec{\psi}_1(t)| = R_1 \cdot |\vec{i}_{1g}(0)| \cdot \sqrt{2 \cdot \frac{1 - \cos(\omega_g \cdot t)}{\omega_g^2}} \quad 0 \leq t \leq T \quad (6)$$

The sampling period in this control concept may vary within the limits $T = 0,4 \dots 0,8$, which corresponds to several milliseconds. Considering the motor's drive state in frequency range $0 \leq \omega_g \leq 2$, can be assumed:

$$\cos(\omega_g \cdot t) \approx 1 - \frac{(\omega_g \cdot t)^2}{2} \quad 0 \leq t \leq T \quad (7)$$

By means of Equation (7) absolute stator flux error in line with Equation (6) amounts to:

$$|\Delta \vec{\psi}_1(t)| = R_1 \cdot |\vec{i}_{1g}(0)| \cdot t \quad 0 \leq t \leq T \quad (8)$$

Following from (8) is the obvious conclusion that absolute error in determining the stator flux space vector is independent of the angular frequency ω_g . Hence, just as neglecting the voltage drop of the stator resistance when calculating the stator flux space vector $\vec{\psi}_1$ in the circular high frequency area is permitted, the same neglect is also allowed at low frequencies. The only restriction is that the IM drive state should be considered only in a short sampling interval of $0 \leq t \leq T$, which in practical microprocessor implementation of vector control is always fulfilled. Estimating phase error, i.e., the spatial position of the error vector $\Delta \vec{\psi}_1$ can similarly be carried out. The space vector $\Delta \vec{\psi}_1$ has the approximate direction that the space vector of the main stator current harmonic \vec{i}_{1g} takes in the middle of the observed interval $0 \leq t \leq T$:

$$\arg \{ \Delta \vec{\psi}_1(t) \} = \arg \{ \vec{i}_{1g}(t / 2) \} \quad 0 \leq t \leq T \quad (9)$$

By introducing the space vector time derivative in polar coordinates it is possible to interpret its " v_1 " module (10) as linear velocity at which the vector peak $\vec{\psi}_1$ moves on a given trajectory. The movement direction is defined by the angle " ζ " (11).

$$\frac{d\vec{\psi}_1}{dt} = \vec{u}_1 = v_1 \cdot e^{j \cdot \zeta_1} \quad (10)$$

$$v_1 = |\vec{u}_1|, \quad \zeta_1 = \arg \{ \vec{u}_1 \} \quad (11)$$

2 Full block versus pulse edge space vector modulation

At full block space vector modulation the on/off inverter switching frequency is equals to that of the fundamental harmonic, i.e., $V_p = f_{\text{vkl}} / f_g = 1$. Hence, the fundamental harmonic of the inverter output in this space vector modulation is at maximum amplitude. In case of full block modulation, the peak of the $\vec{\psi}_1$ space vector moves along the edges of the isosceles hexagon at constant speed equal to $\frac{2}{3}U_d$.

By means of pulse edge vector modulation, symmetrical cropping of the hexagon legs in the edge-area is obtained. The length of these symmetrical deformations is determined by characteristic time T_F between two consecutive pulses of different width. The rotation speed of $\vec{\psi}_1$ still remains constant. In this modulation, in each of the six possible space zones (each zone is a 60° angle) three space vectors are switched on: the carrier vector of the zone with its antecedent and subsequent vector. If the antecedent and subsequent vector are switched on at time T_F ms, the crop length at the sides of the isosceles hexagon's edge-area amounts to $T_F \cdot \frac{2}{3} \cdot U_d$. The carrier vector is switched on during the time

$$\frac{T_g}{6} - 2 \cdot T_F \text{ ms, and hexagon side length is } \left(\frac{T_g}{6} - 2 \cdot T_F \right) \cdot \frac{2}{3} \cdot U_d.$$

When the two zero vectors are switched on, the peak of $\vec{\psi}_1$ space vector stands still and the distance between the switching on of the two zero vectors is determined by time T_N and the line-to-line rotation speed $v = \frac{2}{3}U_d$. If in this modulation the antecedent and subsequent vector of each 60° ($T_g/6$ ms) active zone is switched on T_F ms, then the length of the cropped hexagon sides in the edge-area amounts equal to $T_F \cdot \frac{2}{3} \cdot U_d$. In each zone, the voltage carrier space vector is switched on/off three times (it is separated by two zero vectors) each with duration of $\frac{1}{2} \cdot \left(\frac{T_g}{6} - 2 \cdot T_F - T_N \right)$, T_N , $\frac{1}{2} \cdot \left(\frac{T_g}{6} - 2 \cdot T_F \right)$.

3 Vector Error assessment due to uncertain stator resistance

For the purpose of quantitative and qualitative assessment of the developed electromagnetic torque, current and stator flux space vector errors, due to variation in the winding resistances, the simulation of DTC drive is obtained. Figure 3. shows time diagrams of the developed torque in 30 milliseconds, the torque error, as well as the amplitude and phase errors of the \vec{i}_1 и $\vec{\psi}_1$ space vectors when parameters R_1 и R_2 change their values by 15%. The amplitude error of \vec{i}_1 is limited to 2%, while its angular error to only 0.28° . Amplitude error of $\vec{\psi}_1$ is even lower, 0.6%, and its angular error is 0.05° . The maximum developed torque error is 1.5%. This control structure demonstrably maintains its excellent dynamics and shows excellent stability when the parameters R_1 and R_2 change.

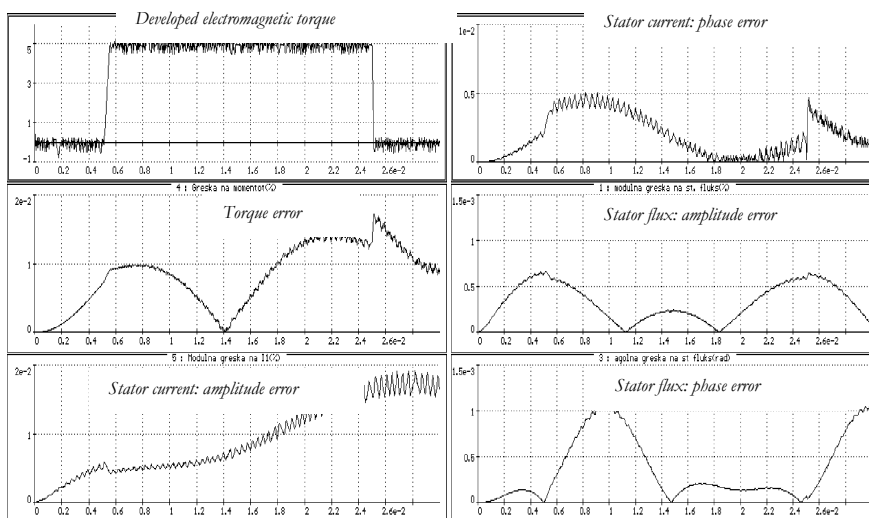


Figure 2: Error assessment in direct vector control system (assumed: R_1 change by 15%)

Conclusion

There is a very simple functional dependence between the stator voltage space vectors and the stator flux space vectors. The stator flux space vector $\vec{\psi}_1$ does not depend either on the stator current space vector \vec{i}_1 , or on the developed electromagnetic torque and consequently on the motor's drive state. Furthermore the absolute error in determining the stator flux space vector is

independent of the angular frequency ω_g . Hence, just as neglecting the voltage drop of the stator resistance when calculating the stator flux space vector $\bar{\psi}_1$ in the circular high frequency area is permitted, the same neglect is also allowed at low frequencies. The only restriction is that the IM drive state should be considered only in a short sampling interval of $0 \leq t \leq T$.

References

- Holtz J. (2003). Sensorless speed and position control of induction motor drives- A Tutorial: *29th Annual Conference of the IEEE Industrial Electronic Society, IECON*, Roanoke/Va USA, Nov. 2-6, 2003.
- Rafajlovski, G., Ratz, E. (1997). Modelling Analysis and Simulation of Motor Parameter Variation in Vector Controlled Electrical Drives: *IEEE PCC, Proceedings*, pp.827-844,0-7803-3823-5/97 Nagaoka, Japan.
- Rafajlovski, G., Digalovski, M. (2015). PWM Inverter dead time impact on vector control system: *International Journal on Information Technologies and Security*, No.4/2015, ISSN 1313-82.

Thermal and Overcurrent Protection on Single Phase Induction Motor by Using Arduino

STEFAN MITROVSKI AND GOGA CVETKOVSKI

Abstract In this paper it is taken into consideration thermal and overcurrent protection on one phase induction motor. Protection has been projected with Arduino Mega 2560 Microcontroller. The main advantages here are the increased useful functions of the protection. This protection forms a database for system operation, data on the fault conditions, and it locates the fault. Also we can use this kind of protection with SCADA systems.

Keywords: • thermal protection • overcurrent protection • induction motor • controller • power drive •

CORRESPONDENCE ADDRESS: Stefan Mitovski, Ss. Cyril and Methodius University, Faculty of Electrical Engineering and Information Technologies, Rugjer Bošković 18, 1000 Skopje, Republic of Macedonia, e-mail: stefan.mitovski@yahoo.com. Goga Cvetkovski, PhD., Professor, Ss. Cyril and Methodius University, Faculty of Electrical Engineering and Information Technologies, Rugjer Boskovic 18, P.O. Box 574, 1000 Skopje, Macedonia, e-mail: gogacvet@feit.ukim.edu.mk.

1 Introduction

In this paper the overcurrent and thermal protection of a single-phase induction motor is analysed and taken into consideration. The protection is being realized with the Arduino Mega 2560 controller. With the development of computer technology, the protection of electromotor drives has improved significantly, and in relation with this the digital relays start to develop in recent days. The protection of the electromotor drive is of exceptional importance in the overall performance of the electromotor drive, due to the fact that with this the reliability of it increases, and with this measure the safety of the electromotor drive also increases. The advantage of such controllers is in the lower cost of this solution compared with some other technologies, as well as in the simplicity of its programming and realization. The controllers can be programmed by using C language and the software named Arduino. The internal architecture of the controller is composed of central unit and the input/output circuits. The central unit consists of processor, memory system and power supply.

2 Protection on induction motor drive

In this paper the overcurrent and thermal protection of a single-phase induction motor is analysed and taken into consideration. The protection is being realized with the Arduino Mega 2560 controller. With the development of computer technology, the protection of electromotor drives has improved significantly, and in relation with this the digital relays start to develop in recent days. The protection of the electromotor drive is of exceptional importance in the overall performance of the electromotor drive, due to the fact that with this the reliability of it increases, and with this measure the safety of the electromotor drive also increases. The advantage of such controllers is in the lower cost of this solution compared with some other technologies, as well as in the simplicity of its programming and realization. The controllers can be programmed by using C language and the software named Arduino. The internal architecture of the controller is composed of central unit and the input/output circuits. The central unit consists of processor, memory system and power supply.

- Mechanism
- Power source
- Environment

Overloads stemming from the working mechanism are frequent and can occur if, for any technological reason, the working mechanism in stationary mode can be countered by a greater moment than the nominal one. In rolling mill, the reason for overloading may be the rolling of cooler pieces or because of the resistance of material deformation that has been increased. This types of fault may be solved with thermal and overcurrent protection. In the low voltage sources, a larger voltage drop is possible. On this occasion we will analyze the consequences from 20-30% gain or reduction in the voltage. The most critical are induction motors because of the dependence of their moment from the square of the voltage. With the reduction of the voltage in induction motor, the speed will fall, but if the static moment is constant, the motor will take greater current from the source to develop the required moment. As well, this fault can be prevented with overcurrent, thermal and overvoltage protection, but in this thesis overcurrent and thermal protection are being taken into the consideration.

In many cases, the technological process takes place in mines, black and white metallurgy, cement, wood and textile industry, where the engine can be covered with dust or other small pieces. In such conditions, the engines are much more difficult to cool and therefore they should be loaded less than nominal load. This type of fault cannot be detected with overcurrent protection because there is obstacle in the cooling process. It can only be detected with thermal protection.

3 Thermal and overcurrent protection

In order to realize thermal and overcurrent protection, we use the digital and analogue inputs and outputs of the controller. If there occurs a fault in the working process of the electric motor, the motor can be switched off by a digital signal that can be given to a certain relay, but if there is a need to measure the current or temperature for the realization of this protection, we will have to deal with analogue signals. It's worth mentioning that the operation with the analogue signals is more specific than the operation with digital signals, because the controller is a discrete system that operates with zeros and ones, while the analogue signal is a continuous signal which has to be transformed into a digital in order to be written in the data table. For the realization of the current protection a current transformer type HWCT004is used, while the thermal protection is realized with the sensor type MCP9700 / 9701. The current transformer is attached directly to the phase of the single-phase induction motor

while the secondary side of the transformer is attached to a resistor which measures the voltage drop, because of the controller's voltage analogue input. In the program the maximum current can be defined, and in case of increased mechanical loads on the electric motor, the motor will draw from the supply a larger current in relation to the previous current value and if this value of the current is higher than the defined maximum value then the protection will act and will switch the motor off. In case of thermal protection at long-term loads, the windings can warm up more than the nominal temperature and in this case the protection will also be activated again the electric motor will be also switched off again. Since the single phase induction motor is supplied by an AC power (current), it is necessary to sample the sinusoidal input current in order to capture its maximum value. The effective value of the current is determined after reading the maximum value, by using mathematical expression presented in equation (1). Also, the effective value can be determined by applying the mathematical relation (2) and taking into account a sufficient number of samples

$$I_{rms} = \frac{I_{max}}{\sqrt{2}} = 0.707 * I_{max} \quad (1)$$

$$I_{rms} = \sqrt{\frac{1}{N} \sum_{n=1}^N |I_n|^2} \quad (2)$$

The proposed protection equipment in laboratory environment and the wiring scheme of the overcurrent and thermal protection is presented in Figure 1.

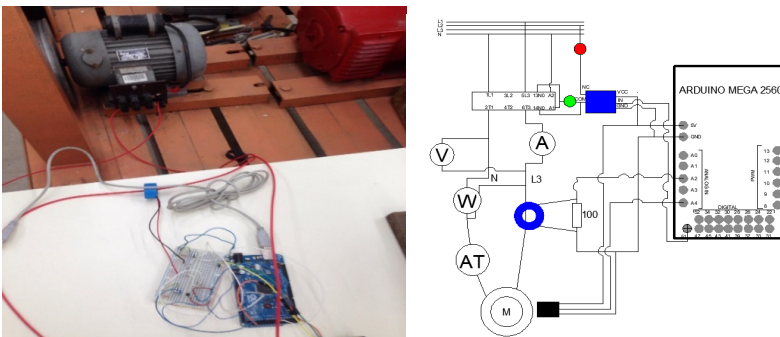


Figure 1: Presentation of the protection equipment used for thermal and overcurrent protection by using Arduino

4 Conclusion

Overcurrent and thermal protection on one phase induction motor is very important for reliability during its work. Reliable protection means that the protection can be reacted when fault occurs in the operation of the electric motor such as overload and short circuits. In the case when the protection does not respond to the occurrence of these errors, it is possible to cause more damage to the equipment from the power drive, as well as catastrophic consequences for the environment. It is important to note that too high sensitivity of the protection is not helpful because the power drive would fail very often even in low overloads. Over the past 15 years, digital protection has been used intensively. The main advantage of this protection are the increased useful functions of the protection. This protection forms a database for system operation, data on the fault conditions, and it locates the fault. Also we can use this kind of protection with SCADA systems. If we change the electric motor, it is very easy to change the parameters of the protection too. In our case, only the control program should be changed. If the old electromagnetic relay protection is used in that case, the entire circuit should be changed.

References

- Brian W. Evans, B. W., (2007). Arduino programming notebook.
Funduino Service Team, (2016). Funduino Tutorials for Arduino.
Mircevski, S. (2008). Electric Drives Control, Printed lectures: Faculty of Electrical Engineering and Information Technologies in Skopje.
Nagesh Vasant Bhakare, Laxman Mukinda Ghanvat, Sandesh Balasaheb Patil and Dodamani Sunanda R., (2016). Detection of Fault of Three Phase Induction Motor Using Arduino Uno R2 Microcontroller.
Shweta hugar, Basavaraj Amarapur, (2016). Protection of Induction Motor using Microcontroller.
Dushyant Patil , Siddharth Divekar , Ajit Kumar, (2018). Protection of 3 Phase Induction Motor using Microcontroller.

Power Performance Investigation of a Wind Turbine Using Nonparametric Methods

MAJA CELESKA, KRSTE NAJDENKOSKI, VLATKO STOILKOV &
VLADIMIR DIMCHEV

Abstract Accurate determination of wind turbine (WT) performance is necessary for economic operation of a wind farm. Currently, the procedure to validate the power performance verification of WT is based on the standard IEC 61400-12. In this paper, nonparametric statistical inference is applied to designing an inexpensive method of verifying the power performance. The method uses the information that is collected by the SCADA system. The study has used data on the monthly output of wind farm in R. Macedonia, and the time measuring interval was 01.01-31.12.2016. The wind farm is consisted of 16 WTs, type SWT 2.3-93. From previous studies, it is evident that WT number 13 has the most questionable working regimes. The method elaborated in the paper estimates the similarity among guaranteed power curve and power coefficient, to the estimated curves obtained from the operation of the WT13 and says whether the power performance of the WT differs significantly from the expected one.

Keywords: • wind turbine • power curve • power performance • wind energy • canonical correlation analysis •

CORRESPONDENCE ADDRESS: Maja Celeska, MSc, Teaching and Research Assistant, Ss. Cyril and Methodius University in Skopje, Faculty of Electrical Engineering and Information Technologies, Rugjer Boshkovikj 18, PO BOX 574, Skopje, Republic of Macedonia, e-mail: celeska@feit.ukim.edu.mk. Krste Najdenkoski, PhD, Professor, Ss. Cyril and Methodius University in Skopje, Faculty of Electrical Engineering and Information Technologies, Rugjer Boshkovikj 18, PO BOX 574, Skopje, Republic of Macedonia, e-mail: krste@feit.ukim.edu.mk. Vlatko Stoilkov, PhD, Professor, Ss. Cyril and Methodius University in Skopje, Faculty of Electrical Engineering and Information Technologies, Rugjer Boshkovikj 18, PO BOX 574, Skopje, Republic of Macedonia, e-mail: vlatko@feit.ukim.edu.mk. Vladimir Dimchev, Ph.D, Professor, Ss. Cyril and Methodius University in Skopje, Faculty of Electrical Engineering and Information Technologies, Rugjer Boshkovikj 18, PO BOX 574, Skopje, Republic of Macedonia, e-mail: vladim@feit.ukim.edu.mk.

1 Introduction

In the process of designing a wind farm (WF), the estimation of the total production of electrical energy is the most essential phase. Power curves are catalogue data that are proclaimed and guaranteed by the manufacturer of the WTs. After a WF is built, the power performance of each WT must be verified in accordance with the international standard IEC61400-12-1 (IEC 61400). Accurate determination of WT performance is necessary for economic operation of a WF. Generally, the application of the method elaborated in the international standard is not inexpensive. For this reason, it is important to devise alternative methods, with wide and simple applicability. In this paper, the power performance verification is carried out by using statistical method, (Everitt et al, 2005). Canonical correlation analysis (CCA) is the one of the oldest and best-known methods for discovering and exploring dimensions that are correlated across sets. The canonical correlation is part of multivariate analysis of variance (MANOVA), which allows to correlate the measured wind speed and power outputs variations, to those provided in the power curve from the WT manufacturer.

2 Methodology

Before implementation of the main procedure for power curve verification, equally important is the methodology of filtering the data from outliers. Outliers are defined as the data points that lie outside the probabilistic WF power curve and are caused by multiple non-meteorological factors: communication error, WT outage or curtailment action, (Ye *et al.*, 2016). In this paper, three identification criteria for outliers are proposed:

- i) All recorded numerical values for power outputs that have values equal or below zero when the wind speed > cut-in speed, are rejected because these values represent faults in the performance of the WT during its operation, or because the turbine status was 0 (not in operation). The recorded negative active power outputs are generally observed for wind speeds 2-7 m/s.
- ii) Determination of outliers on a criterion of greater than three times standard deviations (3σ) from the WT power curve in order to eliminate the power outputs outliers, registered around each wind speed. Here, it is proposed to use modified z score method for

detecting that type of outliers, (Pham, 2006). The modified z-score of an observation is defined as:

$$M_i = \frac{0.6745(P_i - \tilde{P})}{MAD} \tag{1}$$

with MAD denoting the median absolute deviation. We have a sample of N observations with median \tilde{P} . Outliers detected at each wind speed by the modified z-score, are around 0.3%.

- iii) Outliers which are detected below the cut-in wind speed and above 23 m/s. Since, the production of electricity at intake wind speeds in the interval 0-3.5 m/s is insignificant, these data are eliminated. Similar, there were not any significant power output points for the wind speed interval from 23 m/s and along. In the range 23-25 m/s, only 0.08% of data was registered and the output power was not as expected.

Discarded data in percent from the whole data base for WT13, according to the three criteria, is 39,14%. The recorded data for produced electric power and turbine efficiency, compared to the guaranteed curves from the manufacturer, are shown in figure 1.

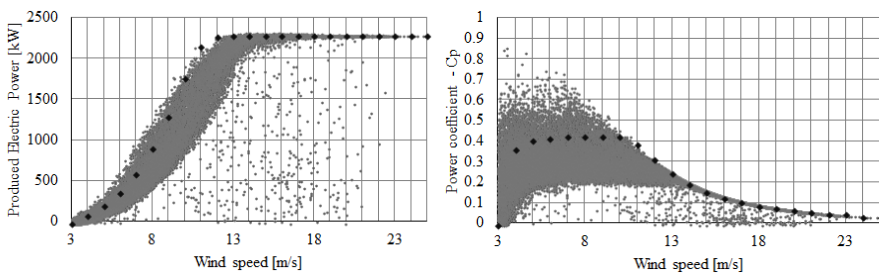


Figure 8: Scatter plot of the wind speed vs the power output and wind speed vs power coefficient, during 2016

There are several ways to study a one-dimensional data set. In this study, we applied the statistical boxplot technique to establish the variabilities of wind turbine power output and efficiency, (Shongwe *et al.*, 2006). This methodology includes information on estimated values, their location (mean or median), scale

(interquartile range), and asymmetry (difference between quartile and median). Having big variations above and under the box plot, means that the maximum and minimum value of measured wind speed appear far from the average calculated values, which cannot be established as a virtue for the certain location. As much as wider boundaries of the box and shorter whiskers it means that there is a small variability of wind and that it blows with unalterable speed. The variations, shown in figure 2, indicate huge dispersed data detected among the wind speed that are the most frequent at this site (3-8 m/s).

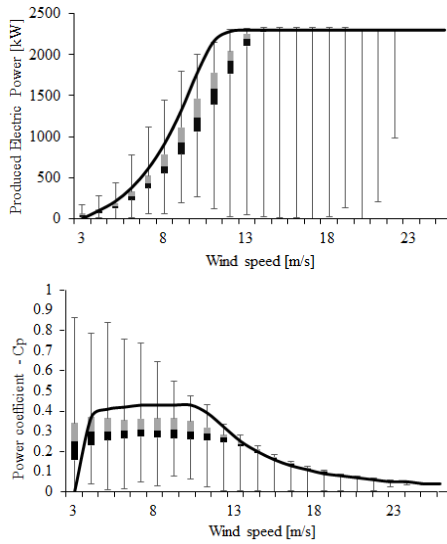


Figure 2: Boxplot showing the variability of power output and power coefficient, during 2016

After establishing the power curves for WT13, the procedure to carry out the power performance verification is next to be done.

Canonical correlation analysis (CCA) represents a method for exploring the relationships between two multivariate sets of variables, all measured on the same individual, (Everitt et al., 2006), (Steiger *et al.*, 1982).

$$\mathbf{X} = \begin{bmatrix} x_{11} & \cdots & x_{1p} \\ \vdots & \ddots & \vdots \\ x_{n1} & \cdots & x_{np} \end{bmatrix} = \begin{bmatrix} X_1 \\ \vdots \\ X_n \end{bmatrix} \wedge \mathbf{Y} = \begin{bmatrix} y_{11} & \cdots & y_{1q} \\ \vdots & \ddots & \vdots \\ y_{n1} & \cdots & y_{nq} \end{bmatrix} = \begin{bmatrix} Y_1 \\ \vdots \\ Y_n \end{bmatrix} \quad (2)$$

For CCA, \mathbf{X} has to be an $n \times p$ and \mathbf{Y} $n \times q$ matrix, with p and q at least 2, where p is the number of variables contained in the set \mathbf{X} and q is the number of variables in the set \mathbf{Y} .

There are different canonical variates within each set. If there are p variables in \mathbf{X} and q variables in \mathbf{Y} , then there are at most $k = \min(p, q)$ canonical variates in either set. These are $U_i = a_i'X$ and $V_i = b_i'Y$, with i ranging from 1 to k . Across each set, U_i and V_i are uncorrelated. The correlation between corresponding canonical variates U_i and V_i is the i^{th} canonical correlation, as shown in (3). In the other words, the first canonical variate is the linear combination of variables in one set that has the highest possible multiple correlation with the variables in the other set, (Steiger *et al.*, 1982).

$$\text{Var}(U_i) = a' \Sigma_{1p} a \ ; \ \text{Var}(V_i) = b' \Sigma_{nq} b \ ; \ \text{Cov}(U_i, V_i) = a' \Sigma_{pq} b \quad (3)$$

The first pair of canonical variables, or first canonical coefficient, is the pair of linear combinations U_1, V_1 having unit variances, which maximize the correlation. The k^{th} canonical coefficient is the pair of linear combinations U_k, V_k having unit variances, which maximize the correlation among all choices uncorrelated with the previous $k-1$ canonical variable pairs, [8]. The existence of overall relationships between two sets of variables is tested by the canonical correlation coefficients and the significance measures the size of relationships. As the correlation coefficients have greater value, the similarity in the set is higher.

Lastly Wilk's lambda, is used as a test of significance of the canonical correlation coefficient. The closer to zero the statistic is, the more the variable in question contributes to the model. The null hypothesis is rejected, when Wilk's lambda is close to zero, although this should be done in combination with a small p -value (Borovsky, 2014). The null hypothesis is that the data among one set are strongly correlated and the significance level is 5 %. Wilk's lambda is given as:

$$\Lambda = \prod_{p=1}^k \frac{1}{1 + \lambda_p} \quad (4)$$

where $\lambda_1, \dots, \lambda_p$ are eigenvalues of from the matrix term produced from the submatrices of the covariance matrix, (Pedersen, 2001).

In our case, WT13 is a single individual, the set X contains the wind speed and power output vector data from GCp, and Y contains the wind speed and power output vector data from the calculated WT curve. Namely, $p=q=2$ (two vector columns for wind speed and power output) and the number of sets is $n=1, \dots, 20$ because of the wind speeds range, 4-23 m/s. Since, we are testing bivariate set of variables, the number of correlation coefficients is two (F_1, F_2). Table 1 shows the calculations obtained with the CCA. Taking into consideration all test score values listed in the table, it can be considered that there is a positive correlation among WT13 with the GCp. "Sig" or significance (p -value) is to quantify the importance of the canonical coefficients. If the significance is small, (i.e. under 0.05) the null hypothesis will be reject. The statistical significance is additional measurement when the values of the canonical coefficients F_1 and F_2 are questionable, or have values with limited importance for the canonical correlation, (Steiger *et al.*, 1982). From Table 1, it can be noted that test measures are significant with $p < 0.05$. The correlation output shows overall model fitting.

Table 1: Results of the CCA at significance level of 5 %

No. WT	F_1	F_2	Wilk's λ_1	Sig. (1)	Wilk's λ_2	Sig. (2)
WT13	0.921	0.097	0.151	0.161	0.991	0.693

3 Conclusion

In the paper, a subsequent methodology for obtaining and verification of power curve of a wind turbine in operation has been presented. The usefulness of the canonical correlation analyses is demonstrated by applying over actual WF data. For a more detailed and more reliable verification of the power curve, the method seeks for similarity among the most frequent data pairs, not only comparison of the WT power output and the one provided by the WT manufacturer. The following experience has been gained by the application of the methodology:

- i) it is well situated to analyze changes of the power curve of WT- both separate for each interval of the GPC, and overall assessment;
- ii) the procedure is not subject to any costs, as only SCADA data is needed
- iii) there is no necessity of air density data normalization, as in IEC 61400-12-1;
- iv) the methodology is less sensitive to site effects than measurements with masts;

- v) the WT power curve verification method is not a significant problem. This however is very dependent on data purification from outliers. As noted in the identification criteria of outliers, the whole process of filtering the data must be accomplished deliberately in order not to remove relevant data from the power performance of the WTs.

References

- Borovsky, J. E., (2014). Canonical correlation analysis of the combined solar wind and geomagnetic index data sets. *Journal of Geophysical Research: Space Physics*, 119, 5364–5381.
- Everitt, B. S., Howell, D., (2005). *Encyclopedia of Statistics in Behavioral Science*. Hoboken, New Jersey, John Wiley & Sons, ISBN: 978-0-470-86080-9.
- IEC 61400. Part 12–1: Power Performance Measurements of Electricity Producing Wind Turbines; IEC 61400-12-1, International Standard; 2005.
- Pedersen, F., Gjerding, S., Enevoldsen, P., Hansen, J. K., Jørgensen, H. K., (2002). Wind turbine power performance verification in complex terrain and wind farms. *Forskningscenter Risoe. Risoe-R; No. 1330*.
- Pham, H., (2006). *Handbook of Engineering Statistics*, Springer-Verlang, 117-118.
- Shongwe, M. E., Landman, W. A., Mason, S. J., (2006). Performance of recalibration systems for GCM forecasts for Southern Africa. *International Journal of Climatology*, 1, 1567-1585.
- Steiger, J. H., Hakstian, A. R., (1982). The asymptotic distribution of elements of a correlation matrix: Theory and application. *British Journal of Mathematical and Statistical Psychology*, 35(2), 208–215.
- Ye, X., Lu, Z., Qiao, Y., Min, Y., O'Malley, M., (2016). Identification and Correction of Outliers in Wind Farm Time Series Power Data. *IEEE Transactions on power systems*, 31(6), 4197-4205.

An Analysis of Possible Applications of Combined Fuzzy Logic to Cause-Effect Analysis

IVICA PETROVIĆ, MARINKO BARUKČIĆ, ŽELJKO HEDERIĆ
& NENAD CVETKOVIĆ

Abstract In the power system, network elements are sometimes exposed to very complex malfunctions and disturbances, the causes and consequences of which are very difficult to see and determine via the power system management. This is especially noticeable at fault in thunderstorms, which are caused by lightning strikes directly or near the plant. This article presents problems related to determining the location of a lightning strike and the failure of a network element at an event of a fault in the network. Combined fuzzy logic applications are featured using expert knowledge of individuals to determine the connection between a nearby lightning or a lightning strike or in the transmission network itself. Data from the SCADA system (real-time network state data) and Lightning Locating System (LLS) data that link lightning current and lightning location data to individual network elements have been used

Keywords: • fuzzy logic • fault detection • cause-effect analysis • expert knowledge • lighting strike •

CORRESPONDENCE ADDRESS: Ivica Petrović PhD, Croatian Transmission System Operator Ltd., Vukovarska 217, 31000 Osijek, Croatia, e-mail: ivica.petrovic@hops.hr. Marinko Barukčić, PhD, Assistant Professor, Faculty of Electrical Engineering, Computer Science and Information Technology Osijek, Kneza Trpimira 2B, 31000 Osijek, Croatia, e-mail: marinko.barukcic@ferit.hr. Željko Hederić, PhD, Associate Professor, Faculty of Electrical Engineering, Computer Science and Information Technology Osijek, Kneza Trpimira 2B, 31000 Osijek, Croatia, e-mail: zeljko.hederic@ferit.hr. Nenad Cvetković, PhD, Assistant Professor, Faculty of Electronic Engineering, A. Medvedeva 14, 18000 Niš, Serbia, e-mail: nenad.cvetkovic@elfak.ni.ac.rs.

1 Introduction

In a large number of scientific papers, the problem of determining the location of fault in transmission networks (Lee et al., 2000), the characteristics of these networks, their protection and automation (Yongli et al., 1994; Vachtsevanos 2006) are being discussed. Problems of allocation and correlation of the lightning strike location and the failure of a network element as an event of a fault in the network are not adequately researched (Hsu et al., 1991; Saha et al., 2010; Petrović et al., 2015). This article presents problems related to determining the location of a lightning strike and the failure of a network element as an event of a fault in the network (Meza et al., 2001).

2 Possibility to determine the correlation between lightning strike and failure location in the network

In Energy Management System (EMS), a cause-effect analysis is based on information from Supervisory Control And Data Acquisition (SCADA) and Live Line Maintenance (LLM) systems. In doing so, along with the applied fuzzy logic, some phenomena and laws important for determining the correlation between lightning strike and failure location will be taken into account. In real-time, the SCADA system performs a system management based on information from the event list, chronology of events, alarms, switch status changes, incentives and actions of protection, changes in voltages and current. Information on lightning strike locations as well as the lightning strike value the system operator receives from the LLM system.

Modern SCADA and LLM systems are highly complex systems. Simultaneous failures in complex determination of faulty element induced by a lightning strike near or network element itself is a major challenge. Determination of the correlation of an event of failure and lightning strike directly or near the plant can be described by changes in the following parameters or sizes: change of switch state of a branch of the network, change of direction or current value to some element of the network, the amount of voltage on a network element, encouragement or protection action, current value of lightning strike in some network element, location of lightning strike in network element (Fig. 1.).

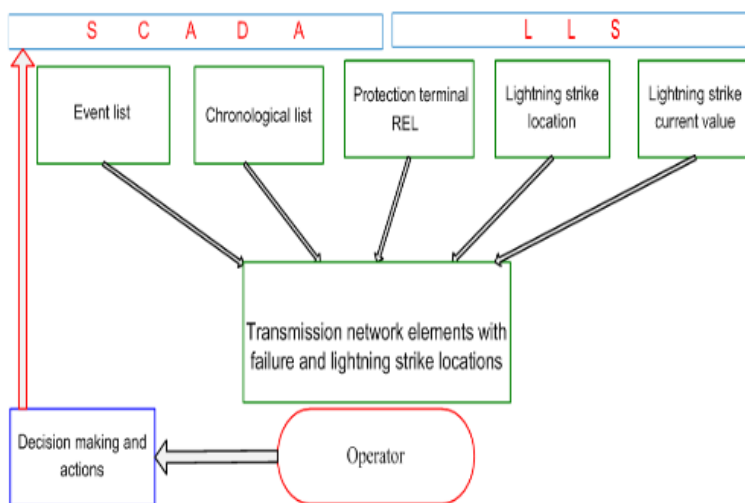


Figure 1: Schematic representation of the flow of information for decision making in Energy Management System.

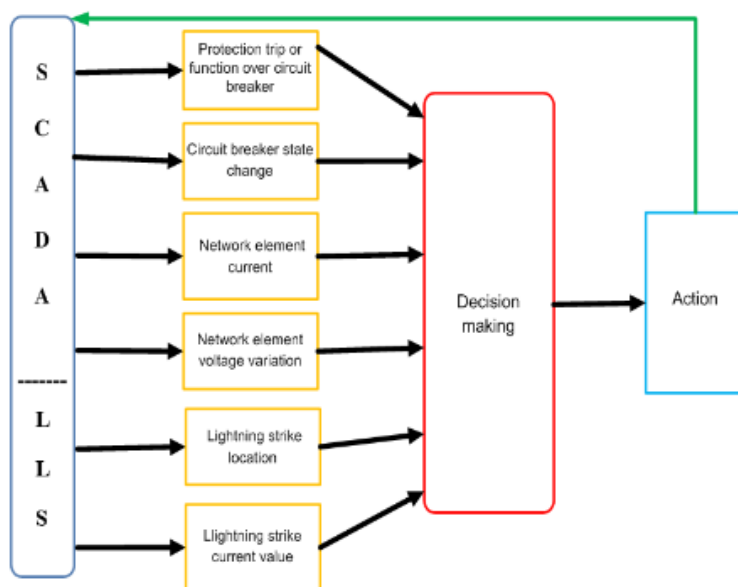


Figure 2: Overview of the fuzzy regulator in Energy Management System

By analyzing the input data, most of the causes and the correlation of the location of fault in transmission networks and the lightning strike locations can be determined. In doing so, to determine the location of the fault, the necessary are

information on changes to the switch, the value and change of the current value, voltage changes, the value of current lightning and lightning location.

Deciding and concluding in conducting a complex process of determining the correlation of the lightning strike location and the location of the failure is based on the expert knowledge and experience. Determination of correlations is based on the values of the six input parameters and the range of their values. Figure 2 shows a decision-making system that uses fuzzy logic to determine the location of the lightning strike and the location of the fault on the network element.

3 Input parameters in the fuzzy control system

For a complete overview of the function of the fuzzy controller and its creation, it is necessary to determine and define its corresponding function for each size. These corresponding functions of affiliation are important for defining the rules of conclusion and decision-making. The action or incentive of the circuit breaker protection of the network element is the first input size of the fuzzy controller and its locking system, which is the value determined by the trigger state or protection order on the network element. There may be two states of the network element: (1) unchanged state - lack of incentives or actions, (2) the changed state - the existence of incentives or actions (shown on Fig. 3.).

The same principle is applied to determination of the membership functions for the input size of the action or incentive to protect the network element switch. Two conditions can occur: (1) unchanged state - no change of switch state of the switch, (2) changed state - change in the switch state of the switch. For the unchanged state, the corresponding affiliation function has a value of 0, and for the changed state the corresponding affiliation function has a value of 1.

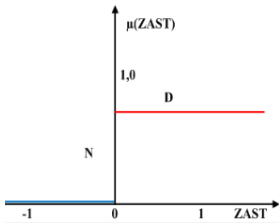


Figure 3. Membership function of the encouragement or protection action (ZAST)

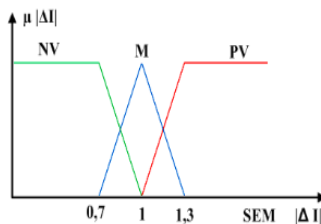


Figure 4. Membership function for absolute sensitivity to current change

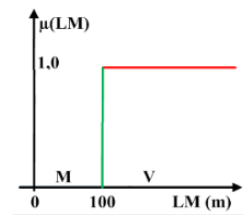


Figure 5. Membership function of the lightning strike location (LM)

The change of current through the network element to the network element is the input size of the system, which represents the change of current through the network element. To determine the change of current through the network element, it is necessary to define and determine the sensitivity indexes of the current change through the network element.

If with $|\Delta I|$ we denote the absolute value of the change of current sensitivity through the network element, then we can define it with the change in the amount and current of the current by the element of the network in relation to the state before that change and current before that change on the given element of the network.

Then the absolute sensitivity of the current change can be expressed as: (1):

$$|\Delta I| = \frac{(I_t - I_n)}{I_n} \quad (1)$$

where I_t is a currents after an event or change, and I_n is a current before an event or before a change of value. The corresponding membership function is defined in Figure 4 where negative high sensitivity is labeled with a NV, a low sensitivity is labeled with a M and positive high sensitivity is labeled with a PV. For the voltage change on the network element is applied the same principle as for the current. The location of lightning strike in a proximity or network element is the input size of a fuzzy controller marked LM and represents the value determined by a lightning strike in the network element. There are two experimentally determined states in the LLM system: (1) lightning strike (up to

100 m), (2) no lightning strike. Figure 5 shows the membership function for the lightning strike location in the LM network element. For a large distance from the network element (V), the corresponding affiliation function has a value of 0 and for a small distance from the network element (M) the corresponding affiliation function has a value of 1.

4 Conclusion on determining the correlation of the lightning strike location and the location of the failure

The baseline of improper system conclusion is determined based on the knowledge of the individual operator and is determined by several basic rules for determining the correlation between the location of the failure and the location of the lightning strike when running the EMS for different network elements.

Table 1. Example of the fuzzy system conclusion to determine the correlation between the location of the failure and the location of the lightning strike

Rule Number	ZAST	SP	SEM	PN	LM	SM	Output X'_i
1	D	D	PV	M			NK
2	D	D	PV	NV			PK
3							NK
...							...
216							NK

Table 2. Conversion of output parameters from the fuzzy system (language variables) to the corresponding numerical output parameters

X_i	PK	NK
numerical output parameters	1	0

Defining the rules of conclusion and making conclusions reduces the possibility of errors that may arise in running EMS. Based on the aforementioned expert rules for determining the failure of the network element, the baseline rule of the fuzzy system for determining the primary failure was derived as symbolically and shown in Table 1.

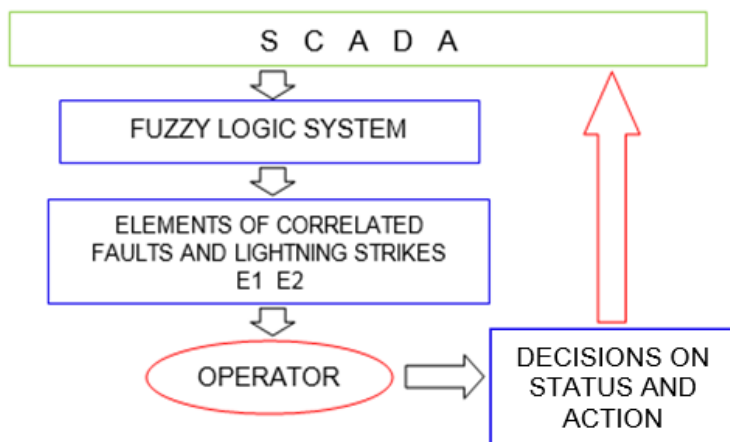


Figure 6. Schematic representation of information processing and decision making

Each tested or diagnosed network element can only occupy one state or one value (1 or 0), ie fault is correlated to the lightning strike or network element fault is uncorrelated to the lightning strike (the same state is if element is OK). Finally, a list of elements E1 and E2 is created, arranged in the order of 1 or 2, as follows: list of elements with correlated faults, list of elements without fault or uncorrelated fault. Creating a list of failures and determining the connection failure from the list of network elements is performed automatically based on the already established priority and order as shown in Figure 6.

5 Conclusion

In the analysis of failures in lightning strikes in real time, it is often extremely difficult to establish a connection between the affected network element and the lightning stroke in the vicinity of the element itself or the network. Existing methods, analysis and fault detection procedures are slow and quite unsafe to detect this linkage, so the success of the test procedure is determined by the knowledge and experience of each operator. This paper presents the application of the combined fuzzy logic to cause-effect analysis for the fault detection in the Transmission Network test with one minute sample period data. The creation of a controller based on fuzzy logic and certain rules of conclusion combined with the classical method enabled the testing and determination of the connection between the lightning strike and the associated failure. This enables operators to provide timely information on system management, which significantly

contributes to faster failure elimination and a significant increase in system security.

References

- Lee H. J., Ahn B. S., Park Y. M. (2000). A fault diagnosis expert system for distribution substations. *IEEE Transactions on power delivery*, 15(1), 92-97.
- Vachtsevanos G., et al. (2006). *Intelligent fault diagnosis and prognosis for engineering systems*. John Wiley & Sons, New Jersey, 2006.
- Yongli Z., Yang Y. H., Hogg B. W., Zhang W. Q., Gao S. (1994). An expert system for power system fault analysis. *IEEE Transactions on power systems*, 9(1), 503-509.
- Saha M. M., Izykowski J., Rosolowski E. (2010). *Fault location on Power Networks*. Springer-Verlag, London.
- Hsu Y. Y., et al. (1991). An expert system for locating distribution system faults. *IEEE Transactions on power delivery*, 6(1), 366-372.
- Petrović I., Jozsa L., Baus Z. (2015). Use of fuzzy logic systems for assessment of primary faults. *Journal of electrical engineering*, 66(5), 257–263.
- E. M. Meza, J. C. S. de Souza, M. T. Schilling and M. B. Do Coutto Filho. (2001). Exploring fuzzy relations for alarm processing and fault location in electrical power systems. *IEEE Porto Power Tech Proceedings (Cat. No.01EX502)*. doi: 10.1109/PTC.2001.964909

Measurement System for Testing of Electric Drives in Electric Vehicles

IZTOK BRINOVAR, GREGOR SRPČIČ, SEBASTIJAN SEME, BOJAN
ŠTUMBERGER & MIRALEM HADŽISELIMOVIĆ

Abstract This paper deals with the implementation of a measurement system, capable of performing real-time data acquisition and control, and allows the performance analysis of electric drives used for electric vehicle propulsion. For applying the mechanical load on the shaft of the tested motor three different test bench configurations with different power and speed ranges can be used. The main objective of the measurement system is to perform routine performance tests and road simulation tests (in terms of driving cycles) of an electric drive. It provides a research environment for analysis, investigation and study of electric drives and control strategies.

Keywords: • measurement system • test bench • electric machines •
electric vehicles • permanent magnet synchronous motor •

CORRESPONDENCE ADDRESS: Iztok Brinovar, Assistant, University of Maribor, Faculty of Energy Technology, Hočevarjev trg 1, 8270 Krško, Slovenia, iztok.brinovar@um.si. Gregor Srpčič, Assistant, University of Maribor, Faculty of Energy Technology, Hočevarjev trg 1, 8270 Krško, Slovenia, grega.srpcc@um.si. Sebastijan Seme, PhD, Associate Professor, University of Maribor, Faculty of Energy Technology, Hočevarjev trg 1, 8270 Krško, Slovenia, sebastijan.seme@um.si. Bojan Štumberger, PhD, Full Professor, University of Maribor, Faculty of Energy Technology, Hočevarjev trg 1, 8270 Krško, Slovenia, bojan.stumberger@um.si. Miralem Hadžiselimović, PhD, Full Professor, University of Maribor, Faculty of Energy Technology, Hočevarjev trg 1, 8270 Krško, Slovenia, miralem.h@um.si.

1 Introduction

Due to high oil consumption rate of the transportation sector and its environmental impact, more and more attention is dedicated in to studies and development of new technologies such as hybrid electric and electric vehicles. Electric vehicles adoption brings several benefits, such as air quality improvements and reduced noise, as well as climate change-related benefits. Compared to conventional vehicles with internal combustion engine (ICE) electric vehicles also have higher energy efficiency and low maintenance costs.

Energy storage systems and electric drives are the main components of electric vehicles that define their cost, energy efficiency, driving range, speed and acceleration performances (Rassölkin et al., 2013). Electric drive system generally consists of an electric motor, power converters and electronic control system. The major requirements of an electric motor for electric vehicle applications are high torque and power density, high starting torque, wide speed range, high efficiency over wide speed and torque ranges, high reliability and robustness appropriate for the vehicle environment and dynamics. In this context, permanent magnet synchronous motors (PMSMs) are considered to be very suitable for electric vehicle propulsion systems (Estima et al., 2012; Zhu et al., 2007).

Consequently, this paper deals with the implementation of a measurement system, capable of performing real-time data acquisition and control, to study electric drives in electric vehicles. The main objective of the measurement system is to perform routine performance tests and road simulation tests (in terms of driving cycles) of an electric drive used for electric vehicle propulsion. Driving cycles are a recognised and objective way to analyse energy consumption of electric vehicles and their electric ranges. The New European Driving Cycle (NEDC, Figure 1) is a driving cycle designed for measurements of emissions and fuel consumption in conventional vehicles and also frequently used for measurements of energy consumption of electric vehicles and efficiency analysis of their electric drives. The following section provides a basic description of the measurement system and its components.

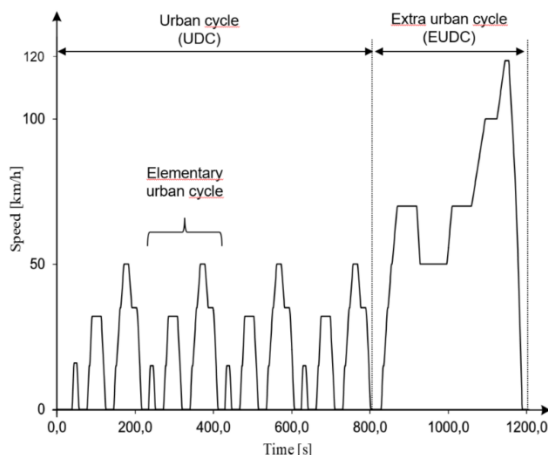


Figure 1: NEDC driving cycle.

2 Basic description of the measurement system

The measurement system, developed in the Electric machines and drives laboratory at the Institute of energy technology, has three main components, as in (Schupbach et al., 2002): active load machine, a real-time data acquisition and control system, and a motor drive under test. The schematic presentation of the measurement system is shown in Figure 2, while general view of the measurement system is shown in Figure 3 (test bench III.). The measurement system incorporates two motor drives. The propulsion motor drive under test consists of a PMSM and a VSI converter.

For applying the mechanical load on the shaft of the tested motor three different test bench configurations with different power and speed ranges can be used:

- test bench I.: induction machine with a power of 200kW and 5000rpm;
- test bench II.: permanent magnet synchronous machine with a power of 75kW and 15000rpm;
- test bench III.: permanent magnet synchronous machine with a power of 15kW and 30000rpm.

The real-time data acquisition and control system is implemented using a HBM T40B torque/speed sensor and the dSpace PPC 1103 controller board. Readings

of electrical and mechanical quantities are also obtained with dSpace PPC 1103 controller board throughout the internal AD converter. The dSpace system interfaces with Matlab/Simulink and allows processing of controlled signals, generation of graphical user interfaces, data analysis and plotting (Schupbach et al., 2002). Additionally, the measurement system is equipped with a high precision power analyser Yokogawa WT1800.

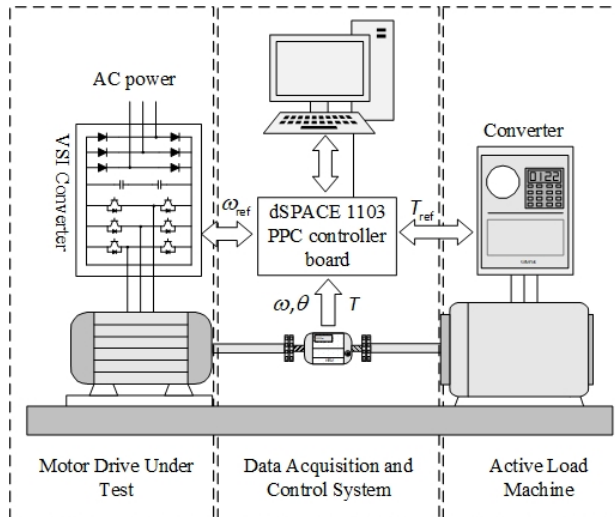


Figure 2: Schematic presentation of the measurement system and its components.

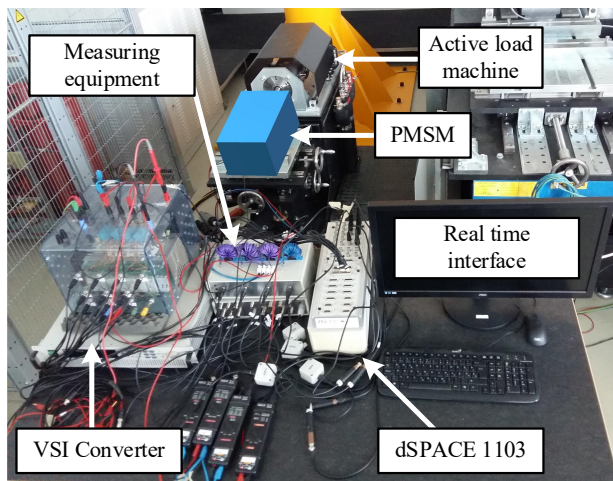


Figure 3: General view of the measurement system (test bench III).

The motor drive under test operates in speed control mode to follow the test cycles (driving cycles in terms of speed profiles) that reproduce the actual operating conditions, whereas the active load drive operates in torque control mode to follow the torque references.

3 Conclusion

This paper deals with the implementation of a measurement system for testing of electric drives in electric vehicles. The presented measurement system is capable of performing real-time data acquisition and control, and allows the performance analysis of electric drives used for electric vehicle propulsion. It provides a research environment for analysis, investigation and study of electric drives and control strategies. It should be noted that the presented paper is a starting point of a larger study within the doctoral dissertation.

References

- A.Rassölkin, V.Vodovozov, (2013). A test bench to study propulsion drives of electric vehicles. *International Conference-Workshop Compatibility and Power Electronics*, Ljubljana, 2013, pp. 275-279.
- J.O.Estima, A.J.Marques Cardoso, (2012). Efficiency Analysis of Drive Train Topologies Applied to Electric/Hybrid Vehicles. *IEEE Transactions on Vehicular Technology*, vol. 61, no. 3, pp. 1021-1031, March 2012.
- Z.Q.Zhu, D.Howe, (2007). Electrical Machines and Drives for Electric, Hybrid, and Fuel Cell Vehicles. *Proceedings of the IEEE*, vol. 95, no. 4, pp. 746-765, April 2007.
- R.M. Schupbach, J.C. Balda, (2002) . A Versatile Laboratory Test Bench for Developing Powertrains of Electric Vehicles. *Proceedings IEEE 56th Vehicular Technology Conference*, 2002, pp. 1666-1670 vol.3.

Minimization of Distribution Network Losses Using Optimal PV Installation, Reactive Power Generation and Network Reconfiguration

NEVENA SREČKOVIĆ, NIKO LUKAČ, BORUT ŽALIK &
GORAZD ŠTUMBERGER

Abstract A necessity for novel algorithms for the distribution network design, control, operation and optimization arises, with a proliferated integration of distributed generation units. This paper discusses the problem of large-scale integration of photovoltaic (PV) systems within the urban low voltage distribution networks, with the goal of minimization of distribution network losses, through simultaneous consideration of PV potential of rooftop surfaces as well as time-dependent network operation and its configurations. Presented methodology has the goal of minimization of annual energy losses in the network, by searching for optimal roof surfaces for PV installation, reactive power generation from PV units, and optimal network configuration. The optimization algorithm is based on differential evolution, and its performance is demonstrated in a case study on a real urban low voltage part of the distribution network.

Keywords: • distribution network • minimization of energy losses • PV potential • reactive power generation • network reconfiguration •

CORRESPONDENCE ADDRESS: Nevena Srečković, MSc, Young Researcher, University of Maribor, Faculty Electrical Engineering and Computer Science, Koroška cesta 46, 2000 Maribor, Slovenia, e-mail: nevena.sreckovic@um.si. Niko Lukač, PhD, Assistant Professor, University of Maribor, Faculty Electrical Engineering and Computer Science, Koroška cesta 46, 2000 Maribor, Slovenia, e-mail: niko.lukac@um.si. Borut Žalik, PhD, Full Professor, University of Maribor, Faculty Electrical Engineering and Computer Science, Koroška cesta 46, 2000 Maribor, Slovenia, e-mail: borut.zalik@um.si. Gorazd Štumberger, PhD, Full Professor, University of Maribor, Faculty of Electrical Engineering and Computer Science, Koroška cesta 46, 2000 Maribor, Slovenia, e-mail: gorazd.stumberger@um.si.

1 Introduction

Evolution of distribution networks from a passive to an active element of electric power systems, driven by the political directives promoting proliferated integration of renewable energy resources, results in the necessity for novel algorithms that will address different aspects of distribution network design, operation and control. Furthermore, urban areas could significantly contribute to the share of photovoltaic (PV) systems, connected to the low voltage networks in a near future, due to net metering and financial subsidies available. Numerous approaches to optimal placement of PV systems already exist. Some of them aim to optimize different aspects of network operation, such as voltage profiles, power losses, operation costs etc. (Ehsan & Yang, 2018), (Pesaran H.A, Huy, & Ramachandaramurthy, 2017), while other search for locations, most suitable for PV installation regarding PV potential of buildings' rooftop surfaces, using Light Detection And Ranging (LiDAR) technologies, GIS-based methods, statistical modelling etc. (Lukač, Seme, Žlaus, Štumberger, & Žalik, 2014), (Mainzer et al., 2014). High resolution calculation of PV potential can furthermore be utilized to determine both the economically and environmentally suitable PV systems in urban areas (Lukač, Seme, Dežan, Žalik, & Štumberger, 2016) as well as to evaluate PV systems' impact on power quality (Seme, Lukač, Štumberger, & Hadžiselimović, 2017).

Novel procedure for determining roof surfaces suitable for installation of PV systems, considering both time-dependent network operation and suitability for installation regarding the PV potential, has been presented in (Srečković, Lukač, Žalik, & Štumberger, 2016). Network configuration and time-dependent network operation are both taken into account, when selecting those roof surfaces with the highest PV potential, resulting in the highest reduction of annual energy losses. This paper presents further development and an improvement of the research presented in (Srečković et al., 2016), in terms of consideration of additional search parameters, such as all possible network configurations and a reactive power generation from the PV systems, resulting in the development of methodology for minimization of annual energy losses in distribution networks. Next section describes the proposed methodology, followed by the presentation of the results achieved when implementing the methodology on a real, urban, low voltage distribution network.

2 Methodology

Proposed methodology for minimization of network losses can be described using the overlapping layers, where first layers include pre-processing of LiDAR data and calculation of rooftops' PV potential using the methodology presented in (Lukač et al., 2014). PV potential assessment is based on the processed LiDAR data, pyranometer measurements of direct and diffuse irradiance, and algorithm for consideration of shadowing (terrain, buildings, and vegetation). Rooftop surfaces are then rated, regarding their suitability for PV installation as having very high, high, medium and low suitability for PV installation. However, surfaces, suitable for installation with respect to PV potential, are not necessarily suitable from the network operation point of view. Therefore, the additional layers introduce the distribution network part of urban area, and include modelling the network, defining possible network configurations and assigning the loading and generation profiles for evaluation of time-dependent network operation. Proper overlapping of the layers allows the calculation of the additional PV generation at consumers' site, their reactive power generation and optimal network configuration, which will result in minimization of annual network losses.

Flowchart of the proposed procedure is presented in Figure 19. After modelling the distribution network, determining its possible configurations and evaluating the annual energy losses of the network operation in its original state, optimization method is utilized to reduce annual energy losses. Differential evolution (DE) (Storn & Price, 1997) is a stochastic optimization method, chosen for determining the optimal amounts of additional PV generation at low voltage consumers' location, reactive power generation from additional PV systems and network configuration, in accordance with the chosen objective function that minimizes the annual energy losses (1). Defined n search parameters $\mathbf{x}_p = \{x_{p,1}, x_{p,2} \dots x_{p,n}\}$, are following:

- $\{x_{p,1}, x_{p,2} \dots x_{p,n-2}\}$: share of possible PV generation at $n - 2$ locations in the network,
- $x_{p,n-1}$: reactive power generation, defined as the share of active power generation at the corresponding location (equal share for all locations)
- $x_{p,n}$: index of the network configuration.

The objective function (1) is defined as the quotient of the annual losses of the currently evaluated solution $W_{\text{loss_addPV}}$, and the losses of the original network W_{loss} . Penalties p ensure that voltage profiles and currents are kept within the prescribed limits

$$q_{\text{fun}} = \frac{W_{\text{loss_addPV}}}{W_{\text{loss}}} + p \quad (1)$$

After DE determines the optimal amount of additional PV generation, the final step of selecting those roof surfaces, which can generate the determined active power, remains. Surfaces that have higher suitability for PV installation are chosen first, followed by those of lower ratings, until the determined value of additional PV generation is achieved, ensuring the selection of minimum number of rooftops.

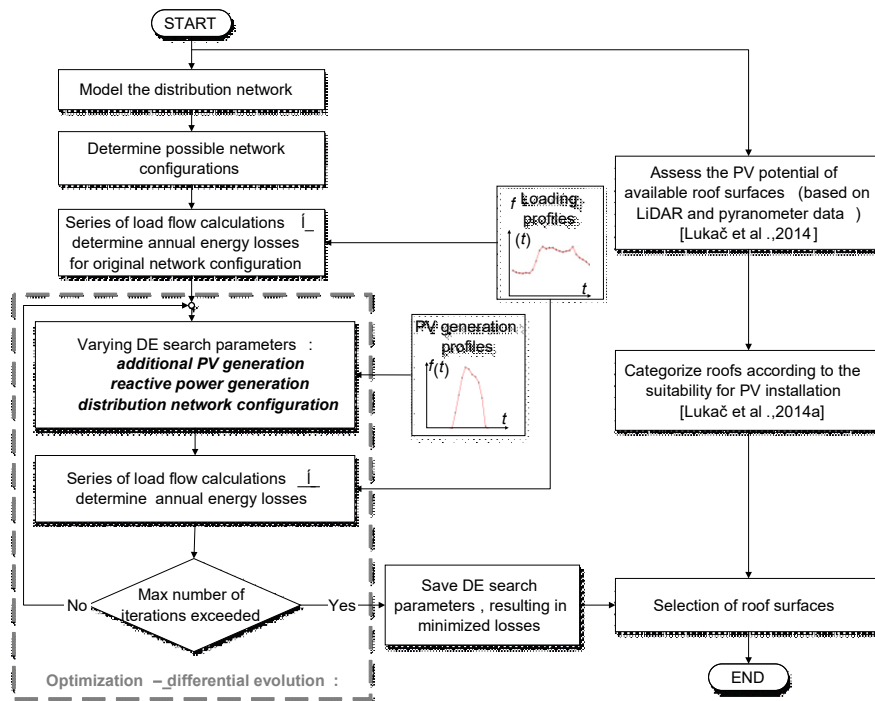


Figure 9: Flow chart of the proposed method.

3 Case study

The proposed methodology was tested in a case study on a part of real urban low voltage distribution network, presented in Figure 20. Topology of the network is defined using a graph, composed of 37 nodes and 39 line segments. Even though the network is designed in a meshed configuration, it operates exclusively radially, with 30 possible radial configurations. Considered part of the network supplies 22 low voltage consumers. Loading profiles, given for average day of every month, are calculated from a yearlong hourly measurements of active and reactive power on a 10.5/0.42 kV substation. Additional electric power generation from PV systems that could be placed on considered rooftop surfaces, for every hour in a year, is determined as in (Lukač et al., 2014), allowing the creation of hourly PV generation profiles for average day of every month. Colored polygons in Figure 20 represent 69 rooftop surfaces of different suitability for installation of PV systems, regarding their PV potential. Polygons are assumed to be connected to the closest low voltage consumer. Number of rooftop surfaces connected to each low voltage consumer, is given in table in Figure 20.

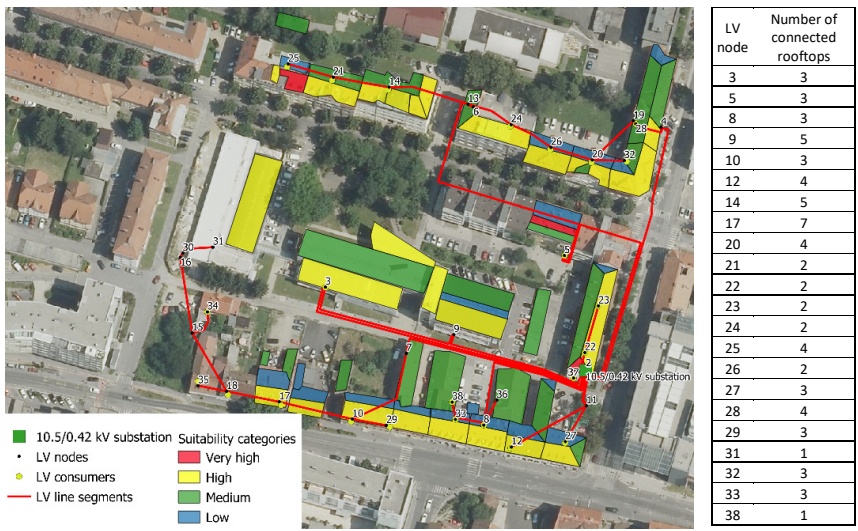


Figure 10: Test distribution network.

they may cause the reverse power flows, increase of losses or violations of voltage profiles or thermal overloading. Therefore, it is important to simultaneously consider both suitability of surfaces for installation of PV systems regarding their PV potential and effects that the PV systems' installation will have on a distribution network operation, through consideration of different distribution network parameters (in this case active and reactive power generation, network configuration, energy losses and voltage and current limitations).

Acknowledgments

This work was supported in part by the Slovenian Research Agency under research contracts: L2-5489, P2-0115, and J2-6764.

References

- Ehsan, A., & Yang, Q. (2018). Optimal integration and planning of renewable distributed generation in the power distribution networks: A review of analytical techniques. *Applied Energy*, 210, 44–59. <https://doi.org/10.1016/J.APENERGY.2017.10.106>
- Lukač, N., Seme, S., Dežan, K., Žalik, B., & Štumberger, G. (2016). Economic and environmental assessment of rooftops regarding suitability for photovoltaic systems installation based on remote sensing data. *Energy*, 107, 854–865. <https://doi.org/10.1016/J.ENERGY.2016.04.089>
- Lukač, N., Seme, S., Žlaus, D., Štumberger, G., & Žalik, B. (2014). Buildings roofs photovoltaic potential assessment based on LiDAR (Light Detection And Ranging) data. *Energy*, 66, 598–609. <https://doi.org/10.1016/J.ENERGY.2013.12.066>
- Mainzer, K., Fath, K., McKenna, R., Stengel, J., Fichtner, W., & Schultmann, F. (2014). A high-resolution determination of the technical potential for residential-roof-mounted photovoltaic systems in Germany. *Solar Energy*, 105, 715–731. <https://doi.org/10.1016/J.SOLENER.2014.04.015>
- Pesaran H.A, M., Huy, P. D., & Ramachandaramurthy, V. K. (2017). A review of the optimal allocation of distributed generation: Objectives, constraints, methods, and algorithms. *Renewable and Sustainable Energy Reviews*, 75, 293–312. <https://doi.org/10.1016/J.RSER.2016.10.071>
- Seme, S., Lukač, N., Štumberger, B., & Hadžiselimović, M. (2017). Power quality experimental analysis of grid-connected photovoltaic systems in urban distribution networks. *Energy*, 139, 1261–1266. <https://doi.org/10.1016/j.energy.2017.05.088>
- Srećković, N., Lukač, N., Žalik, B., & Štumberger, G. (2016). Determining roof surfaces suitable for the installation of PV (photovoltaic) systems, based on LiDAR (Light Detection And Ranging) data, pyranometer measurements, and distribution network configuration. *Energy*, 96. <https://doi.org/10.1016/j.energy.2015.12.078>

Storn, R., & Price, K. (1997). Differential Evolution – A Simple and Efficient Heuristic for global Optimization over Continuous Spaces. *Journal of Global Optimization*, 11(4), 341–359. <https://doi.org/10.1023/A:1008202821328>

Differential Evolution Based Mismatch Loss Optimisation in Photovoltaic Arrays

TOMISLAV MATIĆ, DAMIR BLAŽEVIĆ, DRAŽEN BAJER & IVAN VIDOVIĆ

Abstract Advantages of renewable energy over carbon based sources are more than obvious. Solar power plants are the most appealing green energy sources because of the availability, scalability and simplicity of installation. Nevertheless, solar power plants should be designed carefully to gain most of harvested sun.

In this paper we present a new method for photovoltaic (PV) panel sorting. Method is based on differential evolution (DE) and mismatch loss (MML) cost function. The goal is to minimize MML function for PV array arranged in strings with PV panels. Proposed approach is tested on real data and the results compared with several sorting methods.

Keywords: • photovoltaic • differential evolution • mismatch loss • sorting • DEPS method •

CORRESPONDENCE ADDRESS: Tomislav Matic, Josip Juraj Strossmayer University of Osijek, Faculty of Electrical Engineering, Computer Science and Information Technology Osijek, Kneza Trpimira 2B, HR-31000 Osijek, Croatia, e-mail: tomlav.matic1@ferit.hr. Damir Blažević, Josip Juraj Strossmayer University of Osijek, Faculty of Electrical Engineering, Computer Science and Information Technology Osijek, Kneza Trpimira 2B, HR-31000 Osijek, Croatia, e-mail: damir.blazevic@ferit.hr. Dražen Bajer, Josip Juraj Strossmayer University of Osijek, Faculty of Electrical Engineering, Computer Science and Information Technology Osijek, Kneza Trpimira 2B, HR-31000 Osijek, Croatia, e-mail: drazen.bajer@ferit.hr. Ivan Vidović, Josip Juraj Strossmayer University of Osijek, Faculty of Electrical Engineering, Computer Science and Information Technology Osijek, Kneza Trpimira 2B, HR-31000 Osijek, Croatia, e-mail: ivan.vidovic@ferit.hr.

1 Introduction

Renewable energy sources, wind and solar power plants could have a significant role in the stabilization of energy market prices (GTM Research, 2017; AWEA, 2016). Solar power plants are the most appealing green energy sources because of the availability, scalability and simplicity of installation. Nevertheless, solar power plants should be designed carefully to gain most of harvested sun. In this paper we present a new method for photovoltaic (PV) panel sorting. Method is based on differential evolution (DE) (Storn, 1997) and mismatch loss (MML) cost function.

2 Preliminaries

2.1 Mismatch loss

The goal is to minimize MML function for PV array arranged in M strings with L PV panels, cf. Fig. 1. All panels are characterized by maximum power point (MPP) specifications and fill factor (FF) (Kaushika, 2007). Variations in the current-voltage characteristics of PV panels can lead to significant power loss. Reducing the MML results in increased electricity production, higher efficiency and shorter return on investment period (Bucciarelli, 1979). In this paper MML cost function is defined as

$$\Delta P = \left(1 - \frac{1}{L}\right) \frac{1}{M} \left[\sum_{q=1}^M \omega_q \frac{(C'_q+2)}{2} \sigma_{\eta,q}^2 \right] + \frac{(C'+2)}{2} \frac{\sigma_{\xi}^2}{L} \left[1 - \frac{1}{M}\right] \quad (1)$$

where L is the number of panels per string, M is the number of parallel connected strings, σ_{η}^2 and σ_{ξ}^2 represent the variance of max-power current and voltage, respectively, C' modified cell characteristic factor given by Eq. (2), and ω_q is the ratio of the ideal power output of the q -th string and average ideal power output of all strings in the PV array (Weber, 2013).

$$\overline{FF} = \frac{C'^2}{(1+C')(C'+\ln(1+C'))} \quad (2)$$

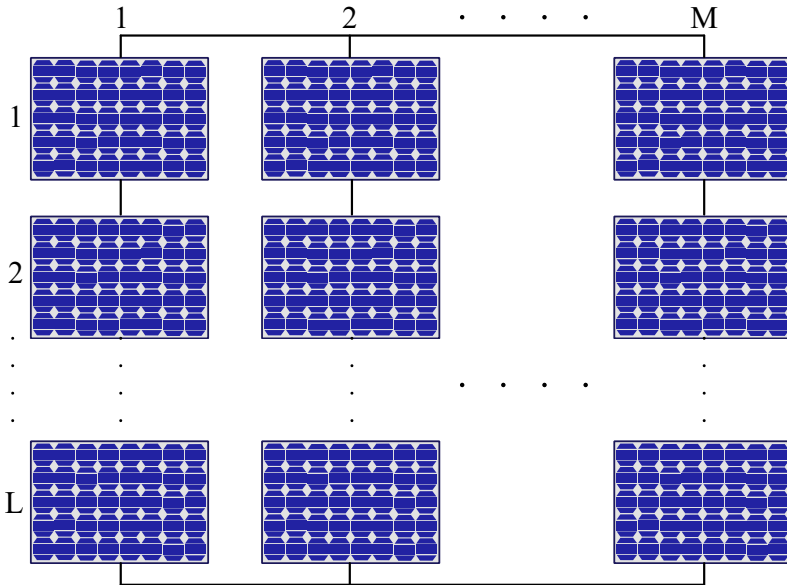


Figure 1: Illustration of a typical PV array.

In Eq. (2) \overline{FF} represents the average FF of the panels in the PV array. In the datasheets of the PV panels FF factor is given, C' is calculated as the polynomial approximation from Eq. (2).

2.2 Differential evolution

Differential evolution is an effective population-based method for global optimisation. Like other common evolutionary algorithms, it employs variation operators on population members for generating new ones, and selection to drive the search towards promising regions of the search space. The mode of operation of the DE algorithm can be briefly described as follows. Each member or vector $\vec{v}^i = (v_1, \dots, v_d)$ for $i = 1, \dots, NP$ of the population is initialised in a random fashion. Afterwards, the main-loop is executed until the termination condition is not met, where variation and selection are performed. The typical variation operators, mutation and crossover, are applied to chosen population members to sample the search space. Arguably, the most important element of DE is its characteristic mutation based on difference vectors. A popular approach to mutant creation is best/1 i.e. the linear combination $\vec{u}^j = \vec{v}^{bst} + F(\vec{v}^{r1} - \vec{v}^{r2})$, where bst is the index of the best population member, r1 and r2 are randomly

chosen indices such that $j \neq r1 \neq r2$, and F is the scale factor. Each mutant is crossed over with the currently selected population member---resulting in an offspring that competes for survival to the next iteration. A discrete crossover operator is typically applied creating the trial vector

$$\vec{t}^j = \begin{cases} \vec{u}_i^j & \text{if } rand(0,1) \leq CR \text{ or } r_j = i \\ \vec{v}_i^j & \text{otherwise} \end{cases} \quad (3)$$

where CR is the crossover-rate, $i = 1, \dots, d$, and r_j is randomly chosen from the set $\{1, \dots, d\}$. The created trial vector \vec{t}^j enters the next iteration if it is better than the target vector \vec{v}^j .

3 Proposed approach

Proposed approach (hereinafter referred to as DEPS) is a modified DE algorithm outlined in Fig. 2. Modifications are introduced to the population initialization and the calculation of candidate solutions. Moreover, a new step for dealing with stagnant solutions is added. The majority of modifications are aimed to increase the exploitation ability of the DE algorithm, while considering also the possibility of search stagnation. In Fig. 2 all made modifications are marked with brief comments (denoted with %).

The first step in the aforementioned direction was made with the population initialization. Initialization of N_D panels consists of two parts. First part, finds $Data_{Comb}$ (c.f. eq. 4) combinations of the available panels and selects N_{Comb} initial solutions with the smallest ΔP . In the second part, rest of the $N - N_{Comb}$ initial solutions are randomly generated. The generated population provides a good starting point for the search.

$$Data_{Comb} = (N_D - LM + 1)(N_D - LM/2 + 1 - (N_D - LM + 2)/2) \quad (4)$$

```
Set Parameters NP, CR and Pe;
Initialise population; %Best ΔP of Datacomb and random
While termination condition not met
  Update parameter F; %Randomly generated in [0.1, 0.5]
  Calculate candidate solutions %Based on DE/best/1/bin with base vector
  %mutation
  Perform selection
  If search stagnation occurred
    Reinitialise population; %10 percent best kept, rest randomly
    regenerated
```

Figure 2. High level outline of the proposed approach.

In order to provide a more diverse set of possible difference vectors, the scale factor is uniformly random generated at the beginning of each iteration.

Since the best/1 mutation strategy is highly exploitative and may lead to premature convergence, it was modified. In that regard, the base vector is mutated with a small probability of P_e . It must be remarked that a copy was generated and used as the base vector, hence elitism is maintained.

To further tackle the problem of premature convergence or search stagnation, a major part of the population is replaced by randomly generated solutions. More precisely, only the top 10% are kept, while the rest is replaced. The replacement occurs periodically i.e. every 50 iterations.

4 Experimental results

The proposed approach, DEPS, is tested on real data. All $N_D = 576$ panels are produced by the same manufacturer and all necessary specifications are given. In Fig. 3 installed panels are depicted. Specifications include FF, and IMPP, UMPP and PMPP which represent MPP current, voltage and power, respectively. The PV panels are sorted into six arrays with 42 panels that are equally divide into two strings ($M = 2, L = 21$). For initial population selection $N = 100$.

In order to present the benefits of DEPS it is compared with several sorting methods. The RND method represents the random selection of panels, while S/N, IMPP, UMPP, PMPP represent sorting by serial number, MPP current, voltage and power (in ascending order), respectively. The results obtained by the different methods are reported in Table I. where ΔP_Σ represents the sum of ΔP

values for all six arrays. From the presented results it can be seen that DEPS gives the best result i.e. lowest ΔP_{Σ} value. When compared to other methods, especially the commonly adopted method of sorting according to IMPP, DEPS produces a ΔP_{Σ} value that is over 16 times lower.



Figure 3: Installed real PV array of the used panels.

Table 1: Values of ΔP_{Σ} for different sorting methods (ratio is calculated relative to the proposed approach).

Sorting	S/N	RND	IMPP	UMPP	PMPP	DEPS
ΔP_{Σ}	1,2262	2,341	0,0285	0,8516	1,9074	0,0017
Ratio	708,5098	1352,6655	16,4688	492,0983	1102,1451	1

5 Conclusion

In this paper a new DEPS method for photovoltaic panel sorting is presented. DEPS is based on differential evolution and mismatch loss cost function. Proposed approach is tested on real data that consists of 579 panels that are produced by the same manufacturer. Results are compared with the RND method (random method), S/N method (sorting by serial number), IMPP method (sorting by serial current), UMPP method (sorting by serial voltage), PMPP method (sorting by serial power). DEPS produces the lowest value of the

mismatch loss cost function, that is over 16 times lower when compared to other tested methods.

References

- AWEA, American Wind Energy Association (2016). AWEA U.S. Wind Industry Annual Market Report, Year Ending 2016. Report.
- Bucciarelli L. L. (1979). Power loss in photovoltaic arrays due to mismatch in cell characteristic. *Solar Energy*, 23, No. 4, 277-288. doi: 10.1016/0038-092X(79)90121-X
- GTM Research, Solar Energy Industries Association (2017). Solar Market Insight Report 2017 Q2. Report
- Kaushika N. D., Rai A. K. (2007). An investigation of mismatch losses in solar photovoltaic cell networks. *Energy*, 32, No. 5, 755-759. doi:10.1016/j.energy.2006.06.017
- Storn, R., Price, K. (1997). Differential Evolution - a Simple and Efficient Heuristic for Global Optimization over Continuous Spaces. *Journal of Global Optimization*, 11, 341-359. doi: 10.1023/A:1008202821328
- Webber J., Riley E. (2013). Mismatch Loss Reduction in Photovoltaic Arrays as a Result of Sorting Photovoltaic Modules by Max-Power Parameters. *ISRN Renewable Energy*, 2013, 1-9. doi: 10.1155/2013/327835

Estimation of the Solar Irradiance on Tilted Surface for Different Types of Pyranometers

SEBASTIJAN SEME, KLEMEN SREDENŠEK, IZTOK BRINOVAR, GREGOR SRPČIČ, MIRALEM HADŽISELIMOVIČ & BOJAN ŠTUMBERGER

Abstract Accurate measurements of solar irradiance are important in many applications such as studying the distribution of received radiation or estimating the final yield of photovoltaic systems. This paper deals with evaluation of different types of pyranometers. The primary objective of this paper is to compare two types of pyranometers, with the use of mathematical model for predicting solar radiation on incline surface. The mathematical model shows that both types of pyranometers receives the highest annual average solar radiation with a surface facing 189° south and inclination angle of 44° . The results in this paper show that the deviation between silicon photodiode and thermopile pyranometer mostly occur, due to irregular calibration, frequent cleaning and errors of silicon photodiode pyranometer under overcast sky conditions.

Keywords: • pyranometer • solar radiation • azimuth angle • inclination angle • accuracy •

CORRESPONDENCE ADDRESS: Sebastijan Seme, PhD, Associate Professor, University of Maribor, Faculty of Energy Technology, Hočevarjev trg 1, 8270 Krško, Slovenia, e-mail: sebastijan.seme@um.si. Klemen Sredenshek, MSc, Researcher, University of Maribor, Faculty of Energy Technology, Hočevarjev trg 1, 8270 Krško, Slovenia, e-mail: klemen.sredensek@um.si. Iztok Brinovar, MSc, Assistant, University of Maribor, Faculty of Energy Technology, Hočevarjev trg 1, 8270 Krško, Slovenia, e-mail: iztok.brinovar@um.si. Gregor Srpčič, MSc, Assistant, University of Maribor, Faculty of Energy Technology, Hočevarjev trg 1, 8270 Krško, Slovenia, e-mail: gregor.srpacic@um.si. Miralem Hadžiselimović, PhD, Full Professor, University of Maribor, Faculty of Energy Technology, Hočevarjev trg 1, 8270 Krško, Slovenia, e-mail: miralem.h@um.si. Bojan Štumberger, PhD, Full Professor, University of Maribor, Faculty of Energy Technology, Hočevarjev trg 1, 8270 Krško, Slovenia, e-mail: bojan.stumberger@um.si.

1 Introduction

High-quality measurements are also necessary for the development of models for the prediction of solar radiation, typically used by meteorologists (Al-Rasheedi et al., 2018). The solar radiation is typically measured by thermopile or silicon photodiode pyranometer. Thermopile pyranometer may achieve the lowest uncertainty under most conditions, but cost more and they require frequent cleaning under arid conditions due to rapid dust soiling (Al-Rasheedi et al., 2018). Silicon photodiode pyranometer have become popular mainly because of their low cost, ease of maintenance and fast time response for high frequency data, but they provide limited spectral response. The evaluation of both types of pyranometers, require side-by-side comparisons, which can rarely be done in practice because many meteorological stations are equipped with only one type of pyranometer. The analysis of pyranometers accuracy was performed with the calculation of the optimal inclination and azimuth angle, which are the most important parameters that affect photovoltaic (PV) systems. The model for predicting solar radiation on different inclination and azimuth angles from typically measured global and diffuse solar radiation on horizontal surface was presented by many authors. Accurate measurements of solar radiation play an important role in determination of roof surfaces that are suitable for the PV system installation (Srećković et al., 2016) and for modelling the uncertainty of photovoltaic power production (Barukčić et al., 2018).

2 Meteorological station

The pyranometers are located on the roof of the Institute of Energy Technology, Krško (45.94° N, 15.51° E). At its final configuration, 6 pyranometers are installed: four silicon photodiode pyranometers facing 180° S with an inclination angle of 0°, 30°, 45° and 60° (K&Z SP Lite 2) and two thermopile pyranometers facing 180° S inclined at 0° and 45° (K&Z CMP10). For an initial analysis of the weather conditions in Slovenia, data from the first full 12-month period (January 2017 to December 2017) for global and diffuse solar radiation on horizontal surface are used. All pyranometers are installed on the pillar (see Fig. 1), without obstruction, that would cause shading. Since silicon-photodiode pyranometers measure only global solar radiation, the data for diffuse solar radiation was used from the nearby meteorological station (Slovenian Environmental Agency, 2017). Fig. 1 shows all 6 pyranometers installed at Institute of Energy Technology in Krško, Slovenia.

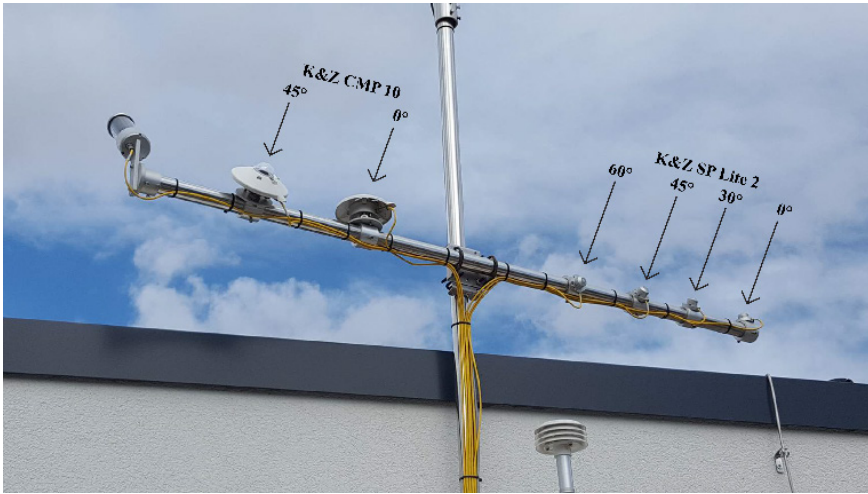


Figure1: Irradiance measurement station located on the roof of the Institute of Energy Technology.

3 Model for predicting solar radiation on inclined surfaces

The model for predicting solar radiation on inclined surface is divided into three basic components: direct (or beam) $G_{b,t}(t)$, diffuse $G_{d,t}(t)$ and reflected $G_{r,t}(t)$ component. The direct solar radiation on horizontal surface is converted into direct solar radiation on inclined surface by simple geometrical relationship between two surfaces. The conversion of diffuse solar radiation is much more complex, because it comes from all points of the sky, except the sun (Gulin et al., 2013). A relatively large number of models for inclined surfaces have been proposed, which includes isotropic and anisotropic models. The isotropic model (Koronakis et al., 1986) was chosen, due to accurate results in determining solar radiation on inclined surface in the four climate region (Slovenia). It is calculated by (1):

$$G_t(t) = G_{b,h}(t) \left(\frac{\cos i(t)}{\sin(\alpha_s)} \right) + G_{d,h}(t) \left(\frac{2 + \cos \beta(t)}{3} \right) + G_h(t) \rho \left(\frac{1 - \cos \beta(t)}{2} \right) \quad (1)$$

Where $G_{b,h}(t)$, $G_{d,h}(t)$ and $G_h(t)$ are direct, diffuse and global solar radiation on horizontal surface, $i(t)$ is incidence angle, $\alpha_s(t)$ solar altitude angle, $\beta(t)$ inclination angle and ρ surface albedo. The values of surface albedo were chosen for each month, based on a long-term measurement.

The statistical normalized root-mean-square error (NRMSE) was used to calculate the deviation between the modeled (see Eq. 1) and measured results. The NRMSE is calculated by (2):

$$NRMSE = \frac{\sqrt{\frac{\sum_{i=1}^n (x_{measured,i} - x_{modeled,i})^2}{n}}}{x_{measured,max} - x_{measured,min}} \quad (2)$$

Where $x_{measured,i}$ and $x_{modeled,i}$ are measured and modeled values of solar radiation on inclined surface, $x_{measured,max}$ and $x_{measured,min}$ are maximum and minimum values of measured solar radiation on inclined surface and n is the number of measurement data.

4 Results

The obtained results from Koronakis et al. (1986) model are compared with the measured results from pyranometers facing 180° south with an inclination angle of 30°, 45° and 60° (see Fig. 2). The modeled results are more accurate at lower inclination angles than the results at higher inclination angles. The modeled values show a stronger deviance, due to the error of assuming a constant surface albedo for each month. At higher inclination angles, both the diffuse and reflected component of sunlight become more dominant in determining the solar radiation on inclined surface (Khoo et al., 2014). The NRMSE method was used to calculate the deviation between modeled and measured results. The NRMSE results for pyranometers facing 180° south, with an inclination angle of 30°, 45°, 60° and 45° are 0.5608 %, 0.7592 %, 0.8396 % and 0.7861 %. It can be seen that as the angle increases, the NRMSEs also increase.

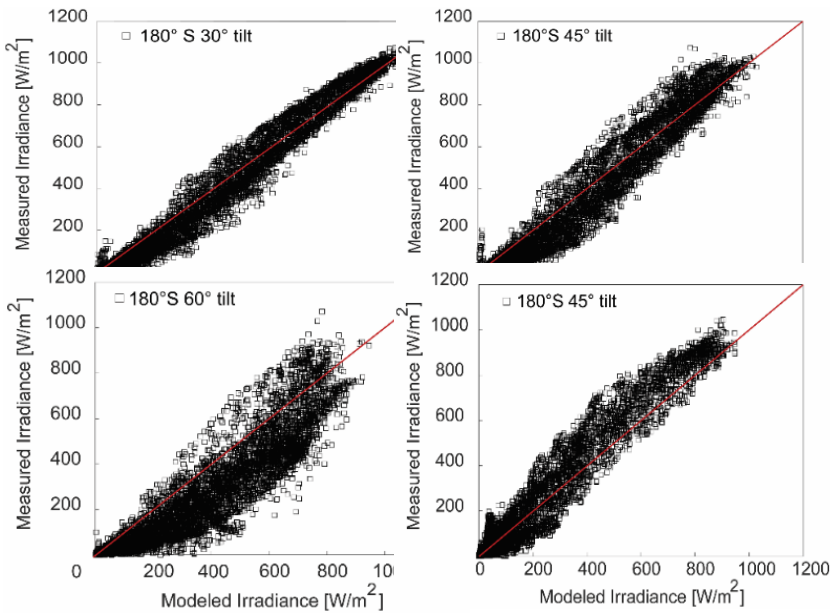


Figure 2: Modeled versus measured solar radiation using the Koronakis et al., (1986) model for pyranometers oriented at 180° S with inclination angles of 30°, 45° and 60°.

Using the Koronakis et al. (1986) model, the annual average solar radiation on inclined surface were calculated for silicon photodiode K&Z SP Lite 2 and thermopile K&Z CMP10 pyranometer from solar radiation data on horizontal surface (0°). Fig. 3 summarizes the results in a polar contour plot.

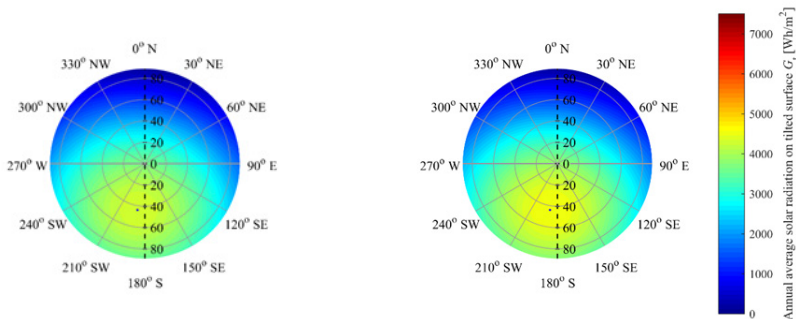


Figure 3: Polar contour plot of solar radiation on inclined surface for different inclination and azimuth angles for: a) pyranometer K&Z CMP10, b) pyranometer K&Z SP Lite 2.

Table 2: Comparison between both types of pyranometers.

	K&Z SP Lite 2	K&Z CMP10	Deviation
Inclination angle β [°]	44	44	0
Azimuth angle γ [°]	189	189	0
Annual solar radiation on inclined surface $G_t(t)$ [Wh/m ²]	4588,3	4337,4	250,9

The silicon photodiode pyranometer is calibrated under sunny, clear-sky conditions, so it closely matches the thermopile pyranometers in those conditions. The silicon photodiode pyranometer subsamples only the short-wave radiation (400 – 1100 nm, Kipp&Zonen, 2016), errors are introduced when the sky conditions change. The results in Fig. 3 and Table 2 show slight deviations of annual average solar radiation on inclined surface (250,9 Wh/m²), due to errors of silicon photodiode pyranometer under overcast sky conditions. The deviations also occur, due to different spectral ranges of pyranometers.

5 Conclusion

To evaluate different types of pyranometers, the model for predicting solar radiation on inclined surface was used to calculate the optimal inclination and azimuth angle. The optimal inclination and azimuth angle were determined by finding the value for which the solar radiation on particular surface was the highest for the one-year period. A comparison of the modeled results with the measured results showed that the modeled results are most accurate at lower inclination angles. Using the Koronakis et al. (1986) model, it was found that optimal inclination and azimuth angle for both types of pyranometers are the same. The difference is observed in annual solar radiation on inclined surface, due to error of silicon-photodiode pyranometer under overcast sky conditions.

References

- Al-Rasheedi, M., Gueymard, C. A., Ismail, A., Hussain, T., (2018). Comparison of two sensor technologies for solar irradiance measurement in desert environment. *Solar Energy*, 161, 194-206, <https://doi.org/10.1016/j.solener.2017.12.058>.
- Barukčić, M., Hederić, Ž., Hadžiselimović, M., Seme, S., (2018). A simple stochastic method for modelling the uncertainty of photovoltaic power production based on measured data. *Energy*, ISSN 1873-6785.
- Gulin, M., Vašak, M., Baotic, M., (2013). Estimation of the global solar irradiance on tilted surfaces. *In: 17th International Conference on Electrical Drives and Power Electronics*, 334–339.

- Khoo, Y. S., Nobre, A., Malhotra, R., Yang, D., Ruther, R., Reindl, T., Aberle, A. G., (2014). Optimal Orientation and Tilt Angle for Maximizing in-Plane Solar Irradiation for PV Applications in Singapore. *IEEE Journal of photovoltaics*, 4, 647-653, doi: 10.1109/JPHOTOV.2013.2292743.
- Kipp&Zonen, (2016). Pyranometers for the accurate measurement of solar irradiance. *Datasheet - Brochure*.
- Koronakis, P. S., (1986). On the choice of the angle of tilt for south facing solar collectors in the Athens basin area. *Solar Energy*, 36, 217-225, [https://doi.org/10.1016/0038-092X\(86\)90137-4](https://doi.org/10.1016/0038-092X(86)90137-4).
- Slovenian Environmental Agency, Official website, 2017. Available from: <http://www.arso.gov.si/>.
- Srećković, N., Lukač, N., Žalik, B., Štumberger, G., (2016). Determining roof surfaces suitable for the installation of PV (photovoltaic) systems, based on LiDAR (Light Detection And Ranging) data, pyranometer measurements, and distribution network configuration. *Energy*, Vol. 96, 404-414, ISSN 0360-5442.

Shadow Impact Determination from DEM Data

PRIMOŽ MAVSAR

Abstract Shadow impact on solar potential determination is significant. This paper shows two methods for shadow determination using digital elevation model (DEM) as input data. The results are presented as a 3D model picturing solar potential determination with and without shadow consideration.

Keywords: • shadow • solar potential • digital elevation model • shadow determination • vector and geometrical method •

CORRESPONDENCE ADDRESS: Primož Mavsar, B.Sc, University of Maribor, Faculty of Energy Technology, Hočevarjev trg 1, SI-8270 Krško, Slovenia, e-mail: primozmusa@hotmail.com.

DOI <https://doi.org/10.18690/978-961-286-241-1.32>
Available at: <http://press.um.si>.

ISBN 978-961-286-241-1

1 Introduction

Solar potential on different surfaces is commonly calculated by division of global radiation on three components — direct, diffuse and reflected solar radiation. The most important is direct solar radiation, while it depends on geometrical variables of the position of the Sun and orientation of the surface. Optimization of the inclination and orientation angle of PV system can be calculated by the mathematical model for predicting solar radiation on tilted surface. In order to optimize the energy yield of the PV system, the solar tracking system (Seme et al., 2011) can be used. But in none of those studies the impact of shadows of nearby objects or terrain was taken into account, while shadow impact has significant role in solar energy yield. Shadows were determined from digital elevation model (DEM) data considering current position of the Sun. Two methods of shadow determination were used and compared. The first method was based on vectors (Corripio, 2003) and the second method on geometrical equations (Lukač et al., 2013a). Calculations were made with simple test DEM model and more complex real DEM model acquired from Geodetic authority of Slovenia. The results obtained from DEM model can be used for more accurate calculation of technical part of the investment in solar power plant, as it was presented by Seme et al. (2018). Those results showed significant drop in solar potential if the shadow impact was taken into account.

2 Terrain shadowing

Shadow determination on terrain model is very complex task while all characteristics of terrain objects (height, shape, dimension) must be known. Those objects must be projected on their surrounding based on current position of the Sun to analyze if they cast shadow or not. All operations of terrain shadowing were performed by scanning a raster made of DEM points. This method has many advantages such as:

- raster algorithms are well known,
- shadow areas from public accessible standard DEM data are fast determinable,
- is compatible with digital orthophoto and satellite images.

For determining the shadows, the sun’s beam path over the model had to be determined. We used the method of line rasterization (figure 1). For this purpose sun’s cartesian coordinates (S) at the given moment were obtained using topocentric coordinate system (Corripio, 2003) (equation 1), where ω is the hour angle, δ is solar declination angle and φ is latitude.

$$S = \begin{pmatrix} -\sin\omega \cos\delta \\ \sin\varphi \cos\omega \cos\delta - \cos\varphi \sin\delta \\ \cos\varphi \cos\omega \cos\delta + \sin\varphi \sin\delta \end{pmatrix} \tag{1}$$

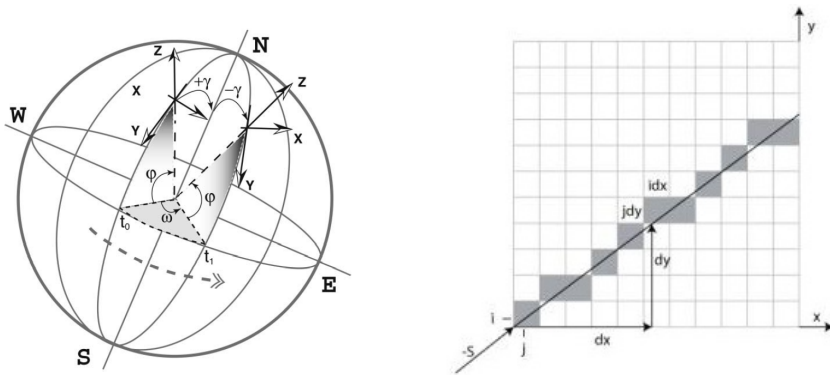


Figure 1: Beam path: a) topocentric coordinate system, b) line rasterization.

If the particular cell on the particular time is in a shadow or not was calculated using two approaches. The first approach (Corripio, 2003) projects raster cells on a beam’s path on a plane S_p perpendicular on a sun vector. Cells projections are then compared and if vector of current cell’s (P'_4) projection is smaller than compared cell’s projection then current cell is in the shadow (figure 2a).

The second approach (Lukač et al., 2013b) determines minimal height necessary that compared cell 2 is not in a shadow by a previous cell 1 (figure 2b). The following equation (2) applies.

$$h_{min} = z_1 - h \quad (2)$$

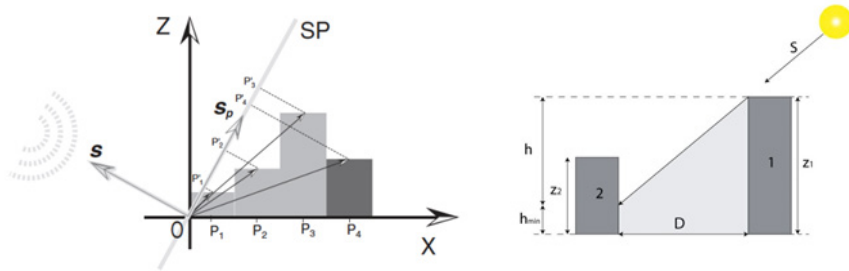


Figure 2: Shadow determination: a) vector based approach, b) geometrical based approach.

The described methods were used to scan entire model for determining the shadows of all objects on a model. If the cell is in the shade, algorithm determines shading factor as 0 otherwise the shading factor is 1. The direct component of solar radiation in equation for solar potential calculation was then multiplied with shading factor. That way the shadow impact was calculated and visualized on DEM model. The results are presented in next chapter.

3 Results

Figure 3 shows the determined cells on a sun's beam path over the model while figure 4 shows only the cells that are in the shadow by the object.

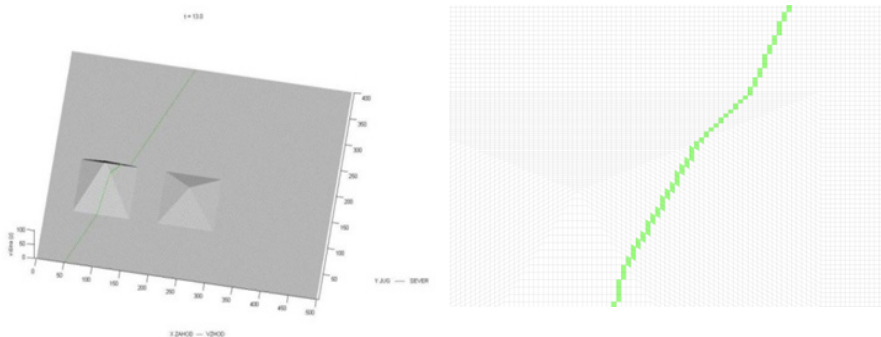


Figure 3. Beam path over the DEM

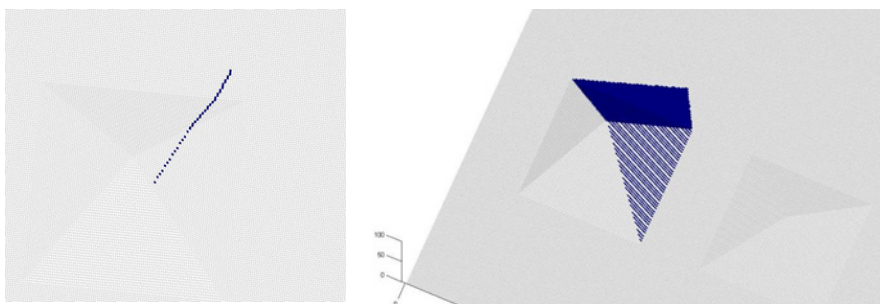


Figure 4: Cells in a shadow a) on sun's beam path, b) entire model

Solar potential was determined on a test model at first without shadow consideration and then also with shadowing that is seen on figure 5.

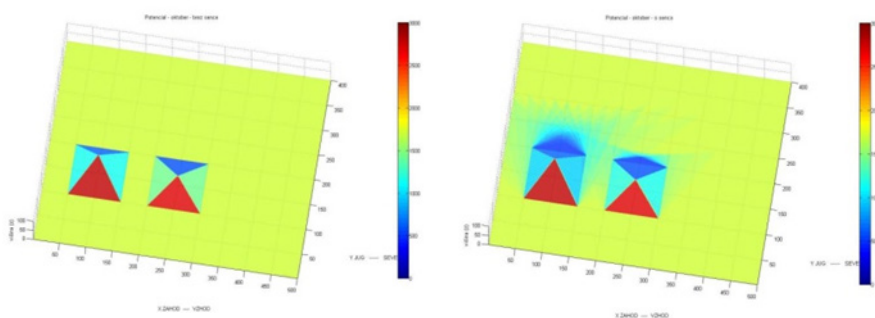


Figure 5: Solar potential on test model - October (Wh/m^2): a) without shadowing, b) shadow impact.

Figure 6 shows solar potential on a real terrain model for one characteristic day in October with and without shadowing. Areas with a big shadow impact are clearly seen (blue areas). In some areas there was a drop of solar potential even by 2/3 or 2 kWh/m^2 during a day.

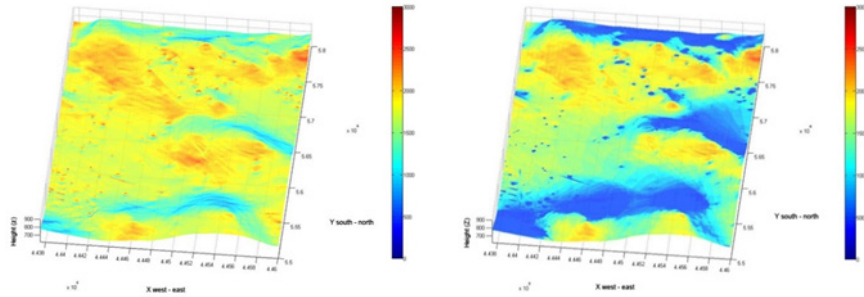


Figure 6: Solar potential - October (Wh/m²): a) without shadowing, b) shadow impact.

4 Conclusion

This paper presents two methods of shadow determination on DEM models and importance of shadow consideration in solar potential determination algorithms. The shadow impact is very big while the direct component of the solar radiation contributes the most energy. Therefore for good solar potential estimation shadows must be taken into account.

References

- Corripio, J.G., (2003). Vectorial algebra algorithms for calculating terrain parameters from DEMs and solar radiation modelling in mountainous terrain. *International Journal of Geographical Information Science*, Vol. 17, No. 1, 1–23.
- Lukač, N., Žalik, B., (2013)a. GPU-based roofs' solar potential estimation using LiDAR data. *Computers & Geoscience*, Vol. 52, 34-41.
- Lukač, N., Žlaus, D., Seme, S., Žalik, B., Štumberger, G.,(2013)b. Rating of roofs' surfaces regarding their solar potential and suitability for PV systems, based on LiDAR data. *Applied Energy*, Vol. 102, 803-812.
- Seme, S., Štumberger, G., Voršič, J., (2011). The optimal tracking strategies for two-axis PV system. *Przegląd Elektrotechniczny*, Vol. 87, 170-174, ISSN 0033-2097.
- Seme, S., Sređenšek, K., Praunseis, Z., Štumberger, B., Hadžiselimović, M., (2018). Optimal price of electricity of solar power plants and small hydro power plants: technical and economical part of investments. *Energy*, Vol. 157, 87-95, ISSN 0360-5442.

Experimental and Numerical Research of Micro Wind Turbine for Low Wind Speeds

MATEJ FIKE, MARKO PEZDEVŠEK, ANDREJ PREDIN & GORAZD HREN

Abstract In this paper, experimental and numerical study of micro wind turbine for low wind speeds is presented. Numerical simulations were performed for two turbines with different blades at various wind speeds. The first geometry was NTNU turbine and the second was modified NTNU turbine with shorter blades. Results from the numerical study showed that more efficient with higher power coefficient is turbine with modified blades.

Keywords: • wind turbine • NREL S826 • CFD • power coefficient
• structured mesh•

CORRESPONDENCE ADDRESS: Matej Fike, PhD, Assistant, University of Maribor, Faculty of Energy Technology, Hočevarjev trg 1, 8270 Krško, Slovenia, e-mail: matej.fike@um.si. Marko Pezdevšek, Assistant, University of Maribor, Faculty of Energy Technology, Hočevarjev trg 1, 8270 Krško, Slovenia, e-mail: marko.pezdevsek@um.si. Andrej Predin, PhD, Full Professor, University of Maribor, Faculty of Energy Technology, Hočevarjev trg 1, 8270 Krško, Slovenia, e-mail: andrej.predin@um.si. Gorazd Hren, PhD, Assistant Professor, University of Maribor, Faculty of Energy Technology, Hočevarjev trg 1, 8270 Krško, Slovenia, e-mail: gorazd.hren@um.si.

1 Introduction

Wind turbine systems are among the most important renewable energy resource in the world. Harvesting energy from low average wind speed profile regions such as the Slovenia is a challenge. Due to the low average of wind speeds in Slovenia, use of large and medium size conventional wind turbines is not economically feasible. These conventional turbines are designed for high rated wind speeds in range of 10 m/s to 15 m/s. However the average wind speed in Slovenia is much lower. The intent of this study is to design a micro wind turbine that fits the low average wind speed regions. The key part in designing wind turbines is the blade. Generally, the main goal in designing a wind turbine blade is maximizing the power coefficient. Micro wind turbine performance evaluation and optimizing can be done using computational fluid dynamics (CFD) as well as Blade Element Momentum (BEM) theory codes. BEM theory codes have an advantage of having much less computational time over CFD. Recent studies have shown that there is a good agreement between BEM theory codes results and experimental results of micro wind turbine [Akour et. al., 2018].

The main objective of the current study is to evaluate performance of two similar wind turbine designs with numerical approach at nominal and low wind speed. The only difference between is the lengths of the blades. Experiment has been conducted to validate simulation analysis.

2 Geometry, mesh and boundary conditions

2.1 Geometry

The research has begun using geometry of NTNU turbine. The NTNU turbine is a small scale wind turbine that has been developed at the Department of Energy and Process Engineering, NTNU in Trondheim. The rotor consists of three blades that have been designed using a single airfoil for simplicity reasons. The airfoil used in the blade design is the NREL S826. The blades are built using the S826 with different twist angle and different chord length at different section of the blade. The nacelle is a circular cylinder with a rounded hub. The blades are 415 mm long and the overall rotor diameter is 900 mm.

A 3D printer is used to prototype the blade final geometry for low wind speed. The maximal length of the blade that we can printed is limited to 300 mm. The

experiments were conducted on modified wind turbine with 300 mm long blades and overall rotor diameter 670 mm. The modified blades are NTNU blades without upper part.

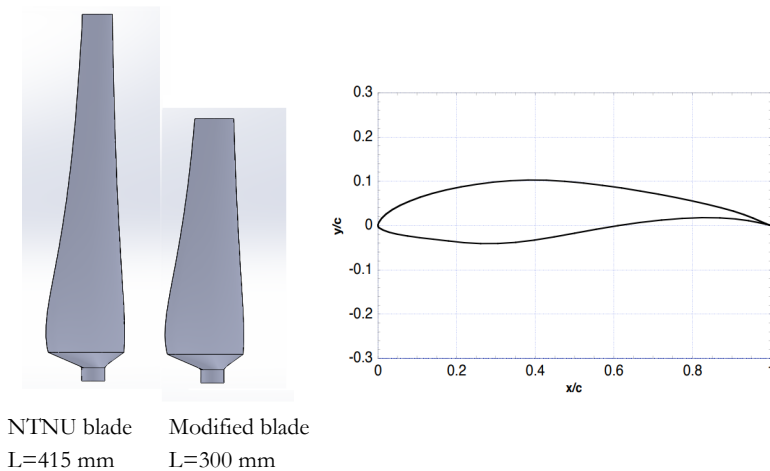


Figure 1: Different length of the blades with NREL S826 profile.

2.2 Numerical mesh

The geometries were imported in ICEM CFD where block structured meshes were created. Meshes had a similar non-dimensional wall distance y^+ and a total number of elements was 8.3 million.

2.3 Boundary conditions

The 3D simulations for NTNU turbine and turbine with shorter blades were performed as steady state calculation in a rotating frame of reference, taking advantage of the symmetry planes to reduce the computational domain to one third of the rotor. Nominal wind speed 10 m/s and low wind speed 3,82 m/s were used as inlet boundary condition.

3 Results

From the simulation analysis, the torque was obtained. The power coefficient c_p and tip speed ratio were calculated with the following equations:

$$c_p = \frac{\omega \cdot M}{\frac{1}{2} \cdot \rho \cdot v_v^3 \cdot A} \quad (1)$$

$$\lambda = \frac{u}{v} \quad (2)$$

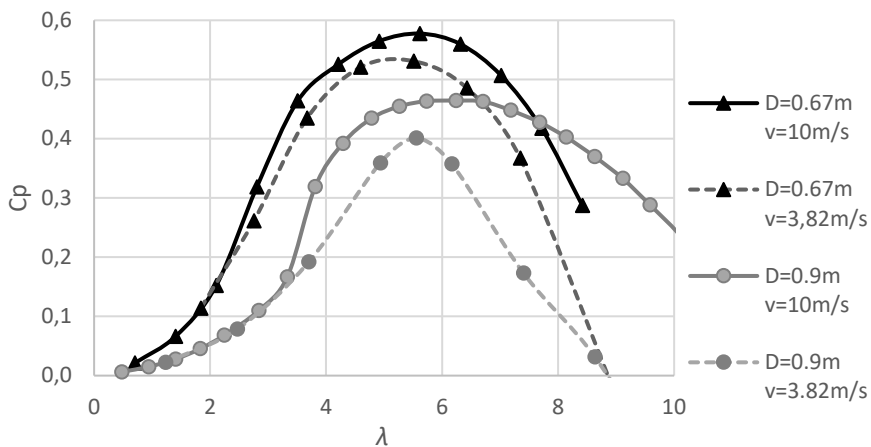


Figure 2: A comparison between numerically obtained values of power coefficient of NTNU turbine and turbine with modified blades at two different wind speeds.

Figure 2 show the comparison of the numerical results for the power coefficients against tip speed ratios for NTNU turbine and modified turbine with shorter blades.

4 Conclusions

Numerical simulations for two wind turbines with different geometry of blades at two different wind speeds 10 m/s and 3.82 m/s were carried out in this study. The first geometry of turbine was NTNU turbine and the second geometry was modified NTNU turbine with shorter blades. The diameter of NTNU and modified turbine was 0.9 m and 0.67 m, respectively. Both turbines had three blades. The performance curves were plotted regarding tip speed ratio.

Numerical results showed that turbine with modified blades has higher maximum power coefficient at both wind speeds. Both investigated turbines had better performance at higher wind speed.

References

- Salih N. Akour, Mohammed Al-Heymari, Talha Ahmed, Kamel Ali Khalil, *Experimental and theoretical investigation of micro wind turbine for low wind speed regions*, Renewable Energy 116, 215-223, 2018.
- Karlsen J. K., *Performance Calculations for a Model Turbine*, NTNU, 2009.
- Oggiano L., *CFD simulations on the NTNU wind turbine rotor and comparison with experiments*, Energy Procedia 58, 111-116, 2014.

Influence of Numerical Mesh Type on Airfoil Aerodynamic Characteristics

MARKO PEZDEVŠEK, MATEJ FIKE, ANDREJ PREDIN & GORAZD HREN

Abstract In this paper, we will examine how different mesh types affect the aerodynamic characteristic of an airfoil. The airfoil used for this paper was the NREL S809. Three different mesh types were created, a blocked structured mesh, an unstructured mesh and a hybrid mesh containing a blocked structured mesh near the surface of the airfoil and an unstructured mesh on the outside perimeter. Steady state simulations were performed for angles of attack between 0° and 22° . Lift and drag coefficient for all created meshes were compared to experimental results from literature. From angles of attack between 2° and 8° all three meshes predict similar lift and drag coefficients. We encountered problems with convergence for the unstructured mesh at angles of attack higher than 8° . Structured and hybrid mesh had similar lift and drag coefficients across all angles of attack.

Keywords: • computational fluid dynamics • NREL S809 • structured mesh • unstructured mesh • hybrid mesh •

CORRESPONDENCE ADDRESS: Marko Pezdevšek, Assistant, University of Maribor, Faculty of Energy Technology, Hočevarjev trg 1, 8270 Krško, Slovenia, e-mail: marko.pezdevsek@um.si. Matej Fike, PhD, Assistant, University of Maribor, Faculty of Energy Technology, Hočevarjev trg 1, 8270 Krško, Slovenia, e-mail: matej.fike@um.si. Andrej Predin, PhD, Full Professor, University of Maribor, Faculty of Energy Technology, Hočevarjev trg 1, 8270 Krško, Slovenia, e-mail: andrej.predin@um.si. Gorazd Hren, PhD, Assistant Professor, University of Maribor, Faculty of Energy Technology, Hočevarjev trg 1, 8270 Krško, Slovenia, e-mail: gorazd.hren@um.si.

1 Introduction

The evolution of computational fluid dynamics (CFD) is driven by the need for faster and more accurate methods for the calculations of flow fields around configurations of technical interest. For a decade, CFD has been the method of choice in the design of many types of industries and processes in which fluid or gas flows play a significant role.

Creating a model of the computational domain is the first step in simulating a problem. The majority of time spent on a CFD project is usually devoted to generating a suitable mesh for the domain geometry that allows a balance between the desired accuracy and solution time. After the creation of a mesh, a solver is able to solve the governing mathematical equations of the problem.

From literature, we can see that many researchers have investigated flow conditions around an isolated profile, experimentally and numerically. (Bitenc et al., 2013) used Ansys CFX to compare flow conditions between an open and closed trailing edge. The flow field around a profile at higher angles of attack was found to be time dependent. Detailed investigation of the flow phenomena requires transient simulations. (Fike et al., 2013), performed an investigation of flow conditions around a profile with steady state and transient simulation using Ansys CFX. (Wolfe et al., 1997) performed two-dimensional CFD calculations for the NREL S809 laminar-flow, wind-turbine airfoil using the commercial code CFD-ACE, while comparing them to experimental data from Delft University. The goal of our study is to examine how different mesh types affect the aerodynamic characteristic of an airfoil. Lift and drag coefficient for all created meshes were compared to experimental results from (Fike et al., 2013).

2 Geometry, mesh and boundary conditions

2.1 Geometry

2D geometry of the NREL S809 airfoil and the computational domain were created in SolidWorks. The size of the square computational domain around the airfoil was 15 lengths of an airfoil chord ahead of the airfoil and 30 lengths behind the airfoil.

2.2 Numerical mesh

The geometry was imported in ICEM CFD where we created three different mesh types. A blocked structured mesh, an unstructured mesh and a hybrid mesh containing a blocked structured mesh near the surface of the airfoil and an unstructured mesh on the outside perimeter. All three meshes were 2D planar and then extruded by one element thus creating three sided prisms in the case of the unstructured mesh, four sided prisms in the case of the structured mesh and a combination of both for the hybrid mesh. All meshes had a similar non-dimensional wall distance y^+ .

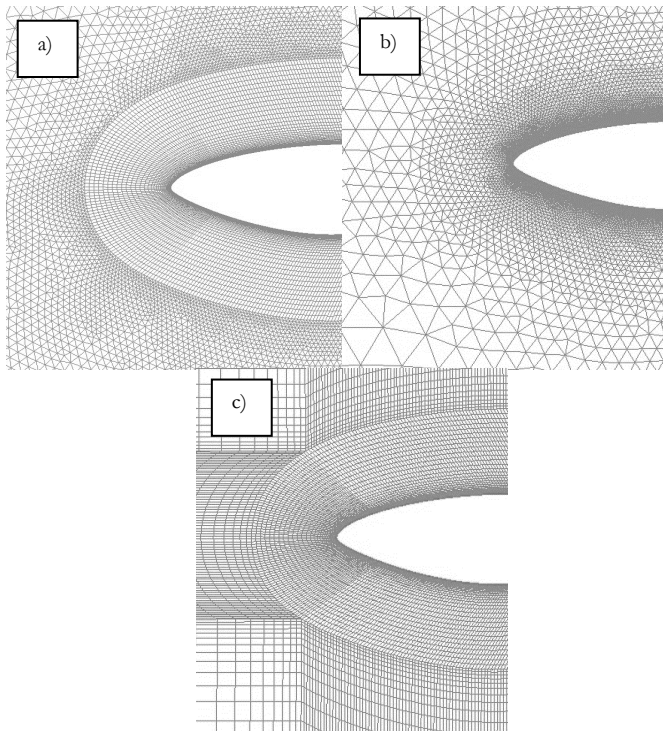


Figure 1: Different mesh types a) Hybrid mesh, b) Unstructured mesh, c) Structured mesh.

2.3 Boundary conditions

The following boundary conditions were defined as inlet, opening, wall and symmetry. The left and bottom sides of the domain were defined as inlets. The upper and right side of the domain were defined as openings. For the front and backside, the symmetry boundary condition was used. The airfoil surface was defined as a no-slip wall. The calculated Reynolds number for this study was 200000. Steady state simulations were performed for angles of attack between 0° and 22°.

3 Results

From numerical simulations, we acquired forces in the horizontal and vertical directions from which we calculated the lift and drag force. The lift coefficient C_l was calculated with the following equation:

$$C_l = \frac{F_l}{\frac{1}{2} \cdot A \cdot \rho \cdot v^2}; \quad (1)$$

The drag coefficient C_d was calculated with the following equation:

$$C_d = \frac{F_d}{\frac{1}{2} \cdot A \cdot \rho \cdot v^2} \quad (2)$$

Lift and drag coefficient for all three mesh types were compared to experimental results from (Fike et al., 2013).

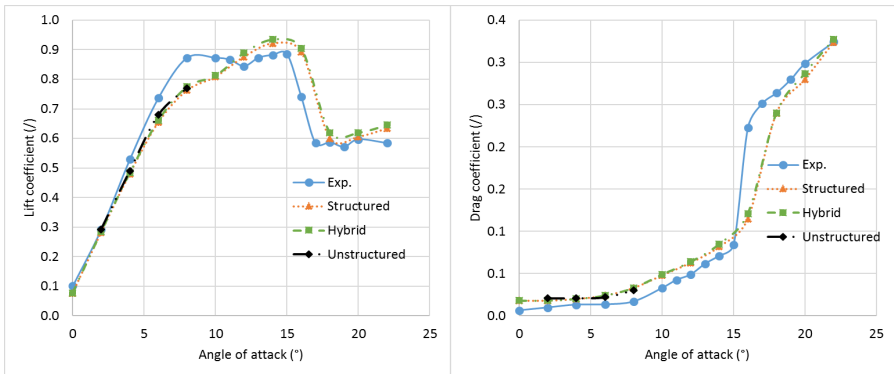


Figure 2: A comparison between numerically obtained values from all three created meshes of lift coefficients (left) and drag coefficients (right) at various angles of attack.

From figure 2, we can see that at angles of attack between 2° and 8° all three meshes predict similar lift and drag coefficients. For the unstructured mesh at angles of attack higher than 8° , we had problems with convergence. Structured and hybrid mesh had similar lift and drag coefficients across all angles of attack. Both meshes show good agreement with the experimental results.

4 Conclusions

At lower angles of attack all three meshes predict similar lift and drag coefficients, and all show good agreement with experimental results. At angles of attack higher than 8° , the structured and hybrid mesh predict similar lift and drag coefficients. At these higher angles of attack convergence was not achieved for the unstructured mesh. Based on the computed results both the structured mesh and hybrid mesh are suitable for the example used in this paper.

References

- Bitenc J., Širok B., Biluš I. (2013). Numerical analysis of flow over a wind turbine airfoil, *Journal of Energy Technology*, 31–46.
- Fike M., Bombek, G., Hriberšek M., Hribernik A. (2013). The unsteady static-stall aerodynamic characteristics of an S809 airfoil at low Reynolds numbers, *Journal of energy technology*, 33-50
- Wolfe, W.P., Ochs, S.S. (1997). CFD calculation of S809 aerodynamic characteristics. *AIAA- 97-0973*.

Usage of DEM Data for Solar Potential Determination

PRIMOŽ MAVSAR

Abstract This paper presents solar potential determination using digital elevation model and measured solar radiation on horizontal surface as input data. Solar potential was determined for each pixel in a model and presented as colored 3D model where colors were chosen respectively by the calculated solar potential.

Keywords: • solar radiation on tilted surface • solar potential • digital elevation model • 3D model of solar potential • meteorological station •

CORRESPONDENCE ADDRESS: Primož Mavsar, B.Sc, University of Maribor, Faculty of Energy Technology, Hočevarjev trg 1, SI-8270 Krško, Slovenia, e-mail: primozmusa@hotmail.com.

DOI <https://doi.org/10.18690/978-961-286-241-1.35>
Available at: <http://press.um.si>.

ISBN 978-961-286-241-1

1 Introduction

The Sun is a very interesting source of renewable energy as it is free, it will not be exhausted and it is clean. This gives us advantages both in the ecological and financial terms. Lukač et al. (2016) presented economic and environmental assessment of rooftops regarding suitability for photovoltaic systems installed based on remote sensing data. Its disadvantages are that we do not have a widely usable and cheap technology yet that would provide us with better energy yields than 15% when we are talking about photovoltaics and unforeseeable weather conditions that prevent us from a good estimation of solar energy yield in the long term (Chen, 2011). Seme et al. (2017) presents the analysis of the impact of photovoltaic systems connected to public distribution grid.

Solar potential greatly depends on terrain configuration. Different angle of the slope and different orientation of the slope receive also a different solar irradiation during a day, a month and a year. In order to optimize the most suitable slope and orientation of the PV system, Seme et al. (2016) presented new methods to determine high yield of energy production for single axis and dual axis PV tracking systems. Those methods are based on open-loop tracking system, while Seme et al. (2017) presents the new design of dual axis PV system, which is based on closed-loop system. How big is this solar potential in a specific area was determined from a meteorological data (solar irradiation on flat surface) and from digital elevation model DEM.

2 Solar radiation on tilted surfaces

Meteorological stations measure global (total) I and diffuse solar radiation I_d on horizontal surface. For the calculation needs those data are divided into the contributions of individual components. These are contributions from direct sunlight, diffuse and reflected solar radiation (Kreith et al., 1978). The most important is the contribution of a direct solar radiation (I_b), which can be calculated from the geometric position of the specific surface and the sun at a given moment. However, the other two contributions are also not negligible, which vary according to the atmospheric conditions (cloudiness) and the surrounding area of the surface (reflection factor). For calculations of direct sun beam component on a horizontal surface the following equation (1) applies, because there is no reflected radiation.

$$I = I_b + I_d \longrightarrow I_b = I - I_d \tag{1}$$

According to the figure 1, solar potential can be calculated as follows in equation (2),

$$G_t = G_{t,b} + G_{t,d} + G_{t,r} \tag{2}$$

where G_t is total solar radiation on tilted surface, $G_{t,b}$ is direct (b - beam) component, $G_{t,d}$ is diffuse (d- diffuse) and $G_{t,r}$ is reflected (r - reflected) component of solar radiation. Direct component of solar radiation on tilted surface can be calculated as in equation (3).

$$G_{t,b} = G_b \cdot R_b = G_b \cdot \frac{\cos i}{\sin \alpha} \tag{3}$$

where R_b is the ratio between direct sun radiation component on tilted surface ($\cos i$) and on plane surface ($\sin \alpha$).

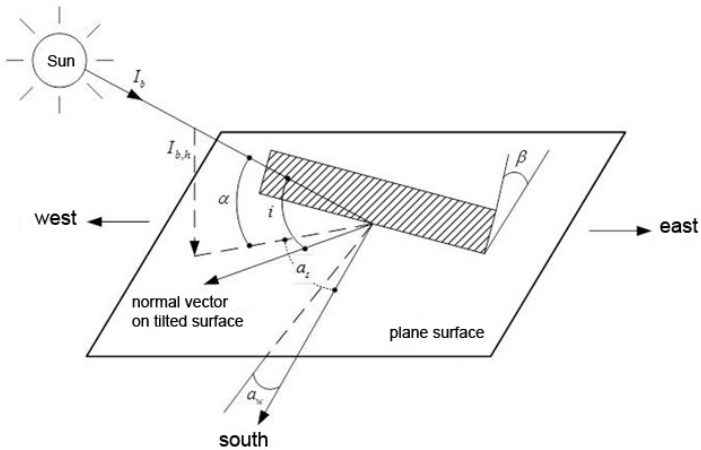


Figure 1: Solar radiation on tilted surface

Variable $\cos i$ in equation (3) is the incidence angle of the sun on the surface and can be calculated by equation (4) and variable $\sin \alpha$ is solar-altitude angle, which is calculated by equation (5) as described in (Kreith et al., 1978).

$$\begin{aligned} \cos i = & \sin \delta (\sin \varphi \cos \beta - \cos \varphi \sin \beta \cos \gamma) + \\ & \cos \delta \cos \omega(t) (\cos \varphi \cos \beta + \sin \varphi \sin \beta \cos \gamma) + \\ & \cos \delta \sin \beta \sin \gamma \sin \omega(t) \end{aligned} \quad (4)$$

$$\sin \alpha = \cos \varphi \cos \delta \sin \omega(t) + \omega(t) \sin \varphi \sin \delta \quad (3)$$

The angle δ is the declination angle of the sun and is determined for each day of the year by equation (6) where n is the number of the day in a year starting with first of january as number 1, φ is the latitude of the location, β is the inclination angle of the surface and a_s is the solar azimuth angle. The hour angle $\omega(t)$ in number of degrees is determined as in eq. (7), where LST is a local solar time.

$$\delta = 23,45 \cdot \sin\left(2 \cdot \pi \frac{284+n}{365}\right) \quad (6)$$

$$\omega(t) = (LST - 12) \cdot 15^\circ \quad (7)$$

The other two components $G_{t,d}$ (diffuse) and $G_{t,r}$ (reflected) were calculated by equations (8) and (9) where ρ in equation (9) is the diffuse reflectance factor of the surface (surface albedo). For example ρ for snow is $\rho \cong 0.75$ for grass and concrete $\rho \cong 0.2$ (Kreith et al., 1978).

$$G_{t,d} = G_d \cdot \cos^2 \frac{\beta}{2} \quad (8)$$

$$G_{t,r} = G \cdot \rho \cdot \sin^2 \frac{\beta}{2} \quad (9)$$

The measurement data for global and diffuse solar radiation on horizontal surface were obtained from meteorological station Novo mesto ($\lambda = 15^\circ 10' 38''$, $\varphi = 45^\circ 48' 06''$) in period of 4 years in a half an hour intervals. Those data were then used to obtain the average values of sun radiation for average day in each month of one year. DEM data were used for creating a model of terrain by regular square grid. Each pixel represented surface with specific inclination and

orientation angle. Solar radiation was calculated for each pixel (surface) in created grid and for each input data time interval. Solar potential (irradiation - H_t) for each pixel in the grid was calculated by equation (10).

$$H_t = \frac{1}{2} \sum_{t=0}^{48} G_t \quad [Wh/m^2] \quad (10)$$

Results are presented using 3D model of terrain where each pixel is colored respectively to calculated solar potential.

3 Results

First tests of algorithm written in Matlab were made using synthetic model of terrain. The very first test model was solid model made in AutoCAD and then imported in Matlab as seen on figure 2a and the second test model was pyramid object located near the observed meteorological station. That model was made from point cloud data using triangulation technique (Fig. 2b). The normal vector was determined for each surface in model algorithm in order to calculate the solar potential.

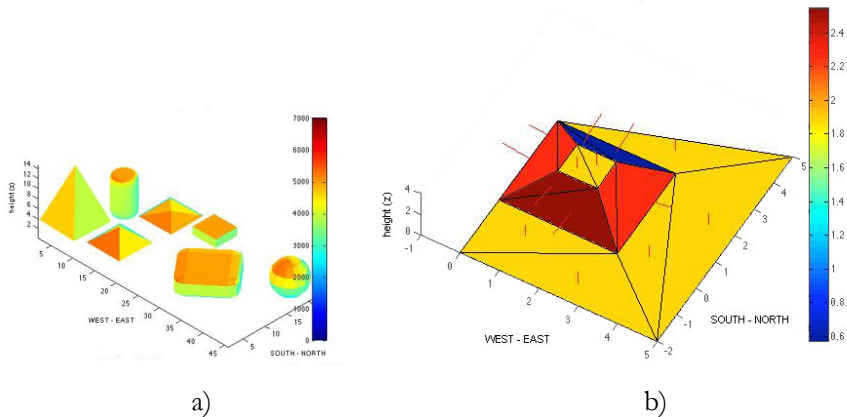


Figure 2: Solar potential: a) solid model, b) triangulated model with surface normal vectors

The approach with regular square grid model was proposed by (Lukač et al., 2013). This approach allowed that the written algorithm could calculate solar potential on every DEM data model, which is distributed as point cloud in ASCII format. Real DEM data and irradiance data was calculated for average day in a

month for every month in a year. In Fig. 3 the areas with steeper and south oriented slopes receive more solar irradiation (2500 Wh/m^2) than those that are more flat or oriented towards north (500 Wh/m^2).

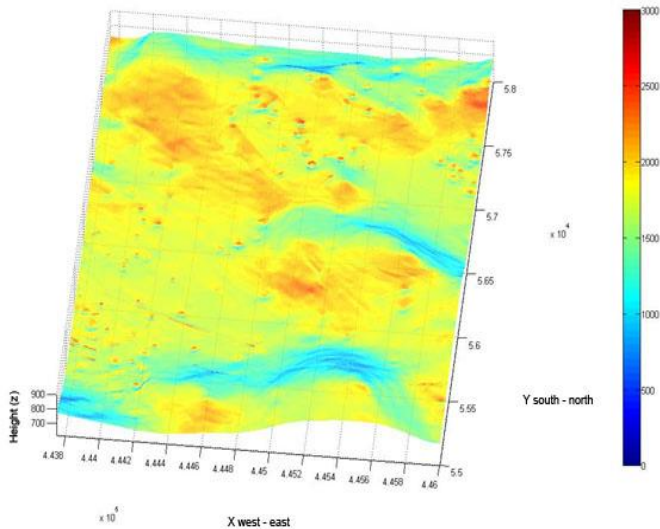


Figure 3: Solar potential - October (Wh/m^2)

4 Conclusion

Using 3D model to calculate the solar potential of an area is a great way to use in branches as solar energetics, agriculture and others for decision making. In the future the results evaluation had to be done by comparing calculated solar potential with measured values of solar irradiation on the field. In the field the shadows also have a big impact on solar irradiation. This paper did not discuss about this impact but it is necessary to incorporate it in the algorithm.

References

- Chen, C.J., (2011). Physics of Solar Energy. *John Wiley & Sons, Inc., Hoboken.*
- Kreith, F., Kreider, J.F., (1978). Principles of Solar Engineering.
- Lukač, N., Žlaus, D., Seme, S., Žalik, B., Štumberger, G., (2013). Rating of roofs' Surfaces regarding their solar potential and suitability for PV systems, based on LiDAR data. *Applied Energy*, Vol. 102, 803-812.
- Lukač, N., Seme, S., Dežak, K., Žalik, B., Štumberger, G., (2016). Economic and environmental assessment of rooftops regarding suitability for photovoltaic systems installation based on remote sensing data. *Energy*, Vol. 107, 854-865, ISSN 0360-5442.

- Seme, S., Štumberger, B., Hadžiselimović, M., (2016). A novel prediction algorithm for solar angles using second derivative of the energy for photovoltaic sun tracking purposes. *Solar energy*, Vol. 137, 201-211, ISSN 0038-092X.
- Seme, S., Srpčič, G., Kavšek, D., Božičnik, S., Letnik, T., Praunseis, Z., Štumberger, B., Hadžiselimović, M., (2017). Dual-axis photovoltaic tracking system: design and experimental investigation. *Energy*, Vol. 139, 1267-1274, ISSN 0360-5442.
- Seme, S., Lukač, N., Štumberger, B., Hadžiselimović, M., (2017). Power quality experimental analysis of grid-connected photovoltaic systems in urban distribution networks. *Energy*, Vol. 139, 1261-1266, ISSN 0360-5442.

Automated Optimal Design of Wells for Electromagnetic Cell Stimulation

PAOLO DI BARBA, LORENZO FASSINA, GIOVANNI MAGENES &
MARIA EVELINA MOGNASCHI

Abstract In the last decades, the electromagnetic stimulation in vitro and in vivo has become a promising research field because it allows to modulate the behavior of cells and tissues. In particular, when the cells are exposed to a time-varying magnetic field, an electric field is induced and thus a current density arises, because the cell culture is in contact with a conductive medium. The interaction between the induced current density and the time-varying magnetic field gives rise to mechanical stress acting on the cells. In this paper, new kind of wells for obtaining a homogeneous stress and stimulation of a considerable large number of cells are designed. This design problem is formulated as a multi-objective one and its solution is found by means of the μ -BiMO algorithm.

Keywords: • automated optimal design • electromagnetic cell stimulation • optimization problem • 3D finite element model • biogeography based optimization algorithm •

CORRESPONDENCE ADDRESS: Paolo Di Barba, PhD, Full Professor, University of Pavia, Department of Electrical, Computer and Biomedical Engineering, Via Ferrata 5, 27100 Pavia, Italy, e-mail: paolo.dibarba@unipv.it. Lorenzo Fassina, PhD, Assistant Professor, University of Pavia, Department of Electrical, Computer and Biomedical Engineering, Via Ferrata 5, 27100 Pavia, Italy, e-mail: lorenzo.fassina@unipv.it. Giovanni Magenes, PhD, Professor, University of Pavia, Department of Electrical, Computer and Biomedical Engineering, Via Ferrata 5, 27100 Pavia, Italy, e-mail: giovanni.magenes@unipv.it. Maria Evelina Mognaschi, University Researcher, University of Pavia, Department of Electrical, Computer and Biomedical Engineering, Via Ferrata 5, 27100 Pavia, Italy, e-mail: eve.mognaschi@unipv.it.

1 Introduction

The research about the biological effects caused by electromagnetic fields (EMFs) has been of great interest in the past decades. In particular, extremely-low-frequency EMFs (ELF-EMFs), with frequency up to 300 Hz and continuously irradiated by civil and industrial appliances, have been investigated to clarify their possible biological effects on the population unceasingly exposed to them.

On the other hand, ELF-EMFs are also applied to cell cultures or tissues in order to enhance positive biological effects. These positive biological effects, which can be described as an electromagnetic modulation of the cellular and tissue functions, have been obtained at extremely low frequencies and very low magnetic fields. In the *in vitro* experience, in order to enhance the biological effects, a similar electromagnetic wave with a frequency of about 75 Hz (instead of the 50 Hz or 60 Hz of the electric devices), with a magnitude of the magnetic field equal to circa 3 mT, can be used (Cornacchione, 2016, Pasi, 2016). The electromagnetic stimulation is delivered by means of the so-called “electromagnetic bioreactor”, which is composed of two solenoids, carrying a given current, preset by the user. In order to understand and justify the experiments, detailed numerical dosimetry inside these electromagnetic bioreactors is needed. In fact, in order to show the specific and effective physical stimulus transduced by the cells *in vitro*, not only by describing the local time-dependent magnetic field, but also by discussing the local hydrostatic forces (perpendicular to the cell membranes) and the local shear forces (parallel to the cell membranes), both caused by the magnetic induction field, the electromagnetic characterization of the bioreactor has been performed by the authors in the past (Mognaschi, 2014).

Inside the bioreactor, a well plate, containing cell cultures or tissues, is positioned; different kind of plates, with wells of different size, exist. However, to the best knowledge of the authors, the wells on the market are circular and no other well shapes exist. In this paper, annulus-shaped wells are considered and their shape is optimized in an automated way (Di Barba, 2018a): to this purpose, a biogeography inspired multi-objective optimization μ -BiMO (Mognaschi, 2017) is used.

2 Forward problem

The “electromagnetic bioreactor” (Fig. 1) is a device based on two solenoids connected in series and powered by a pulse generator at 75 Hz.

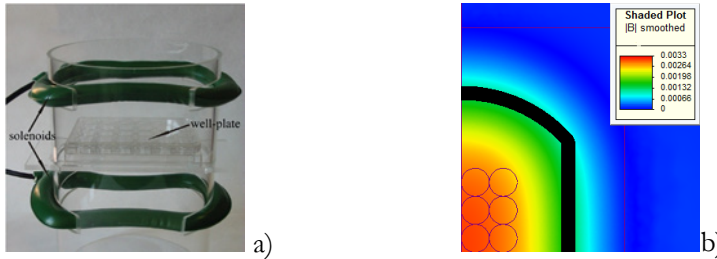


Figure 1: Electromagnetic bioreactor (a), magnetic induction field distribution in the middle of the bioreactor (b).

In order to simulate the magnetic B , induced electric E and induced current density J fields in the bioreactor, a 3D time-dependent finite-element model was implemented in MagNet, a commercial code by Mentor-Infolytica. Once the fields are known, the mechanical stresses acting onto the cells in the well can be calculated. In particular, forces F_t tangentially directed with respect to the lateral surface of the well and F_r radially directed forces can be calculated. The forces F_t are linearly proportional to the induced electric field E , while the forces F_r are linearly proportional to the term $J \times B$. It can be noted that the magnetic field distribution inside the bioreactor is non-uniform as shown in Fig. 1b. Also, the induced electric field is non-uniform and, therefore, non-uniform mechanical stresses F_t and F_r are originated in the wells. For the sake of simplicity, considering a well placed at the center point of the bioreactor, the electric field distribution is symmetric according to annulus-shaped regions: the thinner the annulus, the more homogeneous the stimulation. On the other hand, it is not practical to design very thin annulus-shaped wells, because it is usually necessary to stimulate a large quantity of cells.

3 Optimal shape design

From this consideration, the inverse problem can be stated as follows: find position and radii of the annulus-shaped well (coordinates x, y, z , inner radius R_{in} and outer radius R_{out}) in such a way that the electromagnetic stresses are homogeneously distributed in the physiological fluid and, simultaneously, the space allotted to the well is maximized.

According to the shape synthesis problem, two design criteria are considered:

f_1 : $R_{out}-R_{in}$, to be maximized

$$f_2 = \frac{E_{t,max} - E_{t,min}}{E_{t,ref}} + \frac{|J \times B_{max}| - |J \times B_{min}|}{|J \times B_{ref}|}, \text{ to be minimized.}$$

The terms $E_{t,ref}$ and $J \times B_{ref}$ are the maximum values of force densities referred to the well set at the center of the bioreactor.

3.1 Optimization method

For solving this problem, the μ -BiMO method is applied. The μ -BiMO method is a modification of the Biogeography Based Optimization BBO algorithm. The Biogeography Based Optimisation (BBO) algorithm was first developed by Simon in 2008 (Simon, 2008). This algorithm is suitable for solving single-objective optimization problems.

BBO is based on the process of natural immigration and emigration of species between small islands in the search for more friendly habitats, which is observed in nature. Each solution considered is treated as a habitat or island (design vector or individual in genetic algorithms) composed of suitability index variables (SIV, design variables), and each habitat exhibits a quality given by the habitat suitability index (HSI, objective function). The ecosystem, which is the whole set of islands or habitats, is progressively modified by means of two stochastic operators, i.e. migration and mutation: migration improves the HSI of poor habitats by sharing features from good habitats (exploitation step); in turn, mutation modifies some randomly selected SIV of a few habitats in view of a better search in the design space (exploration step). An appropriate balance between migration and mutation tunes the algorithm.

The multi-objective version of the algorithm was, presented by the authors in (Di Barba, 2016a) and (Di Barba, 2016b), is applied. It is based on the definition of the generalized fitness, which considers simultaneously two or more objective functions by exploiting the concept of non-dominated ranking of solutions in the objective space and crowding distance (Deb, 2002).

The BiMO algorithm showed good results in different field of applications (Di Barba 2017a, Di Barba 2017b, Di Barba, 2018b). However, it happens that, when the number of SIV and the number of islands is small, many duplicates of islands occur. In the original version of the algorithm, the duplicates are handled by randomly varying duplicated islands. This is like implementing a strong mutation on the islands and hence the exploration is improved while the exploitation is worsened.

To overcome this aspect, the authors recently proposed new version of the BiMO, the μ -BiMO algorithm (Mognaschi, 2017). In this new version of BiMO, the role of small rocks in the migration of individuals is considered. As in reality the small rocks help immigrants to colonize islands that otherwise would not be reached, with the concomitant loss of the individuals who would never reach the ground, in the proposed method the rocks have the function not to waste habitats that otherwise would never characterize an ecosystem.

In particular, during the migration procedure it could happen that good habitats are replaced. To recover this, the discarded habitats are stored in a vector (rock vector) that tracks the habitats.

4 Results

The results are shown in Fig. 2. From 5 starting points, two non-dominated solutions are obtained after 100 iterations. They are the two end-points of the approximated Pareto front.

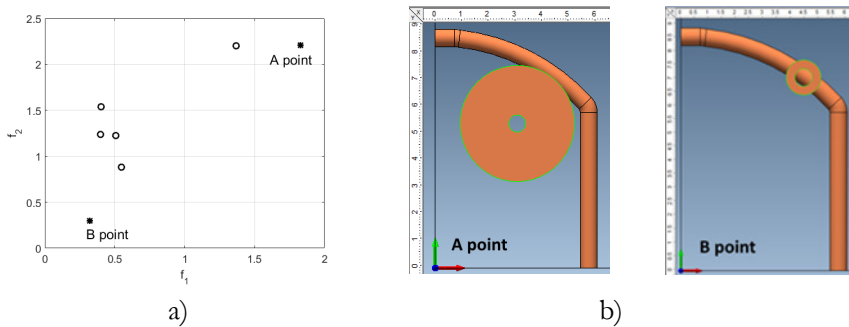


Figure 2: Results: starting points – circle, final non-dominated solutions – star (a), optimal geometries (b)

The algorithm is able to find the two end-points of the Pareto front with few objective function calls. In fact, only 500 (number of islands, 5, times number of iterations, 100) objective function calls are needed.

In Fig. 2b the geometries of the two non-dominated solutions are shown. The solution B-point allows for a homogenous stimulation of cells, but the space allotted to cells is much lower than in solution A-point, which shows a worst homogeneity than B-point.

5 Conclusion

Two optimally-shaped wells for electromagnetic stimulation of cells have been designed. In particular, μ -BiMO method found two non-dominated solutions at the end-point of the approximated Pareto front, with few objective function calls. These results confirmed that the μ -BiMO method is able to find non-dominated solutions with few objective function calls, which, in case of models based on Finite Element Method, help the designer in obtaining a faster optimization procedure.

References

- Cornacchione, M., Pellegrini, M., Fassina, L., Mognaschi, M.E., Di Siena, S., Gimmelli, R., Ambrosino, P., Soldovieri, M.V., Tagliatela, M., Gianfrilli, D., Isidori, A.M., Lenzi, A., Naro, F. (2016). β -Adrenergic response is counteracted by extremely-low-frequency pulsed electromagnetic fields in beating cardiomyocytes. *Journal of Molecular and Cellular Cardiology*, 98, 146-158.
- Deb, K., Pratap, A., Agarwal, S., Meyarivan, T. (2002). A fast and elitist multiobjective genetic algorithm: NSGA-II. *IEEE Transactions on Evolutionary Computation*, 6 (2), 182-197.

- Di Barba, P., Dughiero, F., Mognaschi, M.E., Savini, A., Wiak, S. (2016). Biogeography-Inspired Multiobjective Optimization and MEMS Design. *IEEE Transactions on Magnetics*, 52 (3).
- Di Barba, P., Mognaschi, M.E., Savini, A., Wiak, S. (2016). Island biogeography as a paradigm for MEMS optimal design. *International Journal of Applied Electromagnetics and Mechanics*, 51 (s1), S97-S105.
- Di Barba, P., Mognaschi, M.E., Venini, P., Wiak S. (2017). Biogeography-inspired multiobjective optimization for helping MEMS synthesis. *Archives of Electrical Engineering*, 66(3).
- Di Barba, P., Mognaschi, M.E., Krawczyk, A. (2017) The biogeography-inspired optimization for the design of coils for nerve stimulation. *17th IEEE International Conference on Smart Technologies, EUROCON 2017 - Conference Proceedings*, 542-545.
- Di Barba, P., Fassina, L., Magenes, G., Mognaschi, M.E. (2018). Shape synthesis of a well-plate for electromagnetic stimulation of cells. In press on *International Journal of Numerical Modelling: Electronic Networks, Devices and Fields*.
- Di Barba, P., Dughiero, F., Forzan, M., Mognaschi, M.E., Sieni, E. (2018). New solutions to a multi-objective benchmark problem of induction heating: An application of computational biogeography and evolutionary algorithms. *Archives of Electrical Engineering*, 67 (1), 139-149.
- Mognaschi, M.E., Di Barba, P., Magenes, G., Lenzi, A., Naro, F., Fassina, L. (2014). Field models and numerical dosimetry inside an extremely-low-frequency electromagnetic bioreactor: the theoretical link between the electromagnetically induced mechanical forces and the biological mechanisms of the cell tensegrity. *Springerplus*, 3, No. 473.
- Mognaschi, M.E., (2017). Micro biogeography-inspired multi-objective optimisation for industrial electromagnetic design. *Electronics Letters*, 53(22).
- Pasi, F., Fassina, L., Mognaschi, M.E., Lupo, G., Corbella, F., Nano, R., Capelli, E. (2016). Pulsed electromagnetic field with Temozolomide can elicit an epigenetic pro-Apoptotic effect on Glioblastoma T98G Cells. *Anticancer Research*, 36 (11), 5821-5826.
- Simon, D. (2008). Biogeography-Based Optimization. *IEEE Trans. on Evol. Comput.*, 12(6), 702–713.

Is Specific Absorption Rate (SAR) the Parameter of Mobile Phone?

ANDRZEJ KRAWCZYK, EWA KORZENIEWSKA & PIOTR MURAWSKI

Abstract The paper attempts at analyzing the SAR (Specific Absorption Rate) coefficient as the parameter which determines the level of mobile phone safety. The SAR parameter was created in order to show the energy which is absorbed by tissue exposed to electromagnetic field. The authors analyzed the origin of SAR and how the limitations of it were introduced to the standard. The procedure of determination of SAR for mobile phones (terminals) was shown with the critical comments

Keywords: • specific absorption rate • mobile phone • standards • specific absorption rate measurements • electro magnetic field •

CORRESPONDENCE ADDRESS: Andrzej Krawczyk, PhD, Professor, Military Institute of Medicine, ul. Szaserów 128, 04-141 Warsaw, Poland, e-mail: ankra.new@gmail.com. Ewa Korzeniewska, PhD, Łódź University of Technology, Faculty of Electrical, Electronic, Computer and Control Engineering, Stefanowskiego 18/22, 90-924 Łódź, Poland, e-mail: ewa.korzeniewska@p.lodz.pl. Piotr Murawski, PhD, Military Institute of Medicine, Department of Teleinformatics, Szaserow 188, 04-141 Warszawa, Poland, e-mail: pmurawski@wim.mil.pl.

1 Introduction

Since mobile phone systems have been introduced to common usage there is concern of their influence on human health ("Guidelines for limiting exposure to time-varying electric, magnetic, and electromagnetic fields (up to 300 GHz). International Commission on Non-Ionizing Radiation Protection," 1998). The number of scientific papers reporting the results of research projects is really very vast and the majority of the reported results indicate the lack of the hazard from mobile phone systems. However, the public concern is still elevating. There are two directions of the people protests: the base station antennas and mobile phone terminals. In this paper the first direction will be left aside and the problem of mobile phone terminal will be dealt with. Looking at the problem from the public concern one can distinguish two ways of EMF influence of people's health: warming up the body by EMF and inducing the development of brain cancers. The question whether EMF is carcinogenicity or not is being solved by epidemiological studies made on animals and people and there is no physical index which definitely answers the question. The situation is different if the increasing of temperature inside the body is considered. In this case the energy absorbed by the body is the good indicator which is the measure for the assessing of body warming up. The elevation of temperature was the first and the very hazardous phenomena at that time and still remains as such. The title of article from the Sunday Times describes such a situation (Fig.1). The number parameter which indicates the level of warming up is SAR – Specific Absorption Rate.



Figure 1: Sunday Times (14 April 1996)

To make the situation appropriately, it is important to know current protection policy. There are two international guidelines (ICNIRP ("Guidelines for limiting exposure to time-varying electric, magnetic, and electromagnetic fields (up to 300 GHz). International Commission on Non-Ionizing Radiation Protection," 1998) and IEEE (*Safety Levels with Respect to Human Exposure to Radio Frequency Electromagnetic Fields 3 kHz to 300 GHz in ANSI/IEEE C95.1-2006* 2006)) to protect people from adverse health effects by exposition to RF-EMF. In RF-EMF, thermal effect that causes generation of heat in tissue by absorption of RF-EMF is a primary target of protection in both guidelines. Actually, it is scientifically established that excess heat causes harmful effects such as burns, blindness, sterility, etc. because of tissue damage by heating. Thus, that guideline possesses the basic restriction not to increase temperature for certain level (e.g. $\Delta 1$ K for body core, $\Delta 2$ K for head, torso, testes, eyes and $\Delta 4$ K for other extremities). In Japan, the Ministrial Ordinances to regulate Radio wave usage (Radio Act) has been introduced by same policy and the limit values are basically based on the ICNIRP guideline. In Poland, the policy regulating electromagnetic emission is based on the Act of the Ministry of Environment Protection from 30 October 2003 ("Rozporządzenie Ministra Środowiska z dnia 30 października 2003 r. w sprawie dopuszczalnych poziomów pól elektromagnetycznych w środowisku oraz sposobów sprawdzania dotrzymania tych poziomów," 2003).

The regulation which is to be followed by EMF producers and is applicable in the majority of European countries gives the value the SAR parameter for the range of frequency 100 kHz – 10 GHz. This parameter belongs, together with electric current density for lower frequencies, to BASIC RESTRICTIONS, i.e. the parameters which describe the phenomena in human body. It should be stressed here that both electric current and SAR cannot be obviously measured directly and the ways to get these parameters are as follows: to make computer simulation of the human body or to use the phantom which models the human body.

2 The SAR parameters

Whenever a RF EMF is applied to material object with generalized conductivity, which contains usual conductivity and electric permittivity representing polarization, then heat energy is generated in the object. Note that for the frequency within the range 100 kHz and 10 GHz the major part of generalized

conductivity is that of polarization. SAR is the fundamental metric of RF heating and can be calculated at any point of the exposed material from the internal electric field (E) using:

$$SAR = \frac{\sigma}{\rho} |E|^2 = c \frac{\Delta T}{\Delta t} \quad (1)$$

where σ is the generalized conductivity (S/m), ρ is the mass density (kg/m³),

E is the strength of electric component of EMF (rms V/m), $\frac{\Delta T}{\Delta t}$ is the increase

of temperature in the time unit, c is the specific heat. It should be underlined that the relation (1) to temperature is limited to an „ideal” case with no heat loss by thermal diffusion, heat radiation or thermoregulation. To determine the limitation for SAR one can assume that the safe incremental of temperature amounts 1 K, and $\Delta t = 360$ s (time to temperature steady-state), and c_w for human tissue is equal to 3000 J/kg/K. Then, SAR amounts 8 W/kg. Taking the safety coefficient 20 to 2, one obtains SAR being in the interval (0,4 – 4) W/kg. Now looking at the ICNIRP regulation (EU recommendations): the values of SAR 0,08 W/kg (whole body), 2 W/kg (head and trunk), 4 W/kg (limbs), thus the values close to those calculated ("Guidelines for limiting exposure to time-varying electric, magnetic, and electromagnetic fields (up to 300 GHz). International Commission on Non-Ionizing Radiation Protection," 1998).

3 SAR of mobile phones

Recently, majority of new mobile terminals are provided with the information about value of SAR. It has to witness on the bigger or lower emissivity of EMF by this or that mobile phone. But what it is obvious that SAR is the measure of energy absorbed in the object exposed to EMF, thus it is by definition the internal parameter of human body.

There is a way to overcome the immanent contradictory, namely, as it was mentioned before, one uses phantoms (Figs 2,3) to assess the EMF emission from wireless devices measuring energy absorbed by phantom fluid. According to the IEC regulation (IEC, 2016) the measurement of energy absorbed should be realized under strictly the same conditions for each wireless device which has to be marked by the SAR value. In paragraph 5.1 of IEC document one can read:

“The test shall be performed using a miniature probe that is automatically positioned to measure the internal E-field distribution in a phantom model representing the human head exposed to the electromagnetic fields produced by wireless devices. From the measured E-field values, the SAR distribution and the maximum mass averaged SAR value shall be calculated.”

This recommendation is very general and further in the document one can meet more detailed prescriptions but to do it is not easy as the parameters of phantoms used in testing can differ one by another. Although the IEC document regulates the prescriptions for phantom fluids and positioning of the wireless device it should be stressed that there are some doubts in fulfil the compatibility requirements.

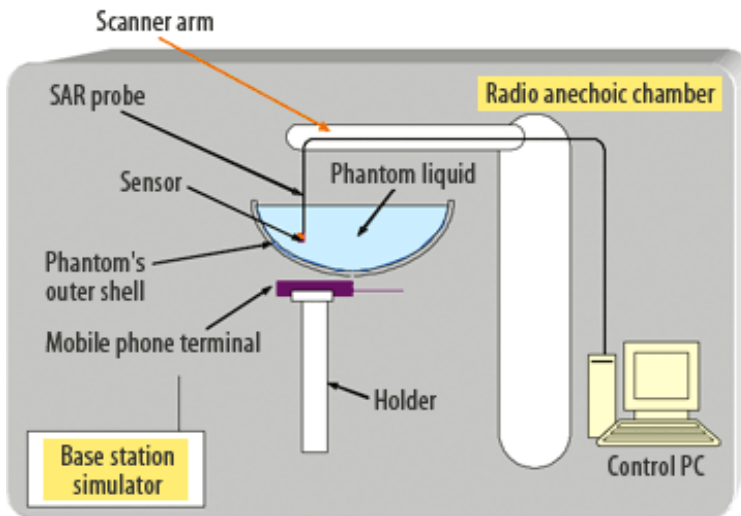


Figure: 2 Scheme of SAR measurement

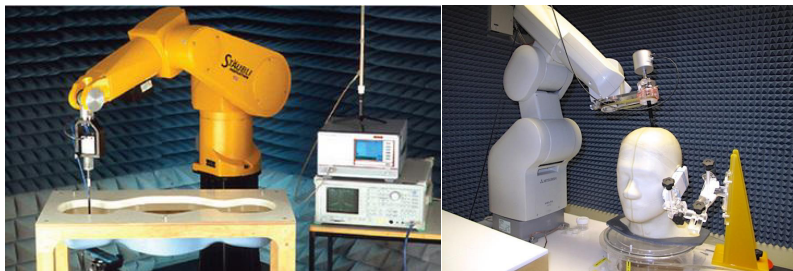


Figure 3: Real phantoms (left: flat phantom, right: head phantom) used during SAR Measurement [5]

On the basis of such measurements the SAR has a particular mobile phone has been measured and after that the measured value is adjoined with the phone as the value which determines the level of its hazard. Let us remember that the SAR was measured for one position of the phone (distance and angle), for one level of power and, what is the most important, for one set of phantom properties. However, people differ much one from another, thus the energy absorption in phantom fluid may be close to energy absorption in one man and completely different for the another. That is the problem with the SAR coefficient as the indicator of mobile phone safety.

As the example one can quote the results of SAR obtained in US for several classes of mobile phones, indicating this with the highest SAR and that with the minimum SAR (Loukil & Siala, 2015): Motorola StartTAC 7860 – 0.24, Ericsson T28 World – 1.49. The standard for a head is SAR equals 2, thus both results are lower than it. But it is far from reality to say to anybody that this mobile phone is better and that is worse.

4 Conclusions

To conclude the above considerations it can be stated as follows:

- 1) the assessment of mobile phones by SAR because of some uncertainty seems to be doubtful,
- 2) even if the doubts are diminished one should be aware that SAR is the measure of EMF energy only, i.e. it shows the increase of temperature only and it has no connection with all the non-thermal effects,
- 3) the main people's concern related to electromagnetic field from mobile phone system is connected with non-thermal action and it is out of SAR analysis

The rough answer to the title question is: the SAR parameter as the assessment index for mobile phones plays the commercial role rather than the real scientific approach.

References

Guidelines for limiting exposure to time-varying electric, magnetic, and electromagnetic fields (up to 300 GHz). International Commission on Non-Ionizing Radiation Protection. (1998). *Health Phys*, 74(4), 494-522.

- IEC (2016). *Measurement procedure for the assessment of specific absorption rate of human exposure to radio frequency fields from hand-held and body-mounted wireless communication devices - Part 1: Devices used next to the ear (Frequency range of 300 MHz to 6 GHz)* (IEC 62209-1:2016). Retrieved from <https://webstore.iec.ch/publication/25336#additionalinfo>.
- Loukil, K., & Siala, K. (2015). EMC standards. In *SAR Specific Absorption Rate, Training Course on Conformity and Interoperability*. Tunis-Tunisia.
- Rozporządzenie Ministra Środowiska z dnia 30 października 2003 r. w sprawie dopuszczalnych poziomów pól elektromagnetycznych w środowisku oraz sposobów sprawdzania dotrzymania tych poziomów, nr. 192 poz. 1883 (2003).
- Safety Levels with Respect to Human Exposure to Radio Frequency Electromagnetic Fields 3 kHz to 300 GHz in ANSI/IEEE C95.1-2006* (2006). Washington: IEEE.

Production, Thermal Analysis and Application of Roll Bond Solar Absorbers for Heating and Cooling in Residential Buildings

JURIJ AVSEC, DANIEL BRANDL, HELMUT SCHOBER, URŠKA NOVOSEL &
JANKO FERČEC

Abstract The effects of global warming are a crucial issue in the near future. The combination of renewable energy sources (RES) and the use of alternative energy technology such as heat pumps and hydrogen technology could solve major ecological problems. In Central Europe, the energy demand for heating and cooling in residential buildings is clearly higher than for generation of electricity or energy for trucking e.g. In this paper, a new solar thermal absorber has been analysed which is produced by using the so called “roll bond” technology (ABS Network, 2018). The focus of this study lies on the determination of the energy efficiency by combining this solar thermal absorber with heat pumps and biomass or geothermal systems in the region of Central Europe.

Keywords: • roll bond solar absorbers • thermal analysis • solar systems • heat pump systems • heating and cooling in residential buildings •

CORRESPONDENCE ADDRESS: Jurij Avsec, PhD, Full Professor, University of Maribor, Faculty of Energy Technology, Hočevarjev trg 1, SI-8270 Krško, Slovenia, e-mail: jurij.avsec@um.si. Daniel Brandl, PhD, Graz University of Technology, Institute of Thermal Engineering, Inffeldgasse 25b, 8010 Graz, Austria, e-mail: daniel.brandl@tugraz.at. Helmut Schober, PhD, Graz University of Technology, Institute of Building Construction, Lessingstraße 25III, 8010 Graz, Austria, e-mail: helmut.schober@tugraz.at. Urška Novosel, PhD, Assitant, University of Maribor, Faculty of Energy Technology, Hočevarjev trg 1, SI-8270 Krško, Slovenia, e-mail: urska.novosel@um.si. Janko Ferčec, TALUM d.d. Kidričevo, Tovarniška cesta 10, 2325 Kidričevo, Slovenia, e-mail: janko.fercec@talum.si.

1 Thermal analysis of the STAF panel (CFD simulation)

With the help of Computational Fluid Dynamics ("ANSYS Fluent 18.2. Userguide/Theoryguide,") (CFD) method a thermal analysis was performed in order to understand the heat transfer mechanism. This numerical simulation method enables to calculate a broad range of different scenarios because geometrical and operative parameters can easily be varied. In this study the thermal performance of the exterior plate of a 3.5 x 1.0 m STAF panel was analysed by using a CFD software package from ANSYS Fluent (ANSYS Inc., 2018). The simulation method was developed and validated in the course of the research project UNAB (ABS Network, 2018). In the simulation aluminium is used as absorber material (with a density of 2700 kg/m³, a specific heat of 896 J/kgK and a thermal conductivity of 201 W/mK).

Furthermore, the simulation considers a thermal insulation with a thickness of 0.15 m which is made of polyurethane (with a density of 40 kg/m³, a specific heat of 1400 J/kgK and a thermal conductivity of 0.025 W/mK) and an interior aluminium plate. At the inner surface of the interior plate a room temperature of 20 °C and a heat transfer coefficient of 5 W/m²K is assumed in the simulation. The sides of the STAF panel are defined as symmetry, the bottom and top surfaces are defined as adiabatic wall. The panel's exterior absorber plate has two inlets at the bottom (1st absorber) where the fluid is introduced to the pipe network. (the used fluid pipe profile is illustrated in Fig. 5). In this simulation a mixture of 70 Vol% water and 30 Vol% glycol is used in order to prevent freezing for fluid temperatures below 0 °C (with a density of 1035 kg/m³, a specific heat of 3617 J/kgK and a thermal conductivity of 0.5 W/mK). The fluid flows upwards through the 1st absorbers, enters the 2nd absorbers and leaves the absorber at the top of the STAF panel.

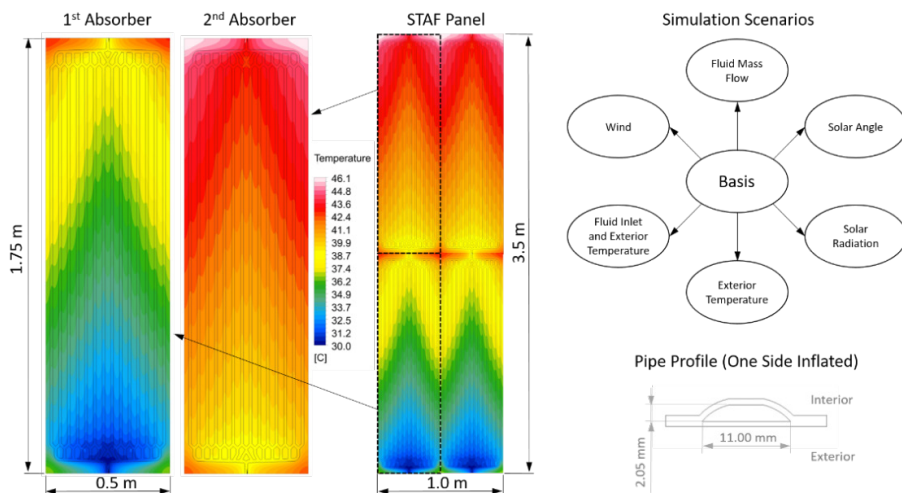


Figure 1: Temperature contours of the exterior surface of (1) the absorber plates, (2) the STAF panel, (3) simulation scenarios, (4) fluid pipe profile

The remaining thermal boundary conditions have been varied in a parameter analysis. In the initial scenario (Basis scenario) the exterior temperature (T_{ext}) amounts 30 °C and the exterior heat transfer coefficient (representing the influence of the average wind speed over a year in Graz, Austria) is 25 W/m²K. Furthermore, a solar radiation of 1000 W/m² and a solar angle of 45° are assumed. The water-glycol mixture is introduced with a volume flow rate (\dot{V}_F) of 100 l/h per inlet and at an temperature ($T_{F,in}$) of 30 °C. The varying parameter are shown in the schematic of the simulation scenarios in Figure 1 while Table I contains the computed fluid temperature ($T_{F,out}$) at the outlet positions of the absorbers pipework as well as the resulting thermal output (\dot{Q}_{STAF}) and efficiency (η_{STAF}) of the whole STAF panel.

Table 1: Results from CFD simulation scenarios

Simulation scenario	\dot{V}_F	T_{ext}	$T_{F,in}$	$T_{F,out}$	\dot{Q}_{STAF}	η_{STAF}
	[L/h]	[°C]	[°C]	[°C]	[W]	[-]
Basis scenario	100	30	30	43.3	1379.7	0.394
Volume flow rate of 200 l/h per inlet	200	30	30	38.4	1742.6	0.498
Volume flow rate of 50 l/h per inlet	50	30	30	48.1	943.0	0.269
Exterior and fluid inlet temperature of 20 °C	100	20	20	33.4	1393.3	0.398
Exterior and fluid inlet temperature of 0 °C	100	0	0	13.7	1421.3	0.406
Solar radiation of 500 W/m ²	100	30	30	36.7	691.4	0.395
Fluid inlet temperature of 20 °C	100	30	20	39.5	2027.5	0.579
Fluid inlet temperature of 0 °C	100	30	0	31.8	3309.5	0.946
Exterior heat transfer coefficient of 5 W/m ² K	100	30	30	48.2	1892.3	0.541
Exterior heat transfer coefficient of 100 W/m ² K	100	30	30	35.9	615.5	0.176
Solar angle of 65°	100	30	30	37.9	824.5	0.236
Solar angle of 20°	100	30	30	47.6	1829.9	0.523

2 Application of the STAF panel (case study)

The purpose of installing STAF panels on buildings is to save as much as possible in the consumption of already used primary energy sources for space and domestic hot water heating and thus contribute to lower greenhouse gas emissions. Buildings with integrated STAF panels are approaching to low-carbon (energy-efficient) buildings, which affects the outcome at the obtaining an energy certificate. With the installation of STAF panels we are approaching to EU objectives, which are always higher regarding the policy of obtaining building permits for new buildings. By installing a modified version of STAF panels for thermal improvement of an existing building, it is necessary to emphasise the construction work is not significant, the architecture remains almost the same, which means that large construction work in the renovation is not required, since the panels are installed on the outside of the wall (façade), thereby the thermal insulation of the building is improved. STAF panels, which can also be installed at the outer wall of a building have some decisive advantages. The use of solar radiation, of course, also depends on the installation of solar panels according to the cardinal directions and the slope of the panels (different values for different areas in the world).

STAF panels can be used as additional heat generators in order to support the existing heating system with the production of heat for space heating and domestic water. For example, imagine residential house built in the vicinity of the municipality of Krško, Slovenia, with the maximum heating power to heat this building 12 kW. Depending on the annual load of the heating plant, the necessary energy for the heating of the residential building including sanitary water preparation is 36580 kWh per year (Bratkovič & Irgl, 2006). For the energy analysis of the application of solar panels for heating of residential buildings we combined the STAF panels with heat pump system (Figure 6). For the determination of the solar radiation, we calculated the number of effective hours for Krško region, Slovenia. With the help of the solar calculator from the solar electricity handbook ("Solar Irradiance,"), we received an effective number of solar hours of 1,224. The principle idea behind the STAF panels is to cover majority the heat demand in the summer time and the highest share in the winter. Figure 2 shows the price for heating and minimal required number of installed STAF panels in dependence of solar coverage with STAF panels (Avsec et al., 2018) and in dependence of 30 %, 50 % or 80 % of the energy demand for heating.

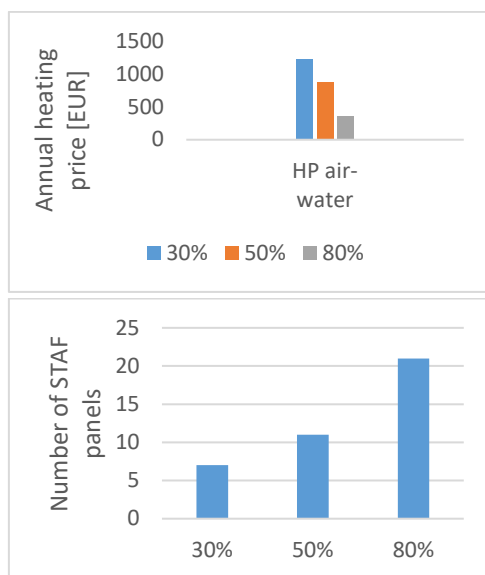


Figure 2: Heating price depending on the energy demand of a family household and the minimal number of required STAF panels

3 Conclusion and outlook

In the presented article we have shown the possible application of STAF panels with the heat pump technology. The results show that an application of STAF panels is very interesting from thermodynamic, ecologic as well as economic perspective.

A various number of CFD simulations were performed in order to analyse the thermal behaviour of STAF panels, the fluid in the pipes was heated up to 48.2 °C. The exterior temperature as well as the wind has a very strong impact on the thermal behaviour and the output. When the ambient temperature is higher than the average surface temperature of the exterior absorber plate, the fluid is additionally heated. Unfortunately, the absorber's heat loss increases as the ambient temperature decreases. The heat loss at low ambient temperatures can be reduced by installing a glass cover for the absorber. In the course of the project "ABS-Network SIAT 125" (ABS Network, 2018), further thermal and structural analyses of the STAF panel will be performed in order to optimize the whole construction and improve the thermal output. Additionally, outdoor tests will be performed at Graz, University of Technology to compare the thermal behaviour of the most promising STAF panel absorber geometries under real climate conditions.

References

- ABS Network. (2018). Interreg-project "ABS-Network SIAT 125" Retrieved from <http://abs-network.eu/en>
- ANSYS Fluent 18.2. Userguide/Theoryguide. Retrieved from <http://www.ansys.com>
- ANSYS Inc. (2018). Fluid Dynamics software "ANSYS Fluent 18.2.0". Retrieved from <http://www.ansys.com>
- Avsec, J., Novosel, U., & Zore, N. (2018). *Uporaba STAF sončnih panelov za ogrevanje : študijska naloga : fazno poročilo - izdelava končne vsebine naloge, vseh predpostavk in vhodnih podatkov*. Velenje: Fakulteta za energetiko.
- Bratkovič, A., & Irgl, R. (2006). *Daljinski sistemi ogrevanja na lesno biomaso*. Ljubljana: Enecon.
- Solar Irradiance. Retrieved from <http://solarelectricityhandbook.com/solar-irradiance.html>

Energy Efficiency Indicators of a Single Unit House

IZTOK BRINOVAR, GREGOR SRPČIČ, ZDRAVKO PRAUNSEIS, SEBASTIJAN SEME, BOJAN ŠTUMBERGER & MIRALEM HADŽISELIMOVIĆ

Abstract This article deals with the evaluation of energy efficiency indicators of an older single unit house with the use of “KI energija 2017” software, which is widely used among qualified Slovenian experts authorized to carry out the energy performance assessments and issue an energy performance certificate. The energy performance analysis before and after the implementation of proposed measures has shown significant energy saving potential in renovation of existing buildings.

Keywords: • energy efficiency • energy indicators • energy performance • building renovation • CO2 emissions •

CORRESPONDENCE ADDRESS: Iztok Brinovar, Assistant, University of Maribor, Faculty of Energy Technology, Hočevarjev trg 1, 8270 Krško, Slovenia, e-mail: iztok.brinovar@um.si. Gregor Srpčič, Assistant, University of Maribor, Faculty of Energy Technology, Hočevarjev trg 1, 8270 Krško, Slovenia, e-mail: grega.srpcic@um.si. Zdravko Praunseis, PhD, Associate Professor, University of Maribor, Faculty of Energy Technology, Hočevarjev trg 1, 8270 Krško, Slovenia, e-mail: zdravko.praunseis@um.si. Sebastijan Seme, PhD, Associate Professor, University of Maribor, Faculty of Energy Technology, Hočevarjev trg 1, 8270 Krško, Slovenia, e-mail: sebastijan.seme@um.si. Bojan Štumberger, Ph. D., Full Professor, University of Maribor, Faculty of Energy Technology, Hočevarjev trg 1, 8270 Krško, Slovenia, e-mail: bojan.stumberger@um.si. Miralem Hadžiselimović, PhD, Full Professor, University of Maribor, Faculty of Energy Technology, Hočevarjev trg 1, 8270 Krško, Slovenia, e-mail: miralem.h@um.si.

1 Introduction

Energy efficiency of buildings is an important element of the European Union (EU) climate and energy policy and is crucial for sustainable development and climate protection. According to statistics, buildings are responsible for almost 40 % of total energy consumption and more than 35 % of CO₂ emissions in the EU, (European commission, 2017). Large share of buildings in Slovenia and other European countries are over 40 years old and most of them are energy inefficient. Therefore, the renovation of existing buildings has a significant energy saving potential. Reduction of energy consumption and the use of renewable energy sources in buildings are important measures needed to reduce energy consumption and CO₂ emissions. Furthermore, energy efficiency improvement of buildings can generate other economic, social, health and environmental benefits. Consequently, this article deals with the evaluation of energy efficiency indicators of a single unit house. Additionally, two types of building renovation measures are proposed and energy efficiency indicators are reevaluated for each proposed measure.

2 Legislative background

The main legislation documents promoting the improvement of energy performance of buildings and providing a stable environment for renovation and investments in this sector are the European Energy Performance of Buildings Directive (EPBD – 2002/91/EC), which was adopted in 2002 and revised later in 2010 (EPBD – 2010/31/EU, (Official Journal of the European Union, 2010)), and the Energy Efficiency Directive (EED – 2012/27/EU, (Official Journal of the European Union, 2012)). These directives obliges EU member states to set up minimum energy performance requirements for new and renovated buildings, and issues the introduction of energy performance certificates and establishment of methodology for the calculation of energy performance of buildings.

Energy performance certificates in Slovenia are enacted by the Energy Act (EA – Official gazette of the Republic of Slovenia, No 17/14 and No 81/15), while the minimum energy performance requirements are determined by the document called “Rules on efficient use of energy in buildings – PURES 2010“, (Euportal.si, 2018). PURES 2010 sets out technical requirements that must be fulfilled for the efficient use of energy in buildings in the field of thermal protection/insulation, heating, cooling, ventilation or their combinations, lighting, the preparation of

hot water, and the use of renewable energy sources for the operation of systems in the building in accordance with EPBD. In Slovenia, the use of PURES 2010 together with the Technical Guideline (TSG-1-004) is mandatory in the construction of new buildings and the renovation of existing ones. The TSG-1-004 specifies construction measures or solutions to meet the requirements of PURES 2010 and determines the methodology for the calculation of energy performance of buildings.

2.1 Energy efficiency indicators of a single unit house

There are a number of different tools and programs available to analyse and document the energy performance of buildings. The evaluation of energy efficiency indicators of a single unit house is carried out in accordance with PURES 2010 and with the use of a software called “KI Energija 2017” developed by company Knauf Insulation (KI Energija, 2017). In Slovenia, this software is widely used among qualified experts authorized to carry out the energy performance assessments and issue an energy performance certificate. The program allows the user to comprehensively review and analyse the energy performance of a building while taking into account the following characteristics :

- thermal characteristics of construction materials (building envelope),
- passive heating,
- thermal bridges,
- heating installation and hot water supply,
- air-conditioning installations,
- natural and mechanical ventilation,
- built in lighting installation,
- the design, positioning and orientation of the building,
- outdoor and indoor climate conditions,
- internal loads,
- etc.

The evaluation of energy efficiency indicators is done for an older single unit house. Additionally, two of the following building renovation measures are proposed: Measure I (installation of new windows) and Measure II (thermal insulation of the building envelope). Figure 1 presents the delivered thermal

energy for heating (extra light fuel oil) and required electrical energy for operation of the building before the renovation, while the impact of proposed renovation measures on energy efficiency indicators is presented in Figure 2.

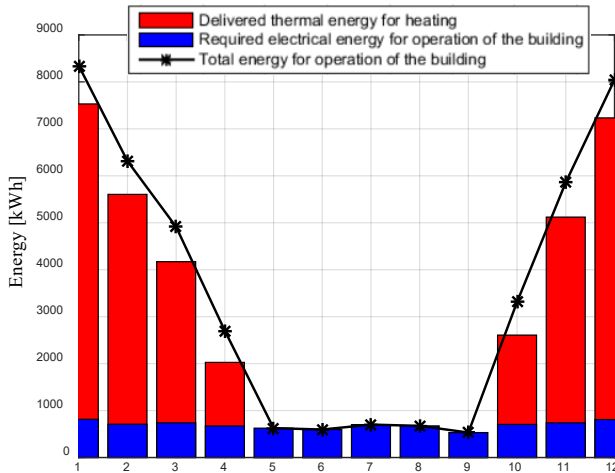


Figure 1: Total energy for operation of the building.

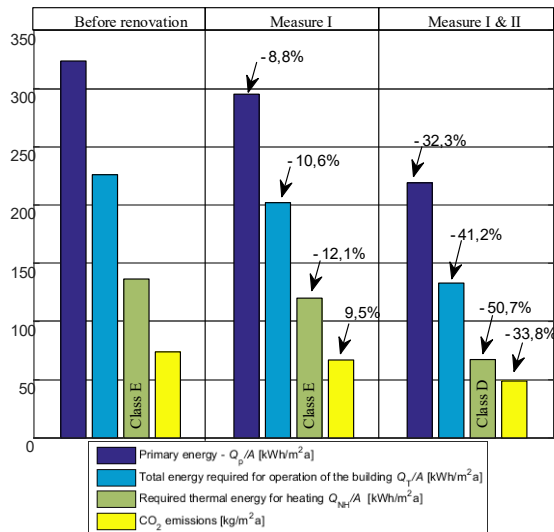


Figure 2: Energy efficiency indicators of the building before and after the implementation of proposed measures.

The energy performance analysis of the building before and after the implementation of proposed measures has shown significant energy saving potential in renovation of existing buildings, as total energy required for operation of the building was reduced by 41,2 %, while the building energy efficiency was raised from class E to class D (this class is determined by indicator Q_{NH}/A - required thermal energy for heating).

3 Conclusion

The analysis has shown significant energy saving potential in renovation of older buildings. In addition to organizational measures several other measures should be proposed and analysed. Any investment in the proposed measures should also be economically validated. Any deviations between actual and calculated values most frequently originate from inaccurate input parameters, the use of the calculation method (simplifications allowed by Technical Guideline), and from inaccuracies that are related to the data acquisition made by the expert.

References

- European Commission, (2017). Available at:
<https://ec.europa.eu/energy/en/topics/energy-efficiency/buildings>
- Official Journal of the European Union, (2010): Directive 2010/31/EU of the European parliament and of the council of 19 May 2010 on the energy performance of buildings. Available at: <http://eur-lex.europa.eu/LexUriServ/LexUriServ.do?uri=OJ:L:2010:153:0013:0035:EN:PDF>
- Official Journal of the European Union (2012): Directive 2012/27/EU of the European parliament and of the council of 25 October 2012 on energy efficiency.
- Euportal.si : Energy performance certificate introduced in Slovenia, (2018). Available at: <http://www.euportal.si/en/slovenia-in-eu/energy-performance-certificate-introduced-in-slovenia/>
- “KI Energija”, (2017). Software developed by Company Knauf Insulation d.o.o..

Evaluation of the Impact of Symmetrical Voltage Sags on the Performance of a Line-Start IPM Synchronous Motor Drive

TINE MARČIČ

Abstract The occurrence of voltage sags may have significant impact on a drive employing a line-start interior permanent magnet synchronous motor (LSIPMSM). This particular motor type may fall out of synchronism and rotor speed may change significantly. Thus, the motor needs to restart the complete drive and resynchronize again after the voltage sag is over. In this work a dynamic model is employed in evaluation of LSIPMSM performance by considering occurrence of symmetrical voltage sags with different loads and drive inertia.

Keywords: • dynamic model • permanent magnet synchronous motor • squirrel cage • voltage sag (dip) • sensitivity analysis •

CORRESPONDENCE ADDRESS: Tine Marčič, Ph.D, Energy Agency of the Republic of Slovenia, Strossmayerjeva ulica 30, SI-2000 Maribor, Slovenia, e-mail: tine.marcic@agen-rs.si.

DOI <https://doi.org/10.18690/978-961-286-241-1.40>
Available at: <http://press.um.si>.

ISBN 978-961-286-241-1

1 Introduction

Voltage sags (also called voltage dips) are decreases of grid-voltage root-mean-square (RMS) value with relative short duration, which can cause undesirable equipment trips (Klaić, 2014) and problems in industrial processes (Kazemi, 2013). They are caused by short-duration increases in currents (Polajžer, 2015) because of faults in the transmission or distribution network (Klaić, 2014), heavy load switching, motor starting and energizing transformers (Bagheri, 2018). The occurrence of voltage sags may have significant impact on a drive employing a line-start interior permanent magnet synchronous motor (LSIPMSM), even more severe than those directly related to induction motors (IMs) (Guasch, 2004). Due to a voltage sag occurrence, the LSIPMSM may fall out of synchronism and its rotor speed may change significantly. As a consequence, the LSIPMSM may need to restart the complete drive and resynchronize again after the voltage sag is over. In this work a dynamic model was employed, which was rigorously tested in (Marčič, 2014). Sinusoidal voltages with voltage sags were fed to the model and a comprehensive sensitivity analysis was performed.

2 Results and analysis

2.1 Symmetrical voltage sag occurrence when the LSIPMSM is not loaded

Following worst case scenarios for a LSIPMSM performance, symmetrical voltage sags are considered in the analysis because they have the most detrimental effect on LSIPMSM line-starting and resynchronisation ability. A symmetrical voltage sag occurs when the lowered voltage amplitudes of individual phase grid voltages remain equal and their phase relationship remains 120° during a sag. Any other type is considered as unsymmetrical (Guasch, 2004). Fig. 1 presents illustrative results of the LSIPMSM performance during a 0.75 p.u. symmetrical voltage sag with a duration of 0.2 s. The presented values have been obtained without any additional mechanical load or inertia. Thus, these results provide detailed insight into LSIPMSM cause and effect relationships during a voltage sag. At 0 s the LSIPMSM is started from line at rated voltage and frequency (380 V / 50 Hz) with help of the cage current torque component, which accelerates the LSIPMSM's own rotor inertia. The motor then reaches steady-state in synchronism. The voltage sag occurs at 0.2 s and lasts till 0.4 s. The instant change of voltage amplitudes at 0.2 s is followed by compensating peaks of phase

currents, which interact with the permanent magnets, as well as peaks of damping cage currents, which together produce a braking torque peak which pulls the rotor out of synchronism and decelerates the rotor inertia to a new steady state occurring at approximately 0.3 s, where the LSIPMSM' speed periodically alternates around zero. At 0.4 s the voltage sag is over and voltage is restored to its initial amplitude. The LSIPMSM is restarted with help of the cage current torque component, it accelerates the rotor and reaches again steady-state in synchronism. The resulting torque envelope during restarting and resynchronisation observed from 0.4 s onwards differs from the initial resulting torque envelope during line-starting observed from 0 s onwards which is caused by different initial current values interacting at the instant following 0 s and 0.4 s, respectively. The here described interactions happened relatively fast since the LSIPMSM was not connected to any load.

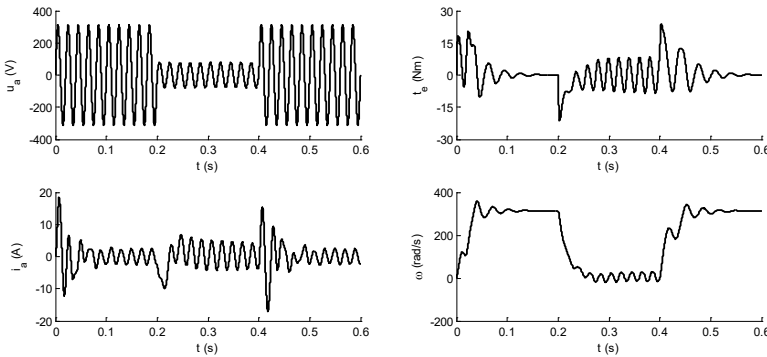


Figure 1: LSIPMSM performance without any additional load or inertia during a symmetrical voltage sag of 0.75 p.u. with a duration of 0.2 s

2.2 Impact of the moment of inertia

Fig. 2a presents a comparison of the LSIPMSM drive performance, where the drive inertia has been varied between 1- and 20-times the LSIPMSM rotor moment of inertia without applying any additional load. The voltage sag started at 2 s and lasted till 3 s, its amplitude was set to 0.9 p.u. in order to simulate the worst case. In Fig. 2a the numbers placed near individual speed characteristics indicate the drive inertia in multipliers of the LSIPMSM rotor moment of inertia. The results presented in Fig. 2a show that increase of the inertia prolongs the time which is needed to reach a steady-state. This poses a problem if the inertia

is too large and the LSIPMSM could not accelerate the drive enough in order to synchronise. Of course this depends on the particular voltage sag case, but notably the results also show that the inertia, which on one hand poses one of the problematic issues in the line-starting transient on the other hand during this particular voltage sag, the larger inertia (20-times the LSIPMSM rotor moment of inertia) actually helped the LSIPMSM to stay for a longer time near the synchronous speed and thus it resynchronised with the larger inertia (20-times the LSIPMSM rotor moment of inertia) at approximately the equal time at which it resynchronised with the smaller inertia (8-times the LSIPMSM rotor moment of inertia).

2.3 Impact of the load torque

Fig. 2b presents a comparison of the LSIPMSM drive performance, where the LSIPMSM was loaded with a torque which was varied between 0, 3.75 and 7.5 Nm. The latter presents the LSIPMSM's rated load torque. The load torque was kept constant at all speeds, thus representing a constant load drive and simulating loads such as screw compressors, conveyors, ball mills, etc. The drive inertia was 8-times the LSIPMSM rotor moment of inertia and the voltage sag started at 2 s and lasted till 3 s. The voltage sag amplitude was set again to 0.9 p.u. In Fig. 2b the numbers placed near individual speed characteristics indicate the load torque in Nm. The results presented in Fig. 2b show that the load torque is additionally braking the LSIPMSM during the voltage sag, thus the drive decelerates faster. Moreover, Fig. 2b also highlights another problem, namely that the load may accelerate the complete drive in the opposite direction if the electromagnetic torque in steady-state during a voltage sag (a detail is shown in Fig. 1) does not counterbalance the load torque, which may present an additional problem when the LSIPMSM must recover and resynchronise after a voltage sag. Although, results show that the tested LSIPMSM successfully restarted and resynchronised in this particular case, if the voltage sag lasted longer, the load would accelerate the drive further to a higher speed in the opposite direction and this in turn could prevent the LSIPMSM to successfully restart and resynchronise when the voltage sag is over.

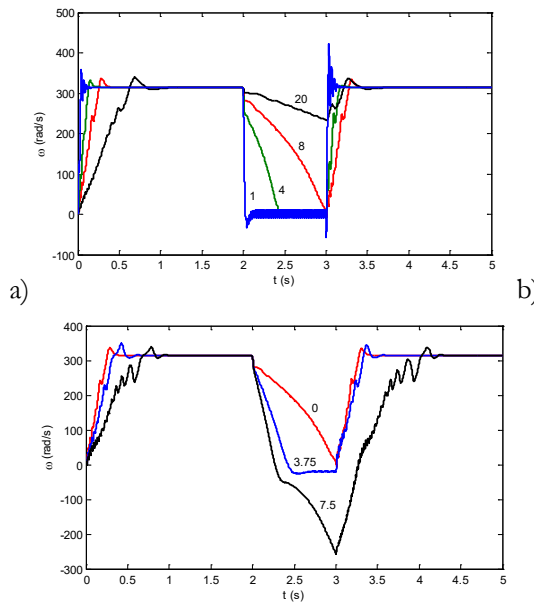


Figure 2: LSIPMSM speed performance curves: a) without any load and with varied inertia, and b) with 8-times the rotor inertia and varied constant load torque

3 Conclusion

This work highlights that the occurrence of voltage sags may have significant impact on a LSIPMSM drive performance. Relevant factors impacting the LSIPMSM restarting and resynchronization capability have been evaluated by employing a dynamic model of the LSIPMSM. Experimental research will be done in future work.

Acknowledgments

The author's research was done at TECES, Pobreška cesta 20, SI-2000 Maribor, Slovenia.

References

- Bagheri A., Bollen M. H. J., Gu I. Y. H. (2018). Improved characterization of multi-stage voltage dips based on the space phasor model. *Electric Power Systems Research*, 154, 319-328. doi: 10.1016/j.epsr.2017.09.004
- Guasch L., Córcoles F., Pedra J. (2004). Effects of symmetrical and unsymmetrical voltage sags on induction machines. *IEEE Transactions on Power Delivery*, 19, 774-782. doi: 10.1109/TPWRD.2004.825258

- Kazemi A., Mohamed A., Shareef H., Zayandehroodi H. (2013). Review of voltage sag source identification methods for power quality diagnosis. *Przegląd Elektrotechniczny*, 89, 143-149.
- Klaić Z., Fekete K., Knežević G. (2014). Analysis of the voltage sag propagation through the distribution network. *Journal of Energy Technology*, 7, 11-26.
- Marčič T.; Štumberger B.; Štumberger G. (2014). Differential-evolution-based parameter identification of a line-start IPM synchronous motor. *IEEE Transactions on Industrial Electronics*, 61, 5921-5929. doi: 10.1109/TIE.2014.2308160
- Polajžer B., Štumberger G., Dolinar D. (2015). Instantaneous positive-sequence current applied for detecting voltage sag sources. *IET Generation, Transmission and Distribution*, 9, 319-327. doi: 10.1049/iet-gtd.2014.0483

Accuracy of Rotational Speed and Torque Sensors for Determining the Mechanical Power of Rotating Electrical Machines

GREGOR SRPČIČ, IZTOK BRINOVAR, BOJAN ŠTUMBERGER, SEBASTIJAN
SEME & MIRALEM HADŽISELIMOVIĆ

Abstract This paper deals with determining the accuracy of measuring systems for determining the characteristics of rotating electrical machines. Efficiency classes and experimental methods for determining efficiency, are given in a standard, which has to be strictly respected. For determining the efficiency of an electrical machine, it is necessary to have a modern and accurate measurement system with sensors of high accuracy classes, which enables the user to carry out precise measurements and consequently, to determine all the characteristics of the electrical machine. This paper will be focused on torque and speed measurements.

Keywords: • efficiency • measuring system • electric machines • torque and rotational sensors • accuracy •

CORRESPONDENCE ADDRESS: Gregor Srpčič, Assistant, University of Maribor, Faculty of Energy Technology, Hočevarjev trg 1, 8270 Krško, Slovenia, e-mail: grega.srpacic@um.si. Iztok Brinovar, Assistant, University of Maribor, Faculty of Energy Technology, Hočevarjev trg 1, 8270 Krško, Slovenia, e-mail: iztok.brinovar@um.si. Bojan Štumberger, PhD, Full Professor, University of Maribor, Faculty of Energy Technology, Hočevarjev trg 1, 8270 Krško, Slovenia, e-mail: bojan.stumberger@um.si. Sebastijan Seme, PhD, Associate Professor, University of Maribor, Faculty of Energy Technology, Hočevarjev trg 1, 8270 Krško, Slovenia, e-mail: sebastijan.seme@um.si. Miralem Hadžiselimović, PhD, Full Professor, University of Maribor, Faculty of Energy Technology, Hočevarjev trg 1, 8270 Krško, Slovenia, e-mail: miralem.h@um.si.

1 Introduction

Electrical machines have been constantly improved since their creation. In the recent period, the direction of the development of electrical machines is geared towards increasing efficiency. Manufacturers of electrical machines are faced with new directives and standards that prescribe efficiency classes. Together with efficiency classes, also restrictions about, which drives can still operate in the European Union, emerged. Efficiency classes and experimental methods for determining efficiency, are given in a standard, which has to be strictly respected. For determining the efficiency of an electrical machine, it is necessary to have a modern and accurate measurement system with sensors of high accuracy classes, which enables the user to carry out precise measurements and consequently, to determine all the characteristics of the electrical machine. In this paper, we will focus on torque and speed measurements, which are both important for determining the mechanical power and together with current and voltage measurements for determining the efficiency of an electrical machine, (Hadžiselimović M. et al., 2017).

2 Efficiency classes, accuracy classes and measurement uncertainty

The current directives or regulations allow the sale of IE2 motors in the European Union insofar as they operate with converters and IE3 motors that are powered directly from electrical grid. Standard IEC/EN 60034-30-1 is concerned with the global harmonization of energy efficiency classes for electric motors. This new standard significantly expands the range of products covered with the inclusion of 8-pole motors and introduces IE4 efficiency performance class for electric motors. Table 1 gives some examples of desired efficiencies for different efficiency classes and sizes of motors. As it can be seen from the table, the difference between efficiency classes between electrical machines with high nominal powers is small. In some cases less than 1%, therefore it is hard to determine the efficiency class precisely due to measurement uncertainty and accuracy classes of the used sensors, (ABB. Technical note: IEC 60034-30-1 standard on efficiency classes for low voltage AC motors. 2014).

Table 1: Examples of threshold levels of the motor efficiency class (efficiency values are given in %) (ABB. Technical note: IEC 60034-30-1 standard on efficiency classes for low voltage AC motors, 2014)

P_N (kW)	4 pole				2 pole			
	IE1	IE2	IE3	IE4	IE1	IE2	IE3	IE4
0,12	50,0	59,1	64,8	69,8	45,0	53,6	60,8	66,5
3	81,5	85,5	87,7	90,4	81,5	84,6	87,1	89,1
11	87,6	89,8	91,4	93,3	87,6	89,4	91,2	92,6
110	93,3	94,5	95,4	96,0	93,3	94,3	95,2	96,3
1000	94,0	95,1	96,0	96,7	94,0	95,0	95,8	96,5

3 Efficiency measurements

For measurements of electrical machines a system, which is composed of three interconnected parts (power, control and measurement part), was designed. This system consists a power supply, test machine, rotational speed and torque sensor, load machine, converter, power analyser, resistance instrument, control part and computers with software, (Hadžiselimović M. et al., 2017). For measuring of the rotational speed and torque, three different sensors were used: Lorenz DR2643 100 Nm, Lorenz DR2643 20 Nm and HBM T40B 100 Nm. All three sensors that were used for torque and rotational speed measurements have an accuracy class of 0,05 %.

The tested machine was a 4 pole 3 kW explosion proof induction machine, with rated efficiency of 87,8 %. The tested machine and its nominal data are presented in in figure 1 and table 2.



Figure 1: The tested explosion proof induction machine

Table 2: Nominal data of the tested machine

f [Hz]	50
$U(Y)$ [V]	400
P [kW]	3
$\cos \varphi$	0,83
n [min^{-1}]	1455
I [A]	5,97
η [%]	87,80
M [Nm]	19,90

4 Conclusion - results

Figure 2 presents the results of performed load tests, for all three sensors for both sides of rotation and at different input voltages to the tested machine. It is evident from the figures that efficiency is dropping while the temperature of the motor is rising. However, efficiency never falls under the limit of the IE3 efficiency class. This means that the tested machine is well designed. As we can see, efficiency measured with different torque and rotational speed is almost the same at similar temperatures, since it is almost impossible to measure with all three sensors at the exact same temperature. In addition, efficiency measurements at similar temperature in the left and right side of rotation were almost the same. From this measurement results we can conclude that our measurement system is precise and all three torque and rotational speed sensors are precise enough in order to measure IE3 efficiency class machines.

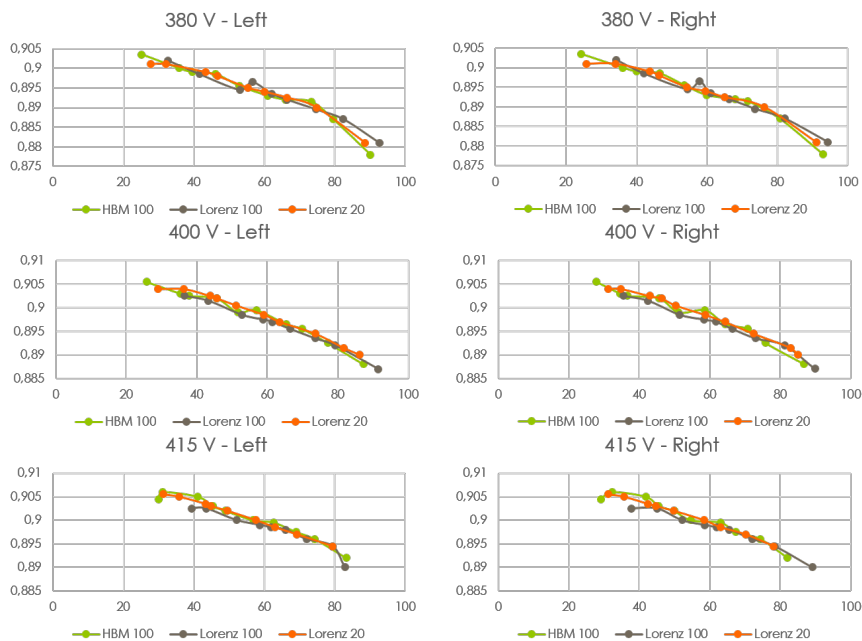


Figure 2: Measured efficiency of the tested machine at 400 V:

References

- Hadžiselimović M., Brinovar I., Srpić G., Seme S., Štumberger B., (2017). Measurement Systems for Determining the Characteristics of Electrical Machines. *International Conference on Modern Electrical and Energy Systems*.
- ABB. Technical note: IEC 60034-30-1 standard on efficiency classes for low voltage AC motors. (2014). Available at: https://library.e.abb.com/public/1018a82e36b29462c1257d41002b3470/TM025%20EN%2008-2014%20IEC60034-30-1_lowres.pdf. 23. 4. 2018

Comparison and Analysis of Mechanical Torque and Efficiency of the Multi-Phase Induction Motor

VENCO ČORLUKA, ŽELJKO HEDERIĆ & MARINKO BARUKČIĆ

Abstract This paper describes the basic performance of multi-phase induction motors. In addition to conventional three-phase induction motors, multi-phase motors are increasingly used where the number of phases can be chosen at will, usually for high-power applications concerning fault tolerant capability and wide range speed-torque characteristics (electrical and hybrid vehicles, aerospace applications, electrical ship propulsion). The problem that arises in multiphase motors is the power supply system that must run via an inverter that outputs a rectangular voltage at the output. The main purpose of providing performance analysis of the multi-phase motor is to improve characteristics such as reducing voltage values per phase, reducing the ripple of torque and greater efficiency. Multiphase induction motors can be carried out for a different number of phases and poles, which requires a particular construction and arrangement of the stator windings in the slots. Since the power supply is simulated by pure sinusoidal voltages for all three types of machine, the influence of the harmonics is not considered.

Keywords: • induction motor • multi-phase winding • pole-phase modulation • efficiency • mechanical torque •

CORRESPONDENCE ADDRESS: Venco Čorluka, PhD, J. J. Strossmayer University of Osijek, Faculty of Electrical Engineering, Computer Science and Information Technology Osijek, Kneza Trpimira 2B, HR-31000 Osijek, Croatia, e-mail: venco.corluka@ferit.hr. Željko Hederić, PhD, Associate Professor, Faculty of Electrical Engineering, Computer Science and Information Technology Osijek, Kneza Trpimira 2B, HR-31000 Osijek, Croatia, e-mail: zeljko.hederic@ferit.hr. Marinko Barukčić, PhD, Assistant Professor, Faculty of Electrical Engineering, Computer Science and Information Technology Osijek, Kneza Trpimira 2B, HR-31000 Osijek, Croatia, e-mail: marinko.barukcic@ferit.hr.

1 Introduction

Multiphase electric machines are becoming more and more important in today's high power applications. The induction machine (IM) is used in a wide variety of applications as a means of converting electric power to mechanical power. Pump steel mill, hoist drives, household applications are few applications of most commonly used of induction machines. In this paper are presented analyses of torque, mechanical power, efficiency and speed for a 4-pole induction motor with 3, 6 and 9 phases distributed in 36 slots on the stator. The phase number appears to be unnecessarily large, but the advantages as a reduction in voltage spike on power switches and DC link supports the selection of large phase number. Multiphase (more than three phases) machines have some advantages over three-phase ones: improved fault tolerance, reduced torque pulsations, lower per phase power handling requirements, enhanced modularity and improved noise characteristics. The simulation model, the calculation of the magnetic field distribution, losses and other parameters are created in the software package ANSYS.

1.1 Machine topology

The 4-pole induction motor (3, 6 and 9 phases, copper windings) nominal power of 3800 W and the rotational speed of 1420 rpm, with aluminium as casting material of rotor cage, being analysed. The stator consists of 36 slots in which are distributed 3, 6 or 9 phase windings (a single layer winding with a single coil group per phase) with pole phase modulation. The slot fill factor is 52% with 20 conductors per slot each of 1.08 mm diameter. Stator bore diameter is $D=175$ mm and core length $L=150$ mm. The rotor with 26 slots is selected considering crawling, cogging and synchronous torque as per the guidelines are given in.

First is presented a case of the 6-phase induction machine with a full pitch winding as a combination of two sets of the 3-phase windings that are displaced 30 degrees in space. The idea is to make two electrically and magnetically independent 3-phase systems so that a fault in one system should not affect the other system. The power supply is from two independent power sources which are 30 degrees displaced in time from each other.

The second case is the 9-phase machine as a combination of three sets of 3-phase windings which are displaced by 20 degrees to each other. The machine is

supplied from three independent power sources which are 20 degrees displaced in time from each other.

The presented cases show a 3-phase machine modified to higher phase machines. To achieve that the slot per pole and per phase are 6, 3 and 2 for the 3, 6 and 9 phase machine. For the selected number of phases and poles, the total number of slots on the stator can be determined according to the expression:

$$N_s = N_m \cdot N_p \cdot k \tag{1}$$

where are: N_s - the total number of slots, N_m - the number of phases, N_p - the number of poles and k - the number of equivalents phase. For 3-phase 4-pole IM the total number of slots according to the expression (1) can be 12, 24, 36,..., for 6-phase 6-pole IM slot number can be: 36, 72,... and for the 9-phase 4-pole slot number can be 36, 72,... The phase and winding pattern for all three types of IM version in the 2-pole view are given in Tables 1, 2 and 3.

Table 1. Phase pattern for 3-phase 4-pole IM 18 slots

3 phase induction machine																	
A	A	A	-C	-C	-C	B	B	B	-A	-A	-A	C	C	C	-B	-B	-B
N									S								

Table 2. Phase pattern for 6-phase 6-pole IM 18 slots

6 phase											
A	-D	B	-E	C	-F	-A	D	-B	E	-C	F
N						S					

Table 3. Phase pattern for 9-phase 4-pole IM 18 slots

9 phase induction machine																	
A	-F	B	-G	C	-H	D	-I	E	-A	F	-B	G	-C	H	-D	I	-E
N									S								

The voltages at each phase are symmetrical and the phase shift depends on the number of phases so that for the 3-phase motor the phase shift is 120 el. degrees, for the 6-phase is 60 degrees and for the 9-phase is 40 el. degrees.

2 FEA Simulation and results

The simulation and FEA model of the distribution of magnetic induction rotor and stator and the time diagrams of torque, power and current are made in the program ANSYS Maxwell 2D. The assembly of all triangles is referred to as the finite element mesh of the model or simply the mesh. The magnetic flux density of the machine is the function of space and time. The distribution of the magnetic induction B of each discrete space in a triangular shape, is solved using Poisson's over-integration equation and energy functional for observed volume by variation method.

Figures 1 show 2D magnetic induction distribution for 6-phase 6-pole IM obtained by FEA simulation in ANSYS. Figure 2 shows the lines of the magnetic field strength in the 9-phase 4-pole IM. The simulation is performed at about nominal load and speed of 1420 rpm for 4-pole IM and 940 rpm for 6-pole IM with a pure sinusoidal waveform input voltage. In both figures, the red colour represents the highest magnetic induction values, which is mostly present in the poles of the upper part of the iron stator core. Blue colour gives the smallest induction and is reflected in the slots of stator and rotor and the air gap. The unequal distribution of magnetic induction around the stator slots arise from the different number of rotors and stator slots and resulting in larger losses in the iron core. To achieve better resolution of the magnetic induction must be obtained higher discretized in space and as many triangular elements, especially in the air gap and around it. From the simulation can be determined all important parameters of IM and their graphical representations such as torque, power, rotor speed, current, voltage, linked magnetic fluxes, EMF, efficiency and losses in the core and windings. In this paper will be analysed comparison of torque, mechanical power and efficiency at the three engines of the same electrical and mechanical characteristics and dimensions of loaded nominal power.

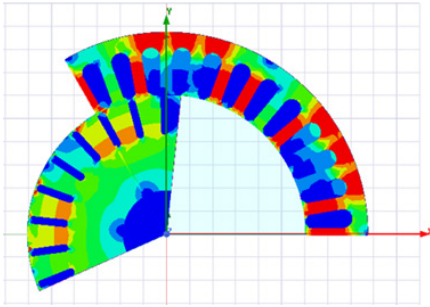


Figure 1: Distribution of magnetic induction for 6-phase, 6-pole IM

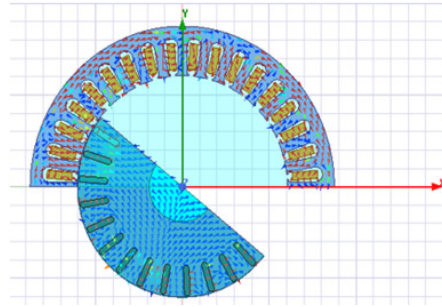


Figure 2: Magnetic field lines phase for 9-phase, 4-pole IM

The efficiency of the analysed 3-phase, 6-phase and phase-9 IM is given in Figure 3 and is obtained as the ratio of output and input power in percents. The curve "a" represent efficiency of the 3-phase 4-pole IM with the value of 57%. Little higher efficiency achieve a 6-phase 6-pole motor (66%) represented with the curve "b", while the highest efficiency has a 9-phase 4-pole motor (85%) represented with the curve "c".

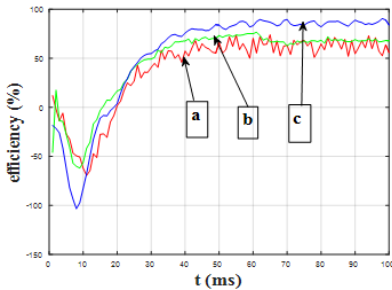


Figure 3: Time diagram of the efficiency for 3-phase, 6-phase and 9-phase IM

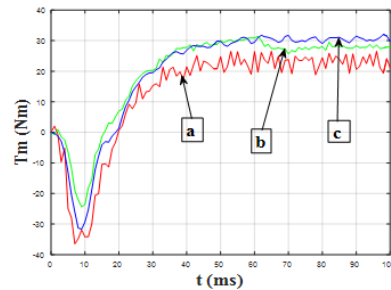


Figure 4: Time diagram of mechanical moments for 3-phase, 6-phase and 9-phase IM

Figure 4 shows mechanical torques for all three IM cases at approximately nominal load of 3800 W. The curve "a" represent the mechanical torque of the 3-phase 4-pole motor from the run-up to steady-state speed of 1420 rpm, the curve "b" represent the mechanical torque of the 6-phase 6-pole motor (steady-state speed of 940 rpm) and the curve "c" represent the mechanical torque of 9-phase 4-pole motor (steady-state speed of 1420 rpm).

Table 4. Comparison of parameter values for three different types of IM obtained by simulation.

Values	3-Phase 4-Pole	6-Phase 6-Pole	9-Phase 4-Pole
P_{el} (W)	6140	4151	5528
P_m (W)	3500	2740	4698
T_m (Nm)	22	27	30

For a better overview, all the values of these parameters are given in Table 4 where are: P_{el} - electric power, P_m - mechanical power T_m - mechanical torque and η - efficiency. From these results, it can be concluded that multiphase motors have better characteristics than 3-phase motors. Here it should be emphasized that the simulation was performed out with a sinusoidal voltage supply and the effect of the harmonic was minimized. This is not a problem with 3-phase motors, but for 4 and more phase motors, the voltages are obtained by using of an inverter which gives a rectangular waveform at the output, so higher harmonics have to be considered.

3 Conclusion

This paper analyses the 4-pole IM with 3, 6 and 9 phase, and a graphical representation of torque, power, efficiency and distribution of magnetic induction on the rotor and stator. Space harmonics in the air-gap field due to winding distribution are neglected. To increase the motor's power per phase and to decrease its weight a multi-phase motor was used. The torque pulsation is least in 9-phase 4-pole IM case and well within limits for all other pole phase combinations. The advantages of the multi-phase motor over the base type 3-phase IM is improved reliability and reduction of the power per inverter leg. Other advantages of the multi-phase motors are the improvement of the noise, a possibility of a reduction in the stator copper losses leading to an improvement in the efficiency and the improvement of the torque-speed characteristics by increasing the low speed torque more than 5 times than in case of the 3-phase induction motors. One of the interesting features of the 6-phases and 9-phases machines is the lower fluctuation in damper bar currents and torque. Iron losses and rotor aluminium losses are reduced by reducing the phase current. Losses in the stator copper are higher in the 9-phase IM and affect the efficiency. Iron losses do not depend on the stator phase number but the harmonic spectrum improvement gained in 6-phase and 9-phase machine definitely helps to improve the losses.

References

- Kashif S.K.(2008). Comparative analysis of multiphase machines. *Master's Thesis in the International Master's programme in Electric Power Engineering*, Goteborg Sweden
- Umesh B. S., Sivakumar K. (2014). Multiphase Induction Motor Drive with 1:3:9:15 Speed Ratios for Gear Free Electric Vehicle Application. *7th International Conference on Information and Automation for Sustainability*, doi: 10.1109/ICIAFS.2014.7069559
- Levi E., Bojoi R., Profumo F., Tolyat H.A., Williamson S. (2007). Multiphase induction motor drives – a technology status review. *Electric Power Application, IET*, vol. 1, pp. 489-5
- Duran M.J., Levi E., Jones M. (2005). Independent vector control of asymmetrical nine-phase machines by means of series connection. *IEEE International Electric Machines and Drives Conference, IEMDC*, San Antonio, Texas, USA, pp. 167- 173.
- Moghadasianx M., Betin F., Yazidi A., Capolino G. A. and Kianinezhad R. (2012). Position control of six-phase induction machine using fractional-order controller. *Proceedings of the Int. Conf. on Electrical Machines ICEM*, Marseille, France, pp. 1048-1054.
- Riveros J., Bogado B., Prieto J., Barrero F., Toral S. and Jones M. (2010). Multiphase machines in propulsion drives of electric vehicles. *Proceedings of the Power Electronics and Motion Control Conf. EPE-PEMC*, Ohrid, Macedonia, pp. T5-201-206.



University of Maribor

Faculty of Energy Technology

17th to 20th June, 2018, Podčetrtek, Slovenia

